Electrothermal Modeling, Simulation and Optimization of Surge Arresters

Elektrothermische Modellierung, Simulation und Optimierung von Überspannungsableitern
Zur Erlangung des akademischen Grades Doktor-Ingenieur (Dr.-Ing.)
genehmigte Dissertation von Yvonne Thea Katharina Späck-Leigsnering aus Offenbach am Main
Tag der Einreichung: 02.07.2019, Tag der Prüfung: 21.08.2019
Darmstadt — D 17

1. Gutachten: Prof. Dr.-Ing. Herbert De Gersem
2. Gutachten: Prof. Dr.-Ing. Volker Hinrichsen
3. Gutachten: PD Dr. rer. nat. habil. Erion Gjonaj

TECHNISCHE
UNIVERSITÄT
DARMSTADT

Electrothermal Modeling, Simulation and Optimization of Surge Arresters
Elektrothermische Modellierung, Simulation und Optimierung von Überspannungsableitern

Genehmigte Dissertation von Yvonne Thea Katharina Späck-Leigsnering aus Offenbach am Main

1. Gutachten: Prof. Dr.-Ing. Herbert De Gersem
2. Gutachten: Prof. Dr.-Ing. Volker Hinrichsen
3. Gutachten: PD Dr. rer. nat. habil. Erion Gjonaj

Tag der Einreichung: 02.07.2019
Tag der Prüfung: 21.08.2019

Darmstadt — D 17

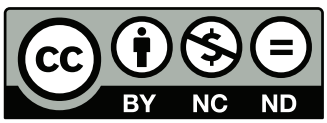

„Eine Wissenschaftlerin zu sein ist, wie eine Entdeckerin zu sein. Man hat diese immense Neugier, diese Sturheit, diesen entschlossenen Willen, vorwärts zu gehen, egal was andere Leute sagen."

Sara Seager (Astrophysikerin)

Danksagung

An dieser Stelle möchte ich all jenen danken, die durch ihre fachliche und persönliche Unterstützung zum Gelingen dieser Dissertation beigetragen haben.

Mein Dank gilt Prof. Dr.-Ing. Herbert De Gersem für die Einladung, am Institut für Teilchenbeschleunigung und Elektromagnetische Felder (TEMF) an einem Thema meiner Wahl zu forschen und mit Studierenden zusammen zu arbeiten. Vielen Dank auch dafür, dass die Bürotür immer offen war, um Rat und Unterstützung zu erhalten. Besonders bedanken möchte ich mich bei Privatdozent Dr. rer. nat. habil. Erion Gjonaj für die federführende Betreuung. Seine Ideen, intensive Begleitung und direktes Feedback trugen entscheidend zum Erfolg dieser Arbeit bei. Ebenso danke ich Prof. Dr.-Ing. Volker Hinrichsen für die stete Begleitung und Förderung während der Promotionsphase und die Übernahme des Korreferats dieser Arbeit. Danken möchte ich außerdem Dr.-Ing. Moritz Gießel für die fachlichen Diskussionen und die gemeinsame Projektarbeit zu praktischen Aspekten von Überspannungsableitern.

Ich bin dankbar, dass ich im Rahmen meiner Promotionsphase mit motivierten und herausragenden Studierenden zusammen arbeiten durfte. Als HilfswissenschaftlerInnen oder in Form von studentischen Arbeiten haben sie zum Gelingen der Arbeit beigetragen. Hierbei möchte ich besonders Greta Ruppert, Robin Scheich und Laura D'Angelo nennen, die mit ihrer ausgezeichneten Arbeit jeweils wissenschaftliche Publikationen ermöglichten. Besonderer Dank gilt Greta Ruppert, die mich als Hilfswissenschaftlerin in der Endphase der Arbeit unterstützte.

Mein Dank geht an die KollegInnen am TEMF, es war eine Freude, mit Euch arbeiten zu dürfen. Ein besonderer Dank gilt Yun Ouédraogo für die vielen fachlichen Diskussionen und die gegenseitige Unterstützung auf dem Weg zur Promotion. Ein herzliches Dankeschön auch an das unterstützende Team am Institut, Heike Koch, Wolfgang Müller, Dragos Munteanu und Achim Wagner.

Ich möchte mich bei meiner Familie, meinen Eltern Dorothee und Helmut, meiner Schwester Marilena und meinen Schwiegereltern, Karin und Franz, für ihre Unterstützung und Liebe bedanken. Ich bin besonders dankbar für ihre Zeit, Liebe und Verlässlichkeit bei der Betreuung unseres Sohnes Laurin in der Endphase der Dissertationserstellung. Ich danke weiterhin all den FreundInnen, die mich auf dem Weg zur Promotion begleiteten. Schließlich danke ich meinem Mann Michael für seine bedingungslose Liebe und dafür, dass er mich immer ermutigt und mit vielen intensiven Diskussionen und Gedanken zu dieser Dissertation beigetragen hat.

Yvonne Thea Katharina Späck-Leigsnering
Mühltal, im August 2019

Abstract

The protection of power transmission systems against voltage surges relies on station class surge arresters. The core of an arrester consists of a stack of metal oxide resistors. The highly nonlinear *U-I*-characteristic of these resistors allows the arrester to clip voltage surges by conducting current to ground and thereby absorbing large amounts of energy. The most important arrester design objectives are, first, to ensure a balanced distribution of the field and temperature stress along the arrester column, and, second, to guarantee the thermal stability of the arrester after, e.g., a lightning strike. Standard laboratory test procedures for evaluating thermal stability are limited to worst case surrogate models of the full-scale arrester. Hence, numerical finite element simulation is increasingly valuable for analyzing full-scale surge arresters as an alternative to conventional design based on laboratory or field testing approaches.

The analysis of arresters, as presented in this thesis, requires transient and coupled finite element simulation of the mutually-dependent electric and thermal fields employing an accurate electrothermal model. This includes detailed knowledge of both, the field- and temperature-dependent metal oxide material characteristics, and the relevant thermal parameters determining the convective and radiative heat transfer properties of the system. The main difficulty for solving this coupled problem, however, lies in the strong nonlinearity of the metal oxide resistor material. This nonlinearity leads to extremely short electrical time scales, whereas the thermal transients are several orders of magnitude longer. Therefore, this thesis adopts a dedicated multirate time integration technique in order to solve the coupled problem efficiently.

The proposed numerical approach is applied to the study of graded and ungraded station class arresters in continuous operation as well as under voltages surges. The simulation results are compared to laboratory measurements. An electrothermal simulation-based procedure for the optimization of the arrester's field grading systems is introduced employing the developed numerical approach. Here, a modeling and optimization approach to avoid the extremely cumbersome solution of the 3-dimensional and transient nonlinear electric field problem is proposed. The optimization procedure uses an equivalent 2-dimensional-axisymmetric arrester model that can reproduce the electric field stress in the resistor column with high accuracy. This is realized by introducing a virtual electrode geometry whose shape and position are determined by a multi-parametric optimization procedure. Subsequently, the grading system of the 3-dimensional station class arrester is optimized efficiently based on transient, electro-quasistatic simulations of the axisymmetric equivalent model. The detailed electrothermal analysis shows that an immense improvement of the field and thermal stress distribution in the resistor column can be obtained.

The most serious limitation in the performance of surge arresters is posed by thermal stability. Overvoltages inject electrical energy that heats up the metal oxide resistors. As a result, the point of operation in the *U-I*-characteristic is shifted towards a higher electrical conductivity, thus, causing a further increase of the power loss. If not sufficiently compensated by an increase of the heat transfer, this process leads to a thermal runaway which is a catastrophic failure of the arrester. To assess thermal stability, the cooling rate is introduced as a key performance indicator. Finite element simulations provide detailed insights in this complex electro-thermally coupled

problem. A station class arrester and its commonly used laboratory surrogate are simulated when subjected to the standard overvoltage stress test procedure. Moreover, various thermally stable and unstable scenarios are analyzed to derive a precise and computationally efficient stability criterion. This criterion allows for the identification of the relevant arrester parameters that influence the thermal stability limit. In the thesis, the effect of the electric characteristics of the resistors on the thermal stability of the arrester as well as selected thermal parameters are investigated. Finally, in order to optimize future arrester designs, a prediction function is introduced to estimate the thermal stability limit based on an affordable set of finite element simulations. Throughout this thesis, the focus lies on the practical applicability of the developed methods to address typical surge arrester design problems.

Kurzfassung

Der Überspannungsschutz von Energieübertragungssystemen basiert auf Überspannungsableitern der Stationsklasse. Im Kern besteht ein Ableiter aus einem Stapel von Metalloxid-Widerständen. Die hochgradig nichtlineare *U-I*-Charakteristik dieser Widerstände ermöglicht es dem Ableiter, Spannungsspitzen durch Absorption großer Energiemengen zu begrenzen. Die wichtigsten Konstruktionsziele für Ableiter sind, einerseits, die Sicherstellung einer ausgewogenen Verteilung der Feld- und Temperaturbelastung entlang der Ableitersäule, sowie, andererseits, die thermische Stabilität des Ableiters nach bspw. einem Blitzeinschlag. Standardlaborprüfverfahren zur Gewährleistung der thermischen Stabilität beschränken sich auf Worst-Case-Ersatzmodelle des Gesamtableiters. Daher wird die numerische Finite-Elemente-Simulation zunehmend als wertvolles Werkzeug zur Analyse des gesamten Ableiters als Alternative zu konventionellem Design auf der Grundlage von Labor- oder Feldversuchen angesehen.

Die Analyse von Ableitern, wie sie in dieser Arbeit vorgestellt wird, erfordert eine transiente und gekoppelte Finite-Elemente-Simulation der voneinander abhängigen elektrischen und thermischen Felder auf der Grundlage eines genauen elektrothermischen Modells. Dazu gehören detaillierte Kenntnisse der feld- und temperaturabhängigen Materialeigenschaften des Metalloxids, sowie der relevanten thermischen Parameter des Systems. Die wesentlichen Wärmeübertragungsmechanismen sind hierbei natürliche Konvektion und Wärmestrahlung. Die größte Schwierigkeit bei der Lösung dieses gekoppelten Problems liegt jedoch in der starken Nichtlinearität des Materials der Metalloxid-Widerstände. Diese Nichtlinearität führt zu extrem kurzen elektrischen Zeitskalen, während die thermischen Transienten mehrere Größenordnungen länger sind. Daher nutzt diese Arbeit eine spezielle Multiraten-Zeitintegrationstechnik zur effizienten Lösung des gekoppelten Problems.

Der vorgeschlagene numerische Ansatz wird auf gesteuerte und ungesteuerte Ableitern der Stationsklasse im Dauerbetrieb, sowie unter Überspannungen, angewendet und die Simulationsergebnisse werden mit Labormessungen verglichen. Auf der Grundlage dieses numerischen Ansatzes wird ein simulationsbasiertes Verfahren zur elektrothermischen Optimierung der Feldsteuerungssysteme von Ableitern vorgestellt. Hierbei wird ein Modellierungs- und Optimierungsansatz zur Vermeidung der extrem aufwendigen Lösung des dreidimensionalen und transienten, nichtlinearen elektrischen Feldproblems vorgeschlagen. Das Optimierungsverfahren basiert auf einem äquivalenten zweidimensional-achsensymmetrischen Ableitermodell, das die elektrische Feldbelastung in der Widerstandssäule mit hoher Genauigkeit reproduzieren kann. Dies wird durch die Einführung einer virtuellen Elektrodengeometrie realisiert, deren Form und Position durch ein multiparametrisches Optimierungsverfahren bestimmt wird. Anschließend wird das dreidimensionale Steuerungssystem des Ableiters basierend auf transienten, elektroquasistatischen Simulationen des achsensymmetrischen Äquivalents effizient optimiert. Die detaillierte elektrothermische Analyse zeigt, dass eine deutliche Verbesserung der Feld- und Temperaturverteilung in der Widerstandssäule erreicht werden kann.

Die größte Einschränkung im Betrieb von Überspannungsableitern ist die thermische Stabilität. Überspannungen injizieren elektrische Energie, die die Metalloxid-Widerstände erwärmt. Dadurch wird der Arbeitspunkt in der *U-I*-Kennlinie in Richtung einer höheren elektrischen

Leitfähigkeit verschoben, was zu einer weiteren Erhöhung der Verlustleistung führt. Wenn dieser Prozess durch Wärmeübertragungsprozesse nicht ausreichend kompensiert wird, führt dies zu einem thermischen Davonlaufen, was einen Totalausfall des Ableiters zur Folge hat. Um die thermische Stabilität zu beurteilen, wird die Abkühlrate als wichtiger Leistungsindikator einge-führt. Finite-Elemente-Simulationen liefern einen detaillierten Einblick in dieses komplexe, elektrothermisch gekoppelte Problem. So werden ein Stationsklasseableiter und sein üblicherweise verwendetes Laborersatzmodell unter dem Überspannungs-Stresstestverfahren gemäß Standard simuliert.

Weiterhin wird nachgewiesen, dass ein gängiges Laborersatzmodell in Bezug auf sein Kühlverhalten nach Überspannungsbeanspruchungen eine Worst-Case-Darstellung des jeweiligen Gesamtableiters ist. Darüber hinaus werden verschiedene thermisch stabile und instabile Szenarien analysiert, um ein präzises und rechnerisch effizientes Stabilitätskriterium abzuleiten. Dieses Kriterium ermöglicht relevante Ableiterparameter, die die thermische Stabilitätsgrenze beeinflussen, zu identifizieren. In der Arbeit wird der Einfluss der elektrischen Eigenschaften des Metalloxids, sowie ausgewählte thermische Parameter, untersucht. Um zukünftige Ableiterdesigns zu optimieren, wird schließlich eine Vorhersagefunktion eingeführt, um die thermische Stabilitätsgrenze anhand weniger und rechnerisch günstiger Simulationen zu schätzen.

Der Schwerpunkt dieser Arbeit liegt auf der praktischen Anwendbarkeit der entwickelten Methoden zur Lösung typischer Probleme beim Design von Überspannungsableitern.

Contents

1 Introduction

Electric power transmission systems evolved since the end of the 19^{th} century. Most of the system network is built as three-phase systems. The grids have been continuously optimized from an economic point of view, and a structure has developed which can be roughly divided into extra-high voltage and high voltage grids (for transmission) (in Germany: 380 kV, 220 kV, 110 kV), medium voltage grids (for distribution) (in Germany: 10 kV, 20 kV, 30 kV) and low voltage grids (<400 V). At the extra-high voltage level, all European grids grew together to form the synchronous grid of Continental Europe, which is one of the largest interconnected power grids in the world. In any electrical network, transient overvoltages occur as soon as the stationary state changes. These overvoltages can be classified as follows. First, switching overvoltages arise from the electric and magnetic field energy stored in capacitances and inductances of the power grid whenever the stationary operation is changed. These changes can be, on the one hand, intended switching operations for grid configuration and for load flow control or, on the other hand, unintended faults, such as short-circuits or ground faults. Second, atmospheric overvoltages occur due to direct lightning strikes in overhead line conductors, lightning strikes in towers and shield wires, and lightning strikes close to power lines (i.e. induced overvoltages). These overvoltages are many times higher than the continuous operating voltage. Thus, the power system equipment cannot withstand these events. This is because a suitable insulation of the components cannot be achieved at all or is economically not feasible. Electrical power transmission systems of all voltage levels, therefore, cannot be operated without overvoltage protection by surge arresters [HN12; Hil99; OO11; Hin11].

Today's surge arresters are metal oxide arresters without spark gaps. Arresters of the highest German system levels 220 kV and 380 kV have overall lengths of $2-3.5$ m, in the (internationally also common) 800 kV level of even approx. $5-7$ m, and in the developing ultra-high voltage levels (China, 1100 kV, India, 1200 kV) well above 10 m. Arresters of these dimensions are affected by stray capacitances causing nonuniform electric field stress in the internal arrester elements. To mitigate this unwanted phenomenon, a field grading system is often installed [Cig13; HGT15]. For the extra- and ultra-high voltage systems, these systems become extremely large and increasingly represent a space problem in substations. Moreover, an optimal grading system for an ultra-high voltage station class arrester would have to be mounted so lowly that an external flashover from the grading ring to the ground occurs in the case of switching overvoltages. This poses the problem that, on the one hand, the grading system systems should be reduced as much as possible. On the other hand, this implies that the arresters are no longer optimally graded, and, thus, may suffer from increased field stress and temperatures [HGT15; Gie18; Cig13; Hin+08; Göh+10].

Moreover, after an energy injection resulting from an overvoltage, thermal instability, a so-called thermal runaway can occur, causing a catastrophic arrester failure. Hence, standard IEC 60099-4 [IEC14] defines the operating duty test in order to guarantee safe and reliable operation of arresters over the lifetime. However, laboratory tests on full-scale station class arresters are impossible [Hin11; HGT15]. Tests are, thus, restricted to laboratory surrogates, which are conservative reduced-scale models and thermally represent a worst case scenario [Hin11]. These are important reasons why the high-voltage engineering community is increasingly turning its attention towards numerical simulations as an alternative to conventional design and testing.

Among all power transmission system equipment, surge arresters pose one of the greatest challenges for numerical field simulation due to following aspects: First, surge arresters protect other equipment and have, thus, extremely high reliability demands [Ric11]. Second, the core of a surge arrester consists of a metal oxide material, that features a strongly nonlinear field and temperature dependence [Cig17; Cig13]. This nonlinear coupled electrothermal problem requires dedicated numerical simulation approaches. Third, the large dimensions of extra-high and ultra-high voltage arresters must be finely resolved in the mesh of the discretized arrester model. This leads to high computational costs. Hence, an efficient implementation of the numerical problem utilizing the specific properties of the arrester simulation model are absolutely required to keep the computational costs manageable.

This dissertation is dedicated to the investigation of the nonlinear electrothermal station class surge arrester problem based on coupled numerical simulation. The numerical field simulation enables a prediction and optimization of the real-life behavior of a station class arrester under various operating conditions. Furthermore, arrester grading systems can be optimized in order to reduce the space required in a substation. The coupled simulation of operating duties, such as lightning strikes, provides detailed insights to the reasons of device failure. It overcomes the current status of cumbersome laboratory investigations on worst case surrogates to obtain a *test passed/test failed* information.

This introduced field grading problem, furthermore, is not restricted to surge arresters. Load fluctuations and the reduction of safety margins require field stress grading of power transmission equipment, as for example in bushings, cable joints, and cable terminations. Nonlinear field-grading materials and metallic grading-electrodes are used to balance electric field stresses (see e.g. [SHH17; DGC11; YCS13]). Besides, elevated operating temperatures of equipment like power transformers, instrument transformers, cables and cable accessories can occur for different operating conditions. Coupled electrothermal field simulation provides insights to the thermal stresses of the equipment already during the design process (see e.g. [Koc+18; Fro+18; SPB15; Cle+06]). The developed concepts for the nonlinear electrothermal arrester problem can be transferred without difficulty to other equipment of power transmission and distribution.

2 Fundamentals of Surge Arresters

2.1 Station Class Surge Arresters

2.1.1 Insulation Coordination

Insulation coordination determines the required dielectric strength of power system equipment. The expected dielectric stresses are estimated based on a calculation procedure provided in the IEC standard [IEC17]. This procedure takes the system parameters and the planned installation site into account. Stresses on the system arise from overvoltage events, such as lightning strikes or switching operations. These overvoltage events are classified by time duration and amplitude in per unit (p.u.) [Hin11]. The p.u. expression describes overvoltage magnitudes as multiples of $U_{\text{basis}} = \sqrt{2/3}U_{\text{s}}$, where U_{s} is the system voltage, as shown in Fig. 2.1. Fast-front overvoltages are caused by single or multiple lightning strikes and are characterized by very short rise times in the range of microseconds and high impulse amplitudes. Slow-front overvoltages occur due to switching operations and have longer rise times in the range of milliseconds and lower amplitudes. The voltage amplitudes that occur at the equipment due to fast-front and slow-front overvoltages must be limited, as these are above the withstand voltage of the equipment (see blue and yellow lines in Fig. 2.1). For this reason, surge arresters are installed in the power system. Arresters clip voltage amplitudes above a critical threshold voltage. In the figure, this is indicated by the green line, the arrester protection level. Temporary overvoltages are caused by load rejection or earth fault events. As shown in the figure, the withstand voltage of the equipment exceeds the expected amplitude. Thus, this class of overvoltages is not critical for the power system equipment. However, temporary overvoltages are characterized by long transients in the range of several seconds, which cannot be limited by arresters. This can thermally overload the installed arrester causing a catastrophic failure. Thus, surge arresters are designed to, on the one hand, provide protection to the power system equipment in the case of fast-front and slow-front overvoltages. On the other hand, they must be constructed such that they can withstand temporary overvoltages without failure.

2.1.2 Arrester Setup

Before the 1990s, so called *gapped arresters* with silicon carbide resistors were widely used. This type had the disadvantage that spark gaps had to be connected in series with the silicon carbide resistors, as, otherwise, the leakage current under continuous alternating current (ac) operation was too high [Ric11].

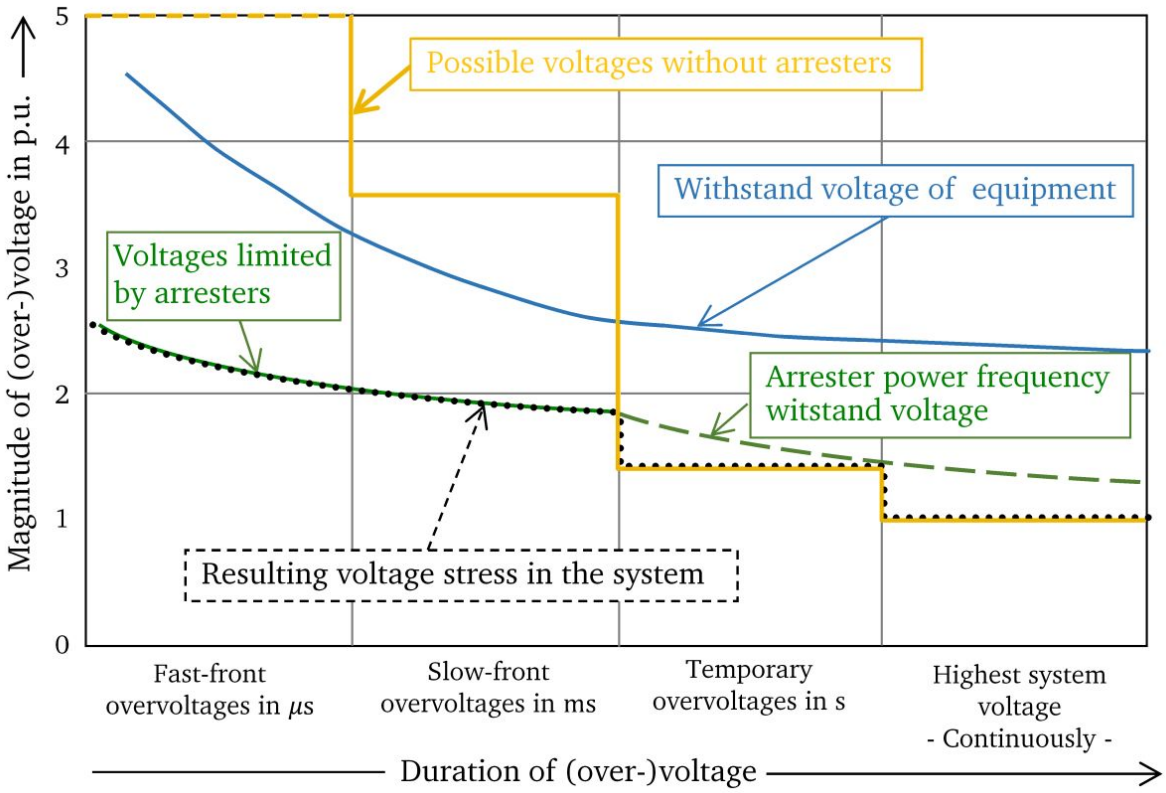

Figure 2.1.: Classification of overvoltages in a high-voltage electrical power system. Surge arresters limit the amplitude of fast-front and slow-front overvoltages caused by lightning or switching events in order to protect the installed power system equipment. Arresters and power system equipment withstand temporary overvoltages caused by e.g. earth fault events. (Adapted from [Hin11] with permission).

The discovery of metal oxide (MO) nonlinear resistors, namely zinc oxide (ZnO) resistors by Matsuoka [Mat71], lead to a completely new design without spark gaps – the *gapless* surge arrester. Due to their simple design and mechanical robustness, this type of arrester nearly completely replaced gapped arresters. Today, gapless MO station class surge arresters are the standard devices for the protection of power transmission system equipment. This development created need for more research on the fundamentals of the MO material to improve its reliability, achieve a high nonlinearity, and reduce effects like electrical aging of the MO material characteristics [Cig17; Hin11].

Figure 2.2 shows the principle setup of a gapless MO station class surge arrester. Arresters for the transmission system level consist of a MO resistor core, the so-called active part, and a housing [Hin11; Ric11; Cig17]. A number of single MO resistors are stacked in a column. The total height of the active part is determined by the protective requirements and can be elongated by metallic spacing elements. The diameter of the MO resistors is determined by the desired energy handling capability and the protection level according to the admissible current density. For production reasons, the MO stack can be divided in separate units [Hin11]. The active part is inserted into the porcelain or polymeric housing. Commonly with porcelain

housing and often with polymeric housing, there is an air gap between the housing and the MO column. As a side effect, this gas-filled volume thermally insulates the MO column from the environment, similarly to the well-known thermos flask. A different design avoids this air gap and is already very common – the injection-molding surge arrester with a silicone-rubber housing, (see [Hin11; Ric11; Cig17]). The MO column is in direct contact with the housing. This design is not further considered in this thesis, as from a simulation perspective, it is simpler than an air gap type arrester (see Sec. 5.2). Metallic flanges connect the single units and the external feeder conductors, respectively. Grading ring systems can be attached to the high voltage terminal. The IEC standard 60099-4 [IEC14] defines admissible arrester operation and test procedures. According to the standard, different characteristic voltage levels are relevant for dimensioning surge arresters (see Table 2.1).

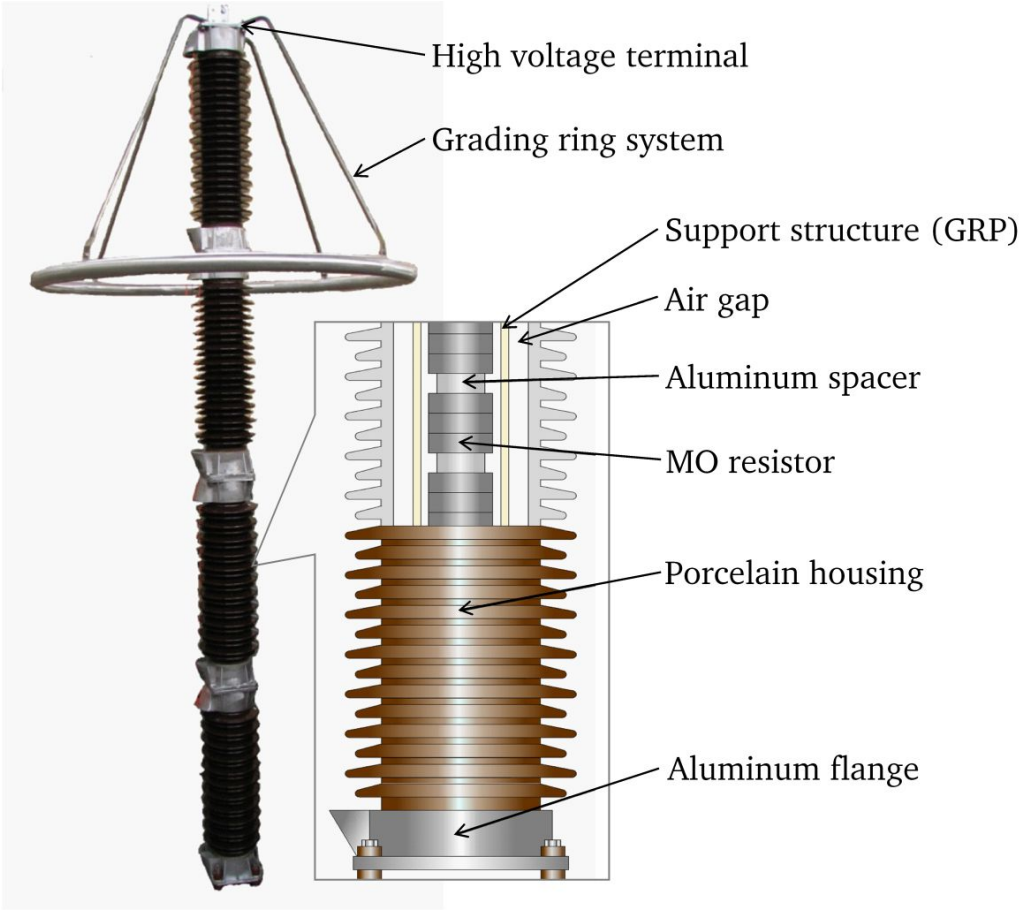

Figure 2.2.: Principle setup of a four-unit station class surge arrester with porcelain housing and grading ring system. The MO active part consists of single MO resistors, metallic spacers, and a glass-reinforced plastic (GRP) support structure. It is inserted into a porcelain housing. The gas-filled volume between the MO stack and the housing, the arrester air gap, is insulated from the environment. Metallic flanges for the top and bottom electrodes of the arrester interconnect the single units. (The annotated cross-section zoom is adapted from [Hin11] with permission).

Table 2.1.: Voltage levels characterizing a surge arrester [IEC14].

Notation	Name	Description
U_c	continuous operating voltage	designated permissible root mean square (rms) value of power-frequency voltage that is applied continuously between the arrester terminals, commonly $U_{c,min} = 1.05U_s/\sqrt{3}$ [Hin11; Gie18].
U_s	system voltage	highest admissible three-phase rms continuous power-frequency voltage of the transmission system.
U_r	rated voltage	maximum permissible rms value of power-frequency voltage, at which an arrester is designed to withstand temporary overvoltage conditions up to 10 s, commonly $U_r = 1.25\ U_c$ [Hin11; Gie18].
U_{res}	residual voltage	peak voltage during the passage of a discharge impulse current (typically several hundred to several thousand of Amperes).

2.1.3 Electric Field Grading

If an arrester was isolated in space, it is a simple series-connection of plate capacitors, i.e. the electric field stresses are uniform in all MO resistor elements. In Fig. 2.3, this case (1) is shown for a typical station class surge arrester. As an example, the IEC [IEC14] three-unit arrester is adopted (see detailed description in Sec. 4). A potential is adopted at the top electrode. Between each unit, isolated metallic flanges are positioned. Inside each flange, the electric field strength is zero. For clarity, these parts are removed from the curve. An isolated arrester is, of course, a purely theoretical case, as this is equivalent to setting the permittivity of the surrounding air to $\varepsilon = 0$. The introduction of a ground potential plane at, e.g., the bottom of the computational domain leads to a distortion of the electric field stresses along the arrester axis due to the stray capacitances (see [Cig13; Küc17]). As Fig. 2.3, case (2) shows, the electric field stresses are increased by a factor of three in the top unit compared to the bottom unit. This field inhomogeneity factor is determined by the ratio of self-capacitance (i.e. the ZnO resistor's capacitance) to stray capacitances. An increase of the self-capacitances (e.g. by increasing the radius of the ZnO resistors) reduces the influence of the stray capacitances and, thus, the field inhomogeneity factor. In contrast, the influence of the stray capacitances is increased if the arrester is positioned, e.g., close to grounded surfaces.

The arrester's MO material, fortunately, reduces this field stress imbalance due to its nonlinear field- and temperature-dependent conductivity, σ, case (3). This self-grading behavior is one of

the key aspects of the arrester operating principle and, thus, of this dissertation and is explained in detail in the Sec. 2.2, Sec. 5.1.3, Sec. 5, and Sec. 6.1. Moreover, station class arresters of more than 2 m in length are additionally equipped with electric field grading systems ([Hin11; Cig13]), such as metallic rings connected to the high voltage potential (see Fig. 2.2) or grading capacitors [Cig17; HGT15; Sjö+10]. The grading system further balances the electric field distribution along the arrester axis, as Fig. 2.3 case (4) shows. The mean field in the top unit is, in this case, still increased by 40% compared to the bottom unit.

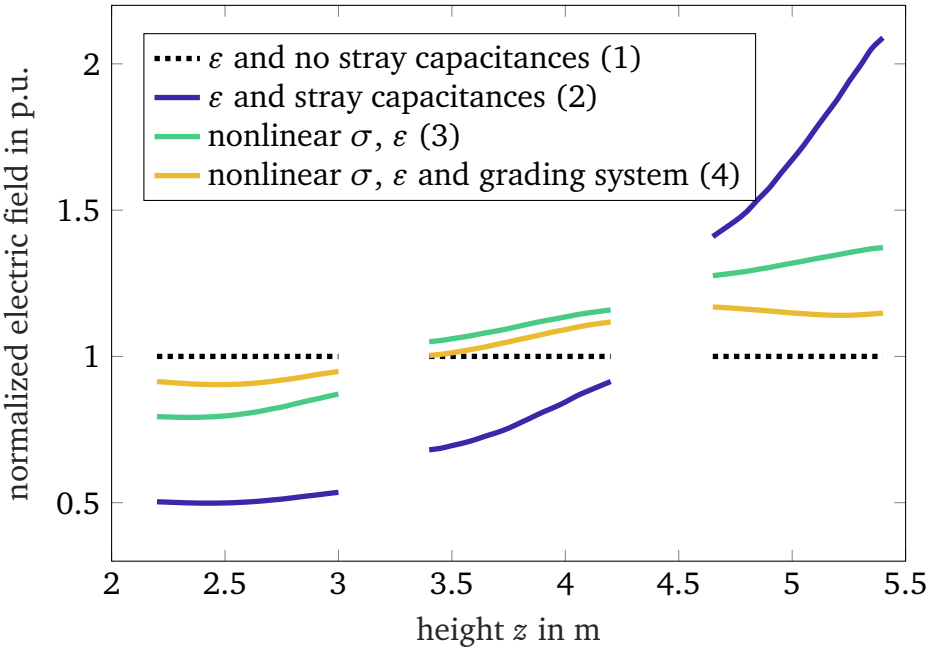

Figure 2.3.: Typical axial electric field distribution in p.u., i.e. $|\vec{E}|/|\vec{E}_{\text{uniform}}|$, in a three-unit station class arrester. Four cases are considered: First, the isolated arrester is a linear capacitor. The electric field stress is uniformly distributed along the arrester axis, $|\vec{E}(z)| = |\vec{E}_{\text{uniform}}|$. Second, the environment, in combination with a ground potential assumption, introduces a field distortion due to the stray capacitances. Third, adopting a nonlinear resistivity reduces the electric field stresses in the upper units. Fourth, a grading ring system further balances the electric field.

2.2 Zinc Oxide Material

ZnO resistors are typically ceramic cylinders with lower and upper metallic electrodes (see Fig. 2.4, left side). The resistor consists of compressed and sintered ceramic powder. This is primarily composed of ZnO and different additives, typically, among others, Bi_2O_3 in powder form [Eda89; Mat71; Cla04]. To minimize the risk of external flash-over and protect the ZnO material from the environment, a glass coating covers the surface of the cylinder (except the electrodes). The dimensions of a resistor are limited due to manufacturing reasons [Hin11] and are, typically, in the range of up to 5 cm in height and up to 10 cm in diameter [Ric11].

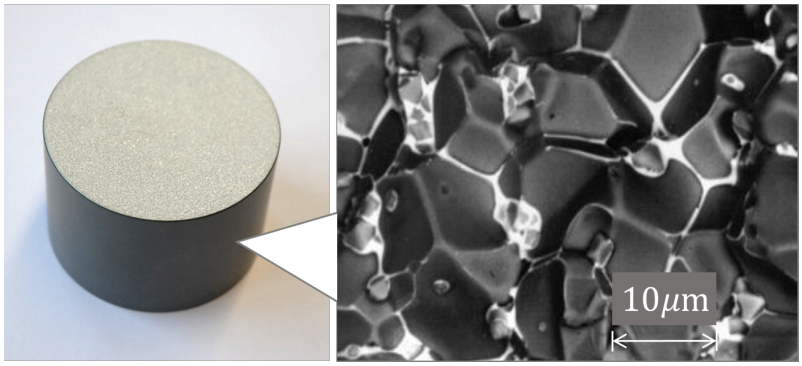

Figure 2.4.: Single ZnO resistor element. The metallic coating on the top is the electrode (left). Etched microscope image of the grain structure within a typical ZnO resistor (zoom, right). (Microscope image is taken from [Cig17]).

The most important feature of a ZnO resistor is its nonlinear voltage-current, i.e. *U-I*-characteristic. The very strong nonlinearity causes a switch-like behavior that clips voltages above the threshold or breakdown level. This switching is remarkably fast, as the transition from the resistive to the highly conductive state happens in nanoseconds [Cla04]. The term breakdown is confusing as the switching is reversible without hysteresis [Cla04]. However, under high electrical loading, the material can degrade [Cla04; Cig17]. ZnO resistors belong to the class of varistors, which stands for **vari**able resis**tor**s.

The switching behavior is attributed to the microstructure of the ZnO polycrystal [Cla04]. As the microscopic image on the right of Fig. 2.4 shows, the intrinsic structure of the varistor is composed of ZnO grains with sizes of the order of μm. Electrically, the grain boundaries can be described as double Schottky barriers. These barriers show an effective electrical response of a pair of back-to-back Zener diodes [Cla04; Cig17]. The investigation of ZnO on the micro-level has been a broad research area. It covers, on the one hand, the physical description and observation of ZnO ceramics, see e.g. [Eda89; LP75; LP77]. On the other hand, (coupled) simulation approaches are developed to mathematically describe the observed behavior and establish a theory for the ZnO grain boundary effects, see e.g. [BGW14; TGD19; BG86; VC97; Bar+96].

The overall *U-I*-characteristic of a ZnO resistor is governed by the interconnection of the vast number of grain boundaries in series and parallel. Figure 2.5 shows the nonlinear temperature-dependent resistive *U-I*-curve of typical station class ZnO material. The characteristic can be divided into two regions [Hin11]. First, the impressed voltage mode is the regime for normal operation with $U = U_c$ at power frequency $f_{exc} = 50 - 60$ Hz. The resistive current is in the μA to mA range. Thus, only a small current, the leakage current, develops, and the conductivity is in the leakage region of several $10^{-7}\mathrm{Sm}^{-1}$. In this region, the current is temperature-dependent and increases with temperature.

Second, the impressed current mode is active when an overvoltage event occurs. Electrical energy is injected in form of current pulses in the range of several kA. The ZnO becomes highly

conductive, the conductivity is of several Sm^{-1} in the breakdown region. Thus, the voltage is clipped to the residual voltage, U_{res}. In this region, the temperature dependence is negligible. From the continuous operating voltage to the residual voltage (which differ by a factor of two only), the ZnO current varies by eight orders of magnitude with respect to the applied voltage. In the breakdown regime, it can be described by,

$$\hat{i}_{\mathrm{res}} = k\hat{u}^{\alpha}, \tag{2.1}$$

where k is a material dependent factor, and α is the nonlinearity exponent, which is in the range of $30-80$ for many commercial ZnO resistors [Cla04]. Based on the relationship between the resistive current and the applied voltage, a nonlinear conductivity can be derived (see Sec. 5.1).

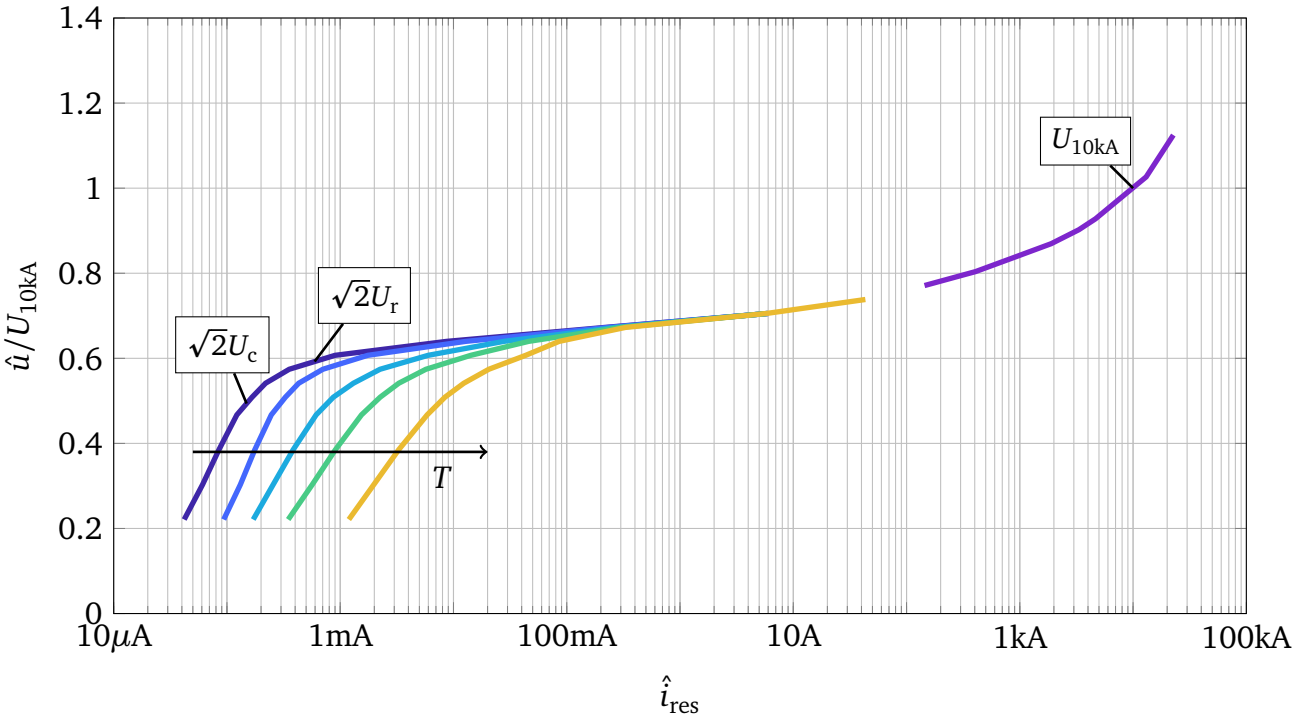

Figure 2.5.: Principle nonlinear temperature-dependent resistive voltage-current-characteristic of ZnO material. The peak values of the applied voltage $\hat{u}$ are normalized by the residual voltage U_{res} for 10 kA. In continuous operation, with applied continuous operating voltage, U_{c}, the ZnO material operates in the leakage current region. The resistive current is in the μA to mA range. The current increases with rising temperature, from ambient temperature 293 K (dark blue line) up to 463 K (yellow line). In the case of an operating duty, i.e. during a lightning or switching energy impulse, the discharge current flows (typically several kA) and the voltage is limited to the residual voltage, U_{res}. In this range, the temperature dependence is negligible (purple line).

In the leakage to early breakdown region, the current response of ZnO to an ac excitation voltage is predominantly capacitive [Hin11; Ric11]. The capacitive effects are, also, nonlinear

with respect to the excitation voltage and the temperature [LP77; Den14; Bla15]. Furthermore, a frequency- and pressure-dependence is reported [LP75; TGD19]. The relative permittivity that quantifies the capacitive behavior is comparably large and lies in the range of several hundreds (see Sec. 5). This is much larger than the relative permittivity of pure ZnO (i.e. $8-10$) [LP75; LP77]. In the literature, this is partially attributed to the extremely thin grain boundaries and to depletion layers adjacent to intergranular layers or trapped electrons.

2.3 Thermal Stability

2.3.1 Physical Phenomenon

To protect power system equipment, surge arresters can almost instantaneously and repeatedly absorb enormous amounts of electrical energy injected by overvoltage events. Arresters withstand thermal and mechanical stresses caused by these pulses without suffering damage. This requires suitable energy handling capabilities [Hin14]. In the literature, two main aspects of energy handling capability are distinguished [Hin12; Tuc15].

First, the *single or multiple impulse* energy handling capability of a single ZnO resistor is of interest. It is investigated which impulse magnitudes and scenarios are withstood by the ZnO element mechanically. The impulse energy handling capability is a fundamental property of a ZnO material configuration and was extensively studied in e.g. [Tuc15; Rei09; BCM96; VC97].

Second, *thermal* energy handling capability defines the injected energy, for which the arrester is still able to cool down while connected to the power frequency voltage. It is a characteristic of the respective arrester design and only partly determined by the ZnO resistors used (see [Hin11; Ric11; Cig17; Lat83]). It is governed by the interplay between the temperature-dependent power loss and the overall heat flow rate in the arrester, as illustrated in Fig. 2.6(a). The power loss, $\dot{Q}_\mathrm{p}$, of a ZnO resistor typically rises exponentially with temperature. The arrester cooling is determined by the thermal energy dissipation from the ZnO resistor stack to the environment, which is described by the heat flow rate, $\dot{Q}$. It is nonlinear with respect to temperature due to the temperature dependence of the convective and radiative heat transfer processes and – to a lesser extent – due to the temperature dependence of the thermal conductivity of ZnO (see Sec. 5.2). The two intersections of the curves represent operating points at which the arising power loss is exactly compensated by the heat transfer to the exterior. The left one is a stable and the right one an unstable operating point. For $\dot{Q}_\mathrm{p} < \dot{Q}$, in between the two intersection points, the heat dissipation is dominant. Thus, the arrester cools down towards the stable operating point with a characteristic time constant. Beyond the thermal stability limit, the heat transfer capability of the arrester is smaller than the power loss. Thus, the temperature in the resistors increases until a device failure, e.g. by mechanical fracture, occurs. This is called thermal runaway.

Figure 2.6(a) is, of course, a strongly simplified schematic of the complex electrothermal stability phenomenon of large station class arresters. It does not take into account that the components of the arrester operate at very different temperature levels (see Sec. 8). Furthermore,

due to the various arrester materials involved, such as ZnO, metallic elements, and porcelain or polymeric composites, different thermal time constants are present. A delayed instability can occur, where the arrester cools down only in the first minutes before becoming unstable. This is the reason why thermal stability is not assessed immediately after the energy injection in a laboratory experiment. It is, instead, monitored for 30 min to exclude a delayed instability [IEC14].

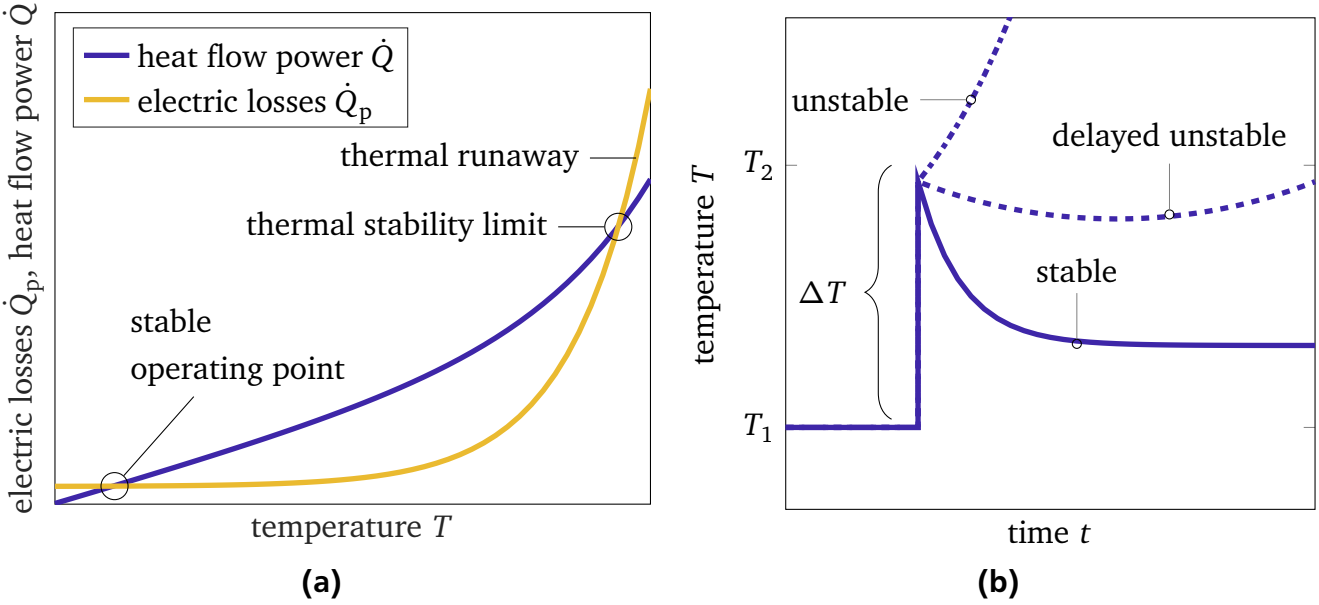

Figure 2.6.: (a) Electric loss, $\dot{Q}_p$, of the ZnO resistor stack and heat flow power, $\dot{Q}$, from the arrester surface to the environment as a function of the temperature, T. As long as the cooling heat flow power exceeds the power losses after an energy injection, the arrester is thermally stable and will cool down to the *stable operating point*. At and beyond the *thermal stability limit*, the thermal dissipation capability of the arrester is smaller than the power losses. A destructive *thermal runaway* occurs. (b) Temperature T over time for stable and unstable scenarios. An operating duty is an energy impulse that increases the arrester temperature instantaneously by ΔT. Due to the different time constants of the arrester materials, a delayed instability can occur. In this case, the arrester initially cools down until the thermal runaway starts after several minutes.

Figure 2.6(b) shows exemplary transient temperature developments after an instantaneous energy injection. Initially, the arrester is connected to the grid and is operating at its steady state temperature, T_1. For simplicity, the temperature distribution in the arrester is disregarded for the moment. The overvoltage injects the electrical energy, W_{imp}, causing an instantaneous temperature rise, $\Delta T = (T_2 - T_1)$, in the ZnO elements. It can be calculated by

$$W_{imp} = V_{zno} \int_{T_1}^{T_2} c_{v,zno}(T) \mathrm{d}T, \tag{2.2}$$

where the ZnO volume is V_{zno} and the volumetric heat capacity is $c_{\mathrm{v,zno}}$. The heat capacity of ZnO increases with temperature [Lat83][1]. For a negligible temperature dependence of the heat capacity, (2.2) simplifies to

$$\Delta T = W_{\mathrm{imp}}(V_{\mathrm{zno}} c_{\mathrm{v,zno}})^{-1}. \tag{2.3}$$

In order to minimize the risk of a thermal runaway, manufacturers commonly refer to the IEC 60099-4 standard operating duty test [IEC14], an experimental procedure for estimating the thermal energy handling capability. However, this test is limited to single arrester units or to a thermally prorated arrester section. Hence, the temperature distribution, which determines the thermal self-grading effect of large station class arresters, is omitted. Consequently, there is a strong interest in the numerical simulation of surge injection scenarios. This thesis covers thermal stability assessment and investigates sources of instability by coupled numerical field simulation.

[1] The technical brochure [Cig17] provides a figure to directly obtain the temperature increase based on the energy per volume assuming the temperature-dependent heat capacitance of [Lat83].

2.3.2 Operating Duty Test

2.3.2.1 General Remarks

The operating duty test evaluates thermal stability of a surge arrester by emulating transient overvoltage scenarios. The experimental procedure requires large impulse energies. Available test circuits with line discharge generators, however, are limited to residual voltages of the test samples of far less than 50 kV [HGT15]. This is not enough to inject the specified impulse energy into a complete station class arrester. Therefore, operating duty tests in the laboratory are limited to thermal equivalents (or thermally prorated equivalent sections) representing the station class arrester. These configurations consist of, generally, two MO resistors placed in a housing (see Sec. 7.2). It must be guaranteed that the thermal behavior is a worst case approximation of the complete station class arrester [Cig17; IEC14; Hin11]. Already in 1990, Hinrichsen [Hin90] criticized that executing the operating duty test on thermal equivalents excludes the dynamic longitudinal electrothermal behavior of complete station class surge arresters. To further investigate this issue, in this dissertation, a thermal equivalent and a complete station class arrester subjected to the operating duty test are compared in Sec. 8.3 by means of coupled electrothermal simulations.

The operating duty test is defined by the IEC standard 60099-4, [IEC14]. Recently, major changes of the operating duty test were introduced in the Edition 3.0 of [IEC14] compared to the previous Edition 2.2, [IEC09]. In this thesis, both editions of the standard are considered and, thus, summarized in the following, focusing on a station class arrester for the 550-kV-system (see Sec. 4).

2.3.2.2 IEC 60099-4, Edition 2.2

The main concept of IEC 60099-4 Edition 2.2 for selecting the required impulse energy is the assignment of arresters to different line discharge classes. The line discharge class defines the energy handling capability of a surge arrester on a scale from one to five and is defined by the manufacturer. For the considered 550-kV-station class arrester of line discharge class 5 and designed for a nominal discharge current of 20 kA, the following experimental procedure is defined (see Fig. 2.7):

1. **Initial measurement:** An 8/20-lightning impulse[2] is applied to obtain the residual voltage.
2. **Conditioning:** Four groups of five 8/20-impulses each are applied while the specimen is connected to an ac voltage of $u = 1.2U_c$. Subsequently, two 4/10-100 kA-impulses[3] are applied.

[2] The standard [IEC09] defines the shape of the lighting current impulse, with a virtual front time of $8\,\mu s \pm 1\,\mu s$ and the time to half-value with $20\,\mu s \pm 2\,\mu s$.

[3] The peak value of the discharge current having a 4/10-impulse shape is 100 kA.

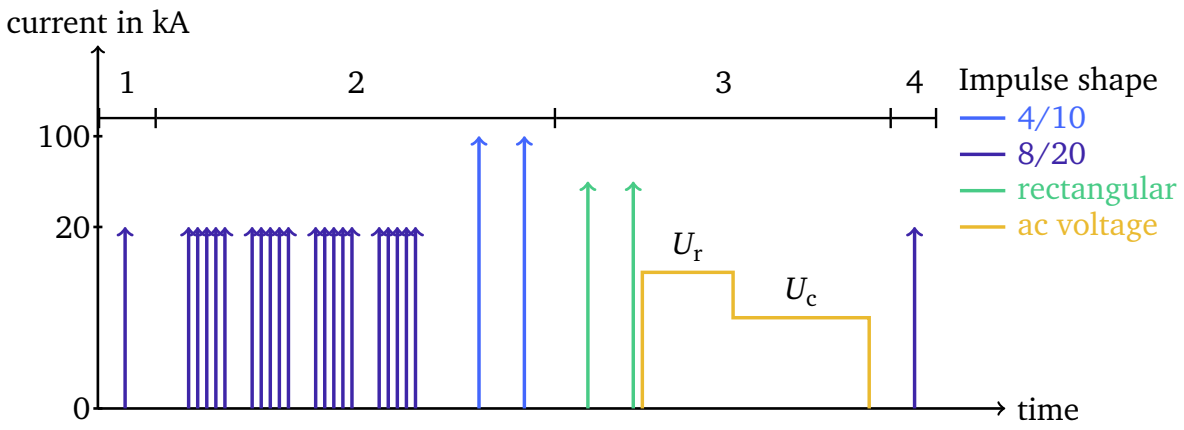

Figure 2.7.: Operating duty test procedure of the IEC standard 60099-4, Edition 2.2 [IEC09]. The test consists of four phases, an initial measurement to obtain the lightning current residual voltage, U_{res}, a conditioning procedure of the material, the actual switching surge operating duty test (see also Fig. 2.8), and the final measurement and examination procedure. (adapted from [Sch16]).

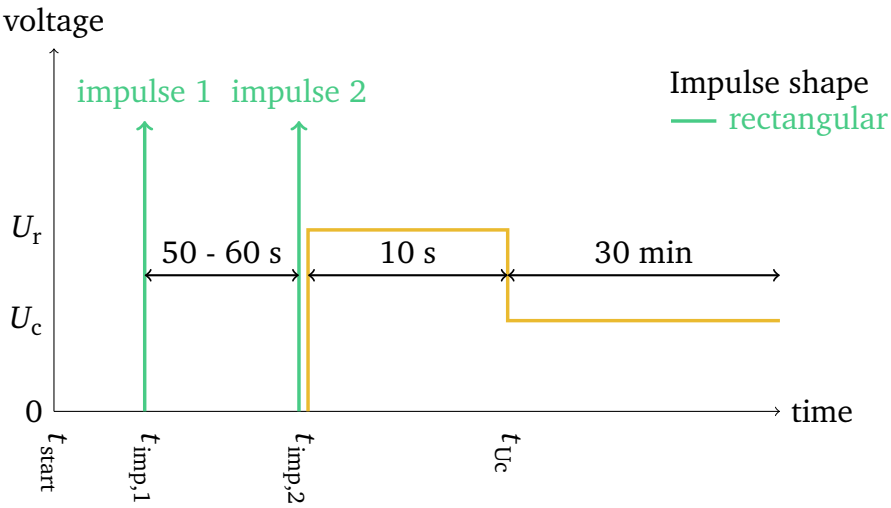

Figure 2.8.: Switching surge operating duty test (stage 3) according to IEC standard 60099-4, Edition 2.2. After the energy injection with rectangular high-current impulses, the specimen is connected to the rated voltage, U_r, for 10 s and, subsequently, to the continuous operating voltage, U_c, for 30 min. (adapted from [Sch16]).

3. **Switching surge operating duty test:** The actual switching surge operating duty test is applied to the preheated (333 K ± 3 K) specimen. Two rectangular long duration current impulses[4] are applied with a time interval of 50 s to 60 s. These two impulses inject the impulse energy and instantaneously heat up the arrester. Right after the second im-

[4] A rectangular impulse is defined by polarity, peak value, virtual duration of the peak and virtual total duration [IEC09].

pulse (within 100 ms), the rated voltage, U_r, is applied for 10 s. Subsequently, continuous operating voltage, U_c, is applied for 30 min.

4. **Test Evaluation:** The residual voltage measurement of step (1) is repeated, and the specimen is examined visually. The test is passed if:
   - the arrester cools down and is, thus, thermally stable,
   - no physical damage, e.g. fracture of a ZnO resistor element, is found,
   - the change of the residual voltage is less than ±5 % before and after the test procedure.

The energy, W_{imp}, injected by the long duration current impulses is given by,

$$W_{imp} = U_{sres}\,(U_L - U_{sres})\,\frac{T}{Z}. \tag{2.4}$$

The parameters of (2.4) are summarized in Table 2.2. The standard requirement on U_L for a complete arrester would be 1121 kV, which cannot be generated by the laboratory equipment. This the reason why the test cannot be performed on a full-scale station class arrester. The switching impulse residual voltage, U_{sres}, is in the standard named U_{res}. It must, however, not be confused with the residual voltage of a lightning discharge. It is, thus, defined in the context of this thesis:

- U_{res} arises at the nominal lightning discharge current of, for the considered 550-kV-arrester, 20 kA. This value is defined by the manufacturer, i.e. $U_{res} \approx 13$ kV for a single ZnO resistor or ≈ 1000 kV for the complete arrester.
- U_{sres} is the voltage of the switching impulse residual voltage test [IEC09]. It is $U_{norm} \approx 0.8 \cdot U_{res}$ [Hin11], as the current is in the range of 1 kA to 2 kA.

Table 2.2.: Parameters for the impulse energy calculation of (2.4) defined in [IEC09] for a 550-kV-station class surge arrester.

Parameter		Value
U_c	continuous operating voltage	345 kV
U_r	rated voltage	431 kV
U_{res}	lightning impulse residual voltage	992 kV
U_{sres}	switching impulse residual voltage	794 kV
U_L	charging voltage of the generator	$2.6 \cdot U_r$
Z	surge impedance of the power line	$0.8 \cdot \frac{U_r}{kV}$ in Ω
T	virtual duration of the current peak	2.8 ms

For the 550-kV-station class arrester, the impulse energy of one impulse based on (2.4) is $W_{imp} = 2.11\,\mathrm{MJ}$. The total injected energy for two impulses is, then, $W_{tot} = 4.22\,\mathrm{MJ}$. The expected temperature rise in the ZnO volume ($V_{zno} = 1 \cdot 10^{-3}\,\mathrm{m}^3$) is 150 K, based on (2.2) assuming a volumetric heat capacity of $c_v = 3.11\,\mathrm{J\,cm^{-3}\,K^{-1}}$ [Lat83; Cig17].

2.3.2.3 IEC 60099-4, Edition 3.0

The current IEC 60099-4 Edition 3.0 of the standard [IEC14] drops the concept of line discharge classes. Instead, the test procedure depends on the type of arrester (station or distribution) and the designated energy handling capability (high, medium or low). The rated thermal energy W_{th} can be calculated or is predefined by the manufacturer. The operating duty test procedure covers the following steps (see Fig. 2.9):

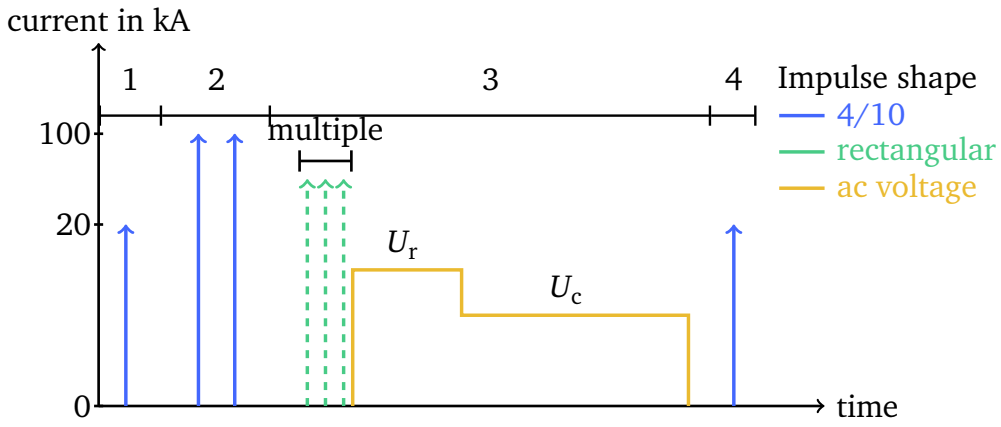

Figure 2.9.: Operating duty test procedure of IEC 60099-4, Edition 3 [IEC14]. The test consists of four phases. The lightning current residual voltage, U_{res}, is measured. This is followed by the 100-kA-conditioning impulses. Subsequently, the switching surge operating duty test (see also Fig. 2.10), and the final measurement and examination procedure is carried out. (adapted from [Sch16]).

1. **Initial tests for sample characterization:** A 4/10-20 kA-impulse is applied to obtain U_{res}.

2. **Conditioning:** Two 4/10-100 kA-impulses are applied. Subsequently, the specimen is preheated to the initial temperature of 333 K or higher.

3. **Switching surge operating duty test:** Multiple rectangular, long-duration or half-sinusoidal current impulses of $2 - 4\,\mathrm{ms}$ time duration are applied within 3 min (see Fig. 2.10). Each impulse injects a fraction of the rated thermal energy W_{imp}. The number of impulses is defined based on the desired energy handling capability. The subsequent procedure is adopted from the previous version of the standard.

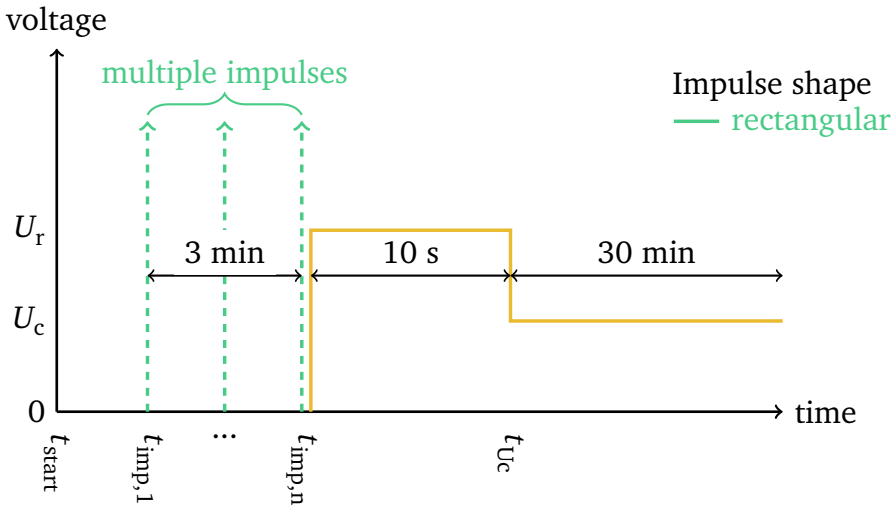

Figure 2.10.: Switching surge operating duty test (stage 4) according to IEC 60099-4 Edition 3.0. After the energy injection with rectangular or half-sinusoidal high-current impulses of $2-4\,\mathrm{ms}$ time duration, the specimen is connected to the rated voltage, U_r, for $10\,\mathrm{s}$ and, subsequently, to the continuous operating voltage, U_c, for $30\,\mathrm{min}$. (adapted from [Sch16]).

The requirement for the rated thermal energy normalized by the rated voltage for the **SH**-classified 550-kV-station class arrester is,

$$\frac{W_{tot}}{U_r} \geq 10\,\mathrm{kJ\,kV^{-1}}, \tag{2.5}$$

where W_{tot} is the rated thermal energy obtained by (2.4)[5]. For the 550-kV-arrester, this yields,

$$\frac{W_{tot}}{U_r} = \frac{4.22\,\mathrm{MJ}}{431\,\mathrm{kV}} \approx 10\,\mathrm{kJ\,kV^{-1}}. \tag{2.6}$$

In the next step, the number of impulses that each inject a portion of W_{tot} is selected, based on the result of (2.5). For the 550-kV-arrester, typically two to five $10\,\mathrm{kJ\,kV^{-1}}$-impulses are applied in the third phase of the operating duty test. This procedure differs from the previous edition, in which two long duration impulses with a gap time of $50\,\mathrm{s}$ to $60\,\mathrm{s}$ are applied. The current edition, in contrast, defines the total thermal energy, which is injected with a specific number of impulses within $3\,\mathrm{min}$. The number of impulses depends on the arrester designation and the total thermal energy per rated voltage.

2.4 Literature Review

The first investigations of the electrothermal arrester behavior were based on lumped element circuits. Already in 1983, Lat [Lat83] presents a thermal network of resistances and capacitances to obtain the stationary temperature distribution of a medium-voltage arrester. The

[5] For comparability, the rated thermal energy of both standard editions should be the same.

model assumes constant electric power losses as heat source. Due to the small dimensions of the considered arrester no axial temperature differences are considered.

Hinrichsen [HP89; Hin90] extends this approach to describe high-voltage arresters by connecting several thermal sub-networks of lumped elements, that represent an arrester unit, in series. The introduced thermal parameters are based on detailed experimental studies and theoretical approximations and are, in part, still valid for today's porcelain-type arresters. The electric model describes the capacitive-resistive behavior of the MO resistors and, additionally, includes stray capacitances. For the first time, a coupled electrothermal model based on lumped element circuits is presented and each subsystem is computed separately with a suitable time step. Both systems are periodically coupled by exchanging power loss and temperature data. The simulation results are validated by comparison to measurements.

Stockum [Sto94] investigates a thermal equivalent by means of a numerical Finite Difference approximation of the transient heat conduction equation. The thermal model includes heat conduction in the solids, convection and radiation in the air gap, as well as convection at the outside of the housing. The source term, the electric losses, is provided by an empirically determined power dissipation function. Due to the small dimensions of the considered arrester, no axial temperature differences (and thus no self-grading along the axis) are considered.

Later, the finite element (FE) method was applied for surge arrester simulation by e.g. [DMM97; Net+04; Cos+14; ZR05; FLD11]. Often, the complexity of the transient surge arrester problem is reduced to a linear problem that can be solved in the frequency domain [DMM97; Cos+14; ZR05; FLD11]. All investigations consider only geometrically small arresters, for which the influence of stray capacitances (and, thus, axial self-grading) can be neglected.

The arrester problem is reduced to a purely electrical problem by e.g. [HN98; Ste+06; Ste+08; He+09; Zha+10; Sjö+10]. These investigations cover, on the one hand, efficient numerical schemes for the nonlinear electro-quasistatic (EQS) problem in time domain [Ste+06; Ste+08]. On the other hand, they analyze the field grading system of large station class arresters [He+09; Zha+10]. Haddad et al. [HN98] present the FE computation of an equivalent capacitance network to consider an arrester's stray capacitances. Sjöstedt et al. [Sjö+10] simulate the capacitive-resistive behavior of ultra-high-voltage arresters with grading systems. The authors compare the traditional single grading ring structure with systems that comprise external grading capacitors. Hinrichsen et al. [Hin+08] formulated the coupled electrothermal FE problem in order to determine the voltage and temperature distribution of the IEC standard arrester [IEC09]. The temperature distribution of the benchmark arrester is computed. However, the nonlinear ZnO material characteristic provided in the IEC standard is not temperature-dependent and the permittivity is assumed constant. Thus, the capacitive and thermal self-grading that is expected for real-life arresters is not taken into account.

Zheng at al. [ZB02; ZB03; Zhe+10] establish a numerical simulation procedure for the nonlinear EQS arrester problem based on an envelope ansatz [ZB02]. Subsequently, heat sink effects of ZnO arresters are investigated based on a small-scale arrester model [ZB03]. Furthermore, in

[Zhe+10], the authors apply energy impulses, according to the IEC operating duty test [IEC09], to a small distribution class arrester. This arrester has no air gap and, thus, a simple thermal model, which is fitted from measurements, is sufficient. In these publications, the simulations are not validated against experimental data.

Denz [Den14] aims at the coupled electrothermal FE simulation of station class arresters. Therefore, he develops a method to obtain the nonlinear field- and temperature-dependent conductivity and permittivity of a ZnO material from measurements. Furthermore, he formulates a fully coupled electrothermal system based on the EQS equation and the stationary heat conduction equation. Due to the full coupling, the computations are extremely cumbersome. This is why he turns to an envelope equation model for simulating the heating and cooling behavior of arresters.

3 Scientific Contribution and Overview

3.1 Scientific Contribution

The scientific contributions of this thesis are summarized as follows:

- **Modeling**:
  The electrothermally coupled problem for the simulation of station class arrester is formulated based on the electro-quasistatic equation and the transient heat conduction equation. The electrothermal model allows for field- and temperature-dependent material characteristics obtained from measurements. In particular, the electro-quasistatic problem considers a field- and temperature-dependent permittivity. A detailed thermal model is developed including the temperature-dependent conductivity and permittivity of the ZnO resistor elements, thermal radiation, external convection and convective and radiative heat exchange in the arrester air gap.

- **Numerical Solution:**
  A multirate time integration scheme is applied in the solution of the 2-dimensional (2D)-axisymmetric FE electrothermal problem. The multirate scheme efficiently deals with the strongly different time constants of the electric and thermal sub-problems. Furthermore, the local electrical stationary state due to the ac excitation is exploited, and an adaptive update scheme based on the nonlinear conductivity is developed.

- **Analysis of Steady State Operation**:
  The self-grading effect for large station class arresters due to nonlinear field- and temperature-dependent ZnO material characteristics is demonstrated by simulations. The steady state temperature distribution of a station class arrester and a thermal equivalent are compared to measurements.

- **Optimization of Continuous Operation with Grading Systems**:
  An optimization procedure for surge arresters with grading system is introduced. For this, a modeling approach is developed that allows for an optimal description of the full 3-dimensional (3D) non-rotational symmetric problem by means of a 2D equivalent arrester model including virtual grading elements. Then, the grading ring system of a station class arrester is electrothermally optimized based on the introduced 2D equivalent model. A suitable goal function is defined to balance the electrothermal stresses over all ZnO resistors.

- **Investigation of Thermal Stability**:
  A simulation approach for the IEC operating duty test [IEC14] is proposed and applied to a station class arrester and a thermal equivalent. A criterion to assess the thermal stability limit based on the cooling rate of the arrester after impulse surge application is derived. Different electrothermal parameters are investigated to increase the thermal stability limit of a station class arrester. A function to predict the thermal stability of a station class arrester by extrapolation from simulations far from the stability limit is introduced.

Cooperation Work

The results of this dissertation have been developed in a joint project of the Institute for Accelerator Science and Electromagnetic Fields (TEMF) with the High Voltage Laboratory at the Technische Universität Darmstadt. The dissertation of Moritz Gießel was finalized in Dec. 2018 [Gie18]. All measurement data used in this thesis for validating simulation results as well as for deriving the ZnO material characteristics used in the simulations were obtained in the High Voltage Lab.

Publications

The following publications have been produced during the period of doctoral candidacy.

Book Chapter

- Cigré Working Group A3.25. *MO Surge Arresters: Metal oxide varistors and surge arresters for emerging system conditions; Technical Broschure 696*. Ed. by Bernhard Richter, Adriano Dellallibera, Felix Greuter, Manfred Holzer, Yoshihiro Ishizaki, M. Kobayashi, Iryani M. Rawi, Maximilian Tuczek, Jonthan Woodworth, Mike Comber, Reinhard Göhler, Volker Hinrichsen, Shinji Ishibe, Bengt Johnnerfelt, Li Fan, Yvonne Späck-Leigsnering, Masatoshi Nakajima, and Ragnar Österlund. Paris: Cigré, 2017

Internationally Refereed Journal Articles

- Yvonne Späck-Leigsnering, Erion Gjonaj, Herbert De Gersem, Thomas Weiland, Moritz Gießel, and Volker Hinrichsen. "Electroquasistatic-thermal modeling and simulation of station class surge arresters". In: *IEEE Transactions on Magnetics* 52.3 (Mar. 2016), pp. 1–4

- Yvonne Späck-Leigsnering, Erion Gjonaj, Herbert De Gersem, Thomas Weiland, Moritz Gießel, and Volker Hinrichsen. "Investigation of thermal stability for a station class surge arrester". In: *IEEE Journal on Multiscale and Multiphysics Computational Techniques* 1 (2016), pp. 120–128

- Laura A. M. D'Angelo, Yvonne Späck-Leigsnering, and Herbert De Gersem. "Electroquasistatic quasi-3D finite element simulation of a graded surge arrester". In: *International*

Journal of Numerical Modelling: Electronic Networks, Devices and Fields (2019), e2575. DOI: 10.1002/jnm.2575

- Yvonne Späck-Leigsnering, Erion Gjonaj, and Herbert De Gersem. "Electrothermal Optimization of Field Grading Systems of Station Class Surge Arresters". In: *IEEE Journal on Multiscale and Multiphysics Computational Techniques* 4 (2019), pp. 29–36. DOI: 10.1109/JMMCT.2019.2896630

Internationally Refereed Conference Papers

- Yvonne Späck-Leigsnering, Erion Gjonaj, Herbert De Gersem, Thomas Weiland, Moritz Gießel, and Volker Hinrichsen. "Thermal analysis of a station class arrester model in continuous operation and under the operating duty test". In: *19th International Symposium on High Voltage Engineering*. Aug. 2015

- **Spack_2015ab**

- Yvonne Späck-Leigsnering, Erion Gjonaj, Herbert De Gersem, Thomas Weiland, Moritz Gießel, and Volker Hinrichsen. *Gekoppelte Simulation des elektro-thermisch stabilen Dauerbetriebszustandes eines 550-kV-Freiluftableiters*. In: *URSI Kleinheubacher Tagung (KHB 2015)*. Miltenberg: U.R.S.I. Landesausschuss in der Bundesrepublik Deutschland e.V., Sept. 2015

- Yvonne Späck-Leigsnering, Robin Scheich, Moritz Gießel, Erion Gjonaj, Herbert De Gersem, and Volker Hinrichsen. "Impulse Operating Duty Simulations for a Thermal Equivalent and a Station Class Arrester". In: *NUMELEC 2017*. Paris, France, Nov. 2017

- Yvonne Späck-Leigsnering, Erion Gjonaj, and Herbert De Gersem. *Optimization Of Electric Field Grading Systems for Surge Arresters*. In: *URSI Kleinheubacher Tagung (KHB 2017)*. Miltenberg: U.R.S.I. Landesausschuss in der Bundesrepublik Deutschland e.V., Sept. 2017

- Yvonne Späck-Leigsnering, Erion Gjonaj, and Herbert De Gersem. "Optimization of Grading Ring Systems for Station Class Surge Arresters". In: *18th International IGTE Symposium*. Graz: Graz University of Technology, Sept. 2018

- Yvonne Späck-Leigsnering, Erion Gjonaj, and Herbert De Gersem. "Field Grading System Optimization of Station Class Surge Arresters". In: *URSI Kleinheubacher Tagung (KHB 2018)*. Miltenberg: U.R.S.I. Landesausschuss in der Bundesrepublik Deutschland e.V., Sept. 2018

- Yvonne Späck-Leigsnering, Erion Gjonaj, and Herbert De Gersem. "Electrothermal Optimization of Grading Ring Geometries for Station Class Surge Arresters". In: *VDE ETG – Fachtagung Hochspannungstechnik 2018*. Berlin, Nov. 2018

- Yvonne Späck-Leigsnering, Maren Greta Ruppert, Erion Gjonaj, Herbert De Gersem, and Volker Hinrichsen. “Thermal Instability Analysis of Station Class Arresters based on Electrothermal Finite Element Simulation”. In: *20th Proceedings of the International Symposium on High Voltage Engineering (ISH)*. Budapest, Aug. 2019
- Moritz Gießel, Volker Hinrichsen, Reinhard Göhler, Yvonne Späck-Leigsnering, Erion Gjonaj, and Herbert De Gersem. “Einfluss unterschiedlicher Steuerringkonfigurationen auf die thermische Stabilität von Überspannungsableitern”. In: *VDE-Fachtagung Hochspannungstechnik 2016*. Nov. 2016
- Moritz Gießel, Volker Hinrichsen, Reinhard Göhler, Yvonne Späck-Leigsnering, Erion Gjonaj, and Herbert De Gersem. “Electro-Thermal Simulations of High Voltage Metal-Oxide Surge Arresters with and without installed Grading Rings with regard to Thermal Stability”. In: *CIGRÉ Winnipeg 2017 Colloquium*. 2017
- Moritz Gießel, Volker Hinrichsen, Reinhard Göhler, Yvonne Späck-Leigsnering, Erion Gjonaj, and Herbert De Gersem. “Electro-Thermally Coupled Finite-Element Simulations of High Voltage Station Arresters with and without Grading”. In: *2017 INMR World Congress*. Nov. 2017

3.2 Thesis Overview

The thesis is structured as follows. Chapter 1 provides an introduction to the challenges for numerical field simulation in high voltage engineering. Chapter 2 summarizes the fundamentals of overvoltage protection and of surge arresters. Section 2.3 is partly adopted from [Spä+16b]. The thesis project of Scheich [Sch16] contributed to Section 2.3.2. Chapter 3 summarizes the scientific contribution of this thesis and gives an overview of the structure of the work.

Chapter 4 introduces the selected lead examples of station class surge arresters and a thermal equivalent thereof. The presented material is partly taken from [Spä+16a; Spä+16b; SGD19; Spä+19; Sch16].

Chapter 5 introduces the electrothermal modeling for the simulation of surge arresters. First, the electric model is introduced, which is based on the electro-quasistatic approximation of MAXWELL’S equations. The self-grading effect of the nonlinear ZnO resistors that balances the electric field stresses in large station class arresters is explained. Second, the heat transfer mechanisms are reviewed based on [VDI10], and a full electrothermal model of a station class arrester is presented. The section is partly based on [Spä14; Spä+19]. Results from the thesis project of [Alj16] are included. Third, the FE discretization of the coupled problem is derived. The nonlinear coupled electro-quasistatic-thermal (EQST) problem for the considered class of applications was first formulated in [Den14], on which this work is based. Fourth, the multirate time integration scheme is presented. The material presented in this section is partly taken from [Spä+16a; Spä+16b; SGD19; Spä+19]. The thesis projects of [Sch16; Rup19] contributed to the numerical parameter analysis subsection.

Chapter 6 analyzes the electrothermal steady state of station class arresters and is partly obtained from [Spä+16b]. Subsequently, Sec. 6.2.1 validates the FE simulation models of the investigated station class arresters against measurements conducted at the High Voltage Laboratory of the Technische Universität Darmstadt. The material presented in this section is partly taken from [**Spack_2015ab**; Spä+19]. The thesis project of [Sch16] contributed to the validation of the thermal equivalent.

Chapter 7 presents the optimization of an arrester's grading system for continuous operation. First, a method to represent arbitrary 3D arrester geometries by an equivalent 2D-axisymmetric model is introduced. Subsequently, the grading system of the IEC standard arrester is optimized with respect to electric field and temperature stresses. The material presented in this chapter is, in part, an excerpt of [SGD19].

Chapter 8 investigates thermal stability of surge arresters. First, the IEC operating duty test is emulated by double temperature impulse simulations. The material presented in this section is partly taken from [Spä+16b]. Second, the thermal stability of the thermal equivalent is investigated for single impulse scenarios. The thesis project of [Sch16] contributed to this section. Third, an approach to detect thermally unstable impulse scenarios directly after the impulse injection is presented. Subsequently, parameters that increase the thermal stability limit are investigated. Finally, a function to predict the thermal stability limit based on a small number of simulations is presented. The thesis project of [Rup19] contributed to this section, and the material is partly published in [Spä+19].

Conclusions are drawn in Chapter 9 and an outlook for future work is given.

4 Station Class Surge Arrester Lead Examples

4.1 IEC Station Class Surge Arrester

The IEC standard [IEC14] defines a station class arrester with a grading ring system to test and validate simulation procedures. This model is, in this work, used for the validation of the EQS simulation tool. Furthermore, the derivation of a 2D-axisymmetric equivalent model and the electrothermal optimization of the grading ring system for continuous operation is shown for the IEC model. The IEC arrester geometry is depicted in Fig. 4.1. It consists of three electrically connected units of 1.2 m height each. Each unit contains a number of ZnO resistors that are enclosed within a porcelain housing with an outer radius of 115 mm. In between the ZnO stack and the housing is an annular air gap of width $\delta_{\mathrm{air}} = 40\,\mathrm{mm}$. The whole setup is mounted on a grounded pedestal of height 2 m. Appendix A, Tab. A.4 and Fig. A.2 summarize the electrothermal materials parameters. The electrical material characteristics are defined in the standard [IEC14]. The thermal material parameters are obtained from literature. The nonlinear ZnO conductivity of [IEC14] depends on the electric field, only. Therefore, it is extended by a temperature-dependence obtained from the measurement data of [Gie18; Den14]. The nonlinear conductivity of the ZnO resistors in the region of interest of these data can be expressed by (5.22) and is introduced in Sec. 5.1.2. The parameters of the conductivity model are fixed to $a_1 = 405\,\mathrm{kV\,m^{-1}}, \alpha = 16.9, a_2 = 1.68 \cdot 10^{-7}\,\mathrm{S\,m^{-1}}, a_3 = 300\,\mathrm{K}$ and $a_4 = 0.02\,\mathrm{K^{-1}}$. These values are chosen such that the electrical characteristic of the ZnO resistors at room temperature fits to the one defined in the IEC standard [IEC14].

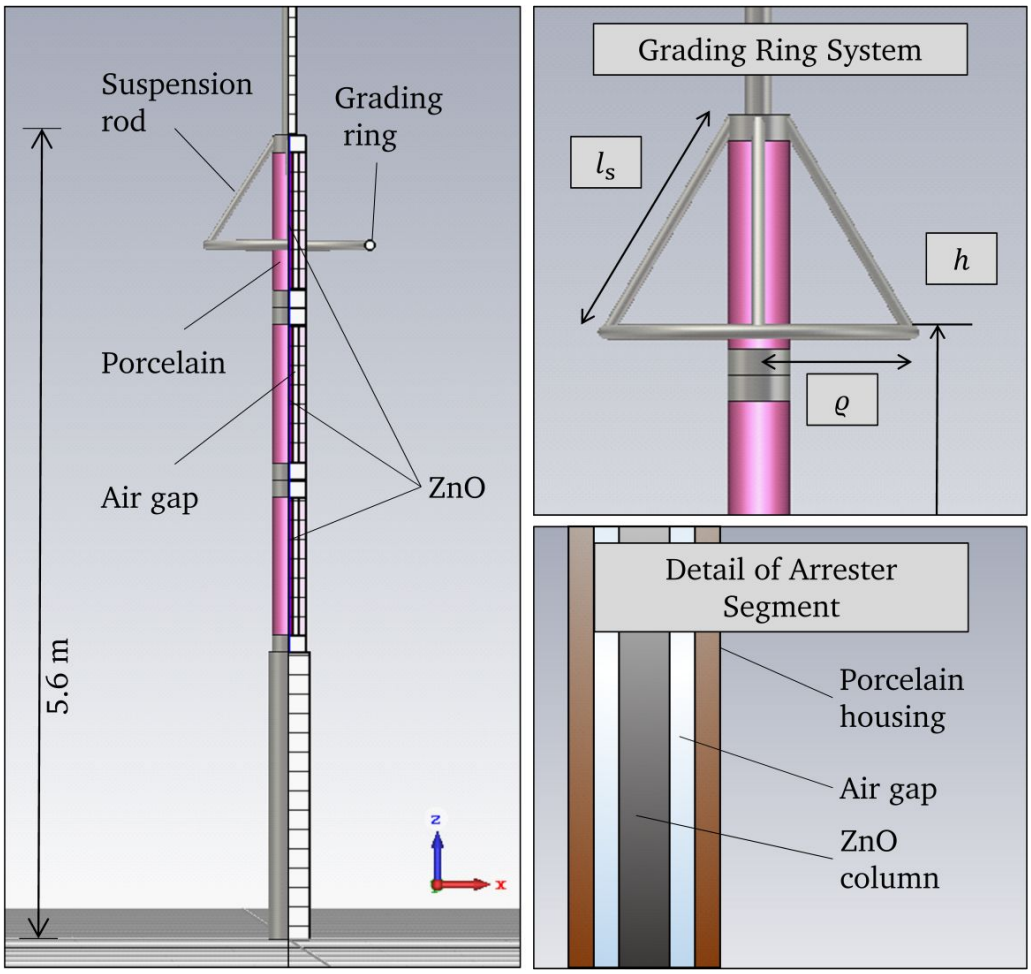

Figure 4.1.: Geometry of the IEC surge arrester, [IEC14]. The station class surge arrester consists of three units, which are interconnected by metallic flanges. The ZnO column is inserted into a porcelain housing. The setup includes a grading ring and four suspension rods and is placed on a grounded pedestal. Further details can be found in [IEC14], Annex L.

4.2 Outdoor Arrester of Station Class

A 550-kV-station class arrester measured at the High Voltage Laboratory of Technische Universität Darmstadt is introduced (see Fig. 4.2(a)) [Dür10; Gie18]. It is designed for the 550-kV-transmission system, thus, $U_s = 550\,\mathrm{kV}$. Its rms continuous operating voltage is $U_c = 345\,\mathrm{kV}$, the rated voltage is $U_r = 431\,\mathrm{kV}$, and the residual voltage is $U_{res} = 992\,\mathrm{kV}$ with a nominal discharge current of 20 kA. This arrester is investigated with two setups. First, the arrester is operated without a grading system and a regular station class ZnO filling [Dür10]. Second, the arrester is equipped with ZnO resistors that feature a smaller diameter. This specimen is investigated with and without a grading ring system. In the following, this configuration is referred to as reduced-diameter 550-kV-arrester [Gie18].

4.2.1 550-kV-Station Class Surge Arrester

The first case considered is that of an *ungraded* arrester, i.e. the field grading ring seen in Fig. 4.2(a) is removed from the system. The vertically piled high voltage ZnO resistor blocks (diameter 7 cm), metallic spacers and flanges compose a total stack height of 420 cm. There are four identical ZnO resistor columns, each of them being enclosed within a porcelain housing (Fig. 4.2(b-c)). The air gap between the resistor column and the arrester housing has a width of 3.5 cm. The computational domain spans 12 m in radial- and 9 m in z-direction, respectively. The floor is grounded, and the arrester is positioned directly on the ground, and no pedestal is considered. The most important figure for arrester operation is the electrical characteristic of its ZnO resistors. For the analyzed specimen, the *U-I*-curves for different temperatures were obtained by measurements on a single ZnO resistor. The relative permittivity is, initially, assumed constant, $\varepsilon_r = 700$. The nonlinear material characteristics are shown in Fig. 4.3, and are obtained from [Den14].

4.2.2 Reduced-Diameter 550-kV-Station Class Surge Arrester

In the second case, the 550-kV-station class surge arrester is equipped with ZnO resistors that have a comparably small diameter of 47.8 mm (see [Gie+16]). This setup increases the influence of the stray capacitances (see Sec. 2.1) and, thus, the uneven electric field and temperature distribution along the arrester axis (see explanation in Sec. 5.1.3). In this setup, the arrester's rms continuous operating voltage is $U_c = 300\,\mathrm{kV}$, the rated voltage is $U_r = 375\,\mathrm{kV}$, and the residual voltage is $U_{res} = 960\,\mathrm{kV}$ [Gie18]. In each unit, the arrester is filled with four distributed metallic heat sink elements and six temperature measurement disks. In this scenario, the porcelain sheds are neglected. In the simulation, the arrester is energized with the ac voltage (50 Hz) of 330 kV (rms). The computational domain spans 8 m in radial- and 9 m in z-direction, respectively. The floor is grounded. Further dimensions and material characteristics are summarized in Appendix A, Tab. A.3. The electrical ZnO ma-

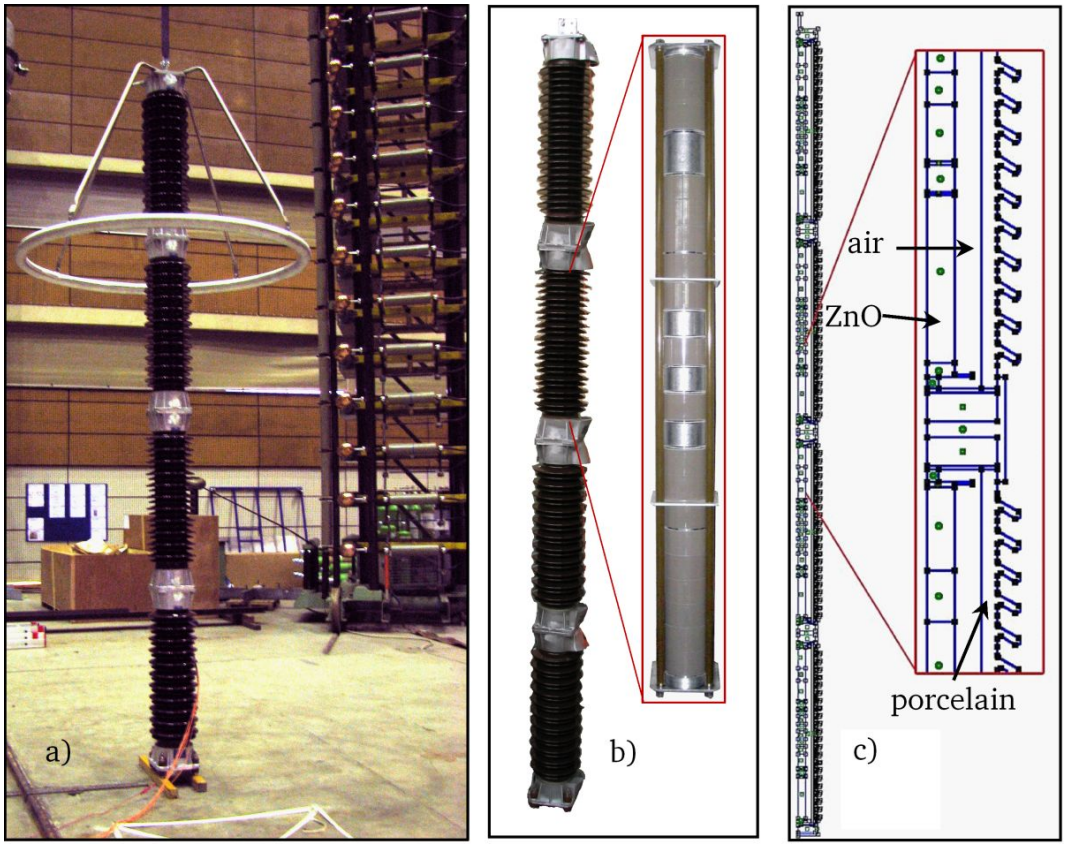

Figure 4.2.: a) 550-kV-station class arrester equipped with a field grading ring and four suspensions. b) Ungraded four-unit arrester, as considered in the simulations, with the ZnO resistor column that is inserted into a porcelain housing. c) Schematic view of a unit composed of ZnO resistors, air gap, porcelain housing and metallic flanges [Spä+16b].

terial characteristics are provided by the analytical, field- and temperature-dependent functions for the permittivity, (5.23), and (5.22). Their respective coefficients are obtained by fitting measured *U-I-T*-curves of the ZnO resistors used in [Gie18]. The fitting coefficients of (5.22) are $a_1 = 4.00 \cdot 10^5\,\mathrm{Vm}^{-1}, a_2 = 1.00 \cdot 10^{-7}\,\mathrm{Sm}^{-1}, a_3 = 290\,\mathrm{K}, a_4 = 0.02\,\mathrm{K}^{-1}$. For (5.23) $b_1 = 2.61 \cdot 10^{-5}\,\mathrm{mV}^{-1}, b_2 = 943, b_3 = 2.90 \cdot 10^{-4}\,\mathrm{K}^{-1}$ and $b_4 = 0.99$ is adopted. The nonlinearity exponent of the resistors is, in a first step, $\alpha = 20$. The resulting material characteristics are shown in Fig. 4.5.

4.2.3 Thermal Equivalent

A thermally equivalent prorated section, in the following referred to as thermal equivalent, of a surge arrester is a geometrically reduced section of a full-scale station class arrester[1]. In contrast to the entire station class arrester, it can be subjected to the operating duty test of [IEC14] in a

[1] According to the current version of [IEC14], Edition 3, the thermal equivalent does not necessarily consist of a *slice* of the full-scale arrester (i.e. with the same cross section). However, it is required that the cooling process

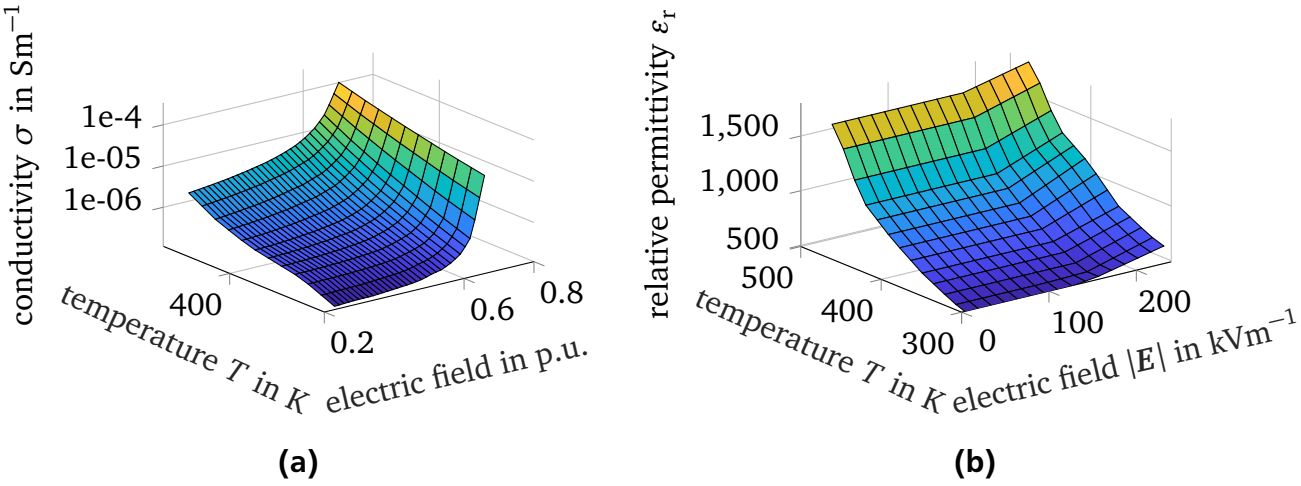

Figure 4.3.: Field- and temperature-dependent material characteristics of the ZnO resistor, obtained from [Den14]. Electric conductivity, σ (left) in p.u., normalized with $U_{\text{basis}} = U(I = 10\,\text{kA})$ in kV and relative permittivity, ε_r (right) (adapted from [Spä+16b]).

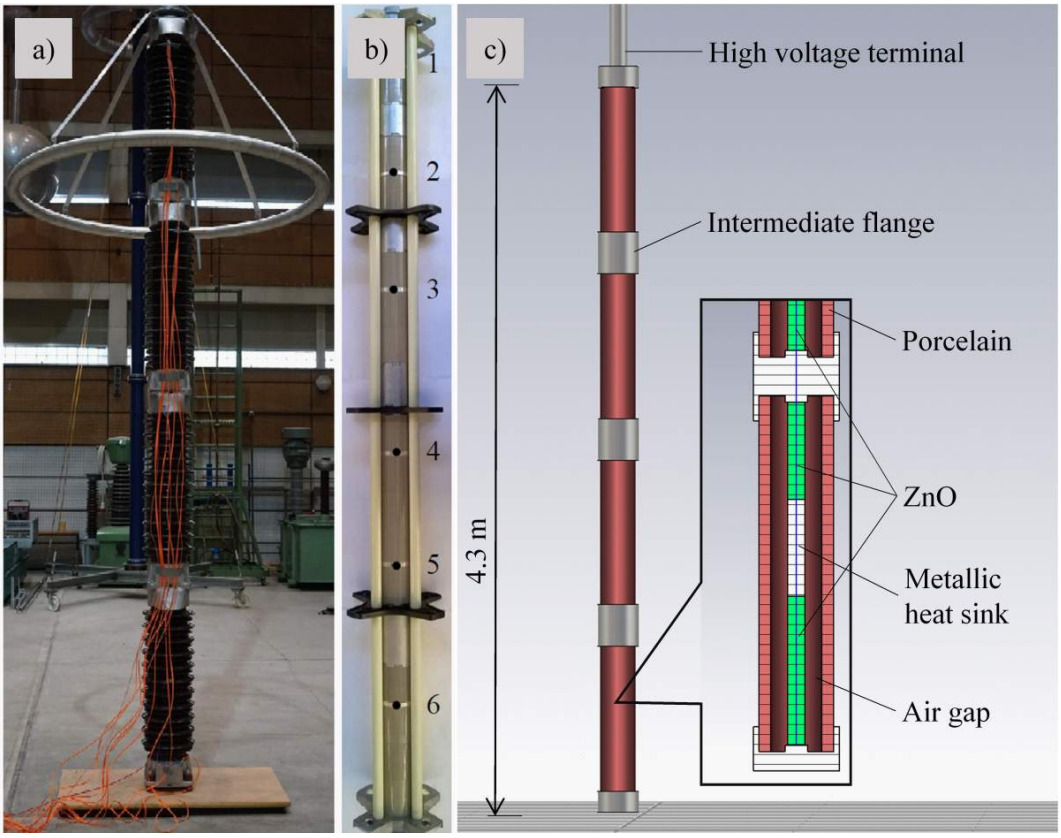

Figure 4.4.: a) Reduced-diameter station class surge arrester setup. b) Detail of single unit ZnO column with distributed heat sink elements and temperature measurement disks. c) Schematic view of the arrester model (without grading system) with detailed view of the ZnO column with centered heat sink element, air gap and porcelain housing [Spä+19].

~~has the same dynamics compared to the full-scale arrester. In this work, a thermal equivalent as specified by~~ the previous edition of the standard, [IEC09], Edition 2.2 is investigated.

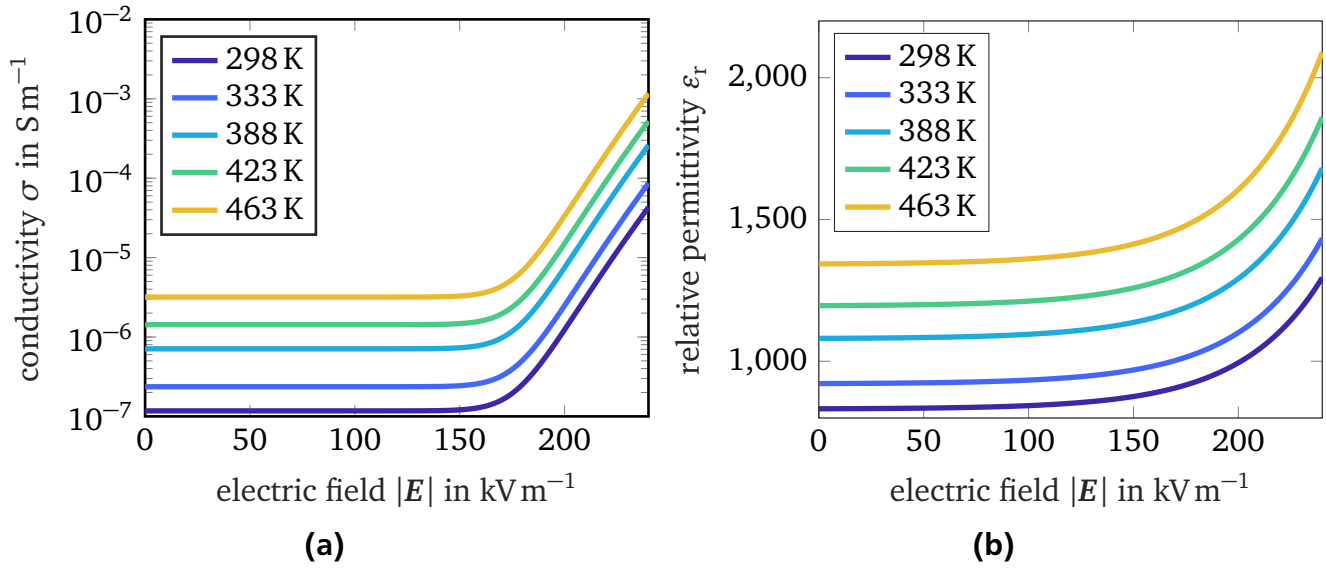

Figure 4.5.: Analytical nonlinear field- and temperature-dependent ZnO material characteristics. Relative permittivity (a) based on (5.23) and electric conductivity (b) based on (5.22) (adapted from [Spä+19]). The conductivity varies by four orders of magnitude in the field strength region of interest.

laboratory. Measurements and simulation results obtained for arbitrary electrothermal scenarios can be compared in order to validate simulation models. The thermal equivalent of the 550-kV-station class arrester is composed of two ZnO resistors (see Fig. 4.6, Fig. 4.7), which are of the same material as used for the 550-kV-arrester (see Fig. 4.3). Cork and wood plates on the top and bottom impede longitudinal heat transfer. Thus, heat dissipates mainly radially via the porcelain housing. The voltage is applied to the two copper conductors at the top and the bottom of the equivalent setup. The specifications and material properties of the thermal equivalent are summarized in the Appendix A, Tab. A.5 and Tab. A.6, respectively. The heat transfer in the air gap is modeled with the proposed effective material approach (see Appendix A, Fig. A.3). The external heat transfer coefficient is $\alpha_{\mathrm{ht}} = 3\,\mathrm{W\,m^{-2}\,K^{-1}}$.

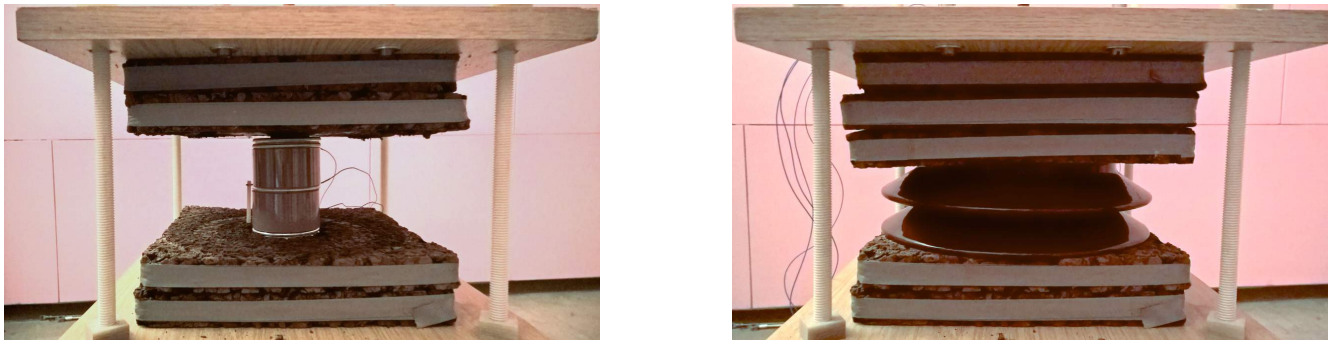

(a) (b)

Figure 4.6.: (a) The thermal equivalent in the laboratory without and (b) with the porcelain housing, as assembled in the high voltage laboratory. Two ZnO resistors are vertically stacked, inserted into a porcelain housing and clamped between insulating cork plates in a wooden frame. [Sch16].

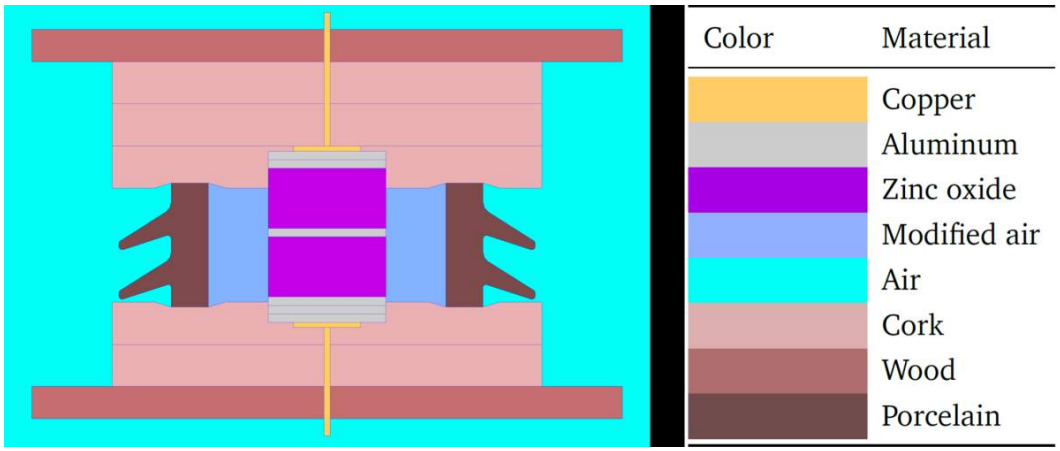

Figure 4.7.: Cross section of the thermal equivalent model (left) and table of the used materials (right), [Sch16]. The gas-filled volume between the ZnO stack and the housing, the thermal equivalent air gap, is insulated from the environment. To account for natural convection and radiation in this air gap, an equivalent nonlinear material, modified air, with a temperature-dependent thermal conductivity is introduced.

5 Electrothermal Modeling

5.1 Electro-quasistatic Field Problem

For sufficiently low frequencies, electric fields are irrotational and can be described by a scalar potential, ϕ. The electro-quasistatic approximation of MAXWELL'S equations is motivated by problems where capacitive-resistive effects are present, but propagation effects of electromagnetic (EM) waves through the region of interest are negligible. The divergence operator is applied to AMPÈRE'S law to obtain the charge conservation equation as,

$$\nabla \cdot \left(\frac{\partial}{\partial t} \vec{D} \right) + \nabla \cdot \vec{J} = \nabla \cdot \left(\nabla \times \vec{H} \right), \tag{5.1}$$

$$\nabla \cdot \left(\frac{\partial}{\partial t} \vec{D} \right) + \nabla \cdot \vec{J} = 0, \tag{5.2}$$

where the magnetic field strength is $\vec{H}$, the electric displacement field is $\vec{D}$, and the current density is $\vec{J}$. In the next step, $\vec{D}$, and $\vec{J}$ are substituted using the constitutive material relations,

$$\vec{D} = \varepsilon \vec{E}, \tag{5.3}$$

$$\vec{J} = \sigma \vec{E}, \tag{5.4}$$

where the permittivity is ε, the electric field is $\vec{E}$, and the conductivity is σ. Furthermore, the electric scalar potential, ϕ, is defined as,

$$\vec{E} = -\nabla \phi. \tag{5.5}$$

For surge arrester problems, the equation is strongly nonlinear due to the electrical characteristics of the ZnO material. The relative permittivity and the conductivity depend on the magnitude of the electric field, $|\vec{E}|$, and the temperature, T, $\varepsilon = f\left(|\vec{E}|, T\right)$ and $\sigma = g\left(|\vec{E}|, T\right)$, respectively. Finally, the EQS equation is obtained as,

$$\nabla \cdot \left(\frac{\partial}{\partial t} \varepsilon \nabla \phi \right) + \nabla \cdot (\sigma \nabla \phi) = 0. \tag{5.6}$$

Equation (5.6) is subjected to boundary conditions specifying either the electric potential or the normal component of the total current density at the boundary. Due to the resistive current, resistive losses or JOULE losses, occur

$$\dot{q}_\mathrm{p} = \sigma\left(|\vec{E}|, T\right) \vec{E}^2 = \sigma\left(|\vec{E}|, T\right) |\nabla \phi|^2. \tag{5.7}$$

5.1.1 Capacitive Resistive Circuit Model

A single cylindrical ZnO resistor element of height, $h = z_2 - z_1$, volume, V, radius, ϱ_{zno}, and the upper and lower conductor cross section, $\vec{A}_{\mathrm{zno}} = \pi \varrho_{\mathrm{zno}}^2 \vec{e}_{\mathrm{z}}$, is considered (see Fig. 5.1). To the upper and lower electrode surface, the voltage, u, is applied,

$$u = -\int_{z_1}^{z_2} \vec{E}(\vec{r}, t) \cdot \mathrm{d}\vec{z} = \phi_1 - \phi_2, \tag{5.8}$$

where ϕ_2 and ϕ_1 are the local potentials at the upper and lower surface. At the radial boundary of the ZnO resistor, $\frac{\partial \phi}{\partial n}|_{\varrho=\varrho_{\mathrm{zno}}} = 0$ is assumed. Thus, the field has only a tangential, i.e. $\vec{e}_{\mathrm{z}}$, component at the radial boundary. This assumption is justified due to the very high relative permittivity of the ZnO resistor ($\varepsilon_{\mathrm{r}} \approx 800$, see Sec. 2.2) compared to air ($\varepsilon_{\mathrm{r}} \approx 1$)[1]. The voltage

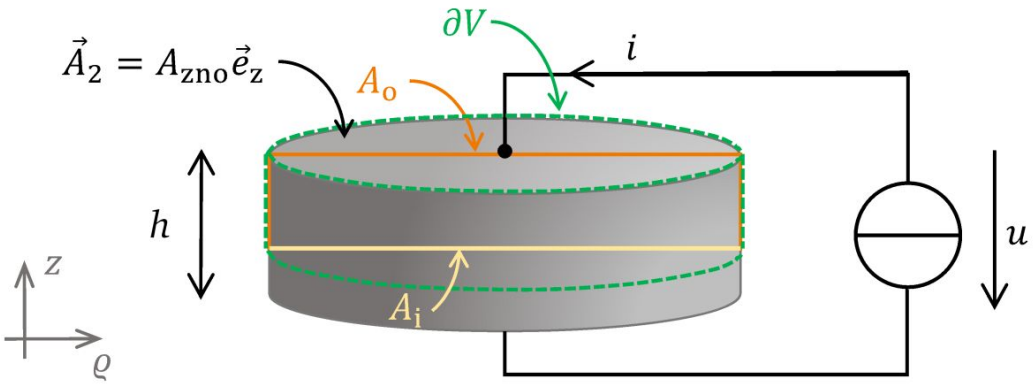

Figure 5.1.: Geometry of a single ZnO element with height, h, and the cross section, A_{zno}. The voltage, u, excites the current, i. By integrating the EQS equation (5.6) over the volume, V, the circuit elements, C and R, can be derived. The surface of V, ∂V (the green dashed line shows the 2D cut of the volume), can be split in a surface outside, A_{o}, (orange line) and a surface inside, A_{i}, (yellow line) of the ZnO resistor.

excites the current, i. Equation (5.6) is integrated over the, in principle, arbitrary volume, V, which spans around the conductor surface $\vec{A}_2$ (see Fig. 5.1). Applying the GAUSS's theorem, the integral reduces to the surface integral over ∂V,

$$\int_{\partial V} \left[\frac{\partial}{\partial t} \varepsilon(|\vec{E}(\vec{r}, t)|) \vec{E}(\vec{r}, t) + \sigma(|\vec{E}(\vec{r}, t)|) \vec{E}(\vec{r}, t) \right] \cdot \mathrm{d}\vec{A} = 0. \tag{5.9}$$

$$\tag{5.10}$$

[1] This assumption simplifies calculation and guarantees that only the field contribution of the ZnO material is obtained. Otherwise, a small contribution of the air resistance and capacitance that is connected in parallel is included.

In the following, the dependencies of $\varepsilon, \sigma, \phi, \vec{E}, \vec{J}$ on $\vec{r}$ and t are not written explicitly for clarity. The surface splits in a part, $\vec{A}_\mathrm{o}$, outside and a part, $\vec{A}_\mathrm{i}$, within the ZnO domain,

$$\underbrace{\int_{A_\mathrm{o}} \left[\frac{\partial}{\partial t}\varepsilon(|\vec{E}|)\vec{E} + \sigma(|\vec{E}|)\vec{E}\right] \cdot \mathrm{d}\vec{A}}_{-i} = -\int_{A_\mathrm{i}} \left[\frac{\partial}{\partial t}\varepsilon(|\vec{E}|)\vec{E} + \sigma(|\vec{E}|)\vec{E}\right] \cdot \mathrm{d}\vec{A} \tag{5.11}$$

The evaluation of the integral on the exterior surface, $\vec{A}_\mathrm{o}$, results in the excitation current, i. Thus, the integral on the inner surface is equal to $-i$. In general, for a nonlinear field- and temperature-dependent material, $\vec{E}$ is obtained in a post-processing step, after solving (5.6) for the boundary condition of the applied voltage (5.8). The general formulation of (5.11) allows for arbitrary, inhomogeneous fields inside the ZnO resistor, e.g. conduction channel formation or inhomogeneities due to an internal temperature distribution. From outside, the domain can, finally, be described by a global capacitance, C, and resistance, R, by evaluating the integral of (5.11) for an arbitrary surface, A_i.

In order to show the derivation of C and R for a nonlinear field- and temperature-dependent conductivity and permittivity, $\sigma(|E|, T)$, $\varepsilon(|E|, T)$, no netto charges are allowed inside the domain. It is assumed that the electric field inside the ZnO resistor is homogeneous and points in vertical direction between the two electrodes, $\vec{E} = -E\vec{e}_\mathrm{z}$. Thus, (5.8) simplifies to,

$$u = Eh. \tag{5.12}$$

Equation (5.14) is evaluated on a surface in z-direction, $\vec{A}_\mathrm{i} = A_\mathrm{zno}\vec{e}_\mathrm{z}$,

$$\int_{A_\mathrm{zno}} \left[\frac{\partial}{\partial t}\varepsilon(|E|, T)E + \sigma(|E|, T)E\right] \mathrm{d}A = i \tag{5.13}$$

$$\tag{5.14}$$

Due to the uniform field, the integral can be simplified. Combining (5.14) and (5.12) yields, then,

$$A_\mathrm{zno}\left[\frac{\mathrm{d}}{\mathrm{d}t}\varepsilon(|u|, T)\frac{u}{h} + \sigma(|u|, T)\frac{u}{h}\right] = i \tag{5.15}$$

$$\underbrace{\frac{\mathrm{d}}{\mathrm{d}t}\left(C(u, T)u\right)}_{i_\mathrm{cap}} + \underbrace{\frac{1}{R(u, T)}u}_{i_\mathrm{res}} = i, \tag{5.16}$$

where the nonlinear capacitance, $C(u, T)$, and nonlinear resistance $R(u, T)$, are defined by,

$$C(u, T) = A_\mathrm{zno}\varepsilon(|u|, T)h^{-1}, \tag{5.17}$$

$$R(u, T) = h\left[\sigma(|u|, T)A_\mathrm{zno}\right]^{-1}. \tag{5.18}$$

The total current, i, splits into a capacitive, i_{cap}, and a resistive component, i_{res}, which are represented by the *circuit elements*. Due to the nonlinearity of $\varepsilon(u,T)$, a differential capacitance $C_{\mathrm{d}}(u,T)$ [Den14] can be introduced,

$$i_{\mathrm{cap}} = \frac{\mathrm{d}}{\mathrm{d}t}\left(C(u,T)\,u\right) \tag{5.19}$$

$$= \frac{\mathrm{d}u}{\mathrm{d}t}\left(\frac{\mathrm{d}C(u,T)}{\mathrm{d}u}u + C(u,T)\right) \tag{5.20}$$

$$= C_{\mathrm{d}}\frac{\mathrm{d}u}{\mathrm{d}t}. \tag{5.21}$$

The nonlinear and, in general, temperature, T, dependent EQS equation is interpreted as a parallel circuit of a nonlinear capacitance, $C(u,T)$, and a nonlinear resistance, $R(u,T)$ (see Fig. 5.2(a)). In a station class arrester, many ZnO resistors are stacked to a column of several meters in height. Thus, in the circuit representation, the external field effects must be taken into account by parasitic stray capacitances as shown in Fig. 5.2(b).

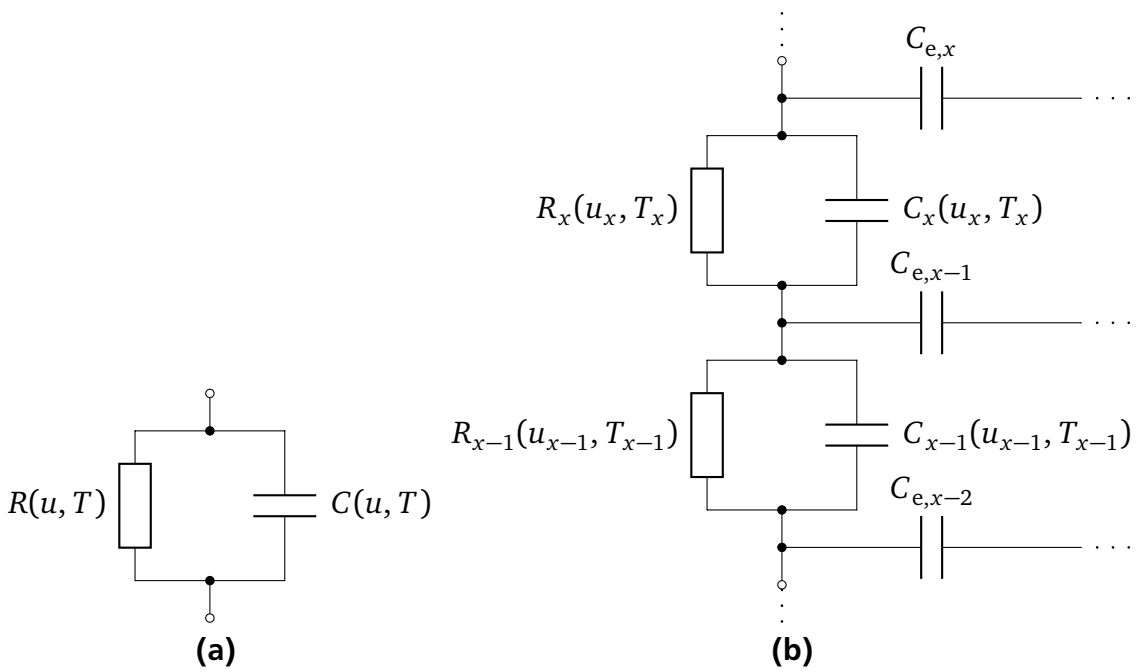

Figure 5.2.: Electrical circuit representation of a ZnO resistor as nonlinear capacitance and resistance connected in parallel (a). Detail of the electrical circuit representation of a surge arrester including stray capacitances C_{e} (b).

5.1.2 Characterization of Nonlinear Zinc Oxide Material

In Fig. 2.5 the nonlinear *U-I*-characteristic of a ZnO resistor was introduced and the nonlinear behavior, including capacitive effects, was discussed. The EQS equation (5.6) that describes the electric problem of a surge arrester is, thus, governed by the nonlinear ZnO conductivity, σ,

and permittivity, ε. Based on (5.16), the respective nonlinear material characteristics can be extracted from *U-I*-measurements on single ZnO resistors, as it represents a plate capacitor with a nearly uniform field distribution.

Many investigations assume, first, a constant permittivity in the region of interest [Bla15; Den14; All16; Gie18]. The material parameters are extracted from sinusoidal ac *U-I*-measurements of different voltage amplitudes, $\hat{u}$. The main idea of this approach is that the resistive and capacitive currents are decoupled at the peak and the zero crossing of the ac excitation voltage. At the ac voltage peak, the capacitive contribution in (5.16) is zero, as $\frac{\mathrm{d}u}{\mathrm{d}t} = 0$, and from the purely resistive total current at this time instant, the conductivity, $\sigma(u)$, is extracted. At the zero crossing, the resistive contribution in (5.16) is zero and the permittivity, ε, is computed. In order to take the temperature dependence into account, the procedure is repeated for the temperatures of interest. However, for arrester ZnO material, the obtained material characteristics fail in reproducing the measured *U-I*-curves for different voltage levels, [Bla15; Den14; All16; Gie18].

Due to the nonlinearity of the permittivity, the decoupling of the capacitive and resistive contribution is not trivial (see (5.16)). Furthermore, this dissertation shows that the steady state temperature stresses in large station class arresters are correctly reproduced only by assuming a nonlinear permittivity [Spä+16b; Gie18]. This nonlinear capacitive self-grading effect is particularly important if an arrester is operated without a grading ring system (see Sec.6). An accurate material description is, thus, decisive for coupled arrester simulations.

Different advanced methods to improve the material characterization have been introduced and discussed in [Den14; Bla15; All16; Gie18]. A comparison of these approaches is presented in [All16; Gie18]. The methods consist of two steps and, first, extract the conductivity at the time instant of the ac voltage peak. At this point, the current described by (5.16) is still purely resistive. Second, to obtain the capacitive contribution, the resistive contribution is subtracted and an integral formulation of (5.16) is solved. The same idea is pursued by the introduction of a complex permittivity that combines the resistive and capacitive current resulting in an *effective flux density* $\vec{D}_{\mathrm{eff}}$ [CDG10]. The capacitive contribution is extracted by drawing the $\vec{D}_{\mathrm{eff}} = f(\vec{E})$ curve and computing the mean value at every point[2].

However, the authors [Den14; Gie18] reported that even the advanced methods are not sufficient to exactly reproduce the measured *U-I*-curves. In [Den14], a mean deviation of more than 12% of measured and simulated current density is reported. This indicates that the ZnO behavior is not described completely by a nonlinear field- and temperature-dependent conductivity and permittivity. Denz [Den14] reduced the error (down to less than 10%) by adopting a relaxation model. Relaxation effects have been reported in the literature by e.g. [Mor73; EA03; ABL91]. Additionally, errors are introduced by the measurement and the numerical solution of the extraction method. In particular, the measurement requires an extremely fine time- and amplitude-resolution due to the strong nonlinearity [All16]. Furthermore, it must be guaran-

[2] The curves have a shape that is reminiscent of a magnetic hysteresis *B-H*-curve. ZnO resistors, however, have no hysteretic behavior [Cla04], as no remanence is observed.

teed that a constant temperature of the test object is maintained during the measurement, even in the breakdown region where the power loss heats up the specimen.

In this thesis, the electrical ZnO material characteristics are obtained from measured *U-I-T*-curves of the ZnO resistors used in the arresters. The influence of the material's dependencies on the coupled arrester behavior is investigated. Therefore, analytical material-data functions are introduced. These function are field- and temperature-dependent and consider, thus, the main dependencies of ZnO material, as reported in the literature. Their respective coefficients are obtained by fitting measured *U-I-T*-curves in the leakage and early breakdown region, as only this region is relevant for coupled arrester simulation (see example for the conductivity in Fig. 5.3). The nonlinear conductivity of the ZnO resistors in the region of interest is defined as,

$$\sigma(|\vec{E}|, T) = \left[\left(\frac{|\vec{E}|}{a_1}\right)^{\alpha} + a_2\right] \exp[(T - a_3)a_4], \tag{5.22}$$

where the fitting coefficients are a_1, a_2, a_3 and a_4. The nonlinearity exponent of the resistors, α, in (5.22) is the most important parameter, as it defines the switching point and determines the steepness of the switching of the arrester. The relative permittivity is, furthermore, approximated by,

$$\varepsilon(|\vec{E}|, T) = \left[\exp(b_1|\vec{E}|) + b_2\right] \exp[b_3 T - b_4], \tag{5.23}$$

where the fitting coefficients are b_1, b_2, b_3 and b_4.

5.1.3 Transient Current Densities in Station Class Surge Arresters

The transient axial distributions of the electric field, $\vec{E}$, and current density, $\vec{J}$, in a station class surge arrester determine the overall EQST behavior. The electric response to an excitation voltage of a station class arrester is described by the EQS equation (5.6) (see Sec. 5). The total current density, $\vec{J}$, is composed of a capacitive, $\vec{J}_{\text{cap}}$, and a resistive, $\vec{J}_{\text{res}}$, contribution (see (5.16)). The overall electrical behavior of a station class arrester is very complex, as it is determined by three aspects:

- The strongly nonlinear electric field dependence of the conductivity, σ, and permittivity, ε, of the ZnO material, which clips overvoltages (see Sec. 5.1.2);
- The strongly nonlinear temperature dependence of the ZnO material, which requires a detailed thermal model to update the operating point in the material distributions for a transient computation (see Sec. 5.1.2);
- the large axial dimensions which introduce an imbalance of the axial field stresses due to the stray capacitances (see Sec. 2.1).

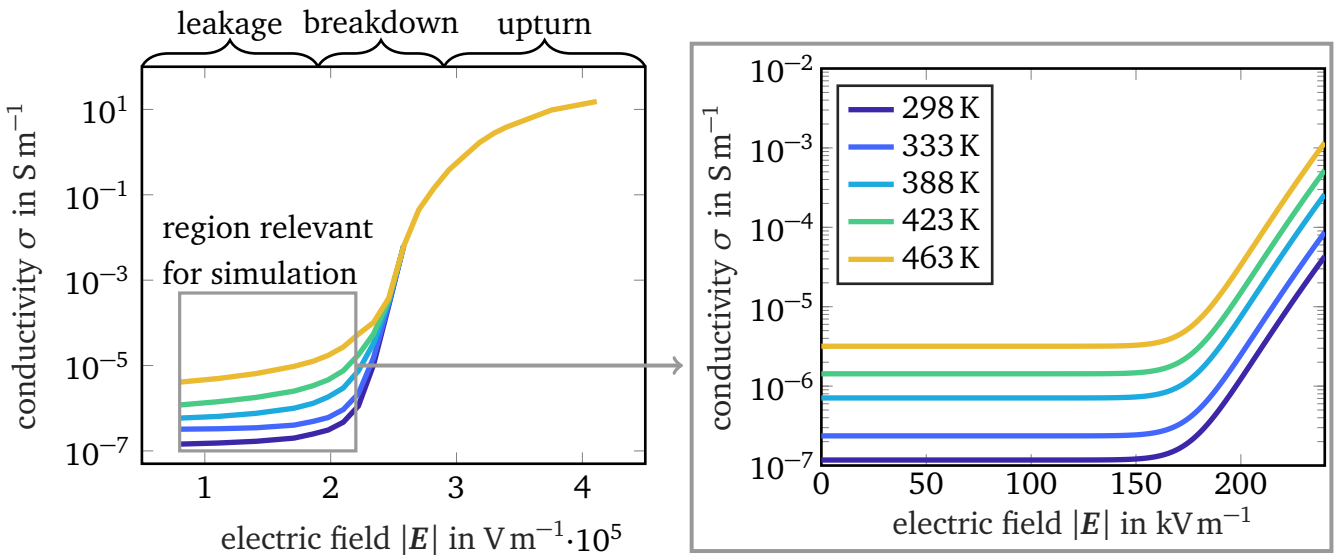

Figure 5.3.: Nonlinear temperature-dependent conductivity curve of a ZnO resistor (left). In continuous ac operation, the arrester operates in the leakage to early breakdown region. The current, here, increases with rising temperature T. In the case of an energy impulse, the arrester operates in the upturn region and is highly conductive. For EQST simulations, the boxed region of the material curve is important and can e.g. be provided by an analytical function (right). (adapted from [Rup19]).

In the following, the effects of these aspects on the transient E-J-characteristic are introduced step by step. For the moment, the temperature dependence of the arrester materials is neglected and the permittivity is assumed constant.

First, a single nonlinear field-dependent ZnO resistor element, which represents a plate capacitor, is considered (see Sec. 5). The electric field, $\vec{E}$, and current density, $\vec{J}$, are, thus, uniform in space (i.e. no stray capacitances are present). The material characteristics defined in the IEC standard [IEC14] are adopted (see Sec. 4). The resistor element is excited with a sinusoidal 50-Hz-voltage of $\hat{u} = 20\,\mathrm{kV}$ and $\hat{u} = 22\,\mathrm{kV}$ in Fig. 5.4(a) and (b), respectively. The figures show the excitation field and the nonlinear current density, which is calculated based on (5.6). The resulting transient current density in Fig. 5.4(a) is predominantly capacitive. A small resistive current contribution arises at the position of the positive and negative ac field peak, at 5 ms and 15 ms. The conductivity (see Fig. 5.3) is thus in the leakage current region of $\approx 0.1\,\mu\mathrm{Sm}^{-1}$. In Fig. 5.4(b), the excitation field is increased by 10%. The resistive current density peak rises by a factor of five compared to Fig. 5.4(a). The current density is, now, mainly resistive. At the ac voltage peak, the conductivity rises by nearly two orders of magnitude compared to the previous case, $\hat{\sigma} = 7.5\,\mu\mathrm{Sm}^{-1}$.

Second, the long axial dimensions of station class arresters cause an uneven distribution of the electric field stresses along the arrester axis. Therefore, the IEC standard arrester [IEC14] is exemplarily considered. It consists of three units that are positioned on a 2 m pedestal and is 3.6 m high (see Sec. 4). In a first step, a *linear* material with $\varepsilon_\mathrm{r} = 800, \sigma = 1\,\mu\mathrm{Sm}^{-1}$ is adopted.

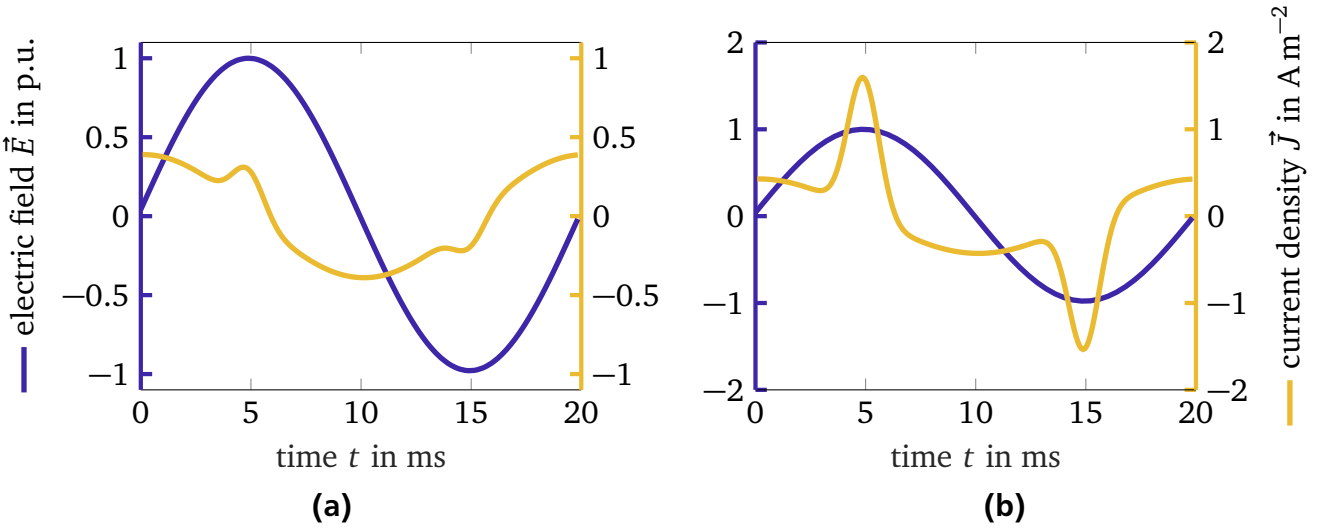

Figure 5.4.: Electric field, $\vec{E}$, in p.u. of the ac field peak, $\hat{E}$ and current density, $\vec{J}$, in Am^{-2} of a single ZnO resistor element with a sinusoidal 50-Hz-excitation voltage of 20 kV and 22 kV in (a) and (b), respectively. $\varepsilon_r = 800$ and the *nonlinear* conductivity defined in the IEC standard (see Sec. 4) is assumed.

Figure 5.5 shows the electric field, $\vec{E}$, at various axial positions in the IEC standard station class arrester. Due to the stray capacitances, the electric field stress is unevenly distributed along the arrester axis and, additionally, phase-shifted. The system can be interpreted as a capacitive-resistive voltage divider (see Sec. 5.1)). The electric field stress at the lowest unit position ($\vec{E}(z = 2.8\,\mathrm{m})$) is by 70% smaller than the stress at the highest unit position ($\vec{E}(z = 5.2\,\mathrm{m})$). This is an unwanted phenomenon, as an uneven field stress distribution over the resistors can cause overloading and may induce thermal aging in the highly stressed regions [Cig17; Tuc15]. The transient electric field response is, due to the linearity of the problem, sinusoidal[3]. The stray capacitances cause a phase shift of the electric field with respect to the excitation voltage. The resulting current density is mainly capacitive and due to the linearity of the problem, sinusoidal (see Fig. 5.6).

Third, the *nonlinear* IEC conductivity (based on (5.22)) is assumed. Figure 5.7 shows the electric field at various axial arrester positions. In comparison to the previously shown linear model, the upper ZnO resistors clip the local electric field and, thus, limit the voltage stress locally. This means that the conductivity in these resistors strongly increases and operates, at the time instants of the clipping, close to the breakdown region, as shown for the plate capacitor (see Fig. 5.4(b)). The conductivity of the lower resistors stays in the leakage current region. This means that the local electric field stress in the upper resistors is reduced. The total voltage drop along the arrester is maintained so that the lower resistors are exposed to increased field stress. This is the *self-grading behavior* of station class surge arresters, which balances the field stress along the arrester axis. The electric field of the highest and lowest position ($\vec{E}(z = 2.8\,\mathrm{m})$ and

[3] Thus, this problem allows for an efficient solution in frequency domain.

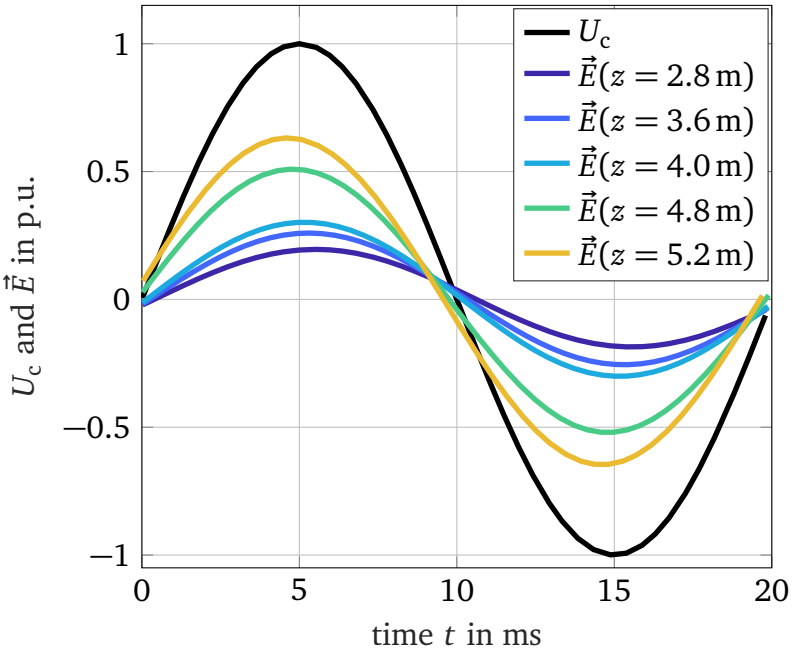

Figure 5.5.: Local electric field, $\vec{E}$, p.u. at various axial positions in the IEC standard station class arrester (see Sec. 4 and [IEC14]) assuming *linear* material, i.e. $\varepsilon_r = 800, \sigma = 1\,\mu\mathrm{Sm}^{-1}$. A sinusoidal 50-Hz-excitation voltage of 333 kV is applied.

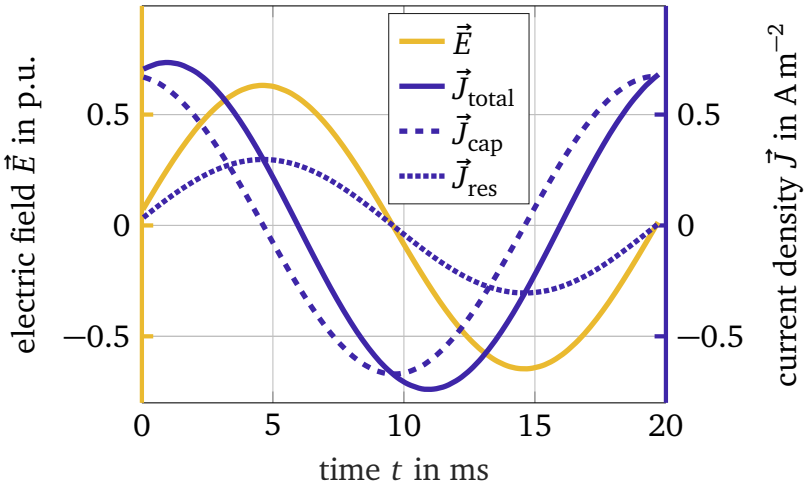

Figure 5.6.: Local electric field, $\vec{E}$, p.u. and current density, $\vec{J}$, in Am^{-2} at the axial position $z = 5.2\,\mathrm{m}$ in the IEC standard station class arrester assuming *linear* material, i.e. $\varepsilon_r = 800, \sigma = 1\,\mu\mathrm{Sm}^{-1}$. A sinusoidal 50-Hz-excitation voltage of 333 kV is applied.

$\vec{E}(z = 5.2\,\mathrm{m})$) differs by 30% (compared to 70% in the linear case). The transient electric field response is clearly nonlinear[4]. Figure 5.7 shows the respective total current densities. Up to 4 m, the current density is mainly capacitive (this corresponds to the lower two units). With increasing axial position, the resistive contribution rises strongly and limits the local electric

[4] Now, a time domain solution is required.

field. The maximum current density at 5.2 m is by a factor of five higher compared to the current density at the lowest position (2.8 m).

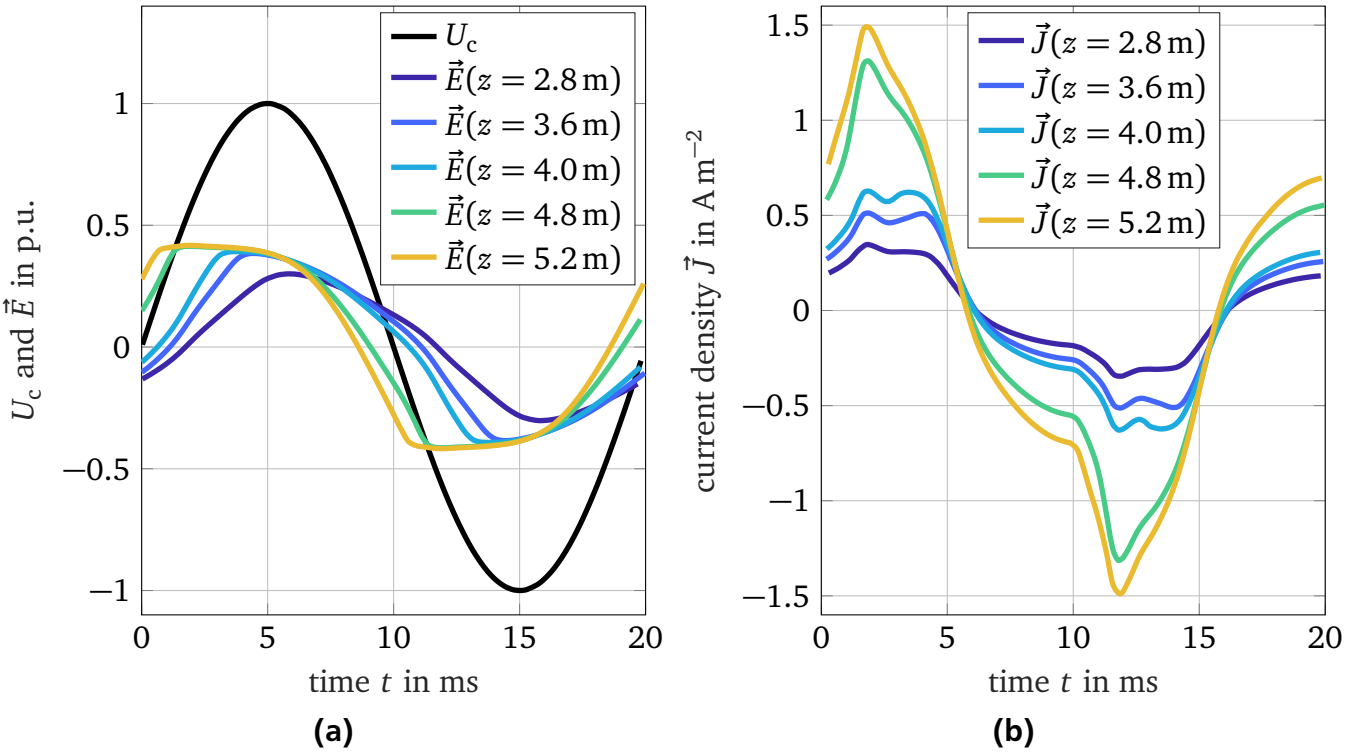

Figure 5.7.: Local electric field, $\vec{E}$, in p.u. (a) and current density, $\vec{J}$, in Am^{-2} (b) at various axial positions in the IEC standard station class arrester assuming $\varepsilon_r = 800$ and the *nonlinear* conductivity defined in the IEC standard. A sinusoidal 50-Hz-excitation voltage of 333 kV (rms) is applied.

In Fig. 5.8, the total current density at the axial position $z = 5.2\,\mathrm{m}$, (in the top unit of the arrester) is split into its capacitive and resistive contribution. The total current density is, in the first 5 ms, dominated by the resistive contribution, as the element is in the voltage-limiting mode. This means that the operating point in the ZnO material characteristic is in the first milliseconds shifted to the breakdown region. Note that the resistive peak is not at the ac excitation voltage peak due to the phase shift and the field clipping. In the time span from $5 - 10\,\mathrm{ms}$, the local field decreases and so does the resistive current density. This change of the excitation field (i.e. a large $\frac{\partial|\vec{E}(t)|}{\partial t}$, see Sec. 5) excites the capacitive contribution, which governs the total current density.

Figure 5.9 shows the total current density at the axial position $z = 2.8\,\mathrm{m}$ (in the bottom unit of the arrester). In contrast to the previously discussed top unit case (see Fig. 5.8), the total current density is almost exclusively capacitive. This means that the operating point in the ZnO material characteristic is in the leakage current region over the complete ac cycle. The voltage limitation in the upper units during the first milliseconds of the ac excitation leads to the capacitive current density peak see (at $t = 1.5\,\mathrm{ms}$). Thus, the axial interplay of the ZnO

resistors mitigates the influence of stray capacitances, as it clips the local increase of the electric stresses caused by the stray capacitances. The field stresses are, then, transferred to the lower resistors which are not critically affected by stray capacitances.

In summary, the transient electric field and current density response of a station class surge arrester to a sinusoidal ac voltage excitation is nonlinear and involves complex interactions of all ZnO resistor elements along the arrester axis. The nonlinear field dependence of the ZnO material characteristic mitigates the effect of the stray capacitances, which cause an axially uneven electric field stress distribution. The temperature dependence and the nonlinearity of the permittivity of ZnO, which were excluded from the discussion, have a similar effect and help to further balance the stresses along the arrester axis (see Sec. 6.1).

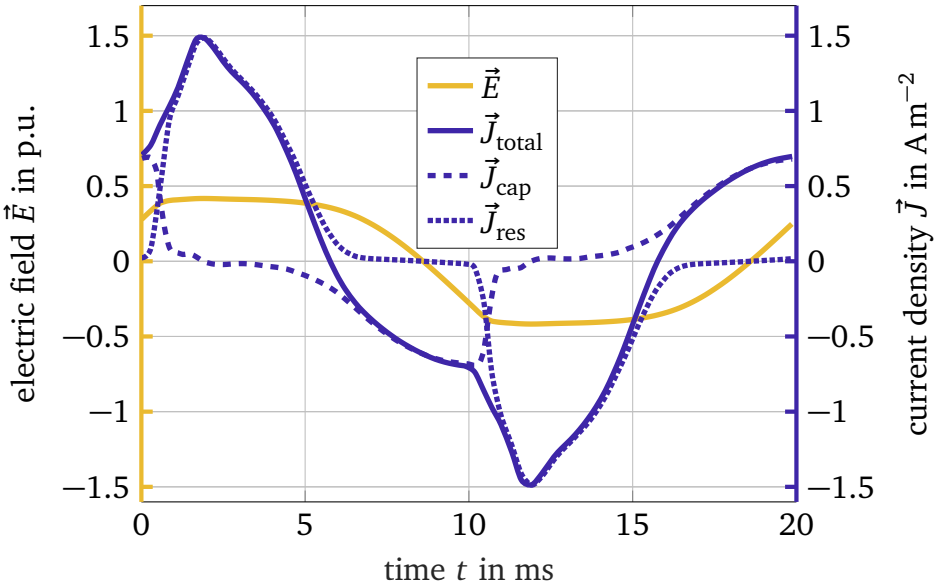

Figure 5.8.: Local electric field, $\vec{E}$, in p.u. and current density, $\vec{J}$, in $\mathrm{Am^{-2}}$ at the axial position $z = 5.2\,\mathrm{m}$ in the IEC standard station class arrester assuming $\varepsilon_r = 800$ and the *nonlinear* conductivity defined in the IEC standard. A sinusoidal 50-Hz-excitation voltage of 333 kV (rms) is applied.

5.1.4 Modeling of Station Class Arrester in Various Operating Conditions

Section 5.1.2 introduced a suitable material characterization for the electrothermal FE simulation of station class arresters. Depending on the specific operating mode, the arrester is at different operating points in the *U-I*-curve of Fig. 2.5.

In the leakage current region, the arrester current is dominantly capacitive. This is the regime of an arrester in normal power-grid operation. If the arrester is small, i.e. of distribution class, or equipped with a large grading ring system, the electric field stresses are uniformly distributed over all ZnO elements. The influence of stray capacitances is small and, hence, no self-grading due to the nonlinear resistive-capacitive coupling occurs. Furthermore, the excitation voltage must be well below the breakdown voltage. Only in this case, the leakage region resistance of

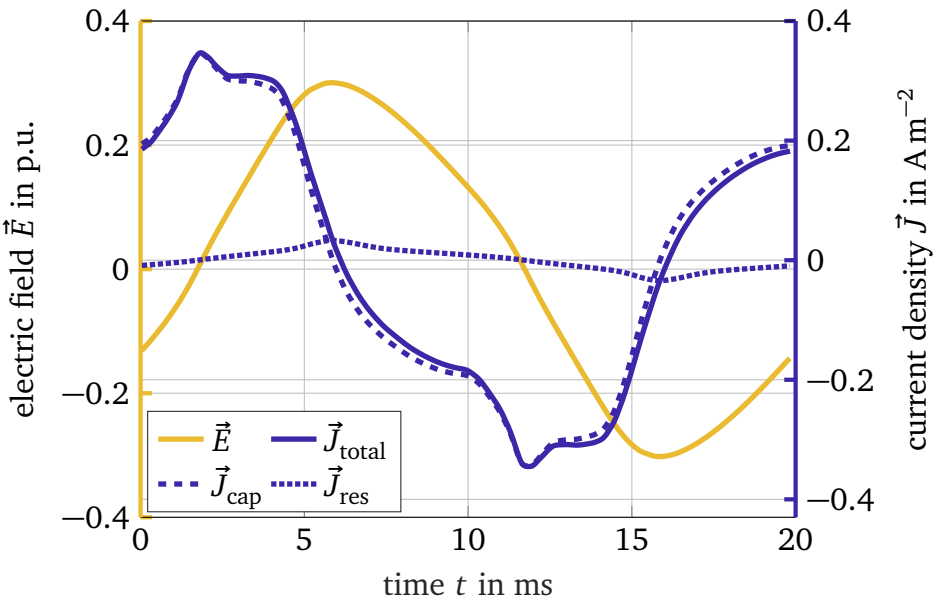

Figure 5.9.: Local electric field, $\vec{E}$, in p.u. and current density, $\vec{J}$, in Am^{-2} at the axial position $z = 2.8$ m in the IEC standard station class arrester assuming $\varepsilon_r = 800$ and the *nonlinear* conductivity defined in the IEC standard. A sinusoidal 50-Hz-excitation voltage of 333 kV (rms) is applied.

the ZnO resistors can be neglected in (5.16). It represents a purely capacitive circuit ($\sigma \to 0$) which is the first limiting case of (5.16). This approximation is e.g. used in [Zha+10; He+09].

The second limiting case of (5.16) is obtained for $\partial/\partial t = 0$ or if $C \ll 1/R$. Then, capacitive effects are neglected and the solution is a stationary current field governed by the ZnO resistances. This case is not considered in this thesis.

A different regime occurs if the arrester is operated at higher voltage levels. The operating point in the ZnO characteristic of Fig. 5.3 is, then, shifted towards the breakdown region. This regime applies to station class arresters in continuous operation, in particular if they are equipped with a reduced or even without a grading ring system. In this case, the stray capacitances strongly affect the voltage distribution, as shown in the previous Sec. 5.1.3. An accurate approach to model the capacitive-resistive behavior of these scenarios is the transient nonlinear EQS equation (cf. [Hin+08; IEC14; WSC09; Sjö+10]). The material characteristics are specified in terms of the nonlinear permittivity and electrical conductivity, $\varepsilon = \varepsilon(|\vec{E}|)$ and $\sigma = \sigma(|\vec{E}|)$.

Moreover, as Fig. 2.5 shows, the ZnO conductivity also depends on temperature. Thus, thermal processes in arresters must be taken into account (see e.g. [Lat83; Hin90]). The material characteristics are, in this case, nonlinear field- and temperature-dependent, $\varepsilon(|\vec{E}|, T)$ and $\sigma = \sigma(|\vec{E}|, T)$. In this work, it is shown that the resulting coupled electro-quasistatic-thermal system of equations is a valid model to accurately describe the electrothermal behavior of surge arresters.

5.2 Thermal Problem

5.2.1 Heat Transfer Mechanisms

When a surge arrester is connected to the power grid, heat is generated due to the resistive losses according to (5.7). This heat is eventually dissipated along the top and bottom flanges and along the housing to the surrounding air. Three fundamental heat transfer mechanisms are distinguished and briefly recapitulated based on [VDI10]: conduction, convection and thermal radiation. The heat flux density is defined as,

$$\dot{q} = \frac{\mathrm{d}\dot{Q}}{\mathrm{d}A}, \tag{5.24}$$

and describes the heat energy, Q, that is transferred per unit of time and per unit area, A.

Heat conduction describes the thermal energy transfer by microscopic interactions between particles due to random movements. The nonlinear transient heat conduction equation describes the evolution of the temperature, T, by,

$$\frac{\partial c_\mathrm{v}(T)T}{\partial t} - \nabla \cdot (\lambda(T)\nabla T) = \dot{q}. \tag{5.25}$$

Herein, the temperature-dependent specific volumetric heat capacity and the thermal conductivity are $\lambda(T)$ and $c_\mathrm{v}(T)$, respectively.

The heat transfer due to convection is attributed to microscopic interactions in a fluid, i.e. diffusion and, additionally, the fluid flow, i.e. advection. Two types of convective heat transfer are distinguished: First, natural convection describes fluid motion driven by buoyancy forces, which are caused by temperature variations in the fluid. Second, forced convection describes fluid motion induced by an internal source, e.g. wind or a cooling fan. The convective fluid flow is described by the Navier–Stokes equations. To numerically compute the convective heat transfer by solving this set of nonlinear partial differential equations is extremely cumbersome. Most computational fluid dynamics (CFD) simulations, therefore, are based on simplified models in particular if the flow is turbulent.

The thermal heat flux density that is transferred from a surface at temperature T_1 and to the surrounding fluid at temperature T_2 due to convection can be approximated by,

$$\dot{q} = \alpha_\mathrm{ht}(T_1 - T_2) = \alpha_\mathrm{ht}\Delta T. \tag{5.26}$$

Herein, the heat transfer coefficient is α_ht. In order to obtain α_ht, the natural and forced convective heat transfer from a boundary surface to a fluid can be described by the Nusselt number, Nu. It describes the ratio of convective to conductive heat transfer normal to the solid-to-fluid boundary and is defined as,

$$\mathrm{Nu} = \frac{\alpha_\mathrm{ht} l_\mathrm{c}}{\lambda} = \frac{\lambda_\mathrm{eff}}{\lambda}. \tag{5.27}$$

Herein, the characteristic convection length is l_c, the thermal conductivity of the fluid is λ, and effective thermal conductivity is λ_{eff}. The latter describes the total heat transfer in the fluid including convective effects.

In general, the NUSSELT number for natural convection depends on the fluid and flow properties and the geometrical dimensions of the problem, $\text{Nu} = f(\text{Gr}, \text{Pr})$. The GRASHOF number, Gr, and the PRANDTL number, Pr, describe the kinematic and intrinsic properties of the involved fluid. They are defined as,

$$\text{Gr} = g\,\beta(T)\,\Delta T\, l_c^3\, \nu(T)^{-2}, \tag{5.28}$$

$$\text{Pr} = \nu a^{-1}. \tag{5.29}$$

Herein, the characteristic length is l_c, the temperature difference is $\Delta T = T_1 - T_2$, the acceleration due to earth gravity is g, the volumetric thermal expansion coefficient is β, and the kinematic viscosity is ν. The thermal diffusivity is $a = \lambda(\rho c_p)^{-1}$, the specific material density is ρ, and the constant pressure specific heat is c_p.

Finally, thermal energy is transferred by radiation emission and absorption from hot body surfaces. The emissive heat flux per unit surface area is given by,

$$\dot{q}_r = \varepsilon_{\text{rad}} C_S T^4. \tag{5.30}$$

Herein, the emissivity is ε_{rad} and the Stefan-Boltzmann constant is C_S. The heat flow power between two parallel surfaces of area, A, and the surface temperatures T_1 and T_2 is given by,

$$\dot{Q}_{12} = A\varepsilon_{\text{rad}} C_S (T_1^4 - T_2^4). \tag{5.31}$$

5.2.2 Thermal Model of Surge Arresters

To model the thermal behavior of arresters, three different cases are distinguished. First, heat is generated and transferred in the solid materials of the arrester. Second, heat dissipates from the arrester surface to the environment. In this work, this is referred to as external heat transfer. Third, heat is transported through the arrester air gap. This is referred to as internal heat transfer.

Heat Transfer in Solids

In surge arresters, the solid parts include the ZnO resistors, the aluminum flanges, heat sinks, and the housing. In these regions, a thermal conductivity, $\lambda(T)$, is defined. Electric losses arise based on (5.7). The heat transfer in the vertical direction is small due to the rather low thermal conductivity of the ZnO resistors. The material characteristics used in this work were measured in collaboration with the High Voltage Lab at the Technische Universität Darmstadt [Gie18] or were obtained from [Hin90; VDI10].

External Heat Transfer

The accurate modeling of the external heat transfer is important to study the arrester's steady state. It is of minor importance for thermal stability investigations, which focus on short-time transient processes after impulse injection events (see Sec. 8), as in station class arresters an air gap commonly separates the ZnO column and the housing. This significantly slows down the transient radial heat transfer to the environment due to the insulating properties of air and the housing material.

The heat transfer from the housing surface to the gaseous environment is modeled by convective and radiative boundary conditions. The boundary condition is defined for each unit and metallic flange, separately. The ambient temperature of the laboratory is constant [Gie18]. The radiative boundary condition parameters are the emissivity of the porcelain housing and the emissivity of the metallic flanges and connectors. They are obtained from [Gie18; Hin90]. The free convection heat transfer coefficient is assumed constant. It is based on selected NUSSELT number correlations obtained from [Boe14; VDI10]. The shed-structure of the porcelain housing is neglected.

In the following, NUSSELT correlations and the resulting heat transfer coefficients from various authors are compared.

A criterion indicates if Nu-approximations correlated from flat-plate scenarios can be applied [Boe14]. It is defined as,

$$\frac{2\varrho_{\mathrm{out}}}{l_{\mathrm{c}}} \geq \frac{35}{\mathrm{Gr}^{0.25}}. \tag{5.32}$$

Herein, l_{c} is the critical length, in this case the height of the unit or flange. The outer radius of the flange and housing is ϱ_{out}. This holds for the unit case as well as for the flange case. Thus, the heat transfer correlations of vertical flat plates are applicable. In this case, the boundary-layer thickness of the resultant buoyant flow is small compared to the diameter of the cylinder.

Another commonly applied correlation was calculated by [CC75] as,

$$\mathrm{Nu}_{\mathrm{Chu}} = 0.68 + \frac{0.67(\mathrm{Gr}\,\mathrm{Pr})^{1/4}}{[1+(0.492/\,\mathrm{Pr})^{9/16}]^{9/4}}. \tag{5.33}$$

It applies to laminar or turbulent flow-cases for a vertical planar surface. Popiel [Pop08] calculated the following correlation,

$$\mathrm{Nu}_{\mathrm{Pop}} = \mathrm{Nu}_{\mathrm{Chu}}\left(1 + 0.3\left(32^{0.5}\mathrm{Gr}^{-0.25}\frac{l_{\mathrm{c}}}{2\varrho_{\mathrm{out}}}\right)^{0.909}\right). \tag{5.34}$$

In 2013, [Day+13] presented the following correlation, that can be applied if $10^2 < \mathrm{Gr}\,\mathrm{Pr} < 10^9$,

$$\mathrm{Nu}_{\mathrm{Day}} = \begin{cases} [-0.2165 + 0.5204\,\mathrm{Gr}\,\mathrm{Pr}^{0.25} + 0.8473] & \text{for } 0.1 \leq \left(\frac{l_{\mathrm{c}}}{2\varrho_{\mathrm{out}}}\right) \leq 1, \\ [-0.06211 + 0.5441\,\mathrm{Gr}\,\mathrm{Pr}^{0.25} + 0.6123] & \text{for } 2 \leq \left(\frac{l_{\mathrm{c}}}{2\varrho_{\mathrm{out}}}\right) \leq 10. \end{cases} \tag{5.35}$$

Kreith et al. [KBM11] calculated the following correlation,

$$\mathrm{Nu}_{\mathrm{Kre}} = \begin{cases} [0.555\,(\mathrm{Gr}\,\mathrm{Pr})^{0.25}] & \text{for } 10^5 < \mathrm{Gr}\,\mathrm{Pr} < 10^9, \\ [0.021\,(\mathrm{Gr}\,\mathrm{Pr})^{2/5}] & \text{for } 10^9 < \mathrm{Gr}\,\mathrm{Pr} < 10^{12}. \end{cases} \tag{5.36}$$

McAdams [McA54] presented the following correlation,

$$\mathrm{Nu}_{\mathrm{McA}} = \begin{cases} [0.59\,(\mathrm{Gr}\,\mathrm{Pr})^{0.25}] & \text{for } 10^4 < \mathrm{Gr}\,\mathrm{Pr} < 10^9, \\ [0.13\,(\mathrm{Gr}\,\mathrm{Pr})^{1/3}] & \text{for } 10^9 < \mathrm{Gr}\,\mathrm{Pr} < 10^{12}. \end{cases} \tag{5.37}$$

Eigenson [Eig40] calculated the following correlation,

$$\mathrm{Nu}_{\mathrm{Eig}} = \begin{cases} [0.48\,(\mathrm{Gr})^{0.25}] & \text{for } 10^6 \leq \mathrm{Gr} \leq 10^9, \\ [51.5 + 0.0000726\,(\mathrm{Gr})^{0.63}] & \text{for } 10^9 \leq \mathrm{Gr} \leq 1.69 \cdot 10^{10}, \\ [0.148\,(\mathrm{Gr})^{1/3}] & \text{for } \mathrm{Gr} \geq 10^{10}. \end{cases} \tag{5.38}$$

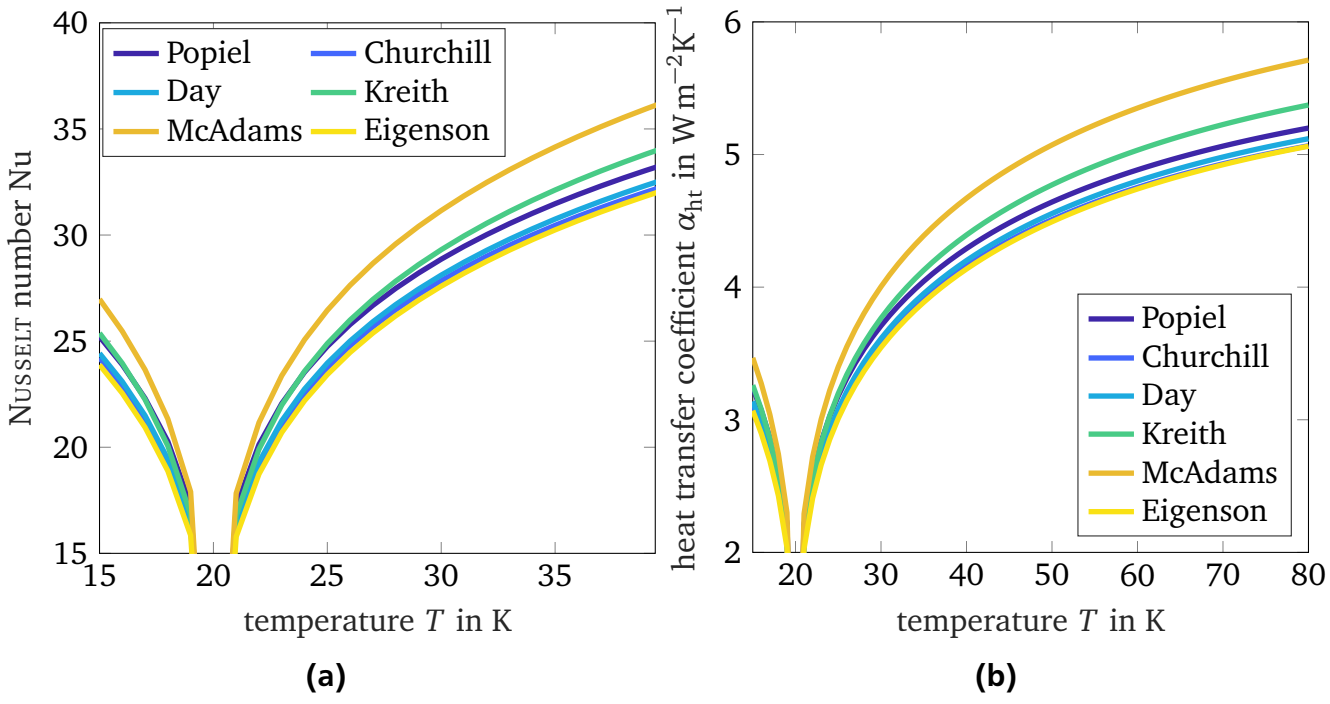

Figure 5.10.: Comparison of different literature Nusselt numbers (a) and heat transfer coefficients (b) with respect to temperature for the arrester flange $h = 0.2\,\mathrm{m}$. The correlations agree well, only the correlation given by [McA54] is slightly above the other curves and yields the highest heat transfer coefficient.

Fig. 5.10(a) compares the different Nu correlations for the arrester flange geometry. A typical flange height for station class arresters of $h = 0.2\,\mathrm{m}$ is assumed. Fig. 5.10(b) compares the resulting heat transfer coefficients α_{ht}. All literature correlations agree well. The correlation

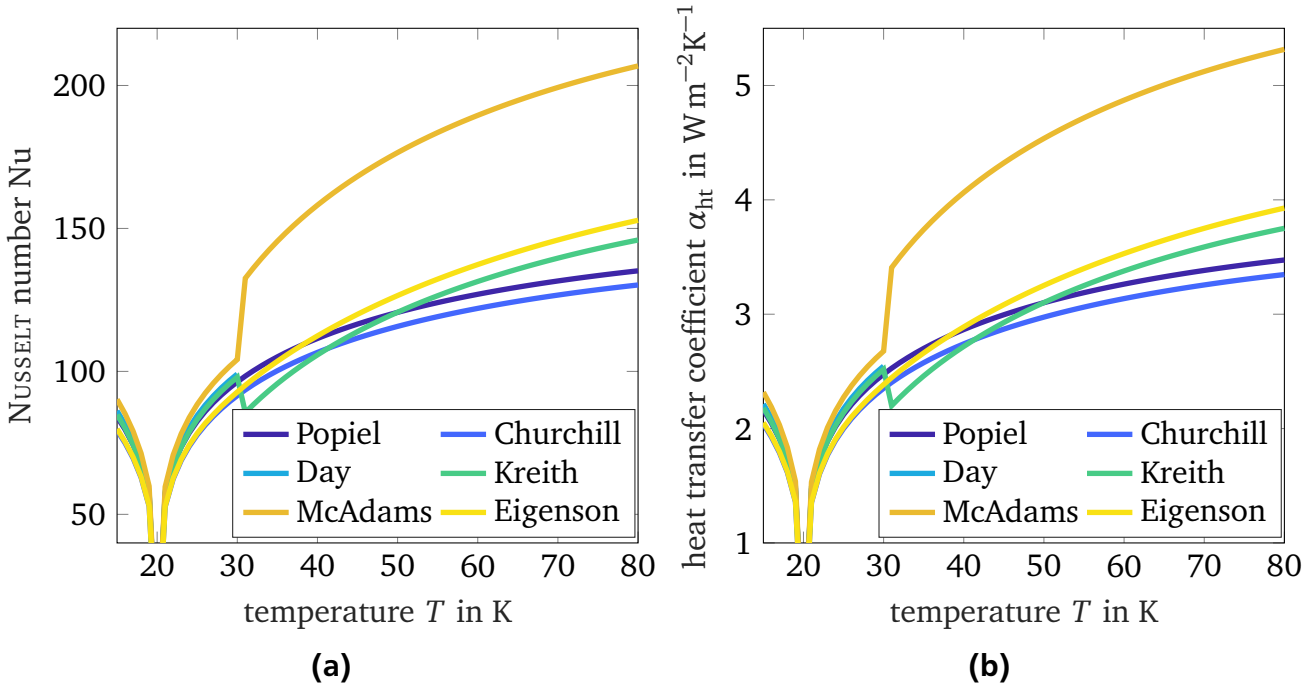

Figure 5.11.: Comparison of different literature Nusselt numbers (a) and heat transfer coefficients (b) with respect to temperature for the arrester unit with $h = 1\,\mathrm{m}$. The correlation of [McA54] does not fit well to the other curves and seems to overestimate the heat transfer.

of [McA54] is slightly above the other curves and yields the highest heat transfer coefficient. The convective heat transfer coefficient is in the range of $3-5\,\frac{\mathrm{W}}{\mathrm{Km}^2}$ over the relevant temperature range. Thus, this range is adopted for the convective heat transfer boundary condition of arrester flanges. Fig. 5.11(a) compares the introduced Nu-correlations and Fig. 5.11(b) heat transfer coefficients for a typical arrester unit of $h = 1\,\mathrm{m}$. Again, the correlation of [McA54] seems to largely overestimate the heat transfer. In contrast to the flange case, a greater spread of the curves is observed. This can be attributed to the fact that the curves are commonly correlated from experiments on smaller cylinders or plates. The adopted convective heat transfer coefficient for an arrester unit is in the range of $2-4\,\frac{\mathrm{W}}{\mathrm{Km}^2}$.

Internal Heat Transfer

The air gap of a station class arrester unit is, basically, a gas filled vertical annulus (see Fig. 5.12). Its outer surface, A_2, at ϱ_2, is assumed to be isothermal. The inner surface, A_1 at ϱ_1, is assumed to be uniformly heated by a heat source. The arrester unit height h defines the length of the annulus. The critical length, l_c for the calculation of Nu is the air gap width, $\delta = \varrho_2 - \varrho_1$.

A numerical computation of the convective heat transfer contribution in the air gap based on CFD simulations is unrealistic for the purpose of simulating and, moreover, optimizing surge arresters.

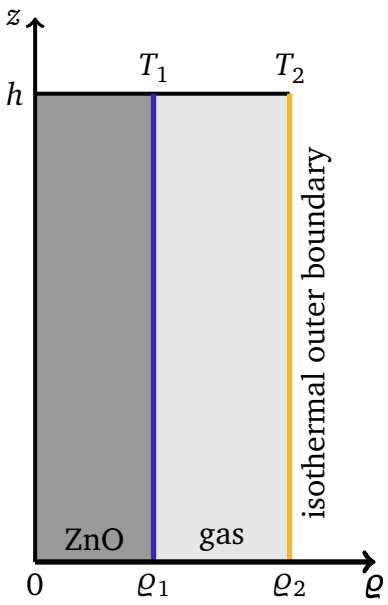

Figure 5.12.: Cut of the geometry of an arrester unit. The gas-filled volume between the ZnO stack and the housing, the arrester air gap is shown. It has the form of a vertical annulus. To estimate the radial convective heat transfer in the air gap, the NUSSELT number is computed assuming a isothermal inner boundary at the ZnO stack and outer boundary at the porcelain housing.

An effective, temperature-dependent thermal conductivity, $\lambda_{\text{gap}}(T)$ is defined that approximates the total internal air-gap heat transfer of a station class arrester unit. It accounts for conductive, convective and radiative heat transfer effects by,

$$\lambda_{\text{gap}}(T) = \lambda_{\text{air}} + \lambda_{\text{conv}} + \lambda_{\text{rad}}(T). \tag{5.39}$$

Herein, the conductive contribution is λ_{air}, the convective contribution is λ_{conv}, and the radiative contribution is $\lambda_{\text{rad}}(T)$. Conductive and convective contributions are combined in the linear heat conductivity λ_{cc} and described by the mean NUSSELT number for a closed annular gap,

$$\lambda_{\text{cc}} = \lambda_{\text{air}} + \lambda_{\text{conv}} = \text{Nu}\lambda_{\text{air}}. \tag{5.40}$$

In [Spä14], different models to evaluate the NUSSELT number for a station class arrester air gap were compared. The models were obtained from [VDI10; Hin90; Cam80; RN08] and agreed well. In this work, the Nu correlation of [VDI10], is selected based on the comparison of [Spä14]. It is given by,

$$\text{Nu} = \frac{c_1 \left(\frac{h}{\delta}\right)^2}{\frac{h^3 \varrho_1}{\varrho_2{}^4} + c_2 \left(\frac{h}{\delta}\right)^{9/4}}. \tag{5.41}$$

Herein c_1 and c_2 are obtained, as,

$$c_1 = 5.62 \cdot 10^{-4} \text{Gr}(T_1 - T_2)\,\text{Pr}, \qquad c_2 = [\text{Gr}(T_1 - T_2)\,\text{Pr}]^{3/4}\, 854^{-1}, \tag{5.42}$$

where the temperature at the inner and outer air gap surface is $T_{1,2}$, respectively.

The radiative heat transfer contribution in the air gap is approximated by a temperature-dependent equivalent thermal conductivity $\lambda_{\mathrm{rad}}(T)$. The emissive power that is exchanged between the air gap surfaces is based on (5.31). It is given by,

$$\dot{Q}_{12} = A_1 \, C_{12}(T_1^4 - T_2^4), \tag{5.43}$$

where the radiation exchange factor is,

$$C_{12} = C_{\mathrm{s}}\,(\varepsilon_{\mathrm{rad},1}^{-1} + \frac{\varrho_1}{\varrho_2} \cdot ((\varepsilon_{\mathrm{rad},2}^{-1} - 1)))^{-1}, \tag{5.44}$$

and the emissivity of each surface is $\varepsilon_{\mathrm{rad},1,2}$, respectively.

A priori, the surface temperature is unknown and (5.43) cannot be applied directly. Furthermore, due to the nonlinearity of (5.43), the radiative heat transfer contribution must be updated iteratively in order to accurately compute coupled arrester behavior. Thus, a FE implementation of the temperature-dependent equivalent thermal conductivity was proposed in [Spä14]. This conductivity, $\lambda_{\mathrm{rad}}(T)$, is established such that the heat transfer described by the Stefan-Boltzmann-law for an annular cylinder equals the conductive heat flux within the equivalent material filling the gap. To derive the conductivity, the space between the air gap surfaces is radially filled with N thin metal foils at $\varrho = \varrho_i$ at temperature T_i, with $i \in [1, N]$. The position of the inner plate and outer annulus surface is $\varrho_{1,N}$, respectively. The radiative heat flow between foil i and foil $i+1$ is given by,

$$\dot{q}_{i \to i+1} = C_{12}(T_i^4 - T_{i+1}^4). \tag{5.45}$$

Writing out $T_{i+1} = T_i - \Delta T$ yields

$$\begin{aligned}
\dot{q}_{i \to i+1} &= C_{12}\left(T_i^4 - (T_i - \Delta T)^4\right) && (5.46)\\
&= C_{12}(T_i^4 - T_i^4 + 4T_i^3\Delta T - 6T_i^2\Delta T^2 + 4T_i\Delta T^3 - \Delta T^4) && (5.47)\\
&= C_{12}(4T_i^3\Delta T - 6T_i^2\Delta T^2 + 4T_i\Delta T^3 - \Delta T^4). && (5.48)
\end{aligned}$$

At first order in ΔT, one gets

$$\begin{aligned}
\dot{q}_{i \to i+1} &= C_{12}\left(4T_i^3\Delta T + \mathcal{O}(\Delta T^2)\right) && (5.49)\\
&\approx C_{12}(4T_i^3\Delta T). && (5.50)
\end{aligned}$$

Combined with (5.26), (5.48) yields,

$$\alpha_{\mathrm{ht},i} = 4C_{12}T_i^3\,. \tag{5.51}$$

In the limit of a continuous medium, $\Delta T \to 0$, the equivalent thermal conductivity

$$\begin{aligned}
\lambda_{\mathrm{rad}}(T) &= \alpha_{\mathrm{ht}} && (5.52)\\
&= \delta 4C_{12}T^3\,\delta. && (5.53)
\end{aligned}$$

is obtained. Finally, the equivalent thermal conductivity (5.53) for the cylindrical annulus is given by,

$$\lambda_{\mathrm{rad}}(T) = 4C_{12}T^3\,\varrho_1 \ln\left(\frac{\varrho_2}{\varrho_1}\right). \tag{5.54}$$

The validity of this approach for the circular annulus case can be easily verified. By applying Fourier's law, one can write the radiative heat transfer as,

$$\frac{\dot{Q}}{A} = -\lambda_{\mathrm{rad}}(T)\nabla T, \tag{5.55}$$

$$\dot{Q} = -2\pi\varrho h\lambda_{\mathrm{rad}}(T)\frac{\partial T}{\partial \varrho}. \tag{5.56}$$

With (5.54), the same heat transfer as by directly solving (5.43) is obtained after integrating both sides of (5.56) over the air gap and inserting the temperature-dependent conductivity (5.54),

$$\int_{\varrho_1}^{\varrho_2} \frac{\dot{Q}}{\varrho}\,\mathrm{d}\varrho = -\int_{T_1}^{T_2} 2\pi h\lambda(T)_{\mathrm{rad}}\,\mathrm{d}T \tag{5.57}$$

$$\ln\left(\frac{\varrho_2}{\varrho_1}\right)\dot{Q} = C_{12}(T_1^4 - T_2^4)\,2\pi h\varrho_1 \ln\left(\frac{\varrho_2}{\varrho_1}\right), \tag{5.58}$$

which is the same as (5.43).

Validation of the Model for Radiative Heat Transfer in the Air Gap

The radiative heat transfer contribution in the air gap can, alternatively, be computed based on a surface-to-surface radiation exchange model. This model was applied in [Gie18]. However, the method requires a dedicated solver to compute the surface-to-surface interaction of all surface-FE cells. The approach is computationally expensive, as the heat exchange of all surface-FE elements is computed in every time step. It is, in this work, used to validate the proposed nonlinear conductivity model for thermal radiation in the arrester air gap. The Surface-To-Surface Radiation module is provided by COMSOL Multiphysics®.

The validation model is set up as follows: A single arrester unit is modeled. The ZnO block is preheated to typical arrester column temperatures after impulse injections. The ambient temperature is $T_{\mathrm{amb}} = 293\,\mathrm{K}$. The ZnO block cools down via radiative heat transfer over the air gap to the porcelain housing. Fig. 5.13(a) shows that the temperature within the ZnO block decreases over time. A very good agreement between both models is obtained (see Fig. 5.13(b)). The relative deviation is always below 0.24%. The deviation reaches the highest values within the first hour, which is attributed to the involved heat capacities of the ZnO and the porcelain material. Consequently, the nonlinear equivalent material model is considered suitable for modeling radiative heat transfer for long annular cylinders such as air gaps of porcelain housed station class arresters.

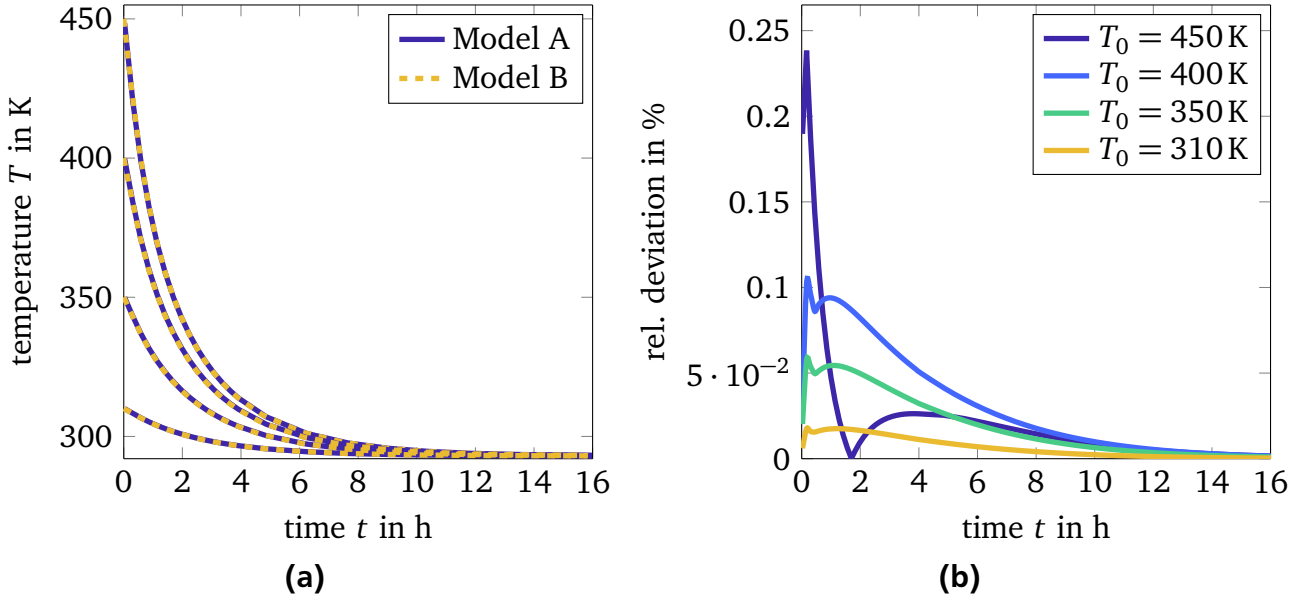

Figure 5.13.: Comparison of the temperature decrease for the developed nonlinear material model (Model A) and the COMSOL model (Model B). (a) shows the temperature decrease for the start temperatures $T_0 = [450\ 400\ 350\ 310]\,\mathrm{K}$. (b) plots the relative deviation between the two models (adapted from [Spä+16a]).

5.2.3 Contribution of the Heat Transfer Mechanisms

The contribution of each heat transfer mechanism to the overall heat transfer is visualized in a Sankey diagram (see Fig. 5.14). The diagrams were presented in the Bachelor thesis of [Alj16]. The thesis was part of a cooperation project together with the Institut für Technische Thermodynamik of the Technische Universität Darmstadt. The heat transfer to the environment and within the air gap was computed based on a steady state heat transfer analysis for a typical 4-unit station class arrester. Fig. 5.14(a) shows the external heat transfer, and Fig. 5.14(b) shows the internal heat transfer in the air gap of a single arrester unit. In Fig. 5.14(a), the radial heat transfer from the arrester surface to the environment is proportionally distributed to radiation (172 W), natural convection (154 W), and forced convection (39 W). In the scope of [Alj16], forced convection due to wind in the laboratory environment was considered. The heat transfer is further separated into a contribution that is dissipated from the porcelain unit housing (Porc.) and the aluminum flange (Al.). It is observed that for the heat transfer to the environment, radiation and convection have a similar contribution. The distribution is different in the arrester air gap (see Fig. 5.14(b)). The radial heat transfer within the air gap is divided into radiation (57 W), convection (36 W), and conduction (15 W). A small share is dissipated longitudinally (all mechanisms combined = 0.5 W). Radiation dominates the heat transfer in the arrester air gap.

To model the convective heat transfer in the air gap, λ_{cc} is calculated only once and is kept constant throughout the entire simulation. The reference temperature at the inner surface is

obtained, if available, from the experiment or from the steady state temperature of each unit. Fig. 5.15 shows the radiative and convective contribution to the heat transfer of the air gap over the relevant temperature range. For high temperatures, the radiative heat transfer exceeds by far the convective contribution. Above 310 K, the convective contribution saturates. This implies that a constant a priori estimation of the convective heat transfer is a valid approximation to study the heat transfer behavior in the air gap, in particular, after impulse injections.

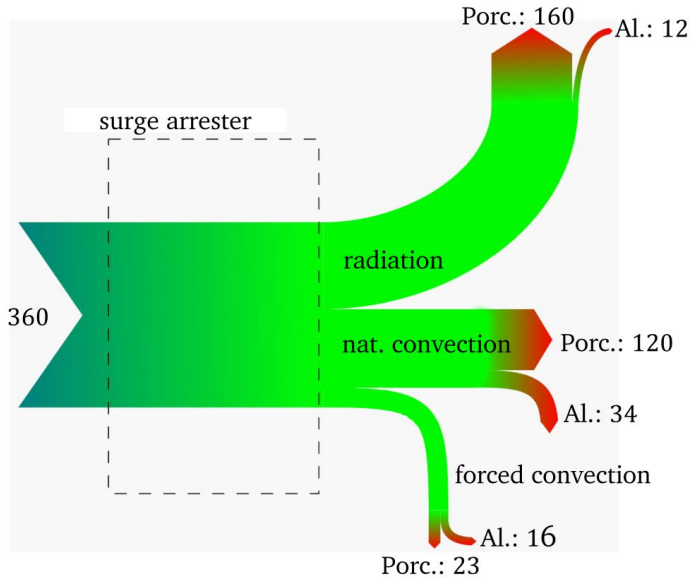

(a)

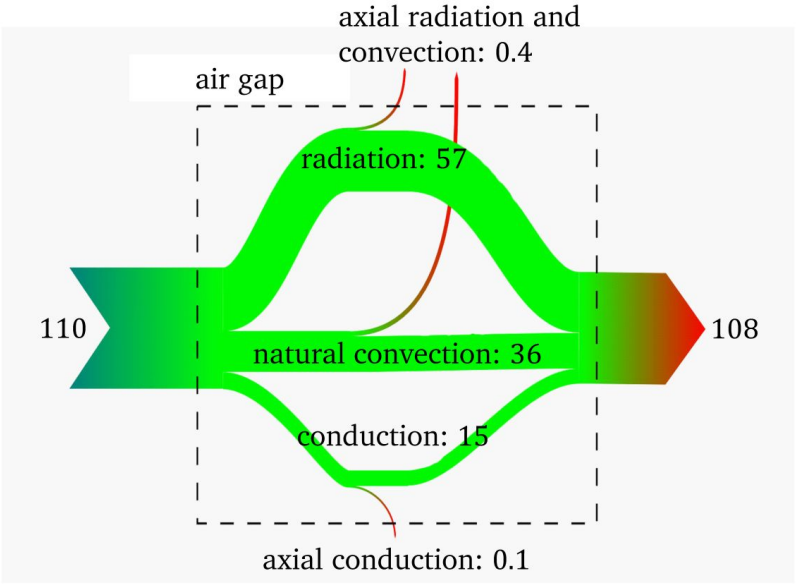

(b)

Figure 5.14.: Sankey diagram of the external heat transfer (a) and internal air gap heat heat transfer in a single unit (b) of the ungraded 550-kV-station class arrester in steady state. The heat transfer contributions are: radiative heat transfer contribution, natural convection, forced convection and heat conduction. The heat is dissipated from the porcelain unit housing (Porc.) and the aluminum flange (Al.). All quantities are given in W (adapted from [Alj16]).

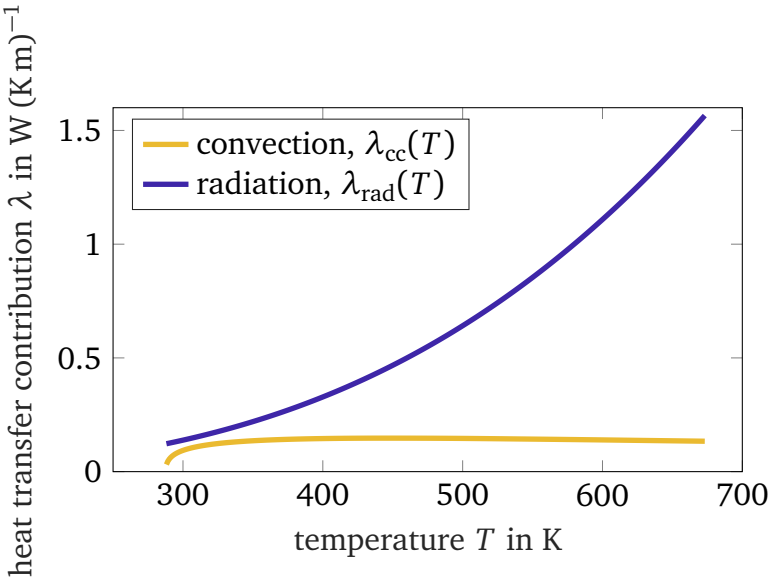

Figure 5.15.: Convective and radiative heat transfer contribution in the arrester air gap. The radiative heat transfer increases nonlinearly $\propto T^3$ according to (5.54). The convective heat transfer contribution based on the NUSSELT number of (5.41) quickly saturates. The radiative heat transfer exceeds by far the convective contribution for higher temperatures.

5.3 Discretized Formulation

The simulation procedure can be divided into different steps. First, pre-processing stages are undertaken. Then, the physical model of the problem is defined, the geometry and material distributions are modeled, and boundary conditions are specified. These steps introduce assumptions and simplifications to the physical problem. Second, the selected set of differential equations is discretized, and the numerical solution of the discretized problem is computed. Third, the quantities of interest are obtained in the post-processing stage. The arrester behavior is described by a time-dependent and strongly nonlinear EQST system of equations. The finite element method (FEM) is a well known discretization method for this kind of time domain problems. The method transforms the partial differential equations to a matrix system that is numerically solved on the basis of algebraic operations.

5.3.1 Time Discretization

The nonlinear field- and temperature-dependent EQS equation (5.6) is a stiff problem and requires, thus, special care for the selection of the time integration scheme [Den14; SGW11; Str04]. For this reason, an implicit time integration approach is adopted. First, (5.6) is integrated over one time step as,

$$[\nabla\cdot(\varepsilon\nabla\phi)]_{t^n}^{t^{n+1}}+\int_{t^n}^{t^{n+1}}\nabla\cdot(\sigma\nabla\phi)\mathrm{d}t=0. \tag{5.59}$$

This yields,

$$\nabla\cdot(\varepsilon\nabla\phi)\Big|^{t^{n+1}}-\nabla\cdot(\varepsilon\nabla\phi)\Big|^{t^n}+\int_{t^n}^{t^{n+1}}\nabla\cdot(\sigma\nabla\phi)\mathrm{d}t=0. \tag{5.60}$$

In the next step, the equation is discretized in time by adopting the backward Euler scheme as,

$$(\nabla\cdot(\varepsilon\nabla\phi)+\Delta t_{\mathrm{el}}\nabla\cdot(\sigma\nabla\phi))\Big|^{t^{n+1}}=\nabla\cdot(\varepsilon\nabla\phi)\Big|^{t^n}, \tag{5.61}$$

where, $\Delta t_{\mathrm{el}}=(t^{n+1}-t^n)$ is the electric time step.

The nonlinear transient heat conduction equation (5.25) describes the time evolution of the temperature depending on the nonlinear material parameters, the volumetric heat capacity, $c_{\mathrm{v}}(T)$, and the thermal conductivity, $\lambda(T)$, respectively. For the time discretization, the same procedure as for the EQS problem is adopted. This yields,

$$(c_{\mathrm{v}}T-\Delta t_{\mathrm{th}}\nabla\cdot(\lambda\nabla T)-\Delta t_{\mathrm{th}}\dot{q})\Big|^{t^{n+1}}=(c_{\mathrm{v}}T)\Big|^{t^n}, \tag{5.62}$$

where, Δt_{th} is the thermal time step.

5.3.2 Finite Element Ansatz for the Electroquasistatic Problem

The time-discretized EQS problem (5.61) is discretized in space based on the FEM. For a detailed discussion on the derivation and fundamentals of the FEM refer to e.g. [SF96; Haf87; Kos94; Ste98]. In the following, the FEM formulation of the 2D-axisymmetric EQS problem is introduced.

A FEM study follows a fundamental scheme that starts with the discretization of a computational domain Ω into a set of mesh cells referred to as *finite elements*. In each of these cells the solution $\phi(\vec{r},t)$ is approximated by linear basis functions as

$$\phi(\vec{r},t) \approx \sum_j w_j(\vec{r}) u_j(t). \tag{5.63}$$

Herein, $w_j(\vec{r})$ are nodal FE shape functions (local piecewise linear hat functions) associated with the nodes of a triangular mesh constructed for the computational domain Ω and $u_j(t)$ are the Degrees of Freedom (DoFs). The Ritz-Galerkin method determines a solution for the DoFs such that the error, i.e. the residual, of the approximated and exact solution is minimized. The discretization of the resistive term in (5.6) is exemplarily shown. Starting with the conductivity term of the EQS equation (5.6), the following transformations are performed,

$$\int_\Omega \nabla\cdot(\sigma\nabla\phi) w_i \mathrm{d}\Omega = \int_\Omega \nabla\cdot(\sigma\nabla\phi w_i)\mathrm{d}\Omega - \int_\Omega (\sigma\nabla\phi\cdot\nabla w_i)\mathrm{d}\Omega, \tag{5.64}$$

$$= \int_{\partial\Omega} \sigma\frac{\partial\phi}{\partial n} w_i \mathrm{d}\Gamma - \int_\Omega (\sigma\nabla\phi\cdot\nabla w_i)\mathrm{d}\Omega. \tag{5.65}$$

The solution is approximated by the basis functions, as defined in (5.63), and becomes,

$$\approx \sum_j u_j \underbrace{\int_{\partial\Omega} \sigma\frac{\partial w_j}{\partial n} w_i \mathrm{d}\Gamma}_{\text{boundary term}} - \sum_j u_j \underbrace{\int_\Omega (\sigma\nabla w_j\cdot\nabla w_i)\mathrm{d}\Omega}_{:=k_{ij}}. \tag{5.66}$$

The first term is determined by the boundary conditions of the problem at hand. In the case of homogeneous Neumann boundary conditions, this term vanishes. At boundaries with Dirichlet boundary conditions the FE test functions, w_i are zero and boundary terms vanish as well. The second term corresponds to line i of the $n\times n$ stiffness matrix $\mathbf{K}_\sigma$. Thus, neglecting the boundary terms, the spatially discretized EQS system of equations is obtained from (5.61) as,

$$(\mathbf{K}_\varepsilon + \Delta t_{\mathrm{el}}\mathbf{K}_\sigma)\mathbf{u}\Big|^{t^{n+1}} = \mathbf{K}_\varepsilon\mathbf{u}\Big|^{t^n}, \tag{5.67}$$

$$\mathbf{K}_\varepsilon^{n+1}\mathbf{u}^{n+1} - \mathbf{K}_\varepsilon^{n}\mathbf{u}^{n} + \Delta t_{\mathrm{el}}\mathbf{K}_\sigma^{n+1}\mathbf{u}^{n+1} = 0, \tag{5.68}$$

where $\mathbf{K}_\varepsilon$ is defined analogously using the permittivity, ε, instead of the conductivity, σ. The superscripts indicate the time steps at which the variables are evaluated.

5.3.3 Finite Element Ansatz for the Transient Heat Conduction Problem

The procedure to obtain the FE-discretized transient heat conduction problem follows the procedure to deduce the EQS problem. Again, the solution for the temperature is approximated as,

$$T(\vec{r},t) \approx \sum_j w_j(\vec{r})\vartheta_j(t), \tag{5.69}$$

where $\vartheta_j(t)$ are the DoFs for the unknown temperature. The integral of the first term of (5.62) becomes,

$$\int_\Omega (c_\mathrm{v} T) w_i \mathrm{d}\Omega \approx \sum_j \vartheta_j \underbrace{\int_\Omega c_\mathrm{v} w_j w_i \mathrm{d}\Omega}_{:=m_{ij}} . \tag{5.70}$$

This corresponds to line i of the mass matrix $\mathbf{M}_{c_\mathrm{v}}$. The source term of the electric losses yields a source term vector, $\dot{\boldsymbol{q}}$. Finally, the discretized heat conduction equation is obtained from (5.62) as,

$$\left[(\mathbf{M}_{c_\mathrm{v}} + \Delta t_\mathrm{th}\mathbf{K}_\lambda)\boldsymbol{\vartheta} - \Delta t_\mathrm{th}\dot{\mathbf{q}}\right]\Big|^{t^{n+1}} = \mathbf{M}_{c_\mathrm{v}}\boldsymbol{\vartheta}\Big|^{t^n} . \tag{5.71}$$

Herein, $\dot{\mathbf{q}}$ is the source term corresponding to the heat sources $\dot{q}_i$. Dirichlet, and Neumann boundary conditions are considered, respectively. The homogeneous Neumannn boundary condition is equivalent to the electrical case and resembles a thermal insulation. Additionally, the inhomogeneous Neumann boundary condition (i.e. a Robin-type boundary condition) is considered, resembling convection, or radiation, respectively. The Dirichlet boundary condition imposes a fixed temperature on the boundary cells of the computational domain. The Neumann boundary condition imposes a *normal* heat flux density $\dot{q}_\mathrm{n}$ on the boundary cells. Thus, in (5.73) additional boundary terms, the vector $\mathbf{b}$ and the matrix $\mathbf{B}$ arise on the left hand side as [Den14],

$$\left[(\mathbf{M}_{c_\mathrm{v}} + \Delta t_\mathrm{th}(\mathbf{K}_\lambda + \mathbf{B})\boldsymbol{\vartheta} - \Delta t_\mathrm{th}(\dot{\mathbf{q}} + \mathbf{b})\right]\Big|^{t^{n+1}} = \mathbf{M}_{c_\mathrm{v}}\boldsymbol{\vartheta}\Big|^{t^n}, \tag{5.72}$$

$$\mathbf{M}_{c_\mathrm{v}}^{n+1}\boldsymbol{\vartheta}^{n+1} - \mathbf{M}_{c_\mathrm{v}}^{n}\boldsymbol{\vartheta}^{n} + \Delta t_\mathrm{th}\left(\mathbf{K}_\lambda^{n+1} + \mathbf{B}^{n+1}\right)\boldsymbol{\vartheta}^{n+1} = \Delta t_\mathrm{th}\left(\dot{\mathbf{q}}^{n+1} + \mathbf{b}^{n+1}\right). \tag{5.73}$$

Each element of $\mathbf{b}$ is obtained as,

$$-\sum_j \vartheta_j \int_\Gamma (\lambda \frac{\partial w_j}{\partial n}) w_i \mathrm{d}\Gamma = \underbrace{\int_\Gamma \dot{q}_\mathrm{n} w_i \mathrm{d}\Gamma}_{\text{contributes to } B_{ij}, b_i} . \tag{5.74}$$

A convection or radiation boundary condition is regarded as a heat flux in the direction normal to the boundary surface. Both conditions are temperature-dependent. Thus, for the convective case, it is obtained from (5.26) as,

$$\int_\Gamma \dot{q}_\mathrm{n} w_i \mathrm{d}\Gamma = \sum_j \int_\Gamma \alpha_\mathrm{ht}(w_j \vartheta_j - \vartheta_0) w_i \mathrm{d}\Gamma, \tag{5.75}$$

where, ϑ_0 is the constant ambient temperature. This is separated to contributions that enter **B** and **b**, respectively, by,

$$B_{ij} = \int_\Gamma \alpha_\mathrm{ht} w_j w_i d\Gamma, \tag{5.76}$$

$$b_i = -\int_\Gamma \alpha_\mathrm{ht} \vartheta_0 w_i d\Gamma. \tag{5.77}$$

The radiative boundary condition is obtained from (5.31) as,

$$\int_\Gamma \dot{q}_\mathrm{n} w_i \mathrm{d}\Gamma = \sum_j \int_\Gamma \varepsilon_\mathrm{rad} C_\mathrm{S} \left((w_j \vartheta_j)^4 - \vartheta_0^4 \right) w_i \mathrm{d}\Gamma. \tag{5.78}$$

In [Den14], this expression is linearized, using the temperature solution of the previous time step, ϑ^{n-1},

$$\int_\Gamma \dot{q}_\mathrm{n} w_i \mathrm{d}\Gamma \approx \sum_j \varepsilon_\mathrm{rad} C_\mathrm{S} \left[\int_\Gamma 4 \left(w_j \vartheta_j^{n-1} \right)^3 w_j \vartheta_j^n w_i \mathrm{d}\Gamma \right. \tag{5.79}$$

$$\left. - \int_\Gamma \left(3 \left(w_j \vartheta_j^{n-1} \right)^4 + \vartheta_0^4 \right) w_i \mathrm{d}\Gamma \right]. \tag{5.80}$$

5.4 Multirate Time Integration

A weakly coupled electrothermal system of equations is defined to study arrester behavior. To efficiently solve the coupled FE problem, a multirate time-integration scheme is adopted. The idea to exploit the extremely different time constants of the electrical and thermal sub-problem was introduced in [Hin90]. In this work, the coupled electrothermal arrester problem was solved based on separated electrical and thermal lumped element circuits. In this thesis, this approach is extended to the computationally much more involved FE discretization of the coupled problem. This requires a detailed numerical analysis to guarantee accurate simulation results, and sharp termination conditions to minimize the computational costs. This basic procedure was presented in [Spä14]. It is, in the following, recapitulated and extended.

5.4.1 Electrothermal Problem Formulation

The discretized fully-coupled electrothermal problem is based on (5.68), (5.73), and given by,

$$\begin{pmatrix} \mathbf{K}_{\varepsilon}^{n+1}\mathbf{u}^{n+1} - \mathbf{K}_{\varepsilon}^{n}\mathbf{u}^{n} \\ \mathbf{M}_{c_\mathrm{v}}^{n+1}\boldsymbol{\vartheta}^{n+1} - \mathbf{M}_{c_\mathrm{v}}^{n}\boldsymbol{\vartheta}^{n} \end{pmatrix} + \Delta t \begin{pmatrix} \mathbf{K}_{\sigma}^{n+1}\mathbf{u}^{n+1} \\ \left(\mathbf{K}_{\lambda}^{n+1} + \mathbf{B}^{n+1}\right)\boldsymbol{\vartheta}^{n+1} \end{pmatrix} = \begin{pmatrix} 0 \\ \Delta t \left(\dot{\mathbf{q}}^{n+1} + \mathbf{b}^{n+1}\right) \end{pmatrix}, \tag{5.81}$$

where superscripts indicate the time step at which the variables are evaluated. The EQS and transient heat conduction equation are coupled by the power losses, $\dot{\mathbf{q}}_\mathrm{p}$, which are evaluated based on the EQS electric field solution by,

$$\dot{\mathbf{q}}_\mathrm{p} = \sigma(|\boldsymbol{E}|, T)\boldsymbol{E}^2. \tag{5.82}$$

The term $\dot{\mathbf{q}}$ on the right hand side of the thermal sub-problem is, then, composed of the power losses and, if present, further heat sources. Furthermore, the electric conductivity and the relative permittivity of the stiffness matrices, $\mathbf{K}_\varepsilon, \mathbf{K}_\sigma$, depend on the temperature, respectively.

5.4.2 Multirate Time Integration Scheme and Implementation

A critical simulation issue is the implementation of the coupling between the two problems. The transients of the electrothermal system are governed by the electrical and thermal time constants, τ_el, τ_th, respectively. A multirate time stepping approach is implemented in order to exploit the large difference between the electrical and thermal time constants. The electric time constant, i.e. the charge relaxation time, is defined by [HM89],

$$\tau_\mathrm{el} = \frac{\varepsilon(|\boldsymbol{E}|, T)}{\sigma(|\boldsymbol{E}|, T)}. \tag{5.83}$$

For surge arresters connected to the grid, the electric conductivity varies by six orders of magnitude during a single ac period. The smallest value for the time constant is obtained in the

ac excitation voltage peak. Then, the conductivity reaches its maximum, $\sigma(|\widehat{\boldsymbol{E}}|, T) = \widehat{\sigma}$. The electrical time constant is typically in the range of $\tau_{\mathrm{el}} \approx 100\,\mu s$ for continuous operation and $\tau_{\mathrm{el}} \approx 1\,\mu s$ after an impulse energy injection (see Tab. 5.1). The thermal time constant for a cylinder-symmetric configuration is defined as [LNS04],

$$\tau_{\mathrm{th}} = \frac{\varrho^2 c_{\mathrm{v}}(T)}{\lambda(T)}. \tag{5.84}$$

Hereby, ϱ is the radius of the ZnO resistors. Typically, the thermal time constant for a station class arrester is in the minute to hour range. Tab. 5.1 shows exemplary results based on typical ZnO parameters from station class arresters.

Table 5.1.: Time constant calculation based on typical parameters for station class arresters in continuous operation (adapted from [Spä14]).

electrical parameters	ε in As/Vm		$\widehat{\sigma}$ in S/m	τ_{el} in s
	$6.2 \cdot 10^{-9}$		$4.0 \cdot 10^{-3}$	$1.6 \cdot 10^{-6}$
thermal parameters	λ in W/Km	c_{v} in J/Km^3	Radius ϱ in m	τ_{th} in s
	23	$3 \cdot 10^6$	$4 \cdot 10^{-2}$	160

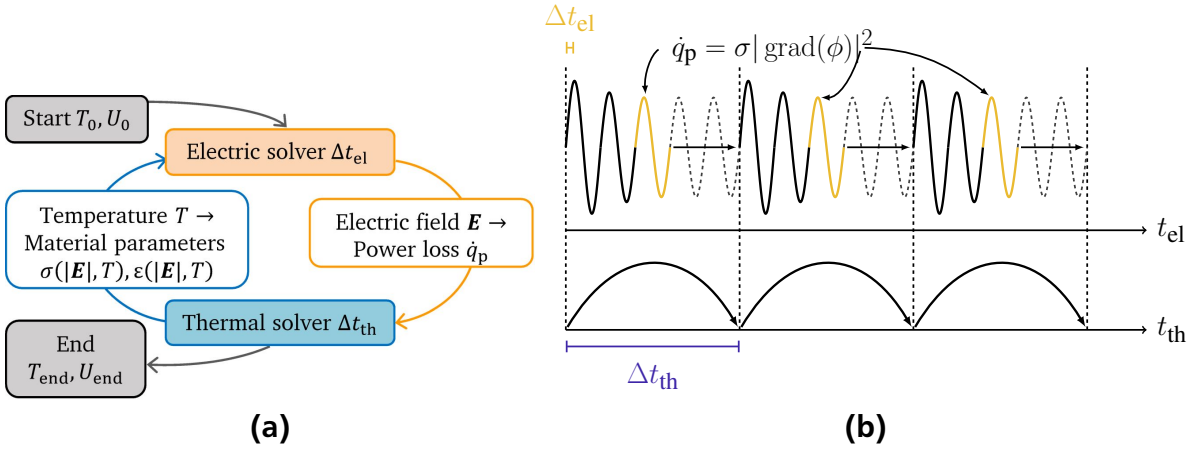

Figure 5.16.: (a) EQST problem with the coupling parameters, the power loss density $\dot{q}_{\mathrm{p}}$ and the electrical material parameters of the ZnO resistors. (b) Multirate time stepping scheme assuming a local EQS stationary state within every thermal time step. For an ac-excited problem, the stationary time-harmonic electric state is obtained after several ac periods. When this state is reached, the average power losses per period can be computed based on (5.85). Then, the thermal solver can advance in time (adapted from [Spä+16b]).

Due to the long thermal transients in arresters, a fully-coupled solving routine for (5.81) is computationally extremely cumbersome and impossible for optimization purposes. However,

the following condition holds for electrothermal surge arrester problems, $\tau_{\mathrm{el}} \ll \tau_{\mathrm{th}}$. Thus, a multirate time integration is adopted. A multirate ansatz is classified as an extension of the modular approach (cf. [SAC12]). Two time steps, the electrical and thermal Δt_{el}, Δt_{th} are distinguished based on the electric and thermal time constants, respectively. The procedure, furthermore, exploits the sinusoidal voltage excitation by assuming an intermediate electrical stationary state. The main idea of the multirate time integration is illustrated in Fig. 5.16. The EQS problem (5.68) is solved with an electric time step of $\Delta t_{\mathrm{el}} < 100\,\mu s$. Due to the nonlinear material properties, a fully transient solution is required. For an ac excitation, however, a stationary time-harmonic electric state is obtained after a short settling time. The arrester currents and voltages are computed for several periods of the sinusoidal voltage until this stationary state is reached (see Fig. 5.16). Then, the average power loss density per ac period, T_{p}, is computed by

$$\dot{q}_{\mathrm{p}} = \frac{1}{T_{\mathrm{p}}} \int_{T_{\mathrm{p}}} \sigma(|\boldsymbol{E}|, T)\boldsymbol{E}^2 \mathrm{d}t. \tag{5.85}$$

Subsequently, the thermal solution (5.73) is advanced in time with a large thermal time step, Δt_{th}, where the total power loss during Δt_{th} is predicted from the previous computation of the power loss within one ac-period in the electric stationary state. The new temperature distribution is used to recalculate the material properties and, thus, obtain a new electric stationary state.

The simulation of the steady state for a station class arrester connected to the power grid is still computationally expensive. This is mainly caused by the many electric solver calls for the long-time simulations. Therefore, the calculation time of the EQST steady state can further be reduced significantly by adopting an adaptive update scheme. The update scheme is illustrated in Fig. 5.17. If the change in the electric conductivity is below a problem specific threshold

$$\frac{|\sigma - \sigma_{\mathrm{old}}|}{\sigma_{\mathrm{old}}} < \xi, \tag{5.86}$$

the change of the power loss distribution is negligible. The electric conductivity computed in the last run of the electric solver is σ_{old}. As long as this condition is fulfilled, no electrical update is required and the thermal solver steps forward in time. If the threshold is exceeded, the updated material properties are passed to the electric solver to recalculate the loss distribution. The procedure is repeated until the simulation is finished. In the case of steady state computations, the conductivity-adaptive scheme significantly reduces the computation time by skipping unnecessary evaluations of the electric problem.

The multirate time stepping procedure is formally first order accurate. In order to resolve the strong nonlinearity of the materials involved, however, extremely small time steps are needed. The formal order of accuracy of the time stepping procedure is, thus, less relevant for the overall simulation accuracy. For the solution of the electrical and thermal problems (5.68) and (5.73), respectively, an in-house, MPI-parallel 2D FEM code based on nodal triangular elements is used. A fixed-point iteration is applied in every time step to handle material nonlinearities.

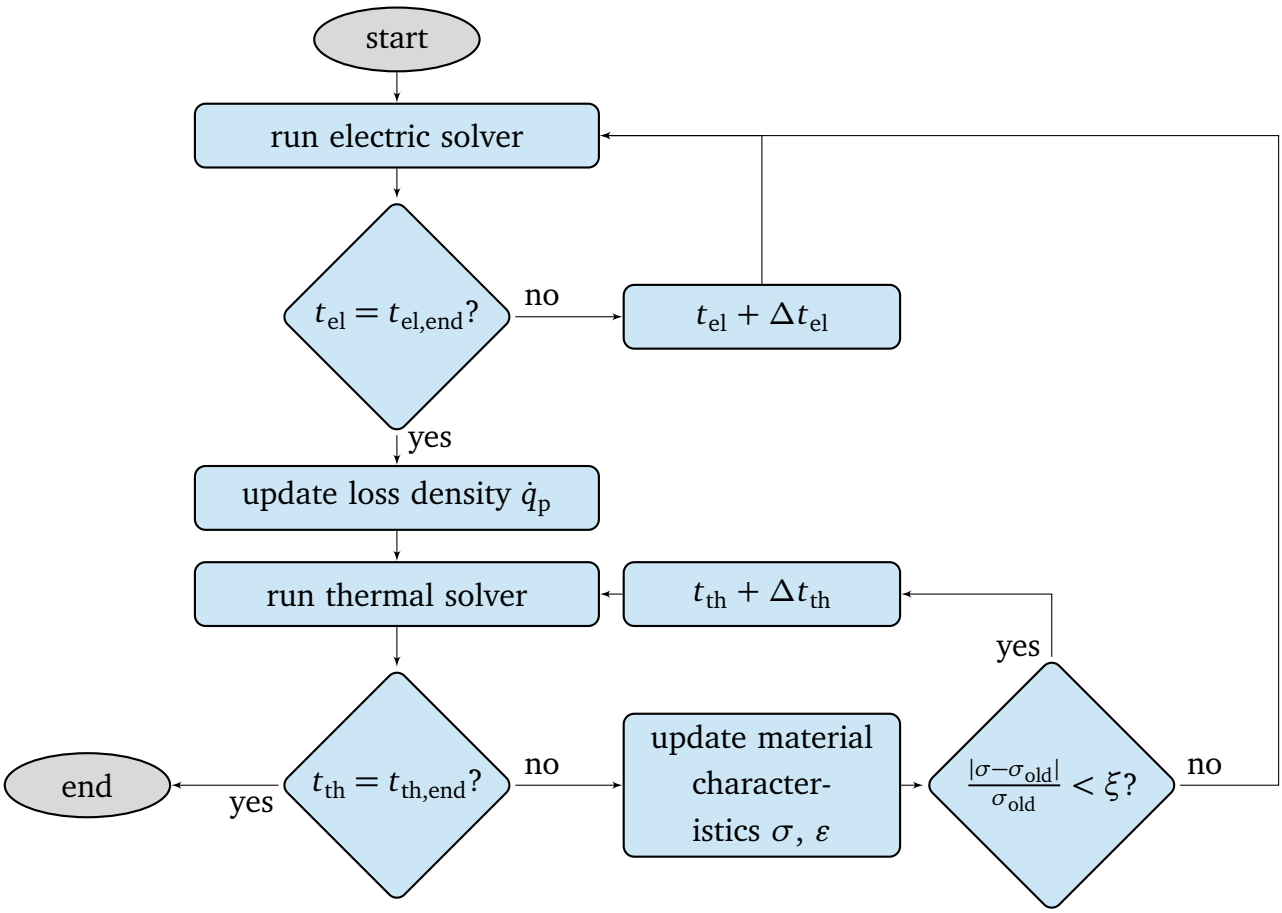

Figure 5.17.: Structural diagram of a coupled electrothermal simulation procedure. First, the electric solver advances in time with the extremely fine electric time step, Δt_{el} until the local ac stationary state is reached after several power-frequency periods, i.e. $t_{el} = t_{el,end}$. Then, the power loss density is computed based on the last ac stationary state period (5.85). Second, the thermal solver advances in time with the thermal time step, Δt_{th} until the end of the simulation, $t_{th} = t_{th,end}$ is reached. After each thermal time step, the electric material characteristics σ and ε are updated. If the change in the conductivity is above the predefined threshold ξ, the electrical solver is restarted in order to update the power losses.

5.5 Numerical Validation

5.5.1 Analysis of the Numerical Parameters

The proposed EQST multirate time integration scheme is numerically tested and the EQS problem is validated according to [IEC14]. For each arrester investigated in this thesis, a detailed convergence test was performed (see e.g. [Spä14; Sch16; Rup19]). In the following, excerpts adapted from [Rup19] show typical convergence tests. The convergence test indicate how to set the parameters of the algorithms in order to simulate numerically the thermal stability of the 550-kV arrester with a sufficient accuracy and an affordable computation time.

The convergence test is set up as follows. An impulse injection of $\Delta T = 200\,\mathrm{K}$ is applied to the ZnO resistors of the arrester. The arrester is connected to the power grid and is, initially, in steady-state. To compute the local relative electric field deviation,

$$e_{i,\mathrm{rel}} = \left| \frac{E_i - E_{i,\mathrm{ref}}}{E_{i,\mathrm{ref}}} \right|, \tag{5.87}$$

a very fine reference solution is simulated with the local electric field, $E_{i,\mathrm{ref}}$. The error is evaluated along the arrester axis, where i is the index of the FE elements along the axis. The mean relative deviation, e_{rel}, is the relative deviation averaged along the arrester axis.

Fig. 5.18(a) shows the mean and maximum relative deviation for different electric time step sizes. A first order convergence of the time integration is observed. The thermal time integration error shows the same behavior (cf. [Sch16]). To obtain an error below $3 \cdot 10^{-6}$, an electric time step of $\Delta t_{\mathrm{el}} = 10\,\mu s$ for impulse simulations is selected. Higher impulses require an adjustment of the electric time step size. This is due to the high impulse temperatures, which shift the operating point in the ZnO conductivity characteristic to the strongly nonlinear region.

The multirate procedure computes the electric losses per period of the sinusoidal voltage excitation when the intermediate electrical stationary state is obtained. The number of electrical periods until this stationary state is reached is, $n_{\mathrm{period,el}}$. Fig. 5.18(b) shows that, in this example, steady state is reached already after two ac periods. The mean relative deviation between this period and reference period is $e_{\mathrm{rel}} = 0.027\%$.

Table 5.2 lists the investigated numerical parameters, electrical time step, Δt_{el}, thermal time step, Δt_{th}, numerical solver precision, and size of the FE mesh cells in the different materials. The values are given for the impulse injection simulation and steady state simulations, respectively. The mesh resolution is valid for the impulse and steady state simulation case, respectively.

5.5.2 Validation of the Electro-Quasistatic Problem

The electric part of the proposed approach is validated by following the procedure defined in the IEC standard [IEC14]. The IEC standard three-unit arrester including its grading ring

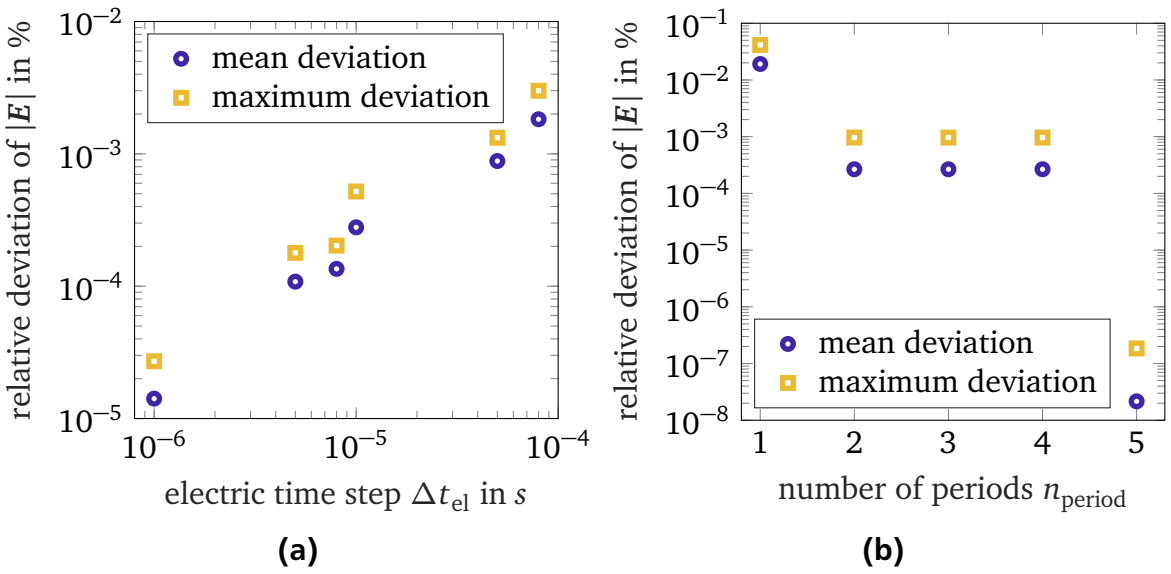

Figure 5.18.: Mean and maximum relative deviation for different electric time steps Δt_{el} (a) and different numbers of computed electrical periods $n_{\mathrm{period,el}}$ (b), (adapted from [Rup19]).

Table 5.2.: Numerical parameters for simulations of the arrester under impulse operation and for stationary state operation, (adapted from [Rup19], [Spä14]).

Type of simulation	impulse injection	steady state
parameter	value	–
Δt_{el}	$10\,\mu s$	$70\,\mu s$
$n_{\mathrm{period,el}}$	2	2
thermal time step Δt_{th}	60 s	100 s
solver precision	10^{-10}	10^{-10}
material	maximum mesh size	
ZnO	5 mm	
air (surrounding)	adaptive	
porcelain	20 mm	
aluminum (flange)	5 mm	
aluminum (heat sinks)	5 mm	

system is considered. The continuous operating voltage of the arrester is $U_{\mathrm{c}} = 333\,\mathrm{kV}$ (rms). The nonlinear electrical conductivity and the permittivity of the ZnO elements are provided in the standard. The maximum voltage stress and the maximum ratio $U_{\mathrm{ct}}/U_{\mathrm{c}}$ resulting from the simulations are summarized in Tab. 5.3. Herein, the ratio of $U_{\mathrm{ct}}/U_{\mathrm{c}}$ is determined by dividing

the calculated maximum voltage stress (here named U_{ct}) along the total length of the arrester axis column by the mean voltage stress along the same length [IEC14]. The standard defines case A as a purely capacitive arrester with a grading ring. Cases B and C correspond to a two-grading ring arrester including capacitive and capacitive-resistive currents, respectively. In both cases, a 2D-axisymmetric model is considered. Fig. 5.19 shows the normalized voltage stresses along the resistor column for the cases B and C. The results are in perfect agreement with the IEC reference data with deviations being well below 1%.

Table 5.3.: Comparison of simulation results (EQS-MR) with the IEC reference data [Spä+16b].

Case	Source	Max. voltage stress (%/m)			Max. U_{ct}/U_c
		Top	Middle	Bottom	
A	EQS-MR	49.8	38.6	26.6	1.43
A	IEC	50	39	26	1.44
B	EQS-MR	43.7	40	27.6	1.26
B	IEC	44	40	27	1.27
C	EQS-MR	41.4	39.3	28.8	1.19
C	IEC	41	39	29	1.18

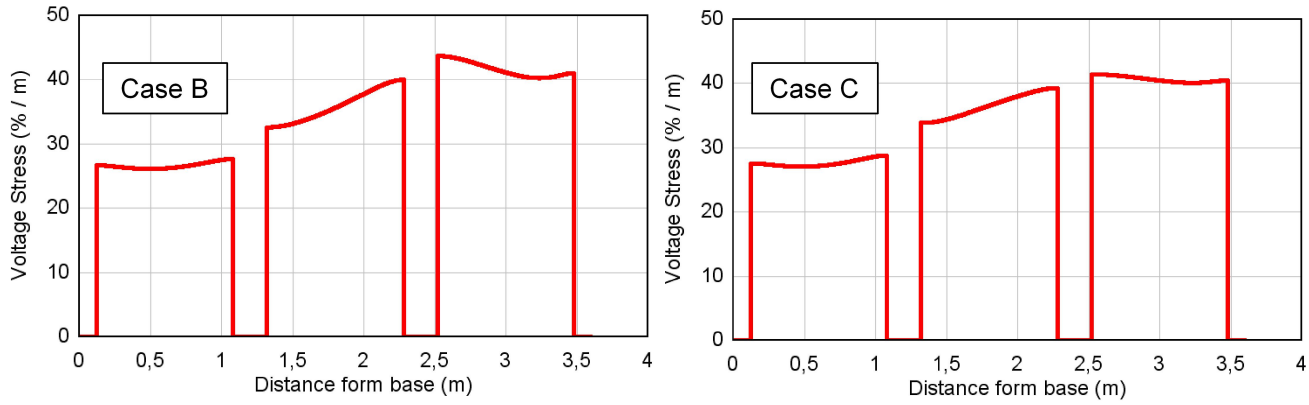

Figure 5.19.: Simulated voltage stress along the resistor column for B and C [Spä+16b].

5.5.3 Validation of Adaptive Multirate Time Integration

The electrothermal steady-state temperature distribution of an arrester is efficiently computed with the adaptive multirate time integration scheme. Fig. 5.20 shows the steady state temperature along the axis of the reduced-diameter 550-kV surge arrester. The steady state is obtained after approximately 6 h. The distribution obtained by the non-adaptive and by the adaptive multirate time integration scheme are compared. The numerical parameters for both simulations are summarized in Tab. 5.4. The threshold of the adaptive conductivity update is $\xi = 0.03$.

An excellent agreement of both curves is achieved (maximal relative error $\epsilon = 0.0021\%$). The calculation time of the steady state is reduced by a factor of five if the adaptive update scheme is used. In this example, the simulation time is 2 h (adaptive) compared to 10.5 h (non-adaptive).

Table 5.4.: Numerical parameters for the adaptive and non-adaptive simulations of the steady state temperature distribution.

electric time step, Δt_{el}	$80\,\mu$s	thermal time step, Δt_{th}	100 s
number of ac periods, $n_{\mathrm{period,el}}$	2	solver precision	10^{-10}

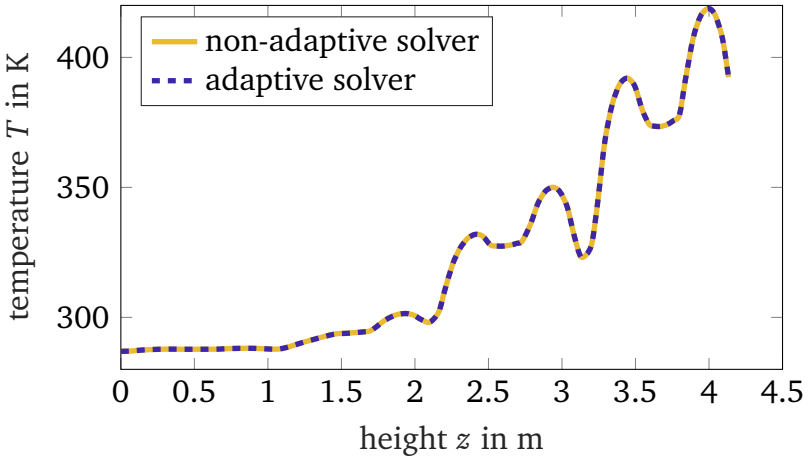

Figure 5.20.: Steady state temperature distribution along the arrester axis obtained by the non-adaptive and adaptive multirate time integration scheme.

6 Station Class Surge Arrester in Continuous Operation

6.1 Self-Grading of an Ungraded Arrester in Steady State

In continuous operation, the *ungraded* 550-kV-station class arrester is energized with U_c at power frequency, i.e. $u_c(t) = \hat{u}_c \sin(2\pi f t)$ with $\hat{u}_c = 488\ \text{kV} = \sqrt{2}U_c$. The arrester's field and temperature distribution at the continuous operation electrothermal steady state is computed with the fully-parallelized multirate FE solver, as introduced in Sec. 5.4. The simulation time of the transient coupled arrester behavior until steady state is in the (low) range of hours for a problem size of tens of thousands of FE nodes. The adaptive conductivity-update scheme significantly reduces the computational costs, as the coupled multirate, non-adaptive scheme takes several tens of hours to complete the calculation (see [Spä14]).

Figure 6.1 shows the electric field stress (top) and temperature (bottom) distribution within the arrester. The electric field stress is unevenly distributed along the arrester axis. The lower two units remain at nearly ambient temperature, whereas the top unit temperature rises by more than 80 K. This is caused by the strong influence of the stray capacitances in the upper units as shown in Sec. 5.1.3.

Figure 6.2(a) shows the electric field strength along the resistor column in the initial and in the steady state. At steady state, the self-grading effect of the ZnO resistors in the top unit can be observed (see Sec. 5.1.3). Due to the higher local field stress and, moreover, the elevated temperature of this unit, the ZnO conductivity and permittivity increase. This results in a reduced field stress in this unit compared to the initial (unheated) arrester state. Consequently, the lower units are exposed to increased electric field stress compared to the initial state, as, in total, the ac excitation voltage drops over all ZnO resistors in the arrester from z_{min} to z_{max} to fulfill,

$$u_c = \int_{z_{\text{min}}}^{z_{\text{max}}} \vec{E}(z,t) \cdot \mathrm{d}\vec{z}. \tag{6.1}$$

As shown in Fig. 6.2(b), the axial power loss density in steady state differs largely from the one in the "cold" arrester at constant ambient temperature. As discussed in Sec. 5.1.3 and Sec. 5.4, due to the nonlinear ZnO conductivity, the average power loss cannot be obtained directly from the rms electric field in the resistors. The electric field stress and resulting current density for the actual temperature are computed for several periods of the sinusoidal voltage until the local

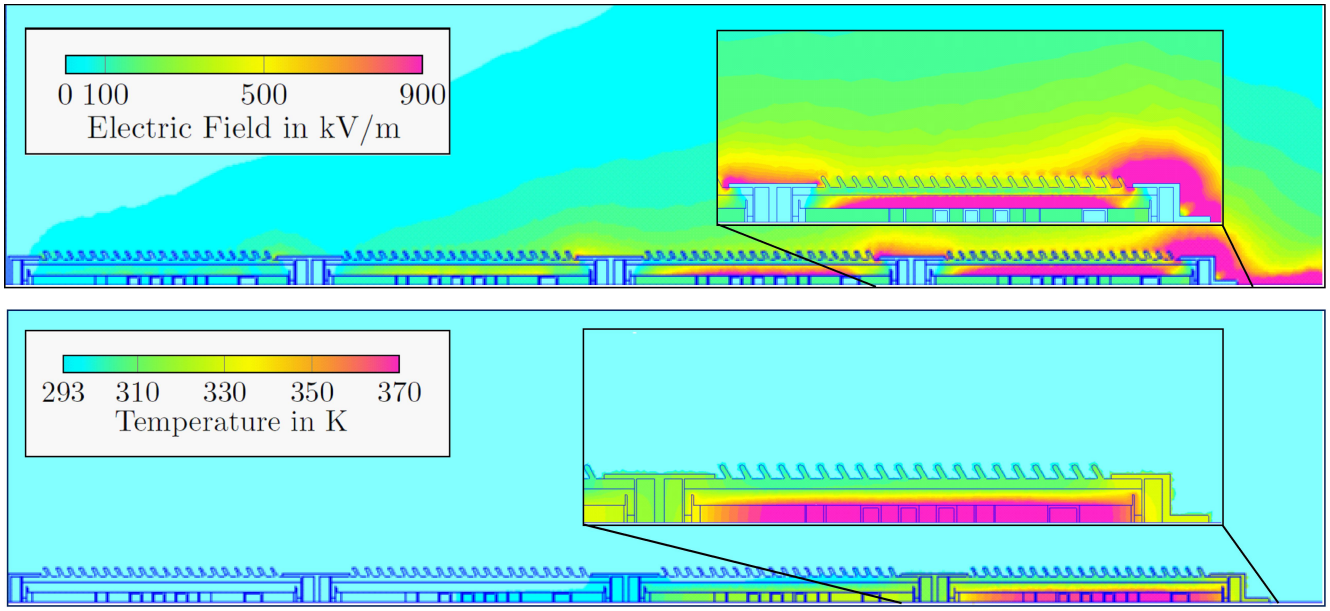

Figure 6.1.: Electric field strength (top) and steady temperature distribution in continuous operation (bottom) in the computational domain (detail). The electric field and temperature stress is increased in the upper units due to the influence of stray capacitances. The lower two units remain at nearly ambient temperature, whereas the top unit temperature rises by more than 80 K [Spä+16b].

electrical stationary state is reached and the losses are evaluated and averaged per ac period based on (5.85).

As the power line voltage is switched on, the arrester units heat up until an electrothermal steady state is reached after approximately 260 min (see Fig. 6.3). Hereby, steady state is defined by a temperature increase of no more than 1 K per hour. Simulations not using a heat conduction model for the arrester air gap (such as presented in Sec. 5) do not converge to a thermal steady state. This indicates that an accurate and complete modeling of thermal phenomena is essential for arrester simulations. Figure 6.1 (bottom) shows the temperature distribution in the arrester at steady state. Due to the uneven distribution of the electric power losses, the temperature stress is concentrated in the upper arrester units.

Figure 6.4 shows the simulated axial steady state temperature distribution in the arrester. The temperature difference between the bottom and top unit of the arrester in steady state is approximately 80 K. The mean axial temperature in each unit (from bottom to the top unit) is $(295, 297, 317, 356)$ K. Thus, the ZnO resistors in the arrester units operate at very different operating points on the electrical characteristic. The temperature results are compared to measurements in Sec. 6.2.1. The measured steady state temperature distribution (see Fig. 6.5) shows an excellent agreement to the simulated distribution.

The electrothermal simulation provides additional information on the local field and temperature stresses compared to a traditional, solely electric field stress distribution based, electrical analysis. Small variations in the electric field distribution will result in extreme changes in the

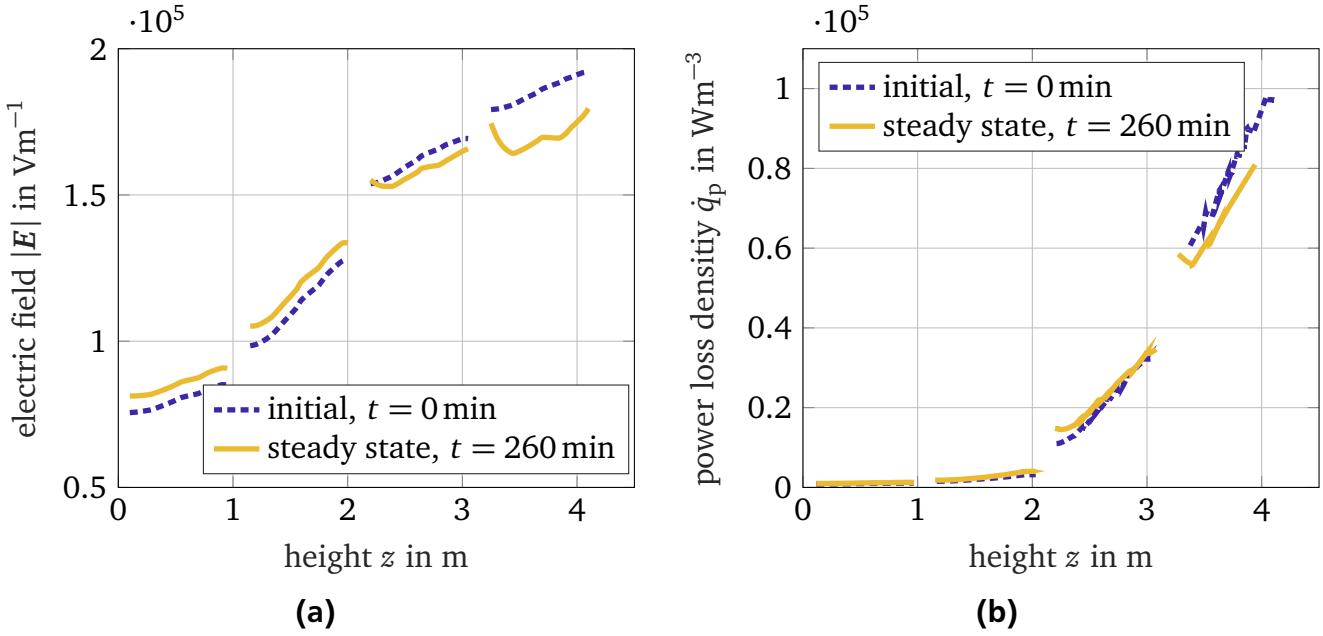

Figure 6.2.: Normalized rms electric field strength (a) along the arrester axis in the initial state at ambient temperature and in steady state continuous operation. Power loss density (b) along the arrester axis, at initial and steady state. The heat sinks are not shown in the curves. The self-grading effect improves the balancing of the field stress along the axis in steady state operation when the upper units operate at elevated temperatures. (adapted from [Spä+16b])

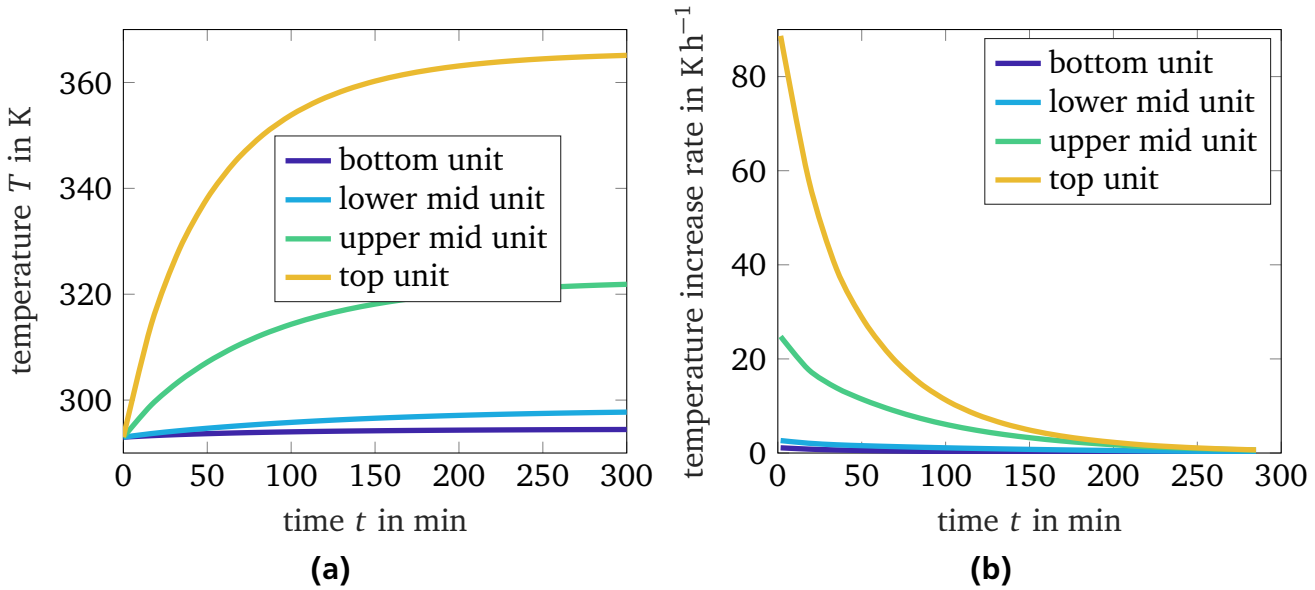

Figure 6.3.: (a) Temperature over time and (b) temperature increase rate over time of each arrester unit in continuous operation. The thermal steady state (defined by $\Delta T/\Delta t < 1\,\mathrm{K/h}$) is reached after approx. 260 min (adapted from [Spä+16b]).

temperature distribution. Moreover, the self-grading effect, as discussed in Sec. 5.1.3, clearly helps to balance the electric field stress in the ZnO resistors. This becomes particularly important for grading ring design studies, where a purely electrostatic analysis overestimates the field stress increase in the top unit. Considering the temperature distribution of large station class arresters may, therefore, be much more important than just looking at the electric field stress distribution [Cig13; HGT15].

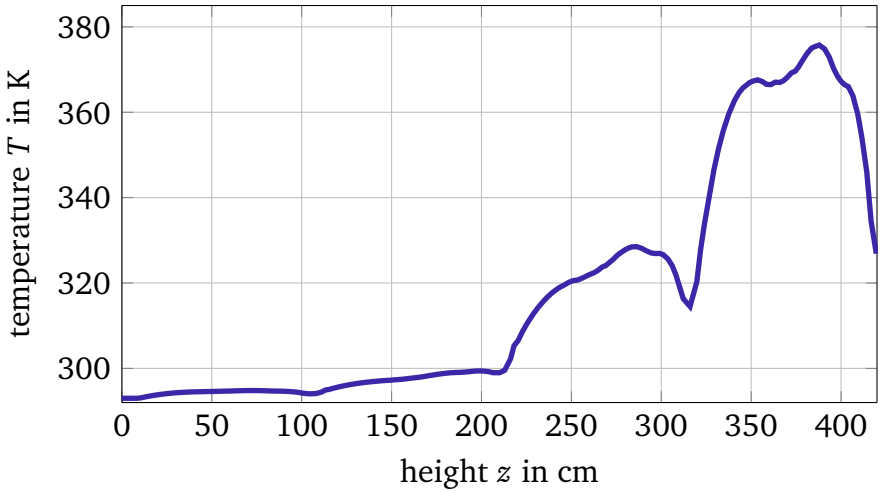

Figure 6.4.: Steady state temperature distribution of the ungraded 550-kV-arrester after 260 min along the center axis of the surge arrester. The mean axial temperature in each unit (from bottom to the top unit) is $(295, 297, 317, 356)$ K. The lower two units do not heat up significantly. The upper two units are exposed to elevated operating temperatures.

6.2 Comparison to Experiments in Continuous Operation

6.2.1 Station Class Surge Arrester Analysis

550-kV-Station Class Arrester

The simulated steady state temperature distribution of the ungraded station class arrester is compared to a measurement conducted at the High Voltage Lab of the Technische Universität Darmstadt (see Fig. 6.5). The measurements were conducted using fiber optic temperature sensors inserted into aluminum spacing elements between the ZnO resistors. The spacers are $3-5$ mm high. Steady state is defined by a temperature increase of no more than 1 K per hour, as this is the resolution of the optical temperature measurement sensors (see [Gie18]). Two cases are simulated. First, a constant relative permittivity of $\varepsilon_\mathrm{r} = 700$ is considered. Second, a nonlinear field- and temperature-dependent relative permittivity, $\varepsilon_\mathrm{r} = f(|\vec{E}|, T)$, is assumed,

based on [Den14]. Overall, both curves show a good agreement between the simulated and measured temperature profile. The relative error shown in Fig. 6.5(b) is obtained by,

$$\epsilon = \frac{|T_{\mathrm{sim,i}} - T_{\mathrm{meas,i}}|}{T_{\mathrm{meas,i}} - 273.15\,\mathrm{K}}, \tag{6.2}$$

where $i \in [1, N]$ is the index of the temperature sensors, N. The nonlinear permittivity model shows a slightly better agreement to the measurement, especially in the top unit, compared to the constant-permittivity model (see Fig. 6.5(b)). The mean error is reduced from 11% to 9.8%. The maximum error of the nonlinear permittivity model is 22%. The deviation of measurement and simulation is attributed to the following aspects[1]:

- A generic material characteristic, obtained from [Den14], was used. These characteristics do not necessarily correspond to the ZnO material used in the experiment. In addition, there is a spread of the material characteristics for the individual resistors. This was not taken into account. Moreover, at the time of the measurements obtained in [Den14], the knowledge on measurement requirements was not yet available (see Sec. 5.1.2).
- Little care was given to the laboratory conditions, including:
  - Uncertain air flow conditions in the laboratory, such as forced convective processes like air breezing, influence the cooling of the arrester and are not considered in the simulation.
  - Influence of the stray capacitances of neighboring laboratory equipment, such as the generator, voltage divider, connector and e.g. other specimens is unknown and, thus, not considered.

Reduced-Diameter 550-kV-Station Class Surge Arrester

The second model is the experimental station class surge arrester setup with the reduced-diameter ZnO resistor column considered in [Gie18]. The measurement data are taken from [Gie+16; Gie18]. Two FE models are simulated. First, the model is equipped with distributed heat sink elements, as shown in Fig. 4.4(b) (likewise to the experimental setup of [Gie+16]). In a second model, all heat sink elements are combined and centered in each unit, as shown in Fig. 4.4(c). After approximately six hours, the arrester reaches the steady state in the experiment and the simulation, respectively. The computation time is, again, in the (low) range of hours for a problem size of tens of thousands of FE nodes.

Figure 6.6 shows the comparison of the measured and simulated steady state temperature distribution. An excellent agreement between measurement and simulation with the distributed heat sink model is obtained (mean relative error $\leq 5.8\%$). The deviations are lower compared to the previous model, as special care was given to measure the ZnO material data. The material

[1] This comparison was conducted at the beginning of the dissertation project and uses a measurement obtained in the student project [Dür10].

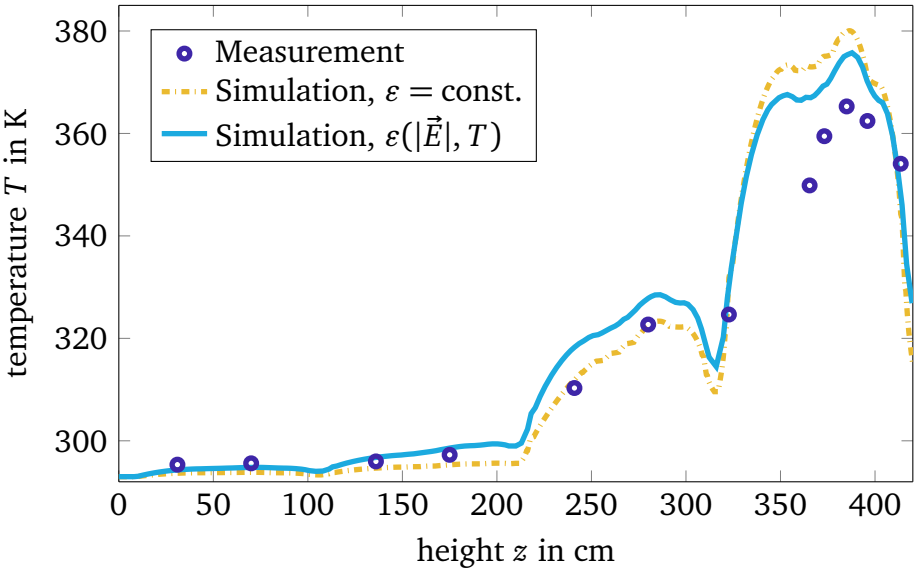

(a)

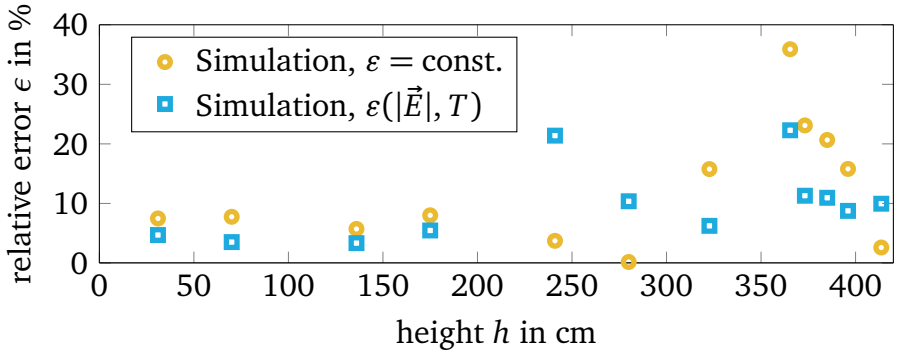

(b)

Figure 6.5.: (a) Simulated and measured steady state temperature distribution along the center axis of the surge arrester. (b) Relative temperature deviation in %. A constant relative permittivity of $\varepsilon_r = 700$ and a nonlinear relative permittivity $\varepsilon_r = f(|\vec{E}|, T)$ is assumed. The generic material characteristics are adopted from [Den14]. The deviation of measurement and simulation can be attributed to the use of generic material characteristics and unknown laboratory conditions.

characteristics were obtained from accurate, high-resolution *U-I-T*-measurements. A nonlinear permittivity, $\varepsilon_r = f(|\vec{E}|, T)$, was extracted from the measurements [All16; Gie18]. The spread of the material characteristics was minimized by selecting ZnO resistors with respect to the residual voltage [Gie18]. Furthermore, special care was given to the laboratory conditions such that they could be reproduced by the simulation. The remaining discrepancies are attributed to the simplified thermal boundary conditions. In addition, material uncertainties in the used ZnO resistors are not taken into account. It is assumed that the statistical spread of the material characteristics stemming from single block measurement data are much larger than the numerical simulation accuracy (see [Gie18; Den14; TH14]).

In Fig. 6.6, the simplified second model with centered heat sinks yields an increased peak temperature, of 419 K. Thus, even for this simplified model, the temperature deviation in the simulation is not larger than 16 K (mean error 10%). The mean temperature of both simulation models is 327 K. In the following, the simplified model with the centered heat sinks is used to study thermal instability as it allows for faster simulations and simpler variation of multiple parameters.

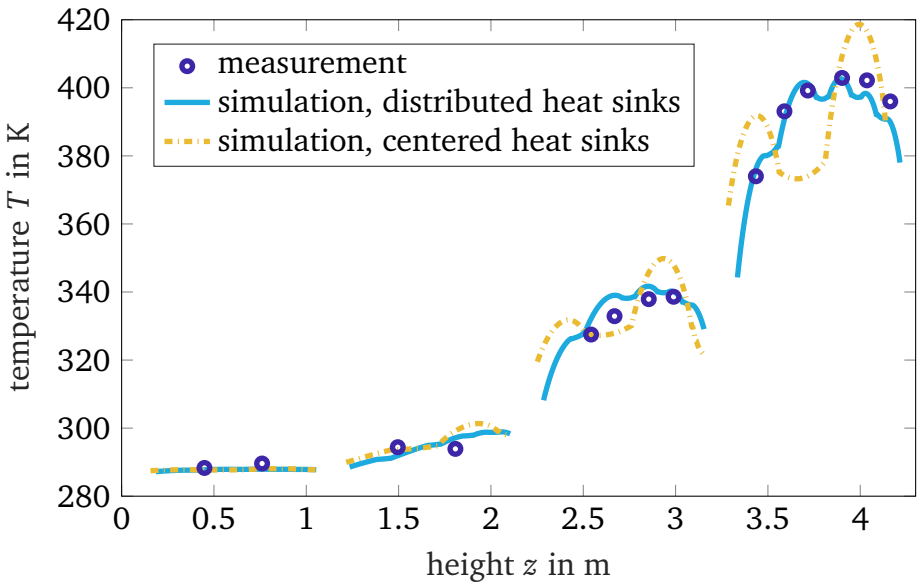

(a)

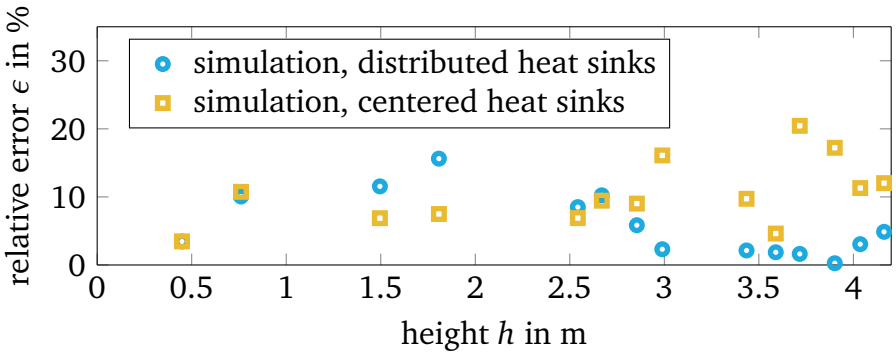

(b)

Figure 6.6.: (a) Simulated and measured steady state temperature distribution along the center axis of the surge arrester (adapted from [Spä+19]). The steady state is reached after ≈ 6 h. (b) Relative temperature deviation in %. A first model is equipped with distributed heat sink elements likewise to the experimental setup of [Gie+16]. In a second model, all heat sink elements are combined and centered in each unit. Compared to the initial validation of the 550-kV-station class arrester (cf. Fig. 6.5), special care was given to reduce measurement uncertainties stemming from the material characteristics and the laboratory conditions.

6.2.2 Thermal Equivalent of the 550-kV-Station Class Arrester

The simulated and measured electrothermal behavior of the thermal equivalent for the 550-kV-station class arrester is compared. First, the purely thermal behavior is investigated. Therefore, the ZnO stack is initially preheated to 421 K and 464 K.

Figure 6.7 compares the measured and simulated cooling process of the thermal equivalent. The temperature distribution in the ZnO is nearly uniform, due to the small dimensions of the thermal equivalent ZnO stack. The relative error of measurement and simulation for all time instants is $\leq$ 3.2%. Thus, with the established thermal model (see Sec. 5 and Sec. 4), the transient thermal behavior of the arrester equivalent can be accurately simulated.

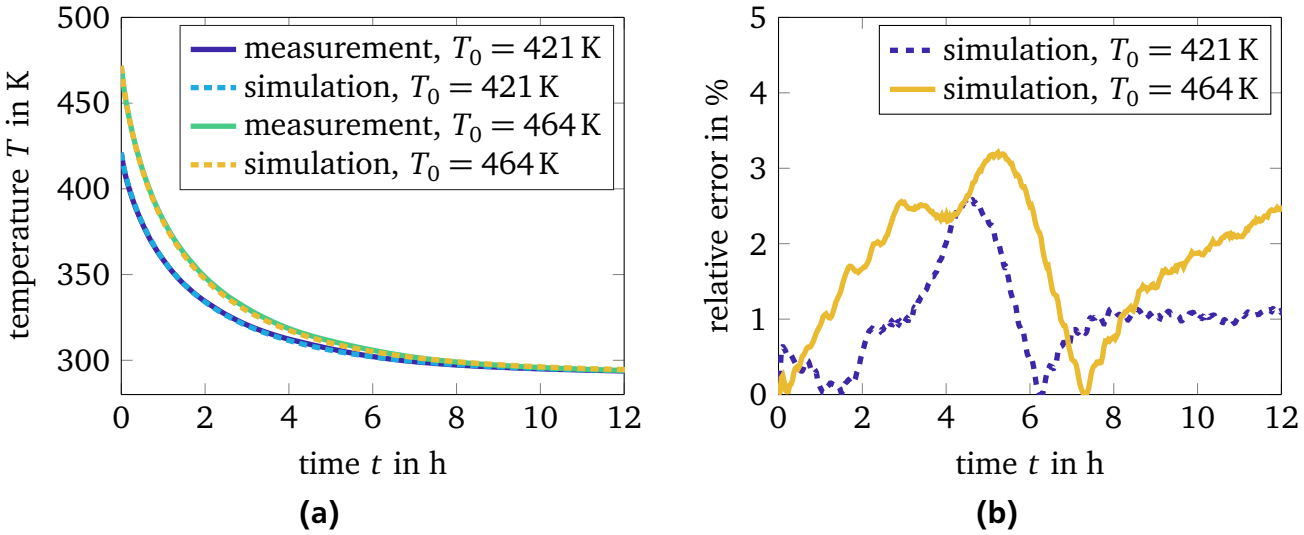

Figure 6.7.: Measured and simulated cooling of the thermal equivalent for an initial ZnO stack temperature of 421 K and 464 K, (a). The relative error of measurement and simulation with respect to time (b).

Subsequently, Fig. 6.8 compares the temperature evolution of two electrothermal scenarios. The ac rms voltage $U_1 = 9.2\,\mathrm{kV}$, Fig. 6.8(a), and $U_2 = 11.074\,\mathrm{kV}$, Fig. 6.8(b), is applied until an operation close to the electrothermal steady state is reached after 7 h. Subsequently, the voltage is switched off and the specimen cools down to the ambient temperature. Figure 6.8 shows a very good accordance of the measured and simulated scenarios (discrepancy $\leq$1 K). Slightly different steady state temperatures of measurement and simulation are obtained, and the simulated temperature decreases faster compared to the measurement. This is attributed to the convection assumed in the models. In this temperature range, which is close to the ambient temperature, radiative heat dissipation is small compared to the convective heat transfer contribution. The estimation of the convective heat transfer based on a NUSSELT number, which is kept constant throughout the simulation time, may cause an overestimation of the convective heat transfer. This is confirmed by the fact that a smaller deviation of measurement and simulation is observed at the higher excitation voltage and steady state temperature (see Fig. 6.8(b)).

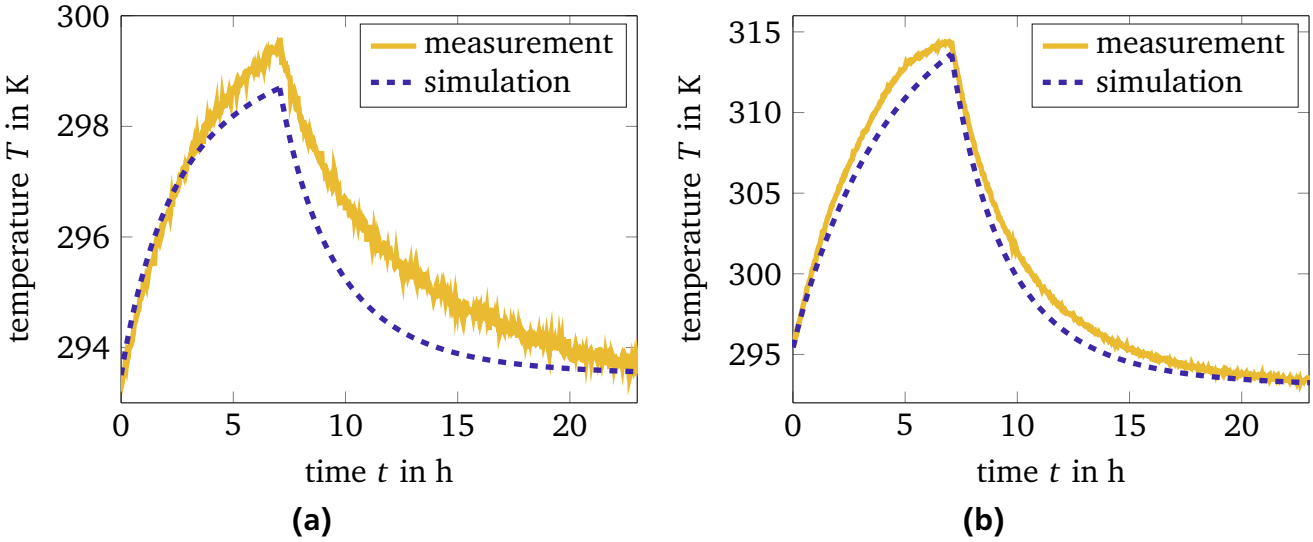

Figure 6.8.: Measured and simulated temperature response of the thermal equivalent with applied ac voltages $U_1 = 9.2\,\mathrm{kV}$, (a), and $U_2 = 11.074\,\mathrm{kV}$, (b) (adapted from [Sch16]). The ac excitation is applied until the electrothermal steady state is reached after $7\,\mathrm{h}$. The voltage is, then, switched off and the purely thermal cooling is computed until the ambient temperature is reached.

7 Optimization of Continuous Operation

7.1 Station Class Surge Arresters with Grading Systems

Station class arresters are typically several meters high. Thus, their performance is affected by stray capacitances to earth causing a nonuniform electric field stress, power loss and temperature distribution in the resistor column. In order to compensate for this effect, one or more field grading rings are often used [Cig13; HGT15; He+09]. The field grading system is carefully designed such that the electrothermal stresses are as much as possible evenly distributed among the ZnO resistors in the column [Göh+10; Sjö+10] (see Sec. 2.1).

The ring is attached to the high voltage terminal by several suspensions (see Figure 4.1). The suspension rods cancel the rotational symmetry of the arrester configuration. At first sight, the asymmetry requires 3D simulations which are computationally expensive. Different numerical approaches have been discussed to reduce the high computational complexity of a full 3D EQS simulation, cf. [Ste+08; Han+05], and to study new designs of graded arresters [Sjö+10], respectively. The main challenge of 3D arrester simulation is posed by the high number of DoFs compared to 2D-axisymmetric arrester simulation. This is, furthermore, severed due to the strongly nonlinear ZnO material characteristic that requires a very fine spatial resolution within the arrester. In particular, the 3D approach is totally unrealistic for the purpose of optimizing the field grading system, as this task would involve several hundreds of transient simulations for different arrester geometries.

One way to overcome this problem is the derivation of suitable equivalent models, as, in principle, suggested in the arrester standard [IEC14]. In this model, the suspension rods are replaced by a virtual ring electrode such that the electric field of the equivalent model in the resistor column coincides with that of the original 3D arrester geometry. This model, however, is tailor–suited to the IEC standard arrester. It will, generally, not work for other arrester and field grading configurations. Moreover, it is not guaranteed that this model reproduces the correct field stresses for operating conditions other than the ones described in the arrester standard [IEC14]. In [Gie18] the method of the standard was adopted, and a scheme to manually improve the reconstruction based on parameter studies was presented. This dissertation introduces a systematic procedure to automatically construct an axisymmetric arrester equivalent. The shape and position of a virtual electrode are obtained by numerical optimization for an arbitrary surge arrester configuration. The approach employs a single solution of a capacitive 3D problem that is numerically easy to obtain. Subsequently, the field grading system of a station class arrester can be optimized based on the equivalent arrester model.

Another way to circumvent 3D simulations is the reduction of the 3D problem to a quasi-3D problem [DSD19]. This method exploits the partial symmetry of the arrester grading ring in the azimuthal direction. The quasi-3D field simulation approach reduces the number of required DoFs compared to a conventional 3D simulation. The main idea of the technique is to extend the standard axisymmetric 2D FE formulation with trigonometric functions along the azimuthal coordinate while preserving the possibility to carry out all calculations on the 2D computational mesh. The suspensions are included in the quasi-3D model by asymmetric Dirichlet boundary conditions, which are incorporated into the computation by a collocation approach. Thus, the asymmetries arising from the support rods in the model are taken into account and, therefore, allow to reproduce the true 3D field distribution. However, the idea was until now only presented for a model with linear and temperature independent material characteristics, allowing for an EQS formulation in frequency domain. The approach has not yet been successfully extended to the nonlinear time-domain problem and is, therefore, not adopted in this work.

7.2 Equivalent Model for Surge Arresters with Grading Systems

7.2.1 Virtual Electrode Configurations

The basic idea of the equivalent arrester model consists in replacing the suspension rods with an axisymmetric virtual electrode that produces essentially the same electric field stress on the arrester axis as in the original problem. The equivalent arrester model is axisymmetric and can be easily handled in numerical simulations. The electric field of the equivalent model far from the arrester axis will generally be different from that of the original arrester. The electrothermal response of the system, however, is determined by the electric field and temperature in the resistor column only. Due to the small radius of the column, the azimuthal field variation in the ZnO resistors can be neglected. Thus, matching the electric field of the equivalent model with that of the true arrester on its axis is fully sufficient for the analysis.

In order to determine the shape and position of a virtual electrode, a reference solution for the electric field of the full arrester geometry including its suspension rods is needed. The 3D reference solutions can be easily obtained by purely electrostatic field simulations. This is due to the fact that a field grading electrode does not carry resistive currents and that it only modifies the stray capacitances of the arrester. Thus, in order to determine an equivalent arrester model, it is sufficient to consider the capacitive field problem only.

With this observation, an equivalent model can be derived by solving the optimization problem,

$$\min_{X \in \mathbb{R}^N} \|\boldsymbol{E}_{2\mathrm{D}}(X) - \boldsymbol{E}_{3\mathrm{D}}(X)\|_2, \tag{7.1}$$

where, $\boldsymbol{E}_{3\mathrm{D}}$ and $\boldsymbol{E}_{2\mathrm{D}}$ denote the 3D electrostatic field along the axis of the arrester and its 2D equivalent, respectively. Furthermore, X denotes N unknown parameters characterizing the

shape and position of the virtual electrode. The solution of this problem yields an optimal axisymmetric equivalent model for any given surge arrester geometry.

Three different configurations for the arrester equivalents are considered (cf. Fig. 7.1). In equivalent model (A), the virtual electrode is a conical screen that is kept at the same potential as the high voltage electrode. The model parameters to be optimized are the distance of the electrode midpoint from the top electrode and the screen length, $X = (\mathrm{d}m, l)$, as shown in Fig. 7.1 (middle). Herein, the electrode midpoint is constrained to be along the shortest path connecting the high voltage electrode to the grading ring indicated as a blue line in Fig. 7.1 (middle). Equivalent model (B) uses a virtual ring electrode that is characterized by its radius and height, $X = (\varrho_\mathrm{v}, h_\mathrm{v})$, as depicted in Fig. 7.1. The thickness of the virtual ring is fixed and is the same as that of the main grading ring. Finally, an equivalent model (C) is considered consisting of a virtual ring placed at half-way along the line connecting the grading ring to the high voltage electrode. This model uses a fixed ring radius and position. Thus, a solution of the optimization problem is not required. Model (C) is considered for comparison purposes only. This model is suggested in the arrester standard [IEC14] and is commonly applied in surge arrester simulations [Hin+08; Gie+17a; Ste+06].

Each of the two equivalent models, (A) and (B), represent a two-parameter optimization problem. Such problems can be solved with standard gradient-free algorithms such as the pattern search or simplex method [Tor97; Lag+98]. The solution procedure is depicted in Fig. 7.2. In each optimization step, the geometry of the virtual electrode is modified, a new FE mesh is generated and the electric field distribution of the 2D model is computed. The result is compared with the 3D reference solution. Then, a set of parameters for the new geometry of the virtual electrode that minimize the goal function (7.1) is generated. This procedure is repeated until the minimum in (7.1) is found.

7.2.2 Equivalent Model for the IEC Arrester

The above approach is applied to the IEC standard arrester equipped with a single field grading ring. The field grading ring is attached to the high voltage electrode by means of four suspension rods. In order to demonstrate the effect of these suspension rods on the field distribution, Fig. 7.3 shows the electrostatic potential of the arrester when a dc voltage of 333 kV is applied at the high voltage electrode. The potential distribution is clearly not axisymmetric.

The electrostatic 3D field distribution for the full arrester geometry, including the four suspension rods, is simulated with CST EM STUDIO® to obtain the reference solution $\boldsymbol{E}_{3\mathrm{D}}$ for different positions of the grading ring. For the calculation of the electric field of the 2D equivalent, $\boldsymbol{E}_{2\mathrm{D}}$, the simulation tool described in Sec. 5.4.2 is used.

Figure 7.4 shows the resulting optimal parameters for the equivalent model (A). The bounds for the optimization are defined by the suspension geometry. Hence, the midpoint distance $\mathrm{d}m$ is constrained (along the suspensions, see the blue line in Fig. 7.1 (middle)) s.t. $\mathrm{d}m \in \{0, l_\mathrm{s}(\varrho, h)\}$. Herein, $l_\mathrm{s}(\varrho, h)$ is the length of the suspension for the current grading ring radius and height

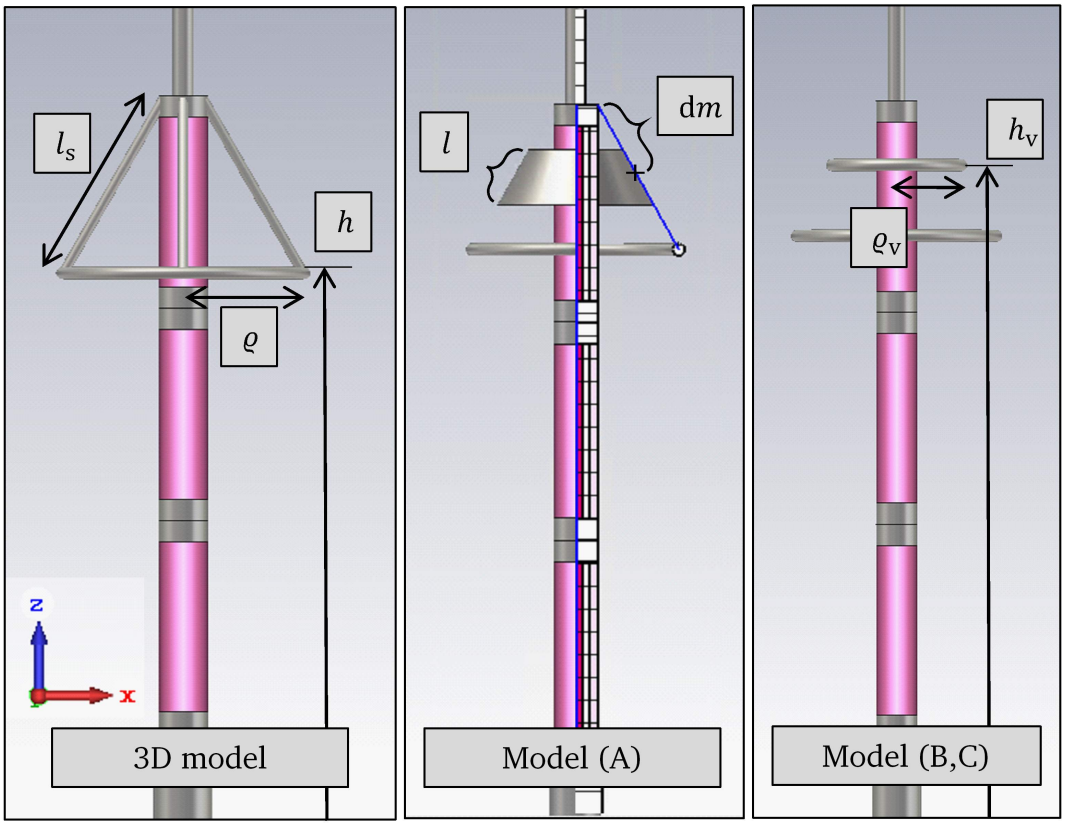

Figure 7.1.: Left: original 3D surge arrester with grading ring and suspensions. Middle: equivalent model (A) using a virtual conical screen. Right: equivalent models (B) and (C) using a virtual ring electrode [SGD19].

(ϱ, h). The length l of the screen is constrained s.t. $l \in \{0, 0.5 l_s(\varrho, h)\}$. The optimal midpoint distance and the screen length are shown for different radii and heights of the grading ring, respectively. The position of the virtual screen depends nearly linearly on the grading ring height and radius. The length of the virtual screen, however, appears to be more sensitive to the variation of the grading ring radius.

For all investigated cases, the global field error,

$$\epsilon(X) = \frac{\sqrt{N^{-1}\Sigma_{i=1}^{N}\left(E_{i,2\mathrm{D}}(X) - E_{i,3\mathrm{D}}(X)\right)^2}}{N^{-1}\Sigma_{i=1}^{N} E_{i,3\mathrm{D}}(X)}, \tag{7.2}$$

of the optimal 2D equivalent model (A) is below 3.8% (cf. Fig. 7.5). However, the parameter region of largest error (yellow/red areas in Fig. 7.5) is not of interest in practice, as it corresponds to cases where the grading ring is positioned too close to the upper mid flange. Such configurations could lead to an electrical flash over. For all realistic grading ring parameters, the global field error of the equivalent model is less than 2%.

In order to compare the accuracy of the three proposed equivalent models (A)-(C), a fixed grading ring configuration with $(\varrho, h) = (0.6\,\mathrm{m}, 4.3\,\mathrm{m})$ is considered. This choice corresponds to a grading ring with long suspensions that is mounted comparably closely to the stack. In Fig. 7.6,

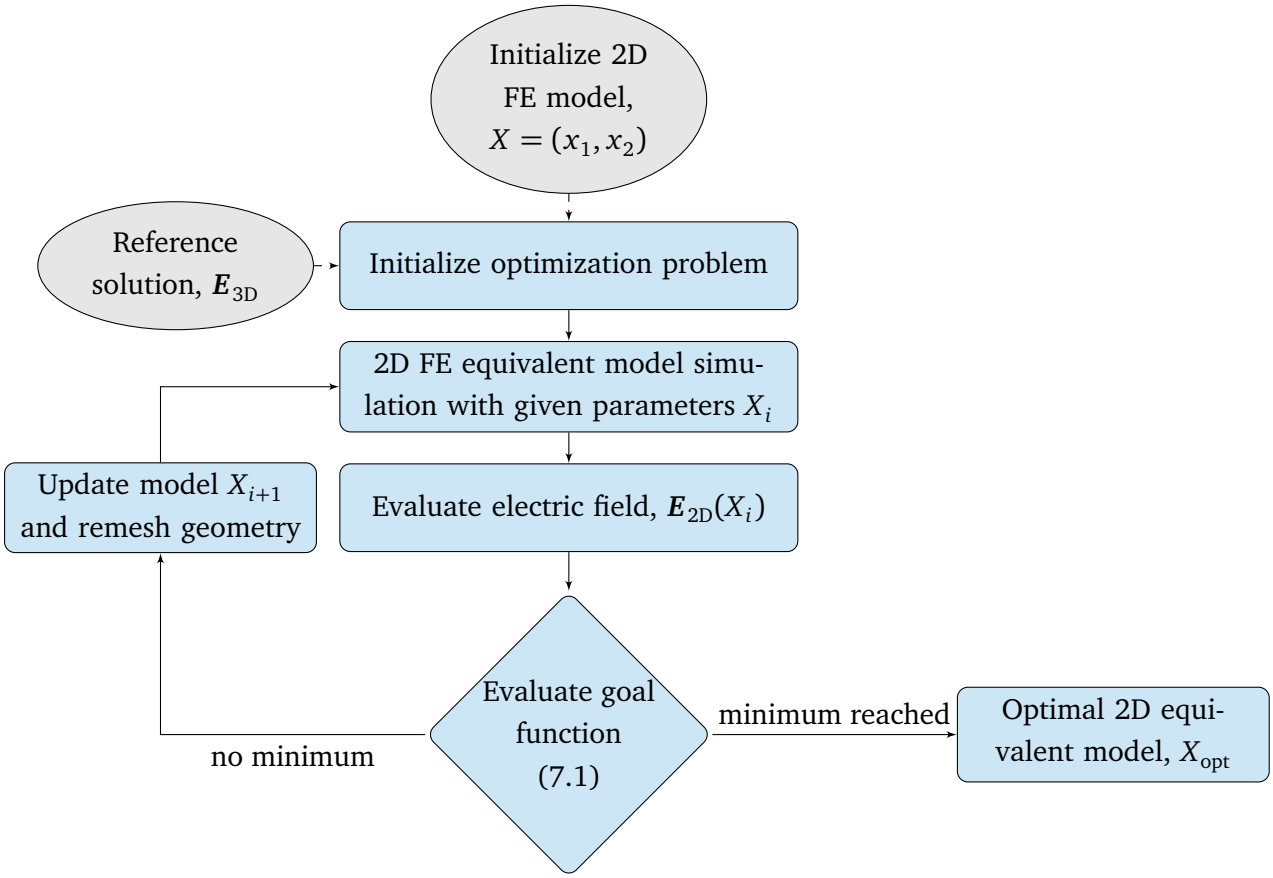

Figure 7.2.: Flow chart of the optimization procedure for the axisymmetric equivalent arrester model (adapted from [SGD19]). After initializing and simulating the 2D FE model with the current virtual electrode parameters X_i, the axial electric field is evaluated. The goal function did not reach a minimum, until the difference of the electric field stresses of the 3D reference and current 2D solution are minimal. The equivalent model is updated by adopting new virtual electrode parameters X_{i+1} and the simulation and evaluation is repeated until the optimal virtual electrode parameters X_{opt} are found (adapted from [SGD19]).

the electrostatic field distribution of the original 3D arrester and those of the corresponding, optimal equivalents are plotted along the arrester axis. Obviously, equivalent model type (A) yields by far the best results. As expected, the largest field errors occur in the top units where the influence of the suspension rods on the field distribution is stronger.

Figure 7.7 shows the global field errors of the three models for various grading ring radii and heights. Again, model (A) yields the best approximation compared to the other two models. For large and low-sitting grading rings, models (B,C) are generally not applicable since they produce large errors of more than 15%. Only for large and highly mounted grading rings, (A) and (B) are equivalent in terms of the resulting error. In all cases, the standard approach used in model (C) fails to reproduce the arrester field with sufficient accuracy. This model yields substantially high errors and is, therefore, not recommended. It works well only for a very limited range of

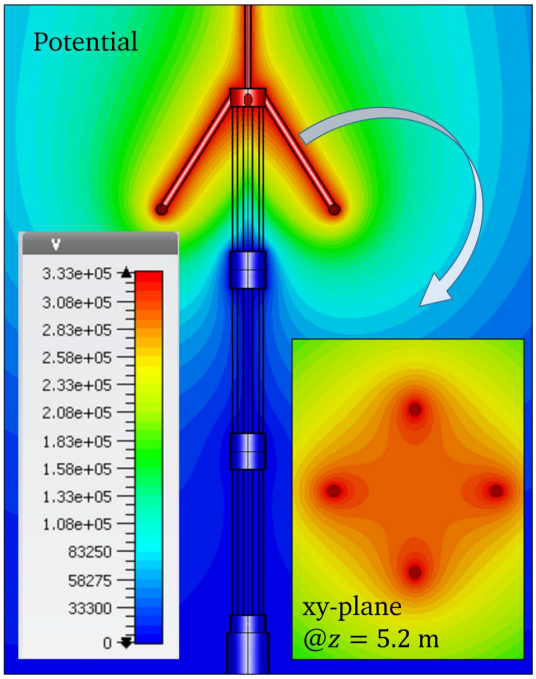

Figure 7.3.: Electrostatic potential distribution in the xz-plane and the xy-plane when a dc voltage of 333 kV is applied to the high voltage electrode [SGD19]. Within the ZnO resistors, no azimuthal variation of the electric field strength is observed. Thus, an equivalent 2D-axisymmetric approach can be introduced.

parameters, such as, e.g. for the particular grading ring configuration used in the IEC standard with $(\varrho, h) = (0.6\,\mathrm{m}, 4.8\,\mathrm{m})$.

The equivalent model is validated for the EQS problem. Therefore, Figure 7.8(a) compares the electrostatic and EQS (rms) 3D field distribution along the arrester axis. The self-grading effect due to the nonlinear conductivity of the ZnO resistors equalizes the field stress in all three units. Figure 7.8(b) shows that the EQS field distribution of the 3D and the equivalent model (A) agree very well (mean relative error $< 1.6\%$). Again, the maximal deviation ($< 6\%$) occurs in the top unit, as shown in Fig. 7.8(c). Thus, the 2D equivalent model is suitable to compute the EQS solution of a 3D surge arrester configuration.

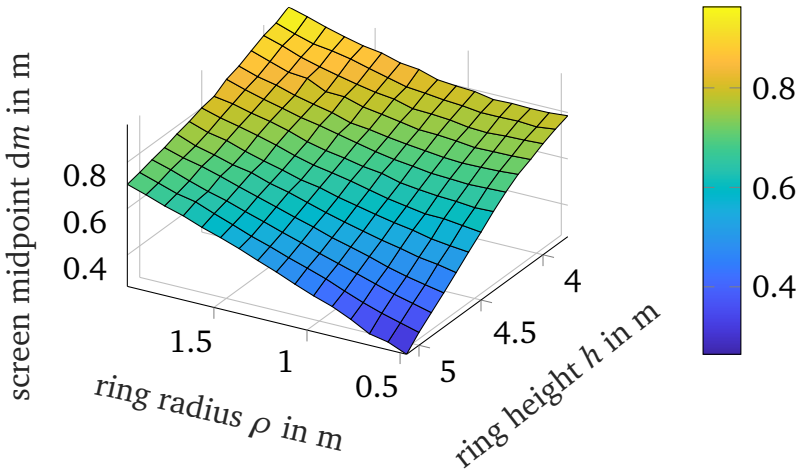

(a)

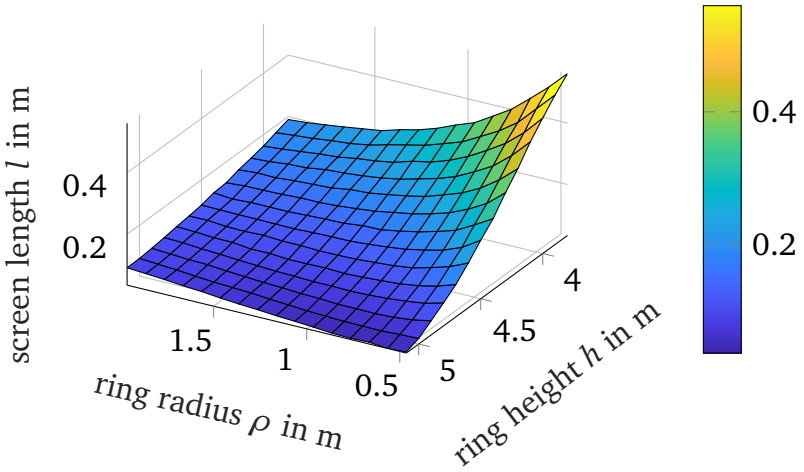

(b)

Figure 7.4.: Optimal parameters for the equivalent model with a virtual conical screen. (a), midpoint, $\mathrm{d}m(\varrho,h)$, and (b), screen length, $l(\varrho,h)$, for various grading ring configurations ϱ,h, respectively (adapted from [SGD19]).

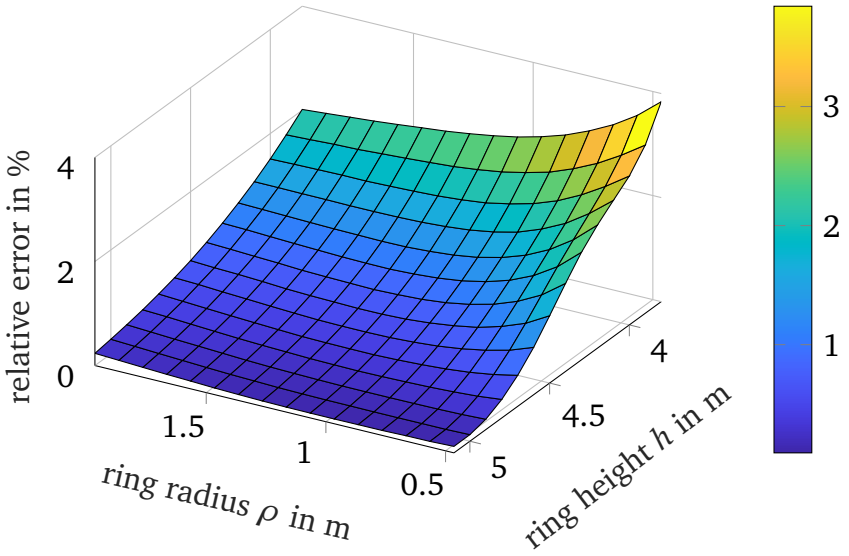

Figure 7.5.: Relative electric field strength error based on (7.2) of the conical screen model in % for various grading ring configurations (ϱ, h) (adapted from [SGD19])). The error for technically relevant configurations is below 3.8%.

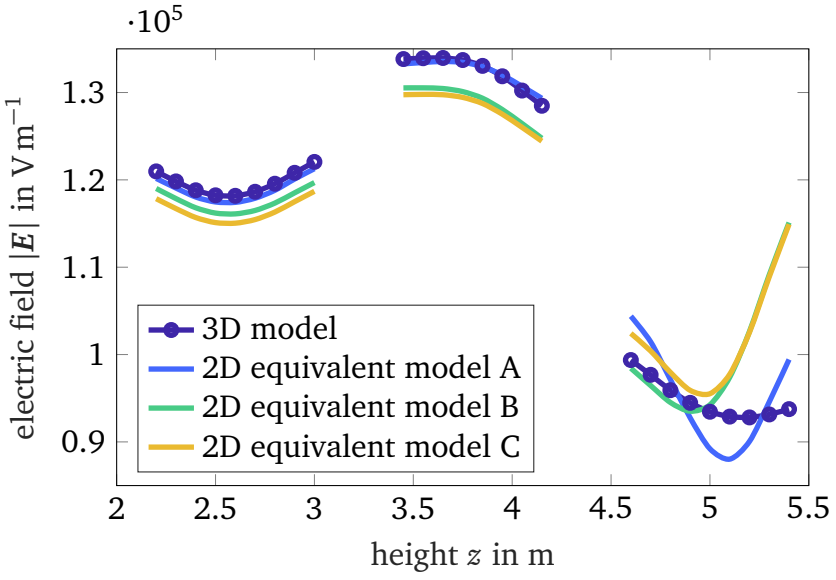

Figure 7.6.: Comparison of the 3D electric field distribution along the arrester axis to the equivalent models (A), (B) and (C), respectively. The grading ring sits at $(\varrho, h) = (0.6\,\text{m}, 4.2\,\text{m})$. Of all three models, model (A) reproduces the 3D field stress best, the mean relative error is smaller than 1.6% (adapted from [SGD19]).

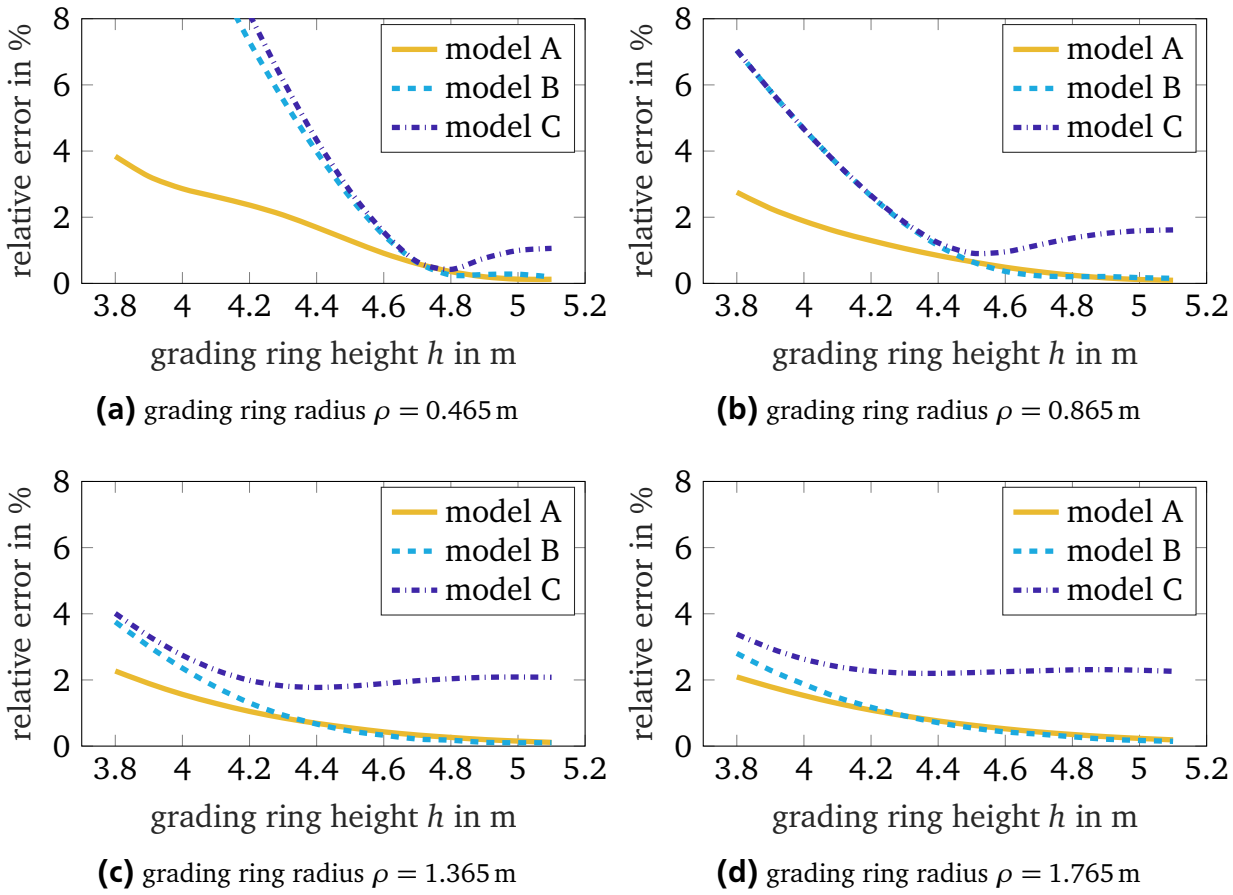

(a) grading ring radius $\rho = 0.465\,\mathrm{m}$

(b) grading ring radius $\rho = 0.865\,\mathrm{m}$

(c) grading ring radius $\rho = 1.365\,\mathrm{m}$

(d) grading ring radius $\rho = 1.765\,\mathrm{m}$

Figure 7.7.: Comparison of the relative errors (referred to the 3D case) for the equivalent (A), (B) and (C), respectively, for different grading ring configurations, (ϱ, h). With model (A), the best reproduction of the 3D field strength along the axis is obtained. If the ring is large and has a low axial position, the deviation of models (B,C) and the 3D field is large (adapted from [SGD19]).

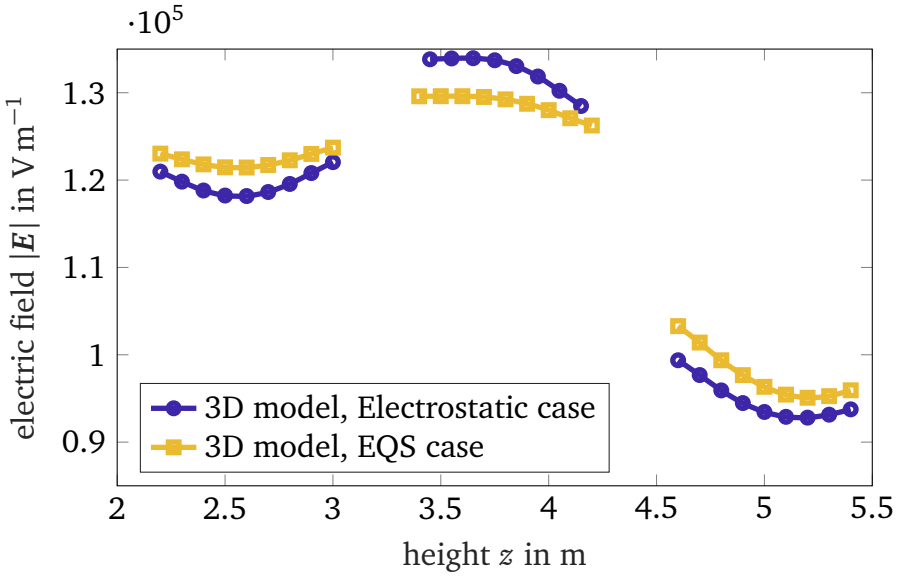

(a)

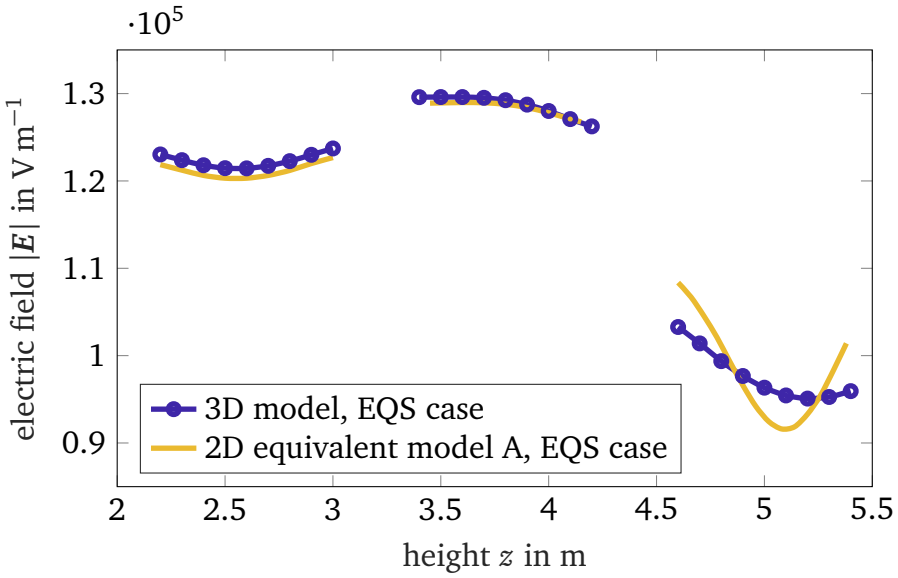

(b)

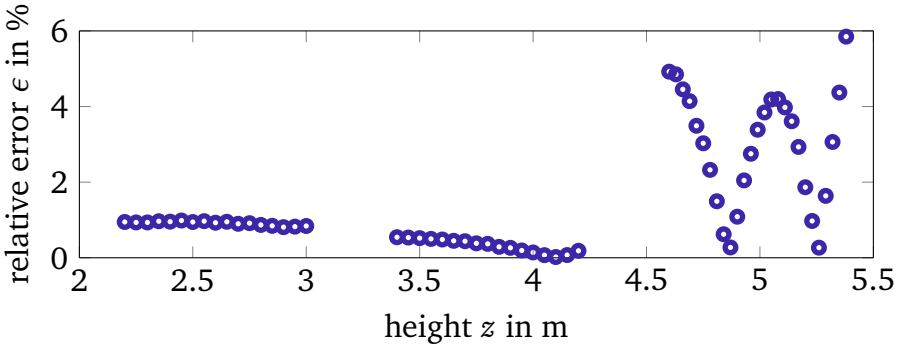

(c)

Figure 7.8.: (a) Comparison of the electrostatic and EQS (rms) 3D field strength distribution along the arrester axis. (b) Comparison of the EQS field distribution of the 3D and the equivalent model (A) respectively. (c) Relative field error in %.

7.3 Electrothermal Steady State Optimization of a Graded Surge Arrester

In a next step, the field grading system of the IEC standard arrester [IEC14] is optimized with respect to the field stress distribution in the resistor column using the previously established equivalent arrester model. It is shown that for the optimized arrester design, the electric field stress and, respectively, the power loss is nearly uniformly distributed across the ZnO resistors. Finally, using coupled EQST simulations, it is shown that the steady state thermal condition of the arrester can be greatly improved.

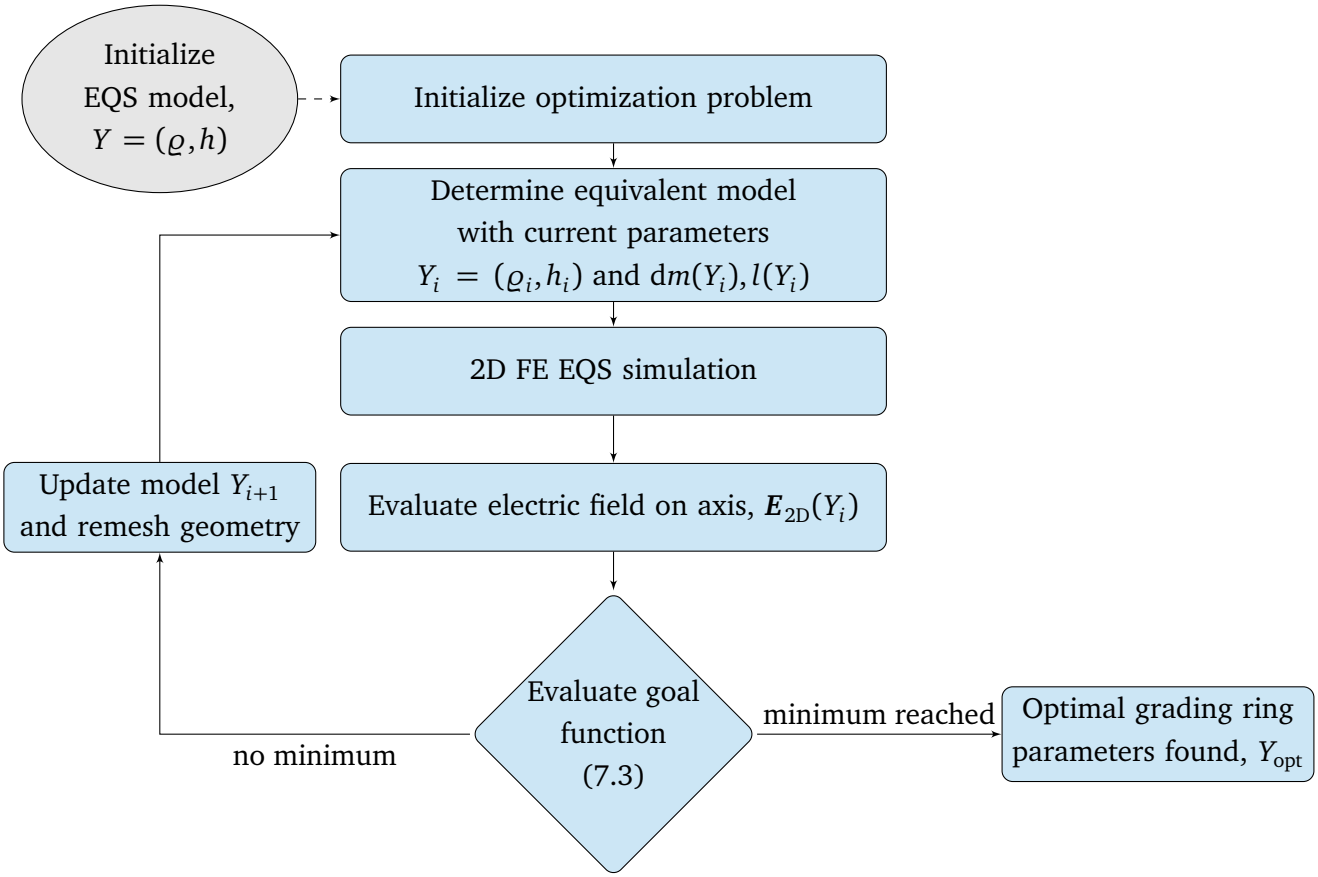

Figure 7.9.: Arrester grading system optimization for ac steady state operation. After the initialization with arbitrary grading ring radius and height, $Y = (\varrho, h)$, the virtual screen parameters $\mathrm{d}m(Y), l(Y)$ are determined. For a large set of grading ring position $Y = (\varrho, h)$, the respective equivalent model was computed a priori and stored in an equivalent model map. The 2D EQS simulation is performed and the axial field stress is computed. The grading ring parameters are updated and the procedure is repeated, until a minimum is obtained, i.e. the optimal grading ring position, Y_{opt} is found. (adapted from [SGD19]).

The aim of this optimization is to ensure a balanced distribution of the electric field stress over all ZnO resistors by choosing a proper design for the field grading system. Denoting the

optimization parameters by $Y = (\varrho, h)$ corresponding to the grading ring radius and height, respectively, the constrained optimization problems is written as

$$\min_{Y \in \mathbb{R}^2} \| \boldsymbol{E}_{\mathrm{rms}}(Y) - \bar{\boldsymbol{E}}_{\mathrm{rms}}(Y) \|_2, \tag{7.3}$$

s.t. $Y \in [\varrho_{\min}, \varrho_{\max}] \times [h_{\min}, h_{\max}]$. Herein, $\bar{\boldsymbol{E}}_{\mathrm{rms}}$ is the spatially averaged rms electric field along the arrester axis. Hence, goal of the optimization is to minimize the spatial variation of the electric field stress in the ZnO resistor column.

A flow chart of the optimization scheme is depicted in Fig. 7.9. In each optimization step, the procedure requires the steady state field distribution of the arrester under ac operating conditions to evaluate the goal function (7.1). If this distribution was obtained from a 3D FE model, each solution of the transient 3D EQS problem would take several tens of hours. This approach is not feasible. The key idea of the proposed method is that any given 3D arrester geometry can be replaced with a corresponding axisymmetric equivalent. The FE solution of such a 2D EQS problem can be efficiently computed (in the range of seconds to minutes) even for large surge arresters. Thus, instead of solving the 3D solution of the current grading ring configuration, $Y_i = (\varrho_i, h_i)$, two steps are carried out. First, the respective equivalent model of type (A) with the virtual electrode parameters, $\mathrm{d}m(Y_i), l(Y_i)$, are determined. This can, in principle, be done by performing the electrostatic equivalent model optimization, as described in Sec. 7.2, on-the-fly. Another, more efficient way that is adopted in this thesis, is to compute the equivalent model for any possible grading ring configuration in the given range of parameters Y a priori. The equivalent models are, then, assembled in a discrete map of data points $\mathrm{d}m(Y), l(Y)$. Any arbitrary equivalent model in terms of $\mathrm{d}m(Y_i), l(Y_i)$ can be obtained by interpolation on the discrete map based on the current grading ring parameters Y_i. Thus, the optimization procedure implicitly takes the 3D effect of suspension rods into account.

In the following, the standard IEC arrester with an applied continuous operating voltage of $U = 333\,\mathrm{kV}$ (rms) is considered as it represents a general arrester setup including a standard grading ring configuration. Fig. 7.10 shows the resulting goal function (7.3) for different grading ring configurations. In this work, the parameter domain is scanned initially (see Fig. 7.10) and provides the bounds for the optimization, $\varrho \in [0.5, 2]\,\mathrm{m}$ and $h \in [3.7, 5.1]\,\mathrm{m}$. In general, there is, of course, no detailed evaluation of the goal function available. However, the high voltage engineering community provides initial parameters based on experimental research and practical experiences, see e.g. [Hin11; Cig13; IEC14] which can be used as (initial) bounds for the optimization. The optimization applies standard gradient-free optimization methods, such as the pattern search or simplex algorithm [Tor97; Lag+98].

Obviously, there exists a unique optimum for the field grading problem that is represented by the global minimum at $(\varrho, h) = (1.29\,\mathrm{m}, 4.41\,\mathrm{m})$. As seen in Fig. 7.10, this optimum appears to be quite sensitive to the ring's height. Contrary, the radius of the ring seems to be less important for the field grading purpose, since the slope of the goal function with respect to radius is rather small.

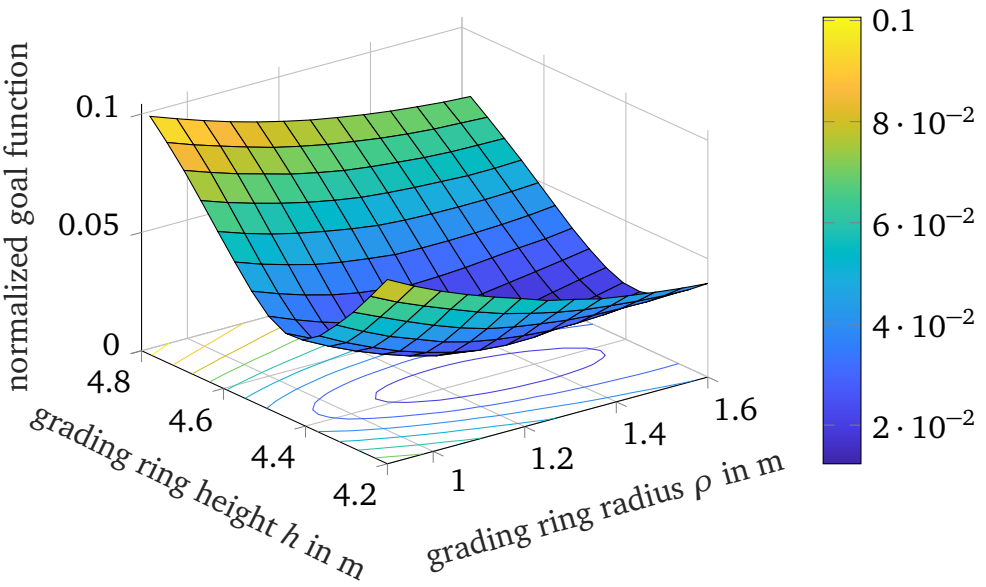

Figure 7.10.: Optimization goal function based on(7.3) for various ring configurations featuring a global minimum at $(\varrho, h) = (1.29, 4.41)$ m. This means that the field is optimally balanced over all ZnO resistors along the axis (adapted from [SGD19]).

The resulting optimal 3D arrester design and its corresponding 2D equivalent are depicted in Fig. 7.11. The grading ring in the optimized configuration is mounted considerably lower than in the IEC standard arrester. Furthermore, the resulting electric field stress on the arrester axis in the optimized case is nearly uniform. The peak field strength is reduced by approximately 10% compared to the standard IEC arrester, and the field flatness is improved from 30% to less than 0.5% in the optimized arrester configuration (see Fig. 7.12).

In order to validate the optimization procedure, the optimized arrester configuration is simulated in 3D using the transient EQS solver of the simulation software CST EM STUDIO®. Fig. 7.13 shows a comparison between these 3D simulations and 2D simulations of the corresponding equivalent for two different voltage levels. The excellent agreement of the field stresses on the arrester axis indicates that the optimization procedure based on axisymmetric equivalent arrester models is reliable.

The effect of grading system optimization on the power loss distribution in the ZnO resistors is depicted in Fig. 7.12. The peak power loss density in the optimized configuration is up to three times lower than in the standard design. Thus, much lower thermal stress in the optimized case is expected.

The comparison between the optimized and standard arrester temperature distributions at the EQST steady state is depicted in Fig. 7.14. A significant reduction of the overall temperature in the optimized case is obtained (see Fig. 7.15). The peak temperature of the optimized arrester is by more than 30 degrees lower than that of the standard arrester. Furthermore, the temperature distribution between the units is uniformly distributed compared to the standard case, where a much larger thermal stress in the top arrester units is observed. These results are supported by

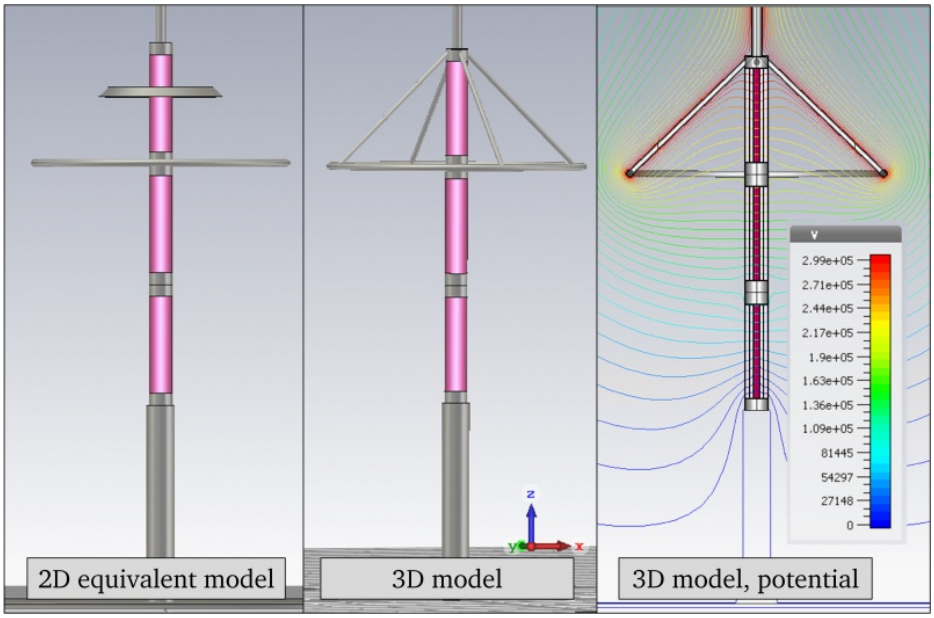

Figure 7.11.: Optimized arrester design. Left: optimal 2D equivalent. Middle: optimized 3D arrester geometry. Right: rms potential distribution at steady state (adapted from [SGD19]).

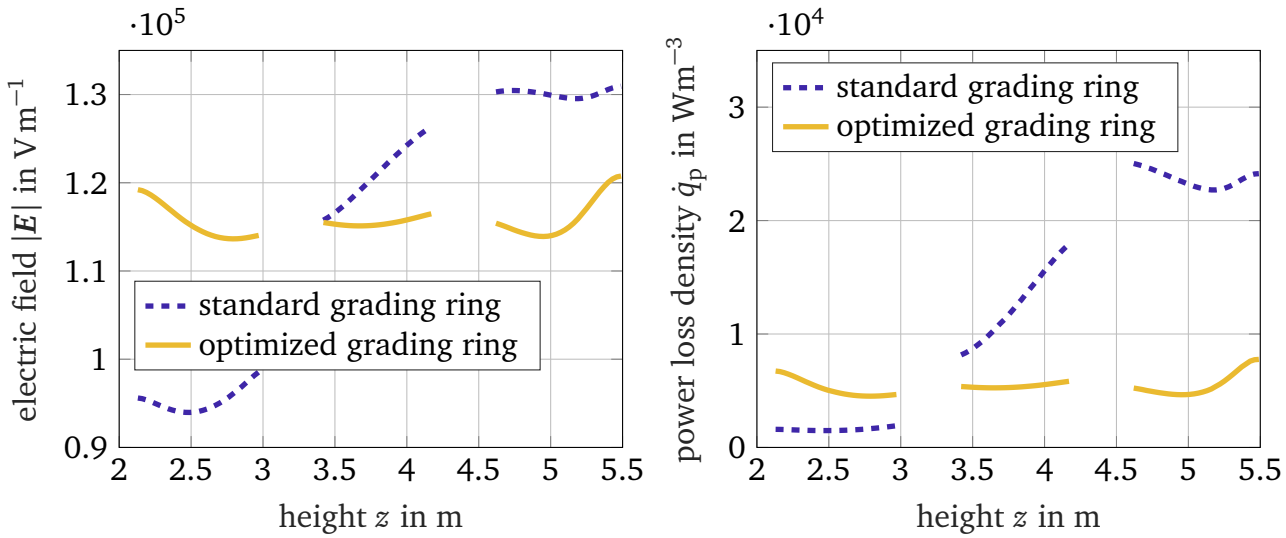

Figure 7.12.: Electric field stress (rms) along the arrester axis (a) for the standard IEC arrester $(\varrho, h) = (0.60\,\text{m}, 4.80\,\text{m})$ and the optimized arrester design $(\varrho, h) = (1.29\,\text{m}, 4.41\,\text{m})$. Average power loss density (b) along the arrester axis for the standard and the optimized grading ring configurations, respectively [SGD19].

laboratory investigations, which reported the beneficial temperature-balancing effect of large grading ring systems [Cig13; HGT15; Gie+16]. It illustrates the importance of grading system optimization, in particular, concerning the issue of degradation of the ZnO resistors due to the thermally induced aging [HGT15].

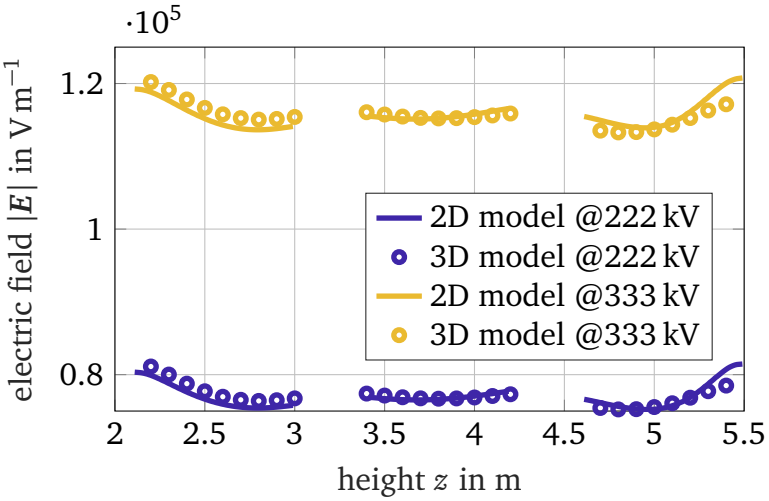

Figure 7.13.: Electric field stress (rms) for the optimized case with excitation voltages (rms), $U = 222\,\text{kV}, U = 333\,\text{kV}$, respectively. The 2D axisymmetric equivalent model is compared with the results of a full 3D transient simulation using CST EM STUDIO®. An very good agreement of the axial field stresses for both excitation voltage levels is observed. (adapted from [SGD19]).

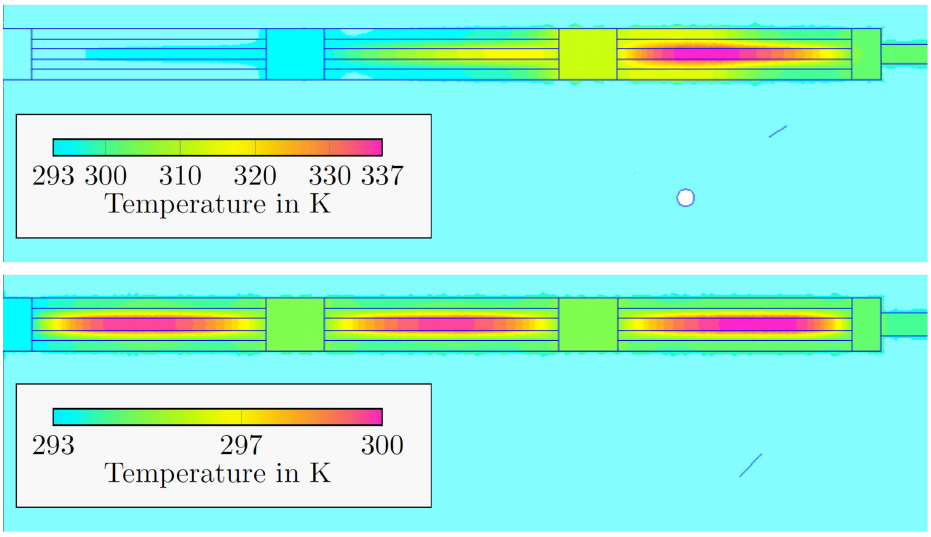

Figure 7.14.: Steady state temperature distribution in the arrester for the standard (top) and optimized (bottom) grading ring configurations, respectively. The overall temperature is significantly reduced with the optimized arrester grading system design [SGD19].

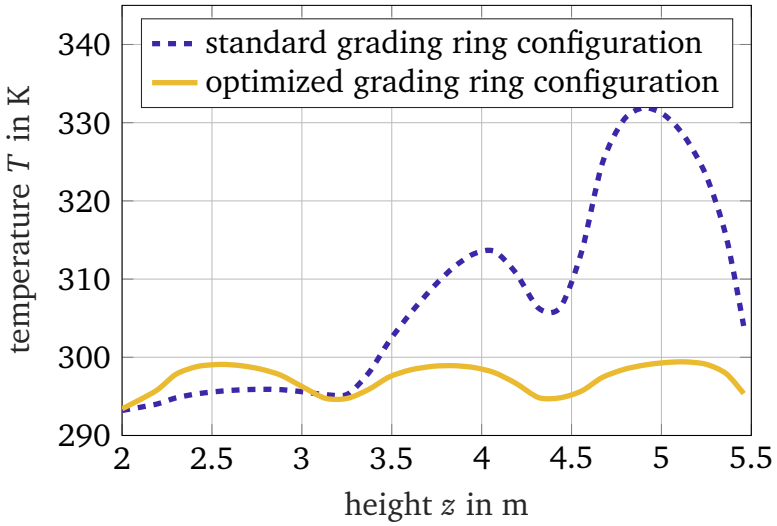

Figure 7.15.: Steady state temperature distribution along the arrester axis in the standard and optimized grading ring configurations. The thermal steady state is reached for the optimized configuration after 7 h and for the standard configuration after 12 h, respectively. For the optimized grading system, the temperature is uniformly distributed compared to the standard design, where large thermal stresses occur in the top arrester unit (adapted from [SGD19]).

8 Thermal Stability Analysis

8.1 Arrester Cooling Rate

Overvoltage events inject energy impulses to station class surge arresters in the power grid. The thermal stability of arresters subjected to energy impulses is studied. Therefore, the arrester cooling rate is defined. As schematically shown in Fig. 2.6, thermal stability involves two competing effects (see Sec. 2.3). The cooling rate summarizes the, in total, three aspects that cause thermal instability: the injected impulse energy, the temperature-dependent power loss and the temperature-dependent heat dissipation.

The injected heat power is dissipated via the air gap and the housing to the ambient air. For a thermally stable case that takes only convective heat dissipation into account, an exponential temperature decay after the impulse injection back to the steady state temperature, T_s, may be expected,

$$T(t) - T_s = \Delta T \exp(-\eta t), \tag{8.1}$$

where the cooling rate, η, is approximately constant.

Another way to express this is by considering that the effective heat flow rate, $\dot{Q}_{\text{eff}}$, is given by the difference between the power loss, $\dot{Q}_p$, and the heat transfer rate to the ambiance, $\dot{Q}$,

$$\dot{Q}_{\text{eff}} = \dot{Q} - \dot{Q}_p \propto -\frac{dT}{dt}. \tag{8.2}$$

The arrester is thermally stable if $\dot{Q}_{\text{eff}}(t, \vec{r}) \geq 0$ in the long term, which means that the cooling process dominates or balances the electric heat generation.

The right hand side of (8.2) becomes zero when the arrester is in steady state. Thus, the effective heat flow rate at longer times can be approximated as,

$$\dot{Q}_{\text{eff}} \propto (T - T_s), \tag{8.3}$$

with the steady state temperature, T_s. By combining (8.2) and (8.3), the cooling rate η, is obtained,

$$\eta = -(T - T_s)^{-1} \frac{dT}{dt}, \tag{8.4}$$

which is equivalent to (8.1). A ZnO element is stable if $\eta(z, t) \geq 0$. If this holds for all ZnO elements for $t \to \infty$, the surge arrester is thermally stable. If the injected energy is above

the arrester's thermal stability limit a thermal runaway occurs, i.e. $T(\varrho, z, t \to \infty) \to \infty$. Otherwise, the arrester cools down to the previous steady state $T(\varrho, z, t \to \infty) \to T_s(\varrho, z, t = 0)$.

Figure 8.1 shows the principle shape of an arrester's cooling rate curve with respect to temperature. The injected impulse energy increases the ZnO temperature instantaneously, based on (2.2). Three regions of the curve can be distinguished. First, the cooling rate rises with increasing temperature. In this regime, the increase of the heat dissipation processes due to temperature-dependence radiative processes is stronger than the increase of the power losses with temperature (cf. Sec. 2.3). This part of the curve is investigated in a first step. For this purpose, energy is injected based on the procedure defined in the IEC operating duty test [IEC14]. The 550-kV-arrester is subjected to double energy injection impulses leading to temperatures far from the thermal stability limit.

In the second part of the curve, the increase of the cooling rate with respect to impulse energy diminishes. The curve reaches a tipping point before it decreases. This is the regime close to the thermal stability limit. It is analyzed by subjecting the arrester thermal equivalent to single energy impulses injected to the ZnO resistors.

The arrester cooling rate becomes negative if the thermal stability limit is exceeded. The investigation of thermally unstable scenarios for the reduced-diameter 550-kV arrester is covered in the last part of this chapter. An efficient detection approach of thermally unstable scenarios is presented. Improvements of the thermal stability limit are achieved. Moreover, a function to predict the thermal stability limit based on few simulations is derived.

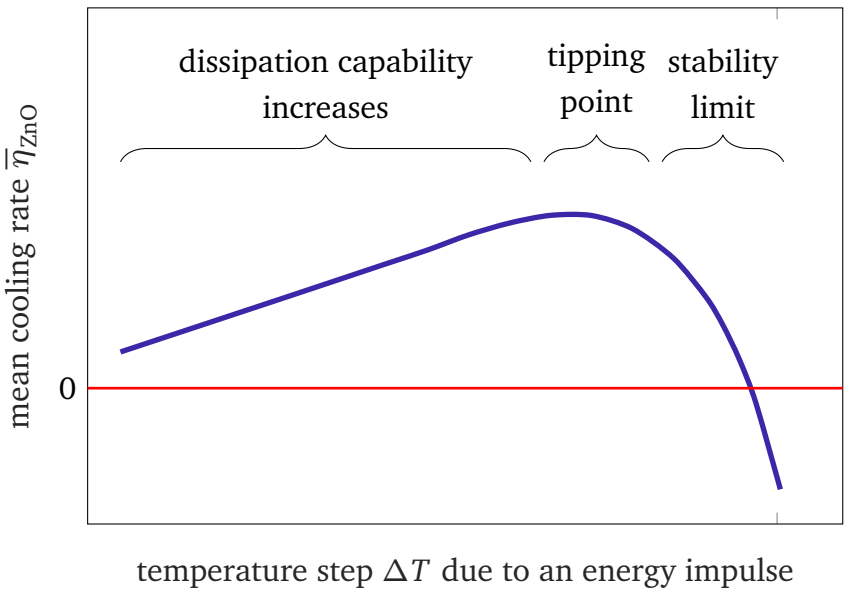

Figure 8.1.: Schematic cooling rate curve of a station class arrester.

8.2 Multiple Impulse Injection Scenarios

In the following, the IEC standard operating duty test is simulated, and the effect of double impulse injections is investigated for the ungraded 550-kV surge arrester. In the IEC standard [IEC14], energy is injected by applying several current impulses to the specimen. Since the impulse duration is much shorter than the thermal time constants involved, the temperature rise, ΔT, in the ZnO resistors is considered to be instantaneous.

The impulse injection procedure of the standard [IEC14] is emulated by applying a two temperature steps separated by a time interval to the ZnO resistors (see Fig. 8.2(a)). The principle temperature profile of the arrester over time is shown schematically in Fig. 8.2(b). Initially, the arrester is in steady state, connected to the grid. The energy impulses cause an instantaneous increase of the ZnO temperature up to $T_{\mathrm{imp},1}$ and $T_{\mathrm{imp},2}$, respectively. The time interval, t_{gap}, between the impulses varies between 0 s and 4 min. Subsequently, the arrester cools down while connected to the rated voltage, U_{r}, for 10 s. Finally, the continuous operating voltage, U_{c}, is applied until the end of the test at $t_{\mathrm{end}} = 60$ min is reached.

The simulations are simplified by the following assumptions. First, the small Positive Temperature Coefficient (PTC) of the ZnO resistance [Fer+03] is neglected. Simple estimations show that for a PTC $< 10^{-3}$, the temperature of all ZnO resistors in the arrester after energy injection is increased by approximately the same amount. For larger PTC values, the nonuniform temperature distribution of the arrester in steady state continuous operation (see Fig. 6.2) would have to be taken into account. Second, the temperature dependence of the ZnO thermal capacitance is not taken into account for the calculation of the temperature impulse (see (2.2)). The error in the temperature distribution due to this assumption after the impulse injection is less than 3% (see [Gie18]). Third, due to the short impulse duration and small power loss in aluminum, the temperature of these parts is assumed to remain unchanged during energy injection [ZB03].

Figure 8.3(a) depicts the spatially averaged temperature of the top unit after pairs of impulses separated by various impulse intervals are applied. The cooling process starts at $t = t_{\mathrm{Uc}} = 0$ s. As all scenarios are thermally stable, the arrester cools down to the initial steady state temperature. Fig. 8.3 (b) shows the temperature a few seconds after impulse injection for $t_{\mathrm{gap}} = 0$ s. Two positions, at the heights $h = 346$ cm and $h = 385$ cm, are selected, respectively. In contrast to the temperature at these positions in the ZnO column, the mean unit temperature increases within the first time instants (until 20 s). This is due to transient heat transfer from the ZnO resistors to the aluminum spacing elements causing the temperature of the latter to increase even after energy injection. Since the arrester cools down in the interval between two impulses, this transient effect is less important for duty tests with large t_{gap}.

In Fig. 8.4(a), the cooling rate (8.4) is computed at $t = 0$ s for different time intervals between the impulses. In order to investigate the thermal stability properties of the arrester, the cooling rate of each unit is computed separately. As discussed above, the arrester temperature increases initially, which explains the negative cooling rates shortly after energy injection. This effect is stronger for small t_{gap}.

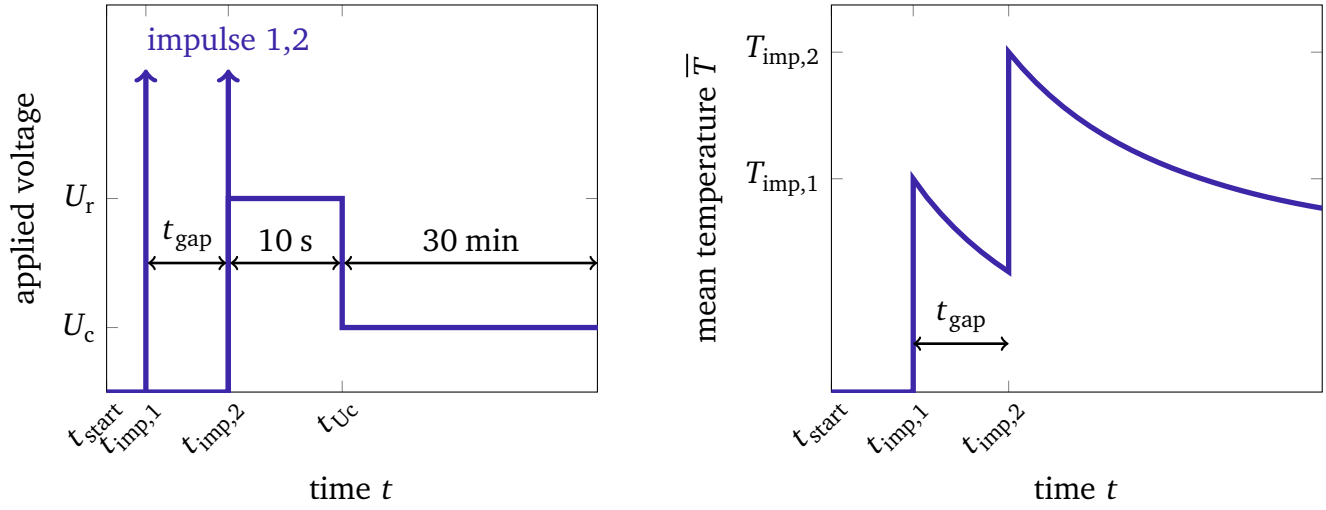

Figure 8.2.: (a) Schematic of the IEC operating duty test [IEC14]. The two current impulses are separated by the time interval t_{gap}. Then, for $t_{imp,2} \leq t \leq t_{Uc}$, $U = U_r$ is applied. Subsequently, the arrester returns to continuous operation at the power line voltage, U_c. (b) Averaged arrester temperature after the double impulse energy injection for thermally stable scenario (adapted from [Spä+16b]).

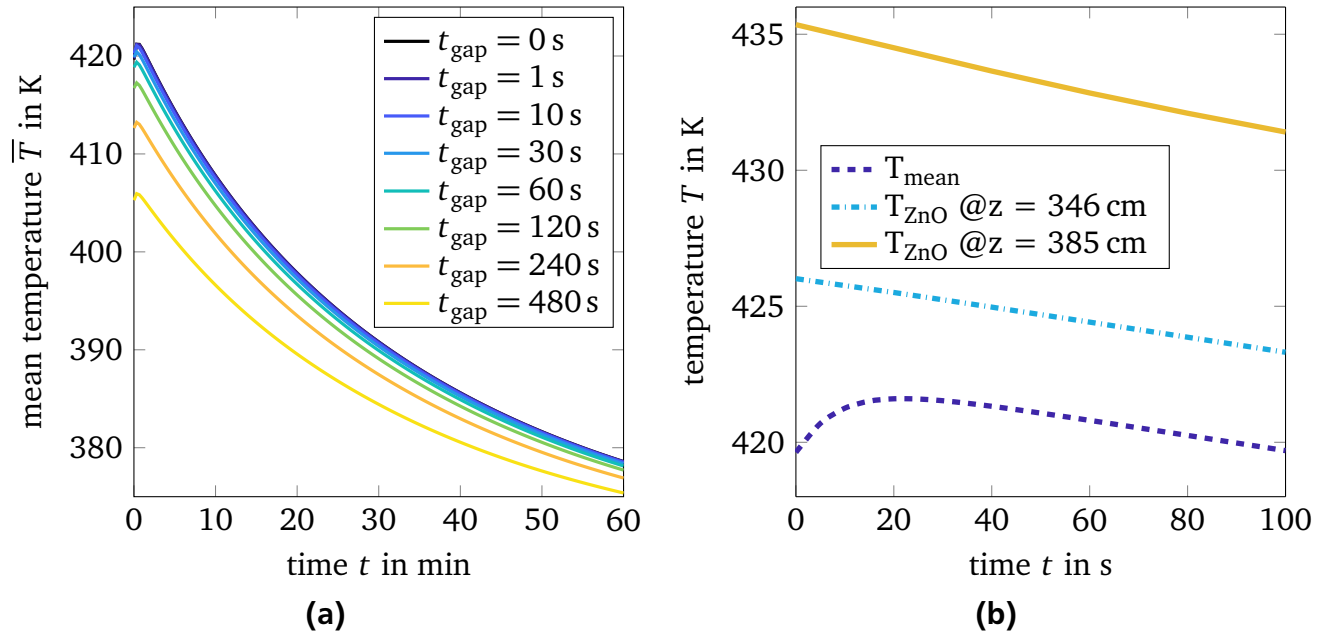

Figure 8.3.: (a) Average temperature of the top unit after energy injection for different impulse intervals, t_{gap}. (b) Mean unit temperature and temperature at the measurement positions at the height $h = 346$ cm and $h = 385$ cm for $t_{gap} = 0$ s (adapted from [Spä+16b]).

At $t = 140$ s (see Fig. 8.4(b)), the cooling rates of each arrester unit reach their asymptotic positive values. The cooling rate varies strongly between the different arrester units. This is partially caused by the nonuniform temperature distribution in steady state continuous operation, before the energy injection is applied (cf. Fig. 6.1). Besides, the heat conduction towards the large aluminum top and bottom flanges leads to enhanced cooling in the respective units. Consequently, the middle units exhibit the lowest cooling rates. The highest η is observed in the top unit, which features the highest steady state temperature as well.

In Fig. 8.5, the time evolution of the cooling rates in the different units is shown. After the decay of the initial transients (see Fig. 8.5(a)), each arrester unit cools down with a nearly constant rate. Furthermore, the cooling rates in the long time limit are independent from the time interval, t_{gap}, between the current impulses (see Fig. 8.5(b)). Thus, the asymptotic cooling behavior is determined by the arrester geometry and electrothermal parameters, rather than by the particular energy injection scheme. This is an important conclusion and validates the approach of the arrester standard [IEC14], since the standard allows a broad range of energy injection scenarios.

In summary, the arrester cooling rate includes the overall effects of the heat transfer capability as well as the local power loss in ac operation. All investigated scenarios considered in this section feature positive cooling rates after energy injection and are, thus, thermally stable. Moreover, the top unit, which exhibits the highest temperatures, is less likely to cause thermal instability. This result supports experimental observations indicating that it is the mean rather than the peak arrester temperature which determines thermal stability [HGT15; Gie18].

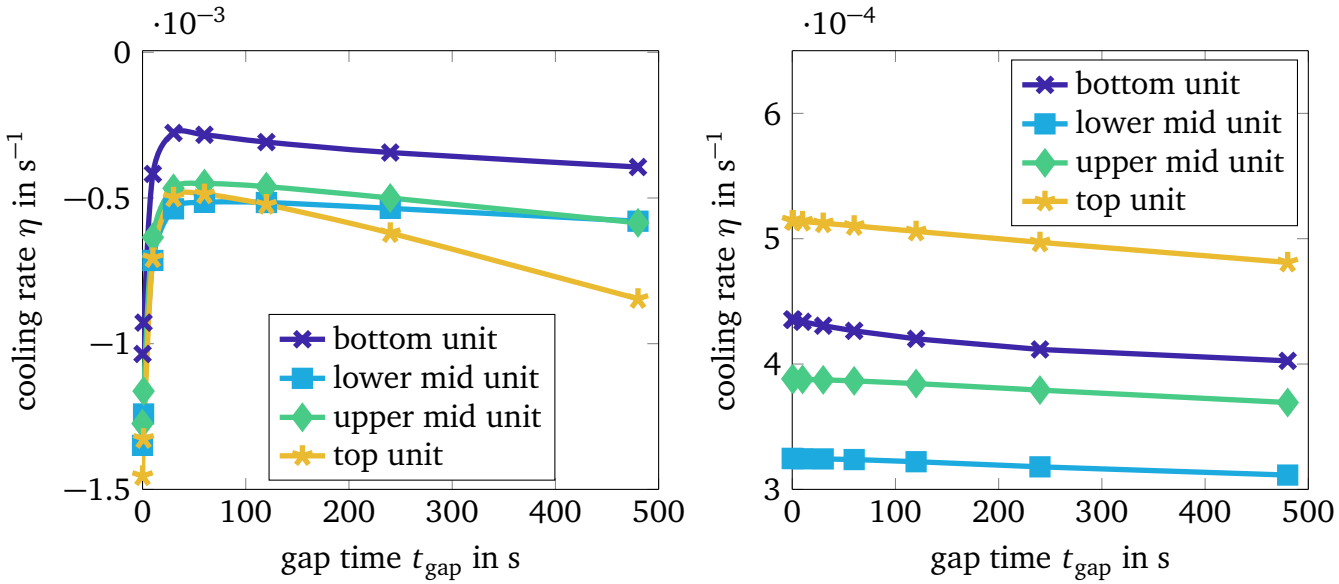

(a) $t = 0\,\mathrm{s}$ **(b)** $t = 140\,\mathrm{s}$

Figure 8.4.: Cooling rates in each arrester unit vs. the time interval between the impulses at (a) $t = 0$ s and (b) $t = 140$ s (adapted from [Spä+16b]).

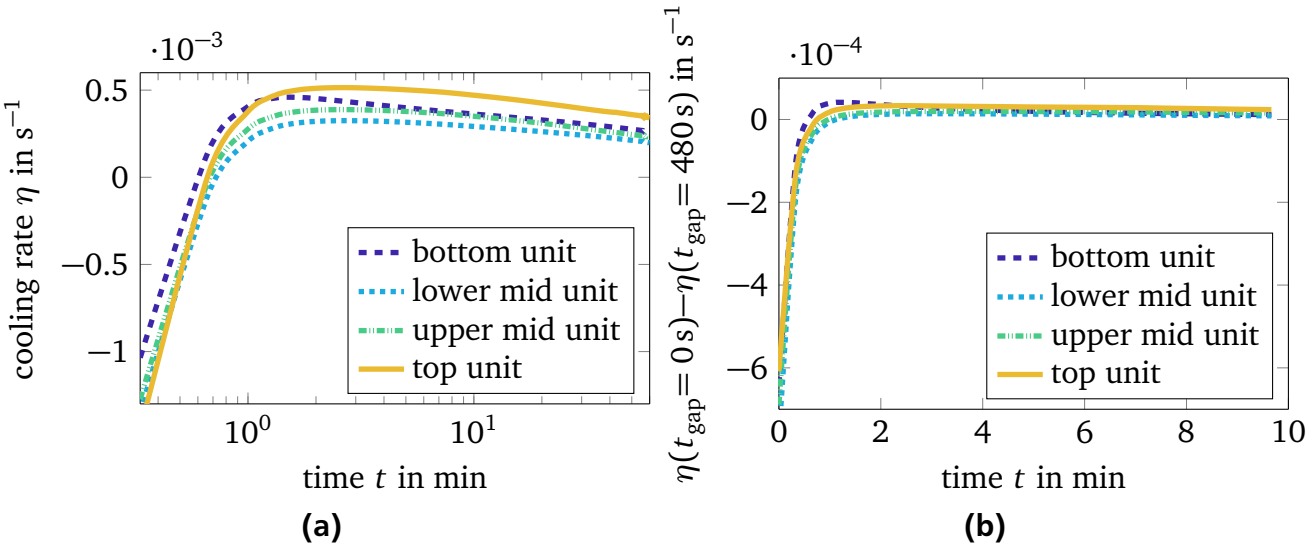

Figure 8.5.: (a) Time evolution of the arrester cooling rates for t_{gap} = 0 s (b) Difference of cooling rates in each arrester unit for the impulse interval t_{gap} = 0 s and t_{gap} = 480 s (adapted from [Spä+16b]).

8.3 Thermal Equivalent

8.3.1 Comparison of Thermal Equivalent and Surge Arrester

The ungraded 550-kV station class arrester and the thermal equivalent are subjected to the impulse simulation procedure based on the IEC operating duty test [IEC14] (see Sec. 2.3.2). In this case, a single temperature step of $\Delta T = 100\,\mathrm{K}$, corresponding to an impulse energy of 113.8 kJ (i.e. $\frac{W}{U_\mathrm{r}} = 10\,\frac{\mathrm{kJ}}{\mathrm{kV}}$), is adopted. The specimens are excited with U_r for 10 s and subsequently connected to U_c. Initially, the thermal equivalent is preheated to 333.15 K [IEC14], whereas the arrester is in steady state continuous operation.

Fig. 8.6(a) shows the transient temperature and the cooling rate (b) after the impulse injection. For this comparison, the average temperature along the axis of the top arrester unit (including heat sinks) is shown. The thermal equivalent temperature is averaged along its axis. The deviation of the starting temperature of the arrester unit and the equivalent is caused by the different initial conditions. The arrester temperature increases in the first seconds and, thus, the cooling rate is negative (not shown in the figure). Nevertheless, the scenario is thermally stable, as the cooling rate converges to a positive value. This behavior was, as well, observed in the previous section 8.2 and is attributed to transient longitudinal heat transfer processes within the unit that contains aluminum heat sinks. If only temperature data points in the ZnO resistors are considered, Fig. 8.6(b) shows that this effect is not observed (see dotted yellow line). To obtain the dotted yellow curve, the evaluation path is of the same length as the thermal equivalent and defined in the hottest region of the unit.

Based on the results of Fig. 8.6, the investigated thermal equivalent is a worst case approximation of the full-scale surge arrester. The steady state value of the cooling rate for the thermal equivalent and the surge arrester is in the range of $1 \times 10^{-4}\,\mathrm{s}^{-1}$ and $2.5 \times 10^{-4}\,\mathrm{s}^{-1}$, respectively. However, the gradients of both curves are different. The cooling rate of the thermal equivalent decreases quickly to its steady state value. The cooling rate of the arrester shows the short term heat capacity processes in the beginning. Afterwards, the cooling rate converges much slower to the steady state value compared to the equivalent.

8.3.2 Cooling Rate for Different Impulse Amplitudes

The influence of the step amplitude on the cooling rate is investigated. Figure 8.7(a) shows the temperature over time of the thermal equivalent after steps of $\Delta T = [100\,\mathrm{K}, ..., 150\,\mathrm{K}]$, corresponding to impulse energies of $[113.8\,\mathrm{kJ}, ..., 170.6\,\mathrm{kJ}]$ (i.e. $[10\,\frac{\mathrm{kJ}}{\mathrm{kV}}, ..., 15\,\frac{\mathrm{kJ}}{\mathrm{kV}}]$). The temperature curves of the lower step levels ($\Delta T \leq 130\,\mathrm{K}$) have the same shape and are shifted by 10 K each. For higher steps, no further increase of the cooling rate is observed. This is attributed to a strong increase of the temperature-dependent losses. Furthermore, for the 160 K step, a thermally unstable scenario is observed.

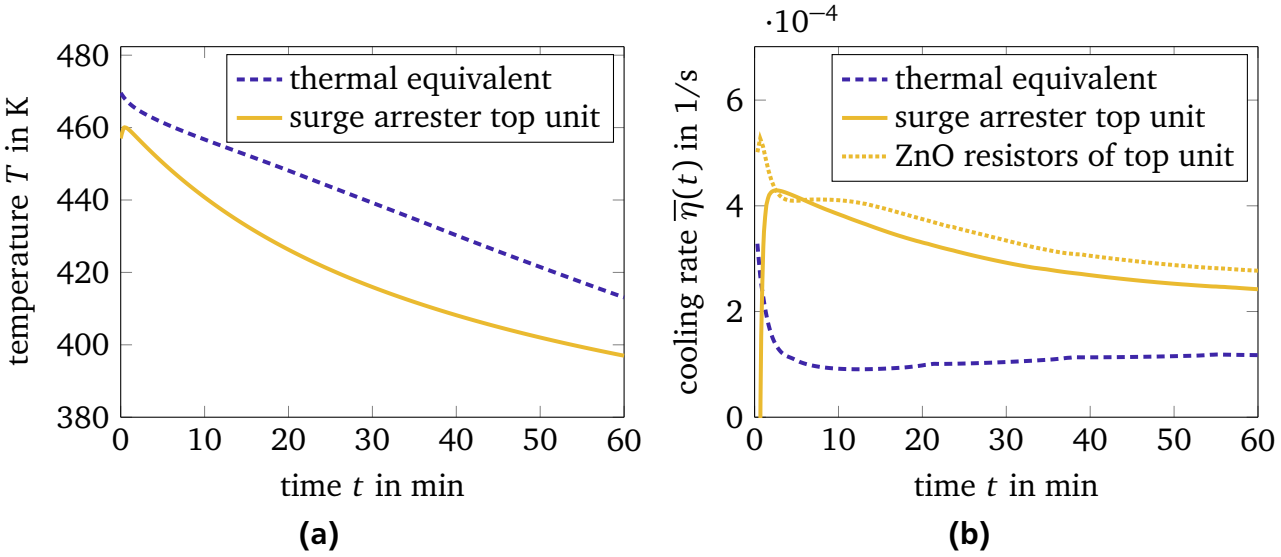

Figure 8.6.: A temperature impulse of $100\,\mathrm{K}$ is applied to the thermal equivalent and the surge arrester. The temperature decreases over time after the impulse, (a), and the cooling rate over time, (b). The cooling rate of the thermal equivalent is below the cooling rate of the arrester unit if only the ZnO resistor cooling (excluding the aluminum heat sinks) is taken into account. The initial transients of the overall arrester temperature are attributed to the heat sinks which heat up in the first time instants after the energy impulse.

Figure 8.7(b) shows the cooling rate $\overline{\eta}_{\mathrm{zno}}(t)$ with respect to the temperature step ΔT that is calculated at successive time instants. Two conclusions are drawn from the results. First, for all impulse scenarios, the cooling rate converges over time. This behavior was also observed in the previous section (see Sec. 8.2). Second, the cooling rate decreases with respect to the magnitude of the impulse. Thus, the impulses are close to the thermal stability limit, as the further increase of the heat dissipation processes barely compensates the increase of the electric losses. This, finally, leads to thermally unstable scenarios. The cooling rate becomes negative if the thermal stability limit is exceeded (in this case by the $160\,\mathrm{K}$ impulse).

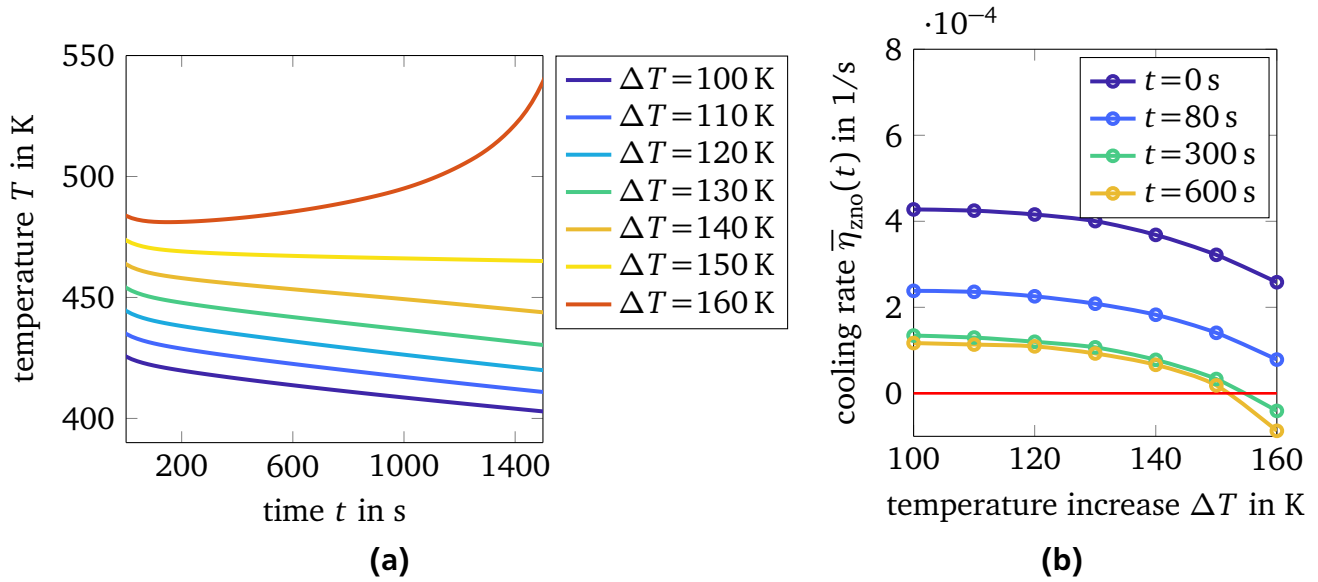

Figure 8.7.: Temperature over time of the thermal equivalent subjected to increasing temperature impulse amplitudes, (a), the cooling rate η over the impulse amplitude evaluated after increasing periods of time, (b). The $160\,\mathrm{K}$ scenario is thermally unstable, as the temperature increases after some $200\,\mathrm{s}$ and the cooling rate becomes negative (adapted from [Sch16]).

8.4 Efficient Detection of Unstable Energy Injection Scenarios

A criterion to detect a thermally unstable scenario is derived for an arbitrary full-scale station class arrester model. Therefore, stable and unstable energy injection scenarios, which are very close to the thermal stability limit, are analyzed using the reduced-diameter 550-kV-surge arrester.

In a first step, the steady state electric field and temperature distribution are simulated, which is required for the calculation of the cooling rate (8.4) (see Fig. 8.8(a) and Fig. 8.8(b), respectively). In this section, $\eta = \eta_{\mathrm{zno}}$ is evaluated only in the ZnO resistors of each unit, the aluminum spacers are excluded. Additionally, Fig. 8.8 shows the field and temperature distribution immediately after a temperature step of 250 K, corresponding to 3 MJ (i.e. $\frac{W}{U_\mathrm{r}} = 8\,\frac{\mathrm{kJ}}{\mathrm{kV}}$). The electric field (see Fig. 8.8(a)) within the arrester is redistributed compared to the initial state. Unlike in the initial steady state, the highest field stress is, now, observed in the lower units. This is attributed to the self-grading effect of the ZnO resistors leading to an increase of the permittivity and conductivity in the units subjected to the highest temperatures (see Fig. 8.8(b)). Consequently, an increased part of the overall excitation voltage drops along the lower units.

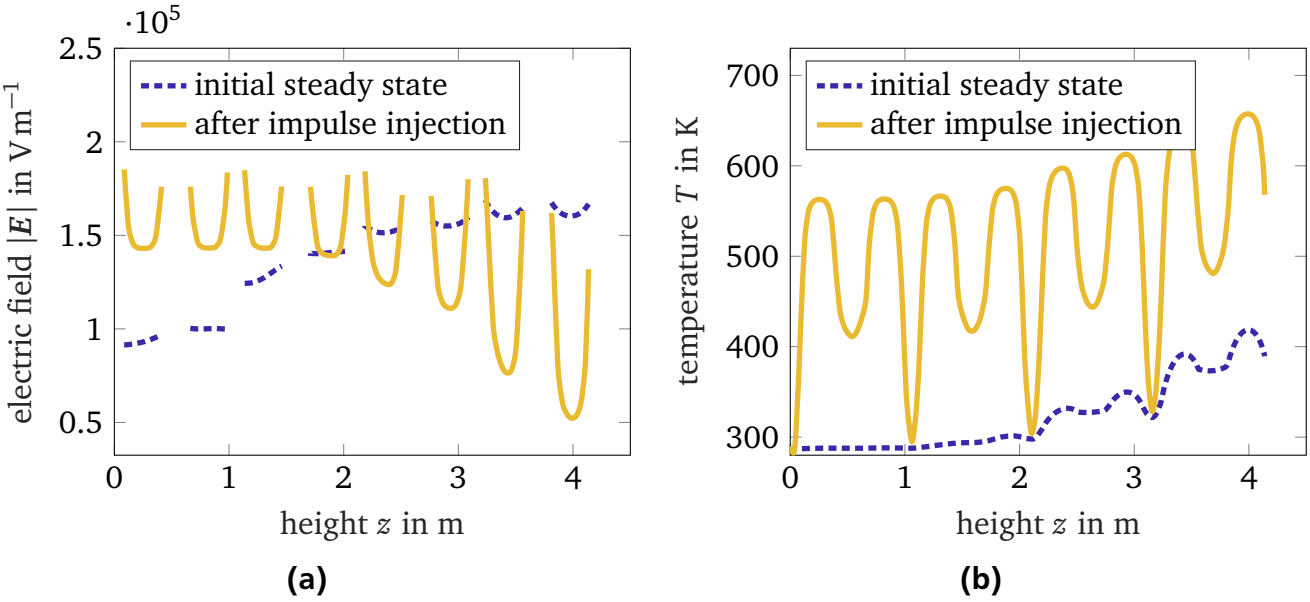

Figure 8.8.: Electric field distribution (a) and temperature distribution (b) of the initial steady state and 2 min after the impulse injection of $\Delta T = 250\,\mathrm{K}$.

Figure 8.9 shows the electric field (a,b), loss density (c,d), and temperature (e,f) distribution after an impulse of 250 K and 270 K (corresponding to 3 MJ and 3.3 MJ, i.e. $8\,\frac{\mathrm{kJ}}{\mathrm{kV}}$ and $8.8\,\frac{\mathrm{kJ}}{\mathrm{kV}}$), respectively. In both scenarios, the maximum electric field stress is located in the lower parts of the arrester immediately after the impulse injection (see Fig. 8.9(a,b)). A high variation of the electric stress in each ZnO section is observed. The field stress increase close to the heat sinks is caused by the temperature drop due to longitudinal heat transfer. In the middle of each ZnO section, the temperature is at its maximum (see Fig. 8.9(e,f)), and thus, the field

is reduced locally. With increasing time in the 250 K case, the electric field balances along the axis, as, initially, the maximum field is increased by nearly a factor of four compared to the minimum field. After ten minutes, this factor is reduced to less than two. This is, again, attributed to the capacitive and resistive self-grading of the ZnO material. The power loss of both scenarios develops differently (see Fig. 8.9(c,d)). In the 250 K scenario, the power loss density decreases over time from a mean value of initially 750 kW m^{-3} to 230 kW m^{-3}. This corresponds to a total power loss of 3.5 kW and 1 kW after 10 min (more than a factor of three). In contrast, the mean value in the 270 K scenario remains almost constant (with 1.2 MW m^{-3} and 1.1 MW m^{-3}, corresponding to 5.6 kW and 5.1 kW). The same trend is observed in the temperature development (see Fig. 8.9(e,f)). The 250 K scenario shows an axial balancing of the temperatures over time. The mean temperature decreases. In the 270 K scenario, the entire arrester continues to heat up – a thermal runaway occurs.

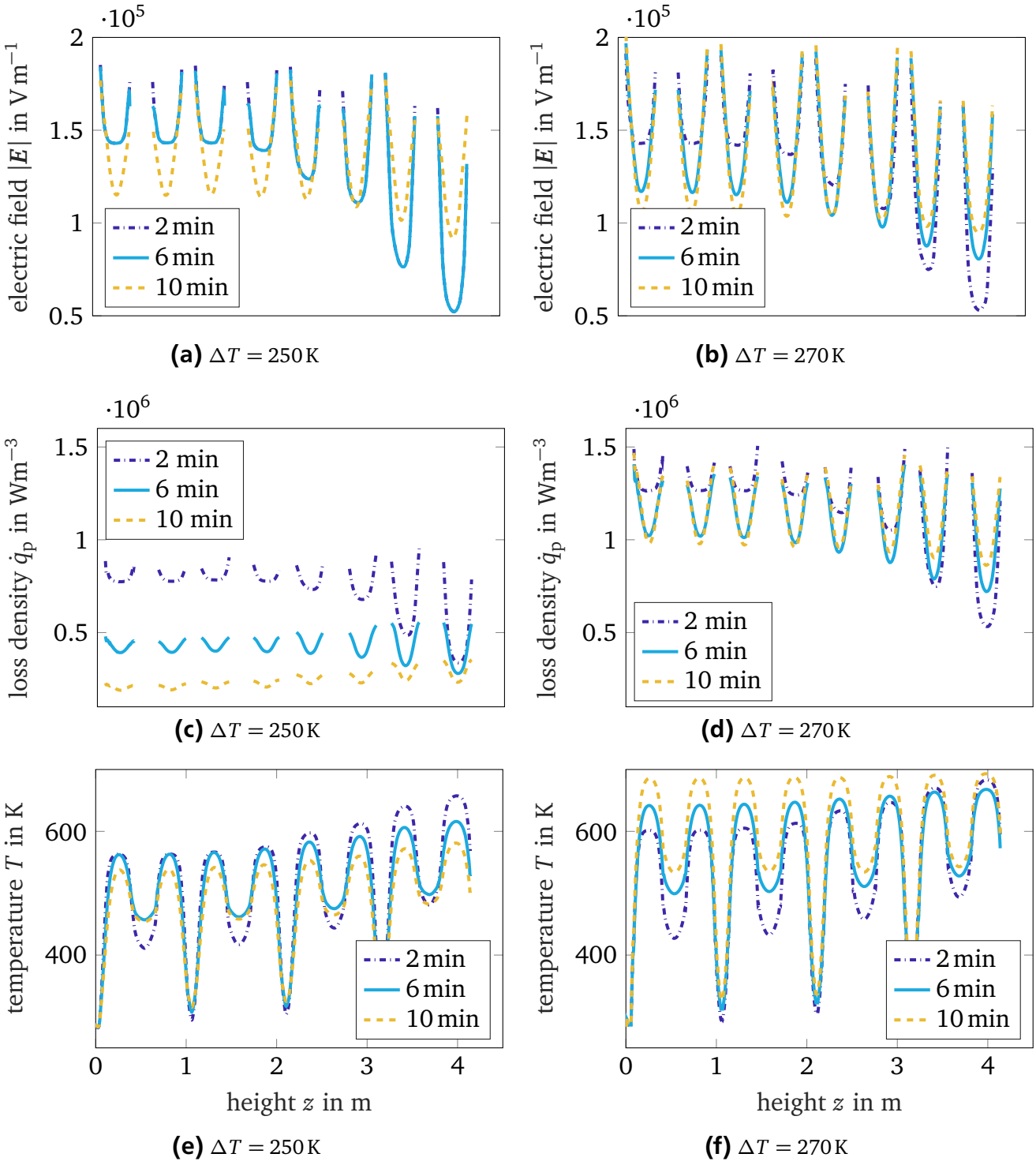

Figure 8.9.: Electric field, loss density, and temperature distribution along the arrester axis several minutes after an impulse of 250 K (a,c,e) and 270 K (b,d,f), respectively. Maximum electric field stresses are located in the lower parts of the arrester. The mean loss density in the 250 K case quickly drops by more than a factor of three. In the 270 K case, all units are in the breakdown mode. The highest temperatures are observed in the upper parts. In (e), the mean temperature decreases, whereas, in (f), the entire arrester heats up – a thermal runaway occurs.

The cooling rate of the ZnO resistors, η_{ZnO}, of (8.4) along the arrester axis is studied. The heat sink elements are not considered for the calculation of the cooling rate, as thermal instability is caused by a thermal runaway in the ZnO resistors. Furthermore, Sec. 8.2 shows that initial heating effects in the aluminum elements are superimposed on the ZnO behavior which is of interest.

First, Fig. 8.10 shows η_{ZnO} along the arrester axis. Immediately after the impulse injection, the cooling rate varies along the axis. Close to the aluminum heat sinks, the resistors cool down quickly, as they axially transfer thermal energy by heat conduction and heat capacity effects to the aluminum heat sinks and flanges. Thus, a highly positive cooling rate is observed close to the aluminum parts (which are, in the figure, shown as gaps). The balancing effect of the nonlinear ZnO self-grading and the attenuation of the heat sink influence diminish the variance in the cooling rate over time. In Fig. 8.10(a), the cooling rate attains positive values after 6 min. This scenario is, thus, thermally stable. In contrast, an unstable scenario is observed in Fig. 8.10(b), as the cooling rate attains negative values after 10 min.

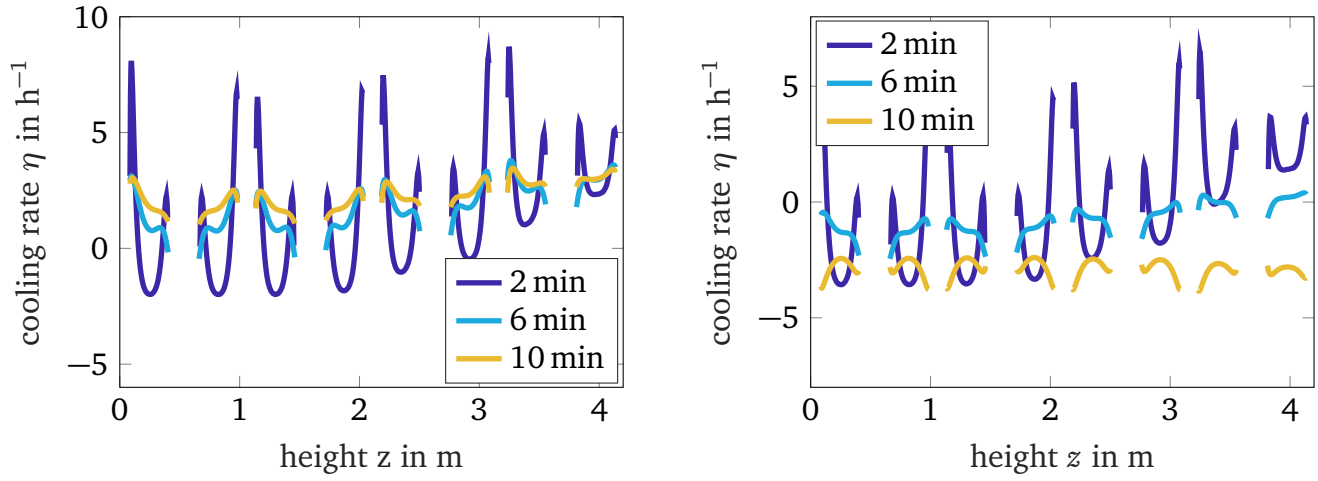

(a) $\Delta T = 250\,\mathrm{K}$ **(b)** $\Delta T = 270\,\mathrm{K}$

Figure 8.10.: Cooling rate along the arrester axis for the stable scenario (250 K) (a) and for the unstable scenario (270 K) (b). The aluminum heat sink regions and flanges are not shown in the figure. Immediately after the impulse injection, the cooling rate varies strongly in each ZnO region. Locally, the ZnO resistors cool down (highly positive cooling rate) close to the aluminum heat sinks, as heat is transferred axially to the heat sinks (see e.g. at 1 m). The self-grading effect and the attenuation of the heat sink influence balance the cooling rate with time along the axis.

The aim is to detect a thermal instability shortly after the energy injection. A first approach is to analyze the median cooling rate per unit. In the first scenario of Fig. 8.11(a), the lower two units heat up initially and, from 2 min on, start cooling down. All other units cool down from the beginning. In the scenario of Fig. 8.11(b), the lower units heat up continuously at all time instants ($\eta \leq 0$). The top unit cools down initially, but finally, all units heat up. A

detection by just looking to, e.g., the top unit after the first time step fails to correctly detect thermal instability. This is due to the self-grading behavior of the temperature-dependent ZnO conductivity and permittivity, which balance the field stresses over all units.

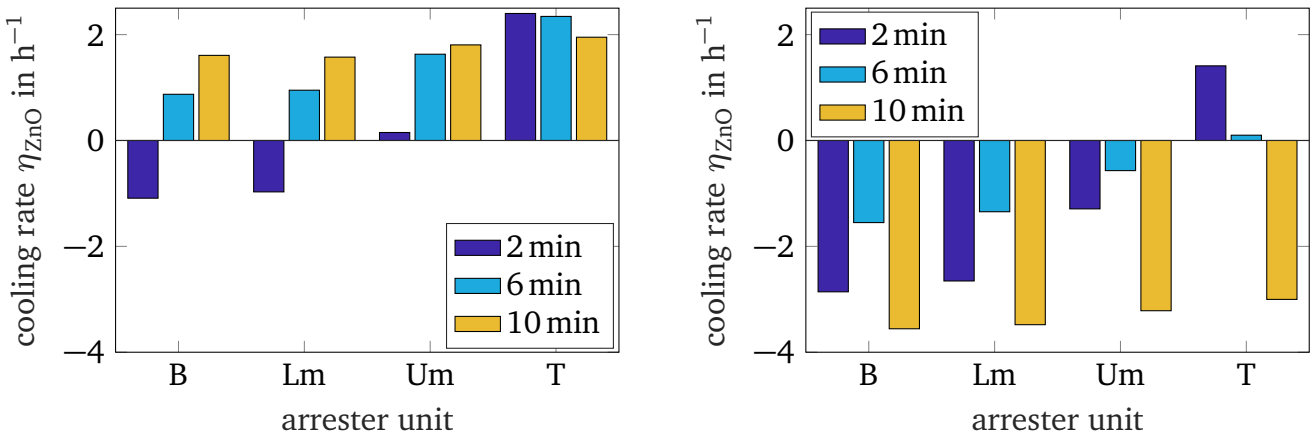

(a) $\Delta T = 250\,\mathrm{K}$ **(b)** $\Delta T = 270\,\mathrm{K}$

Figure 8.11.: (a) Cooling rate in each unit (i.e. from bottom (B), lower mid (Lm), upper mid (Um), to top (T)) for the stable scenario (250 K). (b) Cooling rate in each unit for the unstable scenario (270 K). The self-grading effect is clearly visible, as the cooling rate is balanced with time over all units. Thermal stability cannot be detected immediately after the impulse injection by analyzing a single unit. All units interact and balance field stresses due to the nonlinear behavior of the ZnO material.

Fig. 8.12 shows the mean (averaged over all units) ZnO temperature, $\overline{T}$, and mean cooling rate, $\overline{\eta}(t)$, for both scenarios. It can be observed that the mean cooling rate, which is evaluated immediately after the energy injection, seems to be a suitable estimator of the long term cooling rate development and, thus, for the thermal stability. This observation is confirmed by Fig. 8.13, which shows the distribution of the cooling rate for the stable (a) and unstable (b) scenario in a histogram. Both figures show that, immediately after the impulse injection, the distribution of the cooling rate is widely spread. With increasing time, the distribution narrows due to the discussed balancing processes. In the figure, the circles drawn below the distributions indicate the respective mean value. This mean value predicts, already immediately after impulse injection, the converged cooling rate behavior correctly, i.e. positive (stable) for Fig. 8.13(a) and negative (unstable) for Fig. 8.13(b). The observation that the mean ZnO cooling rate, $\overline{\eta}$, immediately after the impulse injection is a suitable estimator for the converged cooling rate behavior is important, as the numerical simulation of unstable scenarios is computationally expensive. This is because the operating point of the ZnO resistors at very high temperatures is shifted to the severely nonlinear region. In the following, different parameters that affect the thermal stability limit of the arrester are analyzed. Therefore, $\overline{\eta}$ is evaluated after a single thermal step.

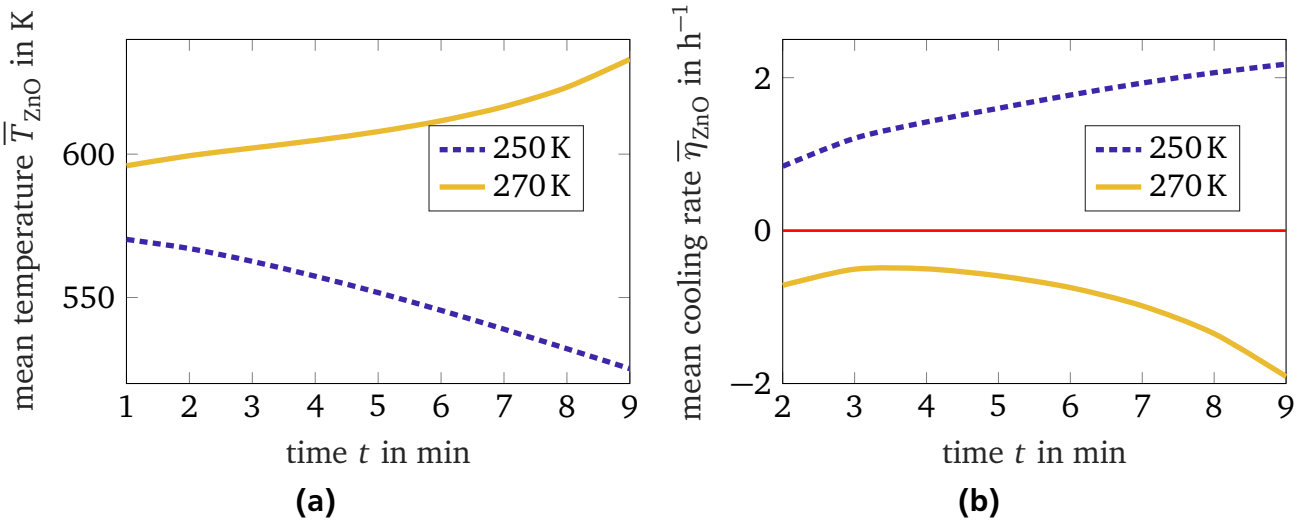

Figure 8.12.: Mean temperature (a) and mean cooling rate (b) of the stable (250 K) unstable scenario (270 K) over time. The mean cooling rate, calculated immediately after the impulse injection, correctly predicts the long time stability behavior of the arrester. In the stable case, it is positive and in the unstable case, it is negative. (adapted from [Spä+19]).

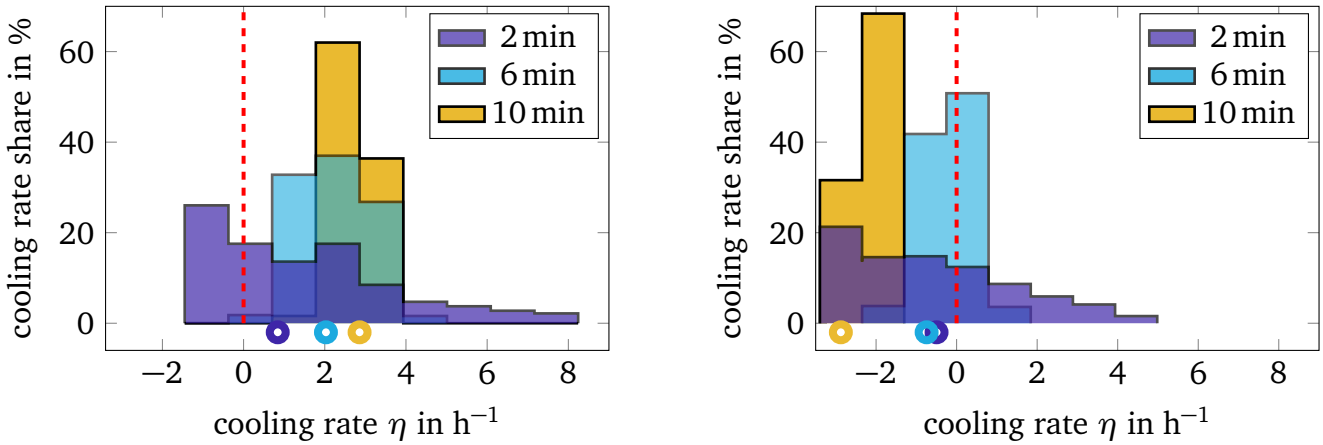

Figure 8.13.: Distribution of the ZnO cooling rate for the stable (250 K) (a) and unstable (270 K) (b) scenario over time. The initially large spread of the cooling rate converges with time due to the balancing effect of the self-grading behavior. The circles indicate the computed mean cooling rate for the shown time instants. It can be observed that the mean cooling rate is a suitable estimator for the converged long-time cooling behavior, as it correctly predicts the stability of the scenario.

8.5 Improvement of the Thermal Stability Limit

How can the thermal stability limit of the arrester be increased? The thermal stability limit is defined as the critical temperature limit above which the dissipated heat of the arrester is smaller

than the power losses (see Fig. 2.6). It may, thus, be possible to improve the thermal stability limit by modifying the thermal and electrical parameters of the arrester configuration. In the following, the influence of various model parameters on thermal stability is investigated. The investigated parameters are shown schematically in Fig. 8.14 and are summarized in Table 8.1.

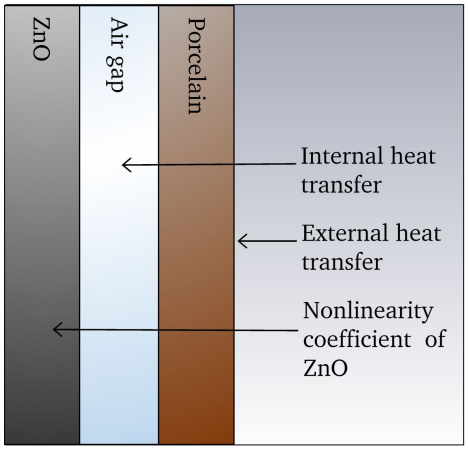

Figure 8.14.: Overview of the investigated model parameters to increase the thermal stability limit. The air gap heat transfer is increased by improving the convective and radiative heat transfer capability. The external heat transfer is improved by assuming perfectly emitting surfaces.

Table 8.1.: Overview of the investigated parameters and their influence on the thermal stability limit compared to the initial model (adapted from [Rup19]).

improved parameter	influence on stability limit
air gap radiation	+8 K
air gap convection	+14 K
air gap convection and radiation	+20 K
flange radiation	0 K
nonlinearity exponent, α	$\alpha = 18$: −45 K
	$\alpha = 19$: −19 K
	$\alpha = 21$: +14 K
	$\alpha = 22$: +25 K

Thermal Modifications

A first approach is to improve the heat transfer in the air gap. Therefore, the arrester unit air gap is divided in separate sub-units of each $h = 0.2\,\mathrm{m}$ (see Fig. 8.15(a)). This enhances the convective heat transfer according to (5.41). Furthermore, the inner surfaces of the air gap vessel are considered to be perfectly heat absorbing ($\varepsilon_{\mathrm{rad},1,2} = 1$). The increased effective thermal

conductivity in the gap is shown in Fig. 8.15(b). Fig. 8.16 shows that these measures are very effective. The maximum steady state temperature is decreased by 15 K, and the thermal stability limit is shifted by more than 20 K. This corresponds to an increase in the energy absorption capability of the arrester by 0.37 MJ (i.e. 7.5% and 1 $\frac{\text{kJ}}{\text{kV}}$). Both modifications may be implemented easily. Non-conducting sheets could be inserted in the units to subdivide the air gap in separate compartments (see Fig. 8.15)[1]. Theoretically, a black coating could be applied to the ZnO column and the inner surface of the housing, respectively. In practice, this may be, however, hardly feasible for conventional glass-coated ZnO resistors and glazed porcelain housing.

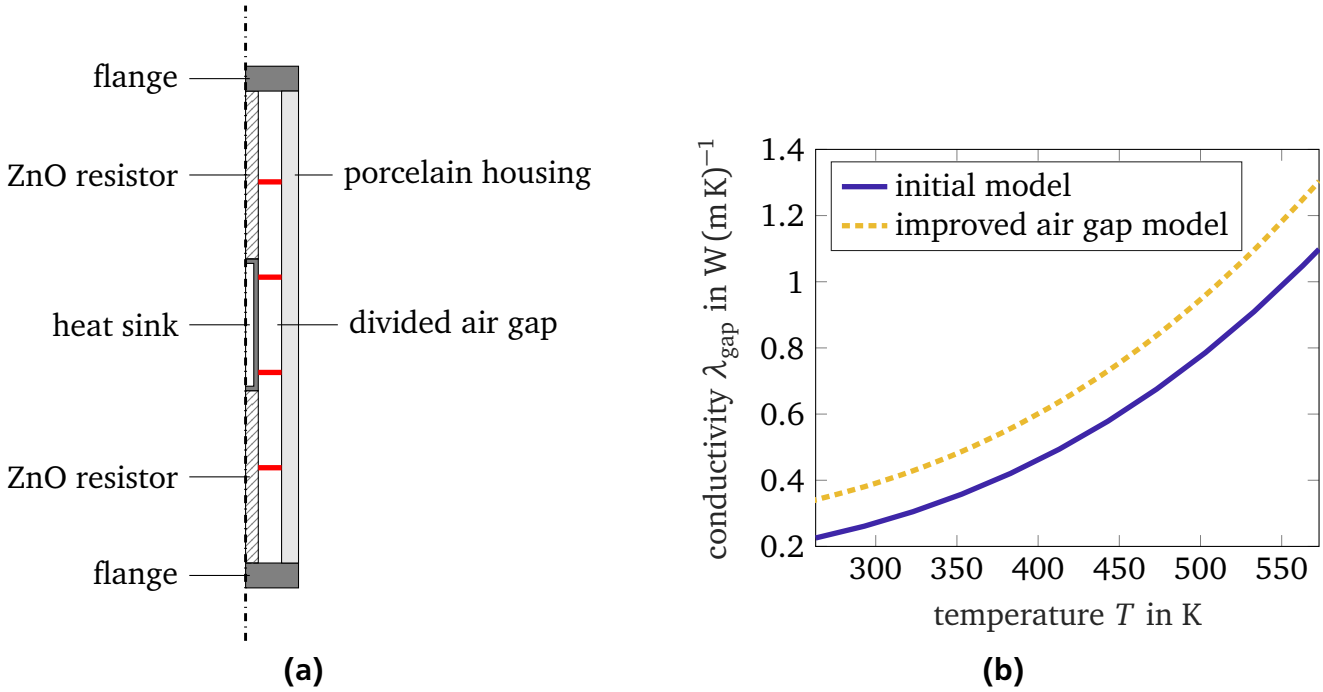

Figure 8.15.: (a) Modified air gap with sub-compartments to increase the natural convection. (b) Comparison of the effective conductivity in the air gap of the initial and the improved model (adapted from [Rup19]).

Third, the external heat transfer is analyzed. The radiative heat transfer from the aluminum flanges to the environment is improved. The flanges are assumed to be perfect emitters ($\varepsilon_{\text{rad}} = 1$). This could be realized by applying a black coating to the flanges. However, also this measure has a negligible effect on the thermal stability limit (see [Rup19]).

Electrical Modifications

Moreover, the electric material nonlinearity influences the thermal stability limit strongly. For the investigated degrees of nonlinearity, the mean and maximum steady state temperatures vary in a range of 16 K and 20 K, respectively (see Fig. 8.17(a)). Fig. 8.17(b) shows the cooling rate for different degrees of nonlinearity, α, in the ZnO conductivity characteristic $\sigma(\alpha, |\vec{E}|, T)$ of (5.22). The stronger the nonlinearity with respect to $|\boldsymbol{E}|$ in (5.22) is, the higher is the thermal

[1] A suitable pressure relief design must be considered.

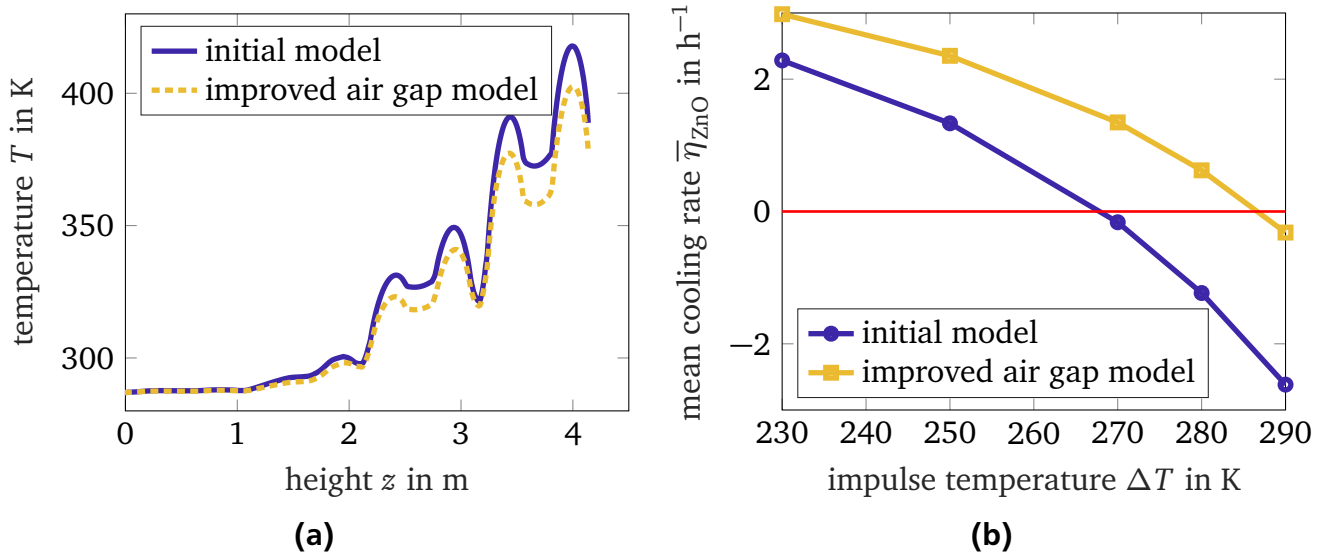

Figure 8.16.: (a) Comparison of the steady state temperatures of the initial and improved air gap heat transfer model, respectively. The maximum temperature of the improved air gap model is decreased by 15 K. (b) Comparison of the cooling rate of both models. The thermal stability limit is improved by 20 K (adapted from [Rup19]).

stability limit. The difference of the stability limit amounts to 70 K between the lowest ($\alpha = 18$) and highest ($\alpha = 22$) degree of nonlinearity considered in the investigation. The reason is that α determines the resistive current contribution during the ac voltage excitation after the impulse injection. In this mode of operation, the current is predominantly capacitive. An increased α-value further reduces the resistive component. Thus, the losses generated by the ac voltage are minimized. Fig. 8.18, additionally, shows that the instability limit cannot be increased indefinitely. A saturation of the critical temperature for high α is observed. An optimization could, thus, aim for an α that balances three aspects: Optimal ac operation, requirements regarding the impulse switching point and the thermal stability limit.

Furthermore, in [Rup19] it is demonstrated that the observed improvements are generally valid for arbitrary arrester configurations, such as e.g. a station class arrester with attached grading ring system.

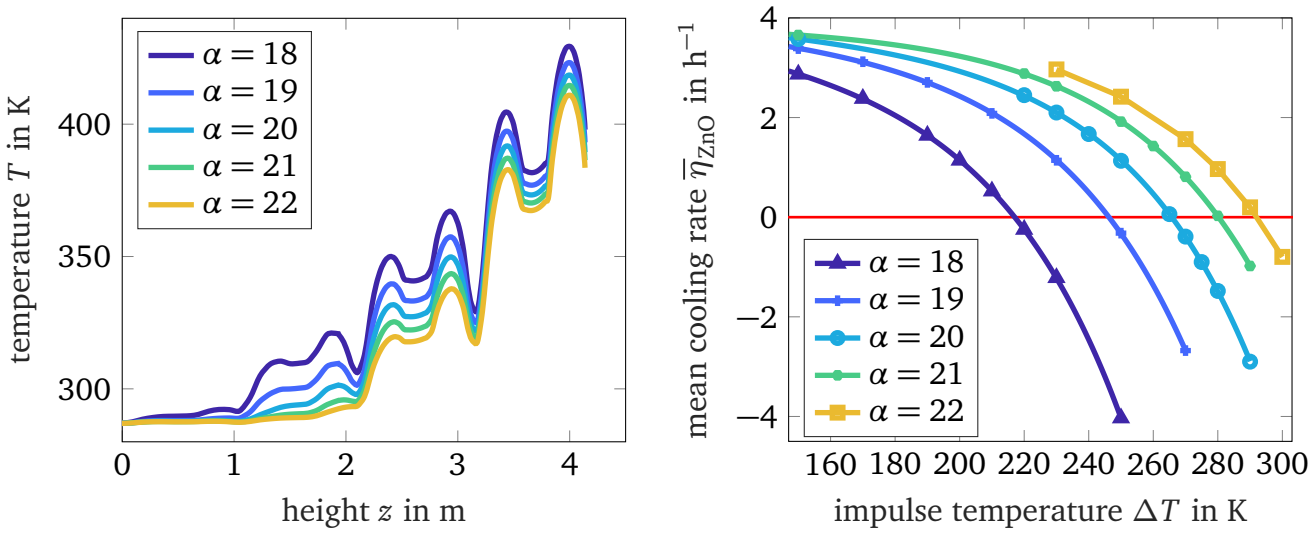

(a) **(b)**

Figure 8.17.: Steady state comparison, (a), and cooling rate comparison, (b), for increasing degrees of nonlinearity α of the ZnO conductivity characteristic, $\sigma(\alpha)$. With increasing α, the steady state temperature is reduced and the thermal stability limit increased [Rup19].

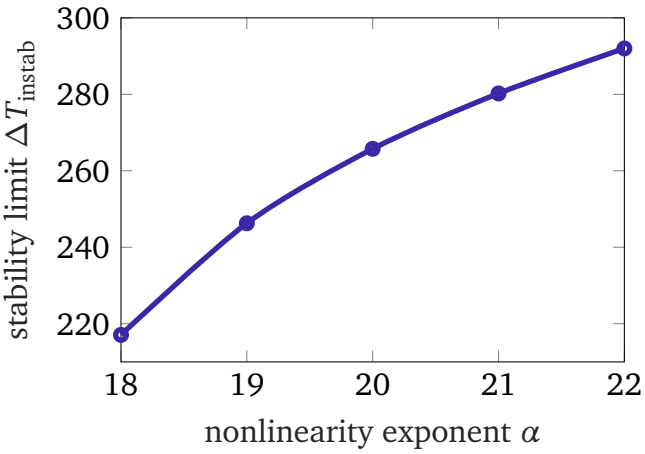

Figure 8.18.: Thermal stability limit over increasing degrees of nonlinearity α of the ZnO conductivity characteristic, $\sigma(\alpha)$ (adapted from[Rup19]).

8.6 Prediction of the Thermal Stability Limit

The numerical solution of the EQST arrester problem after an energy injection corresponding to a temperature step close to the thermal stability limit is numerically expensive. This is due to the severe nonlinearity of the ZnO resistors at elevated operating temperatures. The electrical time step must be very small (in the range of μs) in order to maintain numerical stability and accurately resolve the nonlinearity. Consequently, the computation time of several seconds after impulse injection is in the range of tens of hours. The demands on the electrical time step are less severe for lower energy impulses. The computational costs, in this case, are by two orders of magnitude lower. Therefore, the aim is to predict the stability limit based on just a few impulse injection simulations far from the stability limit at lower temperatures.

Figures 8.16 and 8.17 show the same basic course of the cooling rate curves. Thus, an ana-

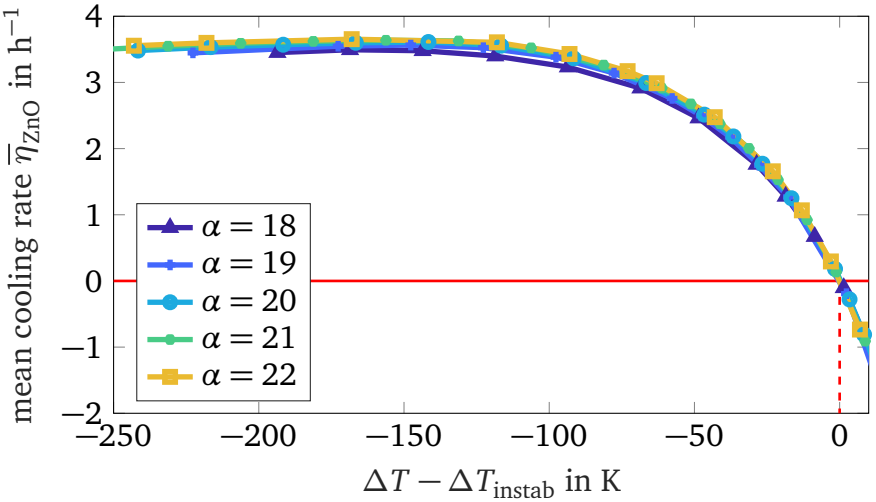

Figure 8.19.: The cooling rates for different degrees of nonlinearity, α (cf. 8.18) are translated such that the stability limits are shifted to the origin.

lytical fitting function to predict the thermal stability limit based on just a few simulation data points can be introduced. From the results of the previous section, it is observed that modifications of the thermal heat transfer shift the cooling rate curve on the abscissa and on the ordinate axis. The principle shape of the curves is retained (see e.g. Fig. 8.16). The electrical modification of the nonlinearity exponent, α, simply shifts the cooling rate curves on the abscissa. The shape of the curve is, again, retained (see Fig. 8.17). The prediction function is fitted based on the presented cooling curves of the previous section. In a first step, the principle shape of the curve is fitted to an analytical curve, independent horizontal and vertical shifts along the axis. Therefore, the nonlinearity-coefficient cooling curves are fitted, as these curves can be superimposed by shifting the thermal stability limit, ΔT_{stab}, to the origin (see Fig. 8.19). A suitable function to fit the curves of Fig. 8.19 is given by,

$$\overline{\eta}_{\mathrm{fit}}(\Delta T, \alpha, c_1, c_2) := c_1(\alpha)\left[\mathrm{e}^{\left[c_2(\alpha)(\Delta T - \Delta T_{\mathrm{stab}})\right]} - 1\right], \tag{8.5}$$

where ΔT is the impulse temperature in K and c_1 and c_2 are the fitting coefficients in h^{-1} and in K^{-1}. In this first step, the fitting coefficients, c_i, are obtained for each set of α data points (see Fig. 8.19) separately and summarized in Table 8.2. The fitting coefficient c_1, varies less than 3.5% and c_1 varies less than 8%. The mean value of each fitting coefficient over all α is given in the last row of Table 8.2. Now, for each α, the general shape of the fitting curve is known.

Table 8.2.: Fitting coefficients of (8.5) for various nonlinearity exponents α.

α	c_1 in h^{-1}	c_2 in K^{-1}
18	-3.621	0.0235
19	-3.657	0.0246
20	-3.729	0.0247
21	-3.760	0.0245
22	-3.750	0.0255
mean	-3.703	0.0246

In the next step, the obtained fitting curve can be used to predict the thermal stability limit by extrapolating the development of the cooling curve based on just two simulation data points. Now, the defined shape of the curve can be shifted on the abscissa and on the ordinate axis by the free parameters, d_1 (in K) and d_2 (in h^{-1}). These parameters describe the horizontal and vertical translation of the fitting curve for a given set of simulation data. The prediction curve is, now, given by,

$$\overline{\eta}_{\text{fit}}(\Delta T, d_1, d_2) := c_1(\alpha)\mathrm{e}^{[c_2(\alpha)(\Delta T - d_1)]} + d_2, \tag{8.6}$$

Based on, at least, two data points, the two free parameters, d_1 and d_2 of (8.6) are obtained. The estimated stability limits are, then, compared to the previously simulated stability limits.

The procedure to predict the thermal stability limit on simulation data points is exemplarily shown for the reference model of $\alpha = 20$. In this case, the principle shape of the fitting function is given by[2],

$$\overline{\eta}_{\text{fit}}(\Delta T, 20, d_1, d_2) = -3.73\mathrm{e}^{[0.025(\Delta T - d_1)]} + d_2. \tag{8.7}$$

To obtain d_1 and d_2, (8.7) is solved for the two data points shown in Fig. 8.20, i.e. $(\Delta T_1, \overline{\eta}_1) = (175, 3.36)$ and $(\Delta T_2, \overline{\eta}_2) = (200, 3.0)$. The resulting fitting function is, then,

$$\overline{\eta}_{\text{fit}}(\Delta T, 20) = -3.73\mathrm{e}^{[0.025(\Delta T - 264)]} + 3.78. \tag{8.8}$$

Now, the thermal stability limit can be estimated by extrapolating the cooling rate beyond the two simulated data points. The zero crossing is the thermal stability limit, in this case, 265 K

[2] For readability, the number of digits of the fitting coefficients is reduced.

(see Fig. 8.20). In the figure, this extrapolation result (dashed red curve) is compared to the previously simulated data points (dark blue circular markers). The simulated thermal stability limit is 266 K. The difference of prediction and simulation is less than 0.4%, which is an excellent agreement.

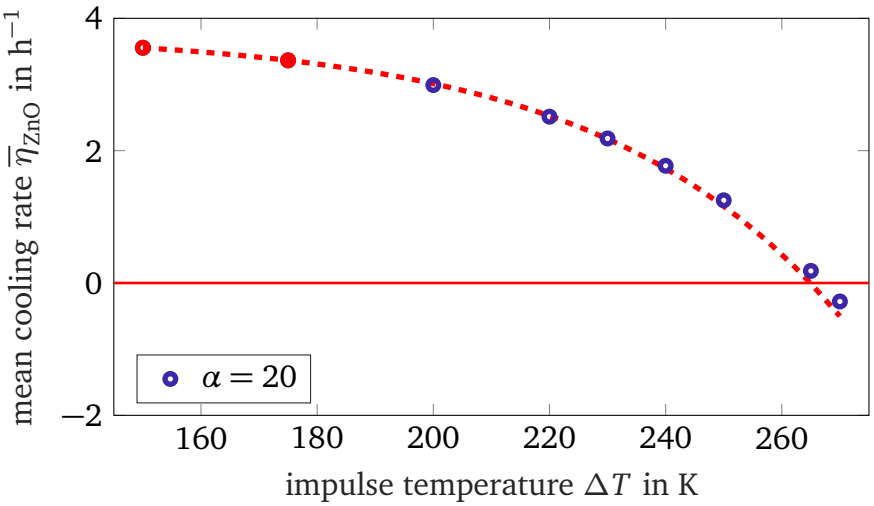

Figure 8.20.: Comparison of $\overline{\eta}_{\mathrm{fit}}$ for $\alpha = 20$ to the simulation data (blue dots). The $\overline{\eta}_{\mathrm{fit}}$ curves and simulation data are represented as lines and markers, respectively. Only two simulation data points are considered in the fitting process for determining d_1 and d_2 of (8.7) and are highlighted in red.

The procedure is repeated for all investigated α. The estimated and simulated stability limits are listed in Table 8.3 and agree very well (absolute deviation $\leq 3\,\mathrm{K}$). Figure 8.21 compares the estimated and simulated cooling curves.

Table 8.3.: Comparison of exact thermal stability limits, $\Delta T_{\mathrm{instab}}$, and estimated thermal stability limits, $\Delta T_{\mathrm{instab,fit}}$, for different degrees of nonlinearity, α.

α	$\Delta T_{\mathrm{instab}}$	$\Delta T_{\mathrm{instab,fit}}$	$\lvert\Delta T_{\mathrm{instab}} - \Delta T_{\mathrm{instab,fit}}\rvert$	d_1	d_2
18	218 K	218 K	0 K	219.5	3.595
19	248 K	251 K	3 K	250.7	3.93
20	266 K	265 K	1 K	264.1	3.779
21	281 K	278 K	3 K	276.3	3.83
22	293 K	293 K	0 K	292.2	3.814

In general, the nonlinearity exponent, α, of a ZnO material characteristic may be unknown. Thus, predicting the thermal stability limit independent of α is desirable. The fitting parameters,

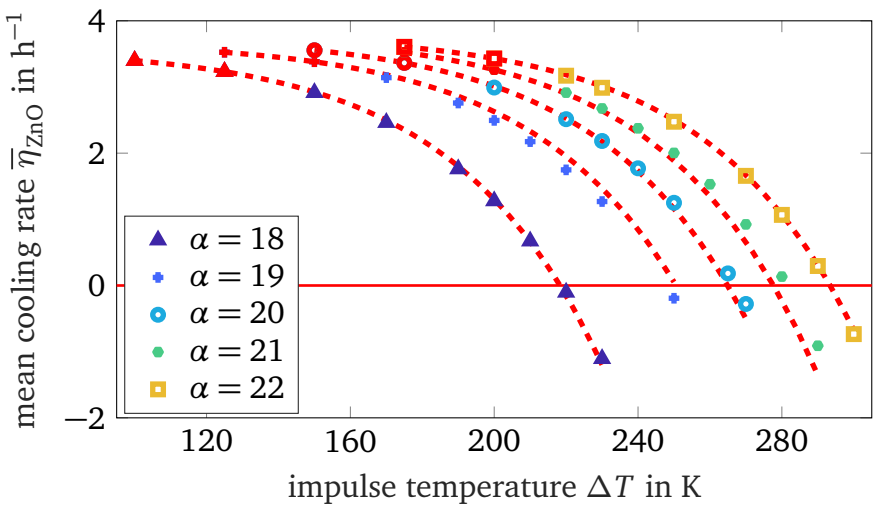

Figure 8.21.: Comparison of $\overline{\eta}_{\mathrm{fit}}$ for all investigated α to the simulation data. The $\overline{\eta}_{\mathrm{fit}}$ curves and simulation data are represented as lines and markers, respectively. For each estimation of α cooling curve, two simulation data points are considered in the fitting process to determine d_1 and d_2. They are highlighted in red.

c_i, of the thermal stability estimator function vary only slightly with respect to α (see Table 8.2). Thus, a robust estimator function is proposed by adopting the mean fitting coefficients as[3],

$$\overline{\eta}_{\mathrm{fit}}(\Delta T, d_1, d_2) = -3.7\mathrm{e}^{[0.025\,(\Delta T - d_1)]} + d_2. \tag{8.9}$$

At least two simulation data points are required to obtain the remaining parameters d_1 and d_2. These points should be close enough to the (unknown) thermal stability limit. Based on the presented examples, the following criterion is proposed: The slope between these points should be negative and $\leq -0.01\,(\mathrm{Kh})^{-1}$.

Two energy injection simulations far from the thermal stability limit (and, thus, computationally less expensive) are sufficient for an accurate prediction of the thermal stability limit of a station class arrester. Differences in the thermal or electrical arrester design do not affect the shape of the cooling rate curve. The observed horizontal and vertical shifts in the cooling rate curve are taken into account by two free parameters in the prediction function. Thus, the predicted thermal stability limit can be used directly, e.g. for optimizing an arrester design. Furthermore, it can reduce the number of required simulations or cumbersome laboratory experiments for determining the exact stability limit.

[3] Again, the digits of the fitting coefficients are reduced, the full coefficient is listed in the last row of Table 8.2.

9 Conclusion and Outlook

9.1 Conclusion

This thesis was dedicated to the electrothermal FE simulation of station class surge arresters, which play an indispensable role in the protection of electric energy transmission components. The core of an arrester consists of ZnO resistors, that absorb impulse energies due to a switch-like conductivity characteristic. The challenge of arrester simulation, thus, lies in accurately resolving the nonlinear electric field and temperature dependence of the ZnO resistors. Therefore, the transient coupled electrothermal problem must be solved in order to optimize an arrester's design and understand its behavior under extreme operating conditions.

Advances in arrester simulation were achieved by introducing a detailed electrothermal model. The electric model is based on the electro-quasistatic approximation. It was shown that, for accurately reproducing measured arrester behavior, the electrical conductivity and, in particular, the permittivity of the ZnO resistors must be represented by nonlinear field- and temperature-dependent material characteristics. Analytical material functions were proposed, which were obtained by fitting measured U-I-characteristics of ZnO resistors in the leakage and early breakdown region. For thermally modeling station class arresters, natural convection and thermal radiation effects in the air gap were considered. A major problem are the long thermal transients in arresters in comparison to the required extremely fine electric resolution due to the nonlinear ZnO characteristic. The multirate time integration scheme used in this thesis exploits the strongly different time constants and the periodicity of the alternating current excitation. The scheme reduces the computational costs by several orders of magnitude compared to a fully coupled routine.

Simulations and measurements were performed for an arrester installed directly on ground and without the grading ring in order to better demonstrate the effects of severely non-uniform field, power loss, and resulting temperature distributions. The simulations accurately reproduced measured steady state arrester operation. On the basis thereof, a systematic procedure for the optimization of the field grading system of surge arresters based on numerical simulations was proposed. In order to obtain a numerically suitable model for the optimization procedure, a 2-dimensional axisymmetric equivalent arrester model was introduced. Hereby, different virtual electrode configurations, which can properly reproduce the electric field stress on the arrester axis, were compared. In particular, the equivalent model using a conical screen as a virtual electrode yields an highly accurate approximation of the arrester field along the axis. In the second step, the grading ring configuration was optimized with respect to the field flatness on the arrester axis. The optimization procedure is based on fast transient EQS simulations

of the 2-dimensional equivalent. It was demonstrated that a huge improvement of the steady state field and temperature distribution in the arrester can be obtained.

In order to determine the thermal stability under energy impulses, the cooling rate was introduced as indicator of thermal stability. Using this criterion, first, the operating duty test of the IEC standard was simulated for an ungraded 550-kV-station class arrester. Thermal stability for various energy injection scenarios was approved.

Subsequently, a thermally prorated equivalent of the station class surge arrester was modeled and validated against measurements. The thermal equivalent and the full-scale arrester were compared when subjected to single impulses. Based on the cooling process, the investigated thermal equivalent can, indeed, be classified as a worst case approximation of the full-scale arrester.

On the one hand, simulations close to the stability limit become numerically extremely cumbersome. On the other hand, it is desired to optimize the thermal stability limit of arresters as accurately as possible. Thus, a precise stability criterion that identifies thermally unstable scenarios after the shortest simulation time possible is required. For the 550-kV-arrester, it was demonstrated that the mean ZnO resistor cooling rate allows for the detection of thermal instability immediately after the impulse injection. Based on this criterion, the influence of different arrester design parameters on the thermal stability limit was investigated. It was shown that by improving the heat transfer of the arrester air gap the thermal stability limit was increased by 20 K. Furthermore, the degree of nonlinearity of the ZnO conductivity characteristic influences the thermal stability limit strongly. The stability limit differs by 70 K between the lowest ($\alpha = 18$) and highest ($\alpha = 22$) investigated nonlinearity exponent. Finally, the computational costs for determining the thermal stability limit can be significantly reduced by the introduction of a prediction function. The predictor proposed in this thesis is based on the fact that the shape of the cooling rate curves over impulse temperature differ only very slightly for all investigated arrester parameters. It was shown that two simulation data points far from the stability limit are sufficient for a very accurate prediction of the thermal stability limit. The computation costs of these data points were, for the investigated example, by a factor 80 lower compared to the cost of a simulation close to the thermal stability limit. This reduced the simulation time from several hours to only a few minutes.

9.2 Outlook

The analytical material-data functions of this thesis consider the field and temperature dependence of ZnO material. As discussed in Sec. 5.1.2, additional physical phenomena may influence the ZnO behavior, such as e.g. frequency or mechanical-stress dependency of the material properties. In order to consider these effects, in a first step, the electric modeling approach of this thesis must be extended. In a second step, new methods to extract even more complex material characteristics from laboratory U-I-measurements on single ZnO resistors must be developed.

When ZnO material is operated in and above the breakdown region, the current is not homogeneously distributed (cf. literature provided in Sec. 2.2) and flows in channels along the conductive grain boundaries. Thus, it is expected that, also, the power loss and temperature is not uniformly distributed in the ZnO resistor. Different researchers work on simulating this phenomenon on the micro-scale level (see Sec. 2.2). A coupling of the macroscopic coupled simulation model of this thesis and the microscopic level of the grain boundary theory would be a promising and challenging approach to gain new insights on arrester behavior.

Recent developments in computational approaches for uncertainty quantification (see e.g. [Lou19]) could be applied to surge arrester simulation. Large station class arresters are composed of several tens of single ZnO resistors. Each resistor has a slightly different material characteristic. Due to the strong nonlinearity, this spread can lead to substantial deviations of expected and measured behavior. Uncertainty quantification could be used to investigate this effect and take it into account for arrester optimization.

Regarding the thermal model, a computational fluid dynamics simulation can contribute to a better understanding of the external flow conditions at the flanges and the shed structure of the ceramic housing. It can be used to validate the Nusselt number approximations of the external heat transfer to the surrounding air.

Surge arresters of ultra-high-voltage systems are composed of several separated ZnO stacks connected in parallel [Gie18]. It is not clear how these arresters can be represented in a 2D-axisymmetric simulation. Future research can, on the one hand, aim for an equivalent model of these configurations. On the other hand, quasi-3D simulation schemes can be developed to solve the electrothermal multi-column ultra-high-voltage arrester problem.

The positioning, volume and number of the heat sinks in the arrester stack is mainly based on experience of high voltage engineers (see [ZB03; Gie18; Hin11]). An optimization, which can handle discrete numbers, of the heat sink distribution can lead to an improvement of the electrothermal arrester design and can aim for the increase of the thermal stability limit.

In this thesis, parameters that increase the thermal stability limit were identified. Furthermore, the prediction function reduced the number of required simulations for determining the exact stability limit. However, the presented predictor is only a first attempt and may be further improved. Based on this two ingredients, an optimization can, then, aim for an arrester design that balances continuous ac operation and the thermal stability limit.

Last but not least, the modeling, simulation and optimization schemes that were developed in the context of the arrester problem can be transferred without difficulty to other equipment of power transmission and distribution. In the design phase of, e.g., cables, cable accessories or bushings, coupled FE analysis and optimization of the overall electrothermal and field grading design is desired to reduce the development costs and the number of laboratory experiments.

A Appendix

A.1 Outdoor Arrester of Station Class

A.1.1 550-kV-Station Class Surge Arrester

Table A.1.: Material properties of the 550-kV-station class arrester.

Material	λ in $\mathrm{W\,m^{-1}\,K^{-1}}$	$\varepsilon_{\mathrm{rad}}$
ZnO	$\lambda = 23.868 - 0.0269 \cdot T$, [Hin90]	0.96, [Hin90]
Porcelain	4.0	0.85, [Hin90]
	vol. heat cap. c_{v} in $\mathrm{J\,cm^{-3}\,K^{-1}}$	ε_{r}
ZnO	$c_{\mathrm{v}} = 2.59 + 0.0044 \cdot T$, [Lat83]	Fig. 4.3
Porcelain	2.34	5.0

Table A.2.: Air gap parameters of the 550-kV-surge arresters.

unit	T in K	$\lambda_{\mathrm{air,conv}}$ in $\mathrm{W\,m^{-1}\,K^{-1}}$
Top	357.1	0.104
Mid 1	316.3	0.084
Mid 2	296.4	0.044
Bottom	295.2	0.036

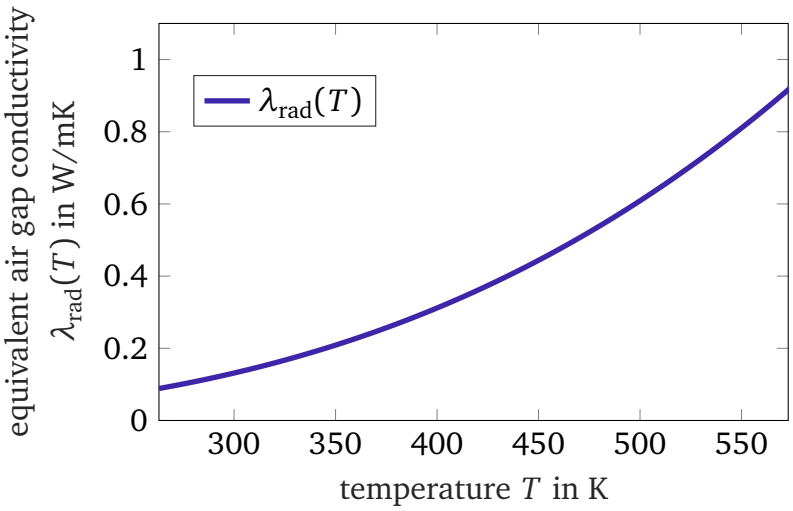

Figure A.1.: Nonlinear radiative equivalent thermal conductivity λ_{rad} of the 550-kV-station class arrester.

Table A.3.: Material properties of the reduced-diameter 550-kV-station class arrester (see [Gie18]).

Name	Unit	Value
total arrester height	mm	4216
height of single unit, h	mm	902
height of ZnO stack per unit	mm	652
ZnO stack radius, ϱ_1	mm	23.9
housing, inner radius, ϱ_2	mm	68
housing, outer radius	mm	100
ZnO thermal conductivity	$\mathrm{W\,m^{-1}\,K^{-1}}$	21.5
ZnO volumetric heat capacity	$\mathrm{J\,cm^{-3}\,K^{-1}}$	2.63
ZnO emissivity, $\varepsilon_{\mathrm{rad},1}$	–	0.96
porcelain relative permittivity	–	6
porcelain thermal conductivity	$\mathrm{W\,m^{-1}\,K^{-1}}$	1.6
porcelain volumetric heat capacity	$\mathrm{J\,cm^{-3}\,K^{-1}}$	2.16
porcelain emissivity, $\varepsilon_{\mathrm{rad},2}$	–	0.85
flange emissivity	–	0.25
external convection coefficient	$\mathrm{W\,m^{-2}\,K^{-1}}$	3

Table A.4.: Material properties of the IEC surge arrester.

Material	ε_r	λ in $\mathrm{W\,m^{-1}\,K^{-1}}$	ε_{rad}	c_v in $\mathrm{J\,cm^{-3}\,K^{-1}}$
ZnO	800	23	0.96	2.59
porcelain	5.0	4.0	0.85	2.34
external heat transfer	α_{ht} in $\mathrm{W\,m^{-2}\,K^{-1}}$	ε_{rad}		
porcelain	5	0.77		
aluminum flange	3	0.25		

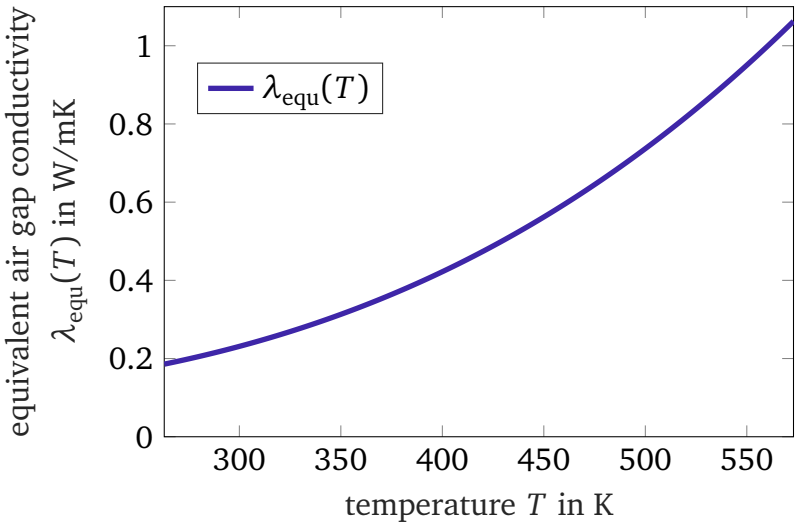

Figure A.2.: Equivalent conductivity of the IEC arrester unit air gap.

A.3 Thermal Equivalent

Table A.5.: Specification of the thermal equivalent.

Name	Value
height of the porcelain housing	72 mm
height of a zinc oxide resistor	35.7 mm
height of an aluminum disc	5 mm
inner diameter of the porcelain housing	141 mm
diameter of the zinc oxide resistor and the aluminum disc	70 mm
continuous operating voltage U_c	9.1 kV
rated voltage U_r	11.375 kV
residual voltage U_{res}	26 kV

Table A.6.: Material data of the thermal equivalent.

Material	ε_r	σ in Sm^{-1}	C_v in $J\,cm^{-3}\,K^{-1}$	λ in $W\,m^{-1}\,K^{-1}$
copper	1	∞	3.45	401
aluminum	1	∞	0.87	160
ZnO	Fig. 4.3	see Fig. 4.3	4.1	$\lambda = 23.868 - 0.0269T$
air	1	0	0.001297	0
cork	1.23	1.2×10^{-10}	0.4	0.04
wood	2	1×10^{-13}	1.2	0.16
porcelain	5	0	2.34	4

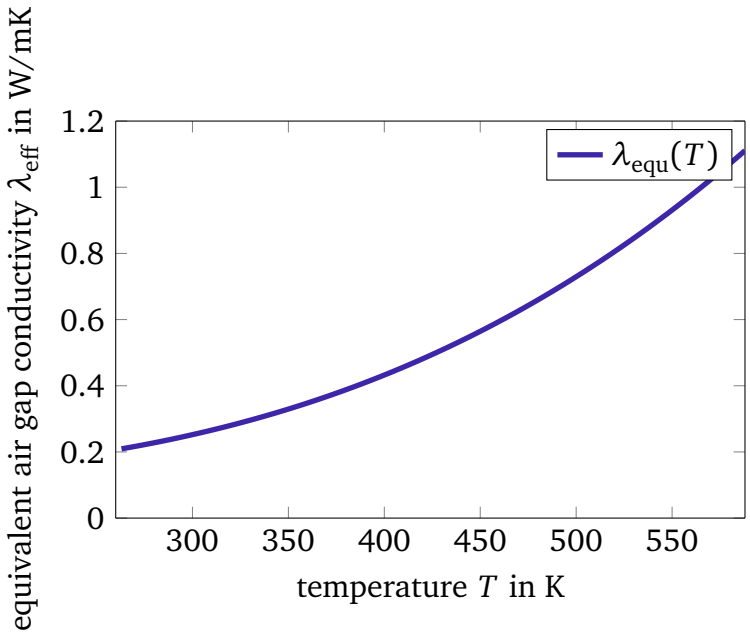

Figure A.3.: Effective conductivity λ_{eff} for the thermal equivalent air gap.

Bibliography

[ABL91] K. Al Abdullah, A. Bui, and A. Loubiere. “Low frequency and low temperature behavior of ZnO-based varistor by ac impedance measurements”. In: *Journal of Applied Physics* 69.7 (Apr. 1991), pp. 4046–4052. DOI: 10.1063/1.348414 (cit. on p. 51).

[Alj16] Florent Alji. “Modellierung des konvektiven Wärmeübergangs für Überspannungsableiter”. Bachelor’s Thesis. Technische Universität Darmstadt, 2016 (cit. on pp. 36, 67, 69, 159).

[All16] Yassine Allani. “Vergleich unterschiedlicher Methoden zur Bestimmung der Leitfähigkeit und Permittivität von Metalloxidvaristoren”. Bachelor’s Thesis. Technische Universität Darmstadt, 2016 (cit. on pp. 51, 88, 159).

[Bar+96] M. Bartkowiak, G. D. Mahan, F. A. Modine, and M. A. Alim. “Influence of ohmic grain boundaries in ZnO varistors”. In: *Journal of Applied Physics* 79.1 (Jan. 1996), pp. 273–281. DOI: 10.1063/1.362708 (cit. on p. 20).

[BCM96] M. Bartkowiak, M. G. Comber, and G. D. Mahan. “Energy handling capability of ZnO varistors”. In: *Journal of Applied Physics* 79.11 (1996), pp. 8629–8633. DOI: 10.1063/1.362484 (cit. on p. 22).

[Ber19] Christian Bergfried. “Electrothermal Analysis of a Pluggable Station Class Surge Arrester Grading System”. Bachelor’s Thesis. Technische Universität Darmstadt, 2019 (cit. on p. 159).

[BG86] Gianni Blatter and Felix Greuter. “Carrier transport through grain boundaries in semiconductors”. In: *Physical Review B* 33.6 (Mar. 1986), pp. 3952–3966. DOI: 10.1103/physrevb.33.3952 (cit. on p. 20).

[BGW14] Konstantinos Bavelis, Erion Gjonaj, and Thomas Weiland. “Modeling of electrical transport in Zinc Oxide varistors”. In: *Advances in Radio Science* 12 (2014), pp. 29–34. DOI: 10.5194/ars-12-29-2014 (cit. on p. 20).

[Bla15] Sébastien Blatt. “Untersuchungen zu einem möglichen Einsatz von Mikrovaristoren in der Isolation umrichtergespeister Antriebe”. PhD thesis. Technische Universität Darmstadt, 2015 (cit. on pp. 22, 51).

[Boe14] Sandra Boetcher. *Natural Convection from Circular Cylinders*. SpringerBriefs in Applied Sciences and Technology. Springer International Publishing, 2014 (cit. on p. 61).

[Cam80] Josef Sebastian Cammerer. *Der Wärme- und Kälteschutz in der Industrie*. Springer, 1980 (cit. on p. 64).

[CC75] Stuart W. Churchill and Humbert H.S. Chu. "Correlating equations for laminar and turbulent free convection from a vertical plate". In: *International Journal of Heat and Mass Transfer* 18.11 (1975), pp. 1323–1329. DOI: https://doi.org/10.1016/0017-9310(75)90243-4 (cit. on p. 61).

[CDG10] Thomas Christen, Lise Donzel, and Felix Greuter. "Nonlinear resistive electric field grading part 1: Theory and simulation". In: *IEEE Electrical Insulation Magazine* 26.6 (Nov. 2010), pp. 47–59. DOI: 10.1109/mei.2010.5599979 (cit. on p. 51).

[Cig13] Cigré Working Group A3.25. *MO Surge Arresters: Metal oxide varistors and surge arresters for emerging system conditions; Technical Broschure 696*. Ed. by Bernhard Richter, Adriano Dellallibera, Felix Greuter, Manfred Holzer, Yoshihiro Ishizaki, M. Kobayashi, Iryani M. Rawi, Maximilian Tuczek, Jonthan Woodworth, Mike Comber, Reinhard Göhler, Volker Hinrichsen, Shinji Ishibe, Bengt Johnnerfelt, Li Fan, Yvonne Späck-Leigsnering, Masatoshi Nakajima, and Ragnar Österlund. Paris: Cigré, 2017 (cit. on pp. 13, 14, 18, 19, 34, 86, 93, 104, 106).

[Cig17] Cigré Working Group A3.17. *MO Surge Arresters: Stresses and Test Procedures; Technical Broschure 544*. Ed. by Bernhard Richter, J.L. De Franco, Reinhard Göhler, Felix Greuter, Volker Hinrichsen, Manfred Holzer, S. Ishibe, Y. Ishizaki, B. Johnnerfelt, M. Kobayashi, K. Lahti, T.M. Ohnstad, R.S. Perkins, M. Reinhard, J.H. Sawada, and A. Sironi. Paris: Cigré, 2013 (cit. on pp. 14, 16, 17, 19, 20, 22, 24, 25, 28, 54).

[Cla04] David R. Clarke. "Varistor Ceramics". In: *Journal of the American Ceramic Society* 82.3 (Dec. 2004), pp. 485–502. DOI: 10.1111/j.1151-2916.1999.tb01793.x (cit. on pp. 19–21, 51).

[Cle+06] Markus Clemens, Thorsten Steinmetz, Daniel Weida, and Volker Hinrichsen. "Coupled Thermal-Electroquasistatic 3D Field Simulation of High-Voltage Surge Arrester Structures". In: *Computational Electromagnetics Conference (CEM)*. Aachen, Germany, Apr. 2006 (cit. on p. 14).

[Cos+14] Edson G. Costa, Rafael M.R. Barros, Helem M.M. Alves, and Marcelo A. Bastos. "Thermal behavior analysis of ZnO polymeric surge arrester using the finite elements method". In: *High Voltage Engineering and Application (ICHVE), 2014 International Conference on*. Sept. 2014, pp. 1–4. DOI: 10.1109/ICHVE.2014.7035395 (cit. on p. 30).

[DAn16] Laura A. M. D'Angelo. "Quasi-3D Finite-Element Method for Electroquasistatic-Thermal Simulation of High-Voltage Arresters". Bachelor's Thesis. Technische Universität Darmstadt, 2016 (cit. on p. 159).

[Day+13] Jerod Day, Matthew Zemler, Matthew Traum, and Boetcher Sandra. “Laminar Natural Convection From Isothermal Vertical Cylinders: Revisting a Classical Subject”. In: *ASME Journal of Heat Transfer* 135.2 (2013). DOI: http://dx.doi.org/10.1115/1.4007421 (cit. on p. 61).

[Den14] Frank Denz. “Modeling and Simulation of Varistor-Related Problems”. PhD thesis. Technische Universität Darmstadt, Apr. 2014 (cit. on pp. 22, 31, 36, 39, 41, 43, 50, 51, 71, 73, 74, 87, 88).

[DGC11] Lise Donzel, Felix Greuter, and Thomas Christen. “Nonlinear resistive electric field grading Part 2: Materials and applications”. In: *IEEE Electrical Insulation Magazine* 27.2 (Mar. 2011), pp. 18–29. DOI: 10.1109/mei.2011.5739419 (cit. on p. 14).

[DMM97] J. P. Ducreux, G. Marques, and F. Macula. “Electro-thermal behavior of metal oxide surge arresters : numerical modeling by resolution of Maxwell’s equations in a nonlinear complex permittivity dielectric”. In: *10th International Symposium on High Voltage Engineering*. Aug. 1997 (cit. on p. 30).

[DSD19] Laura A. M. D’Angelo, Yvonne Späck-Leigsnering, and Herbert De Gersem. “Electroquasistatic quasi-3D finite element simulation of a graded surge arrester”. In: *International Journal of Numerical Modelling: Electronic Networks, Devices and Fields* (2019), e2575. DOI: 10.1002/jnm.2575 (cit. on pp. 34, 94).

[Dür10] Annette D. Düren. “Auswirkung von Temperaturschiefverteilungen auf die thermische Stabilität eines 550 kV- Überspannungsableiters”. MA thesis. Darmstadt: Technische Universität Darmstadt, Mar. 2010 (cit. on pp. 41, 87).

[EA03] H. Elayyan and S. Al-Refaie. “Dielectric relaxation assessment of a heat treated metal oxide varistor”. In: *IEE Proceedings - Science, Measurement and Technology* 150.4 (July 2003), pp. 141–147. DOI: 10.1049/ip-smt:20030453 (cit. on p. 51).

[Eda89] Kazuo Eda. “Zinc Oxide Varistors”. In: *IEEE Electrical Insulation Magazine* 5.6 (Dec. 1989), pp. 28–41 (cit. on pp. 19, 20).

[Eig40] Louis Eigenson. “Les lois gouvernant la transmission de la chaleur aux gaz biatomiques par les parois des cylindres verticaux dans le cas de convection naturelle”. In: *Dokl. Akad. Nauk SSSR*. Vol. 26. 1940, pp. 440–444 (cit. on p. 62).

[Fer+03] D. Fernandez-Hevia, J. de Frutos, A. Caballero, and A. Fernandez. “Bulk-grain resistivity and positive temperature coefficient of ZnO-based varistors”. In: *Applied Physics Letters* 82.2 (2003) (cit. on p. 111).

[FLD11] Oliver Fritz, Marlene Ljuslinder, and Bernhard Doser. “Heat Transfer in High-Voltage Surge Arresters”. In: *Proceedings of the COMSOL Conference*. Stuttgart, 2011 (cit. on p. 30).

[Fro+18] Saskia Josefine Frobin, Claudius Freye, Christoph Felix Niedik, Frank Jenau, Dominik Haering, and Gero Schroeder. “Thermal Modelling of HVDC Cables under Consideration of Measured Temperature Profiles”. In: *VDE ETG – Fachtagung Hochspannungstechnik 2018*. (Berlin). Nov. 2018 (cit. on p. 14).

[Gie+16] Moritz Gießel, Volker Hinrichsen, Reinhard Göhler, Yvonne Späck-Leigsnering, Erion Gjonaj, and Herbert De Gersem. “Einfluss unterschiedlicher Steuerringkonfigurationen auf die thermische Stabilität von Überspannungsableitern”. In: *VDE-Fachtagung Hochspannungstechnik 2016*. Nov. 2016 (cit. on pp. 36, 41, 87, 89, 106).

[Gie+17a] Moritz Gießel, Volker Hinrichsen, Reinhard Göhler, Yvonne Späck-Leigsnering, Erion Gjonaj, and Herbert De Gersem. “Electro-Thermal Simulations of High Voltage Metal-Oxide Surge Arresters with and without installed Grading Rings with regard to Thermal Stability”. In: *CIGRÉ Winnipeg 2017 Colloquium*. 2017 (cit. on pp. 36, 95).

[Gie+17b] Moritz Gießel, Volker Hinrichsen, Reinhard Göhler, Yvonne Späck-Leigsnering, Erion Gjonaj, and Herbert De Gersem. “Electro-Thermally Coupled Finite-Element Simulations of High Voltage Station Arresters with and without Grading”. In: *2017 INMR World Congress*. Nov. 2017 (cit. on p. 36).

[Gie18] Moritz Gießel. “Elektrothermisches Verhalten von Hochspannungs–Metalloxid–Ableitern mit reduzierten Steuersystemen in Wechselspannungsnetzen”. PhD thesis. Technische Universität Darmstadt, 2018 (cit. on pp. 13, 18, 34, 39, 41, 42, 51, 60, 61, 66, 86–88, 93, 111, 113, 135, 139).

[Göh+10] Reinhard Göhler, M. Schubert, K. Weck, Volker Hinrichsen, Maximilian Nikolaus Tuczek, Markus Clemens, and R. Appel. “Special Requirements on Surge Arrester Design for UHV A.C. Systems above 800 kV System Voltage”. In: *CIGRÉ Konferenz Report A3-104-2010*. Paris, Aug. 2010 (cit. on pp. 13, 93).

[Haf87] Christian Hafner. *Numerische Berechnung Elektromagnetischer Felder: Grundlagen, Methoden, Anwendungen*. Springer, 1987 (cit. on p. 72).

[Han+05] S. J. Han, J. Zou, S. Q. Gu, J. L. He, and J. S. Yuan. “Calculation of the potential distribution of high voltage metal oxide arrester by using an improved semi-analytic finite element method”. In: *IEEE Transactions on Magnetics* 41.5 (May 2005), pp. 1392–1395. DOI: 10.1109/TMAG.2005.844350 (cit. on p. 93).

[He+09] Jinliang He, Jun Hu, Shanqiang Gu, Bo Zhang, and Rong Zeng. “Analysis and Improvement of Potential Distribution of 1000-kV Ultra-High-Voltage Metal-Oxide Arrester”. In: *IEEE Transactions on Power Delivery* 24.3 (July 2009), pp. 1225–1233. DOI: 10.1109/TPWRD.2009.2014034 (cit. on pp. 30, 58, 93).

[HGT15] Volker Hinrichsen, Moritz Gießel, and Maximilian Tuczek. “Thermal Stability of HV and UHV Arresters with Reduced Grading Systems”. In: *The 2015 INMR World Congress on Insulators, Arresters, Bushings & Cable Accessories*. Munich, Oct. 2015 (cit. on pp. 13, 14, 19, 25, 86, 93, 106, 113).

[Hil99] Andrew R. Hileman. *Insulation Coordination for Power Systems*. Taylor & Francis Inc, June 15, 1999. 767 pp. (cit. on p. 13).

[Hin+08] Volker Hinrichsen, Reinhard Göhler, Markus Clemens, Thorsten Steinmetz, and P. Riffon. “External Grading Systems for UHV Metal-Oxide Surge Arresters - A New Approach to Numerical Simulation and Dielectric Testing”. In: *CIGRÉ Konferenz Report A3-205*. Paris, Mar. 2008 (cit. on pp. 13, 30, 58, 95).

[Hin11] Volker Hinrichsen. *Metal-Oxide Surge Arresters in High-Voltage Power Systems - Fundamentals*. 3rd. Siemens AG, 2011 (cit. on pp. 13–22, 25, 27, 104, 135).

[Hin12] Volker Hinrichsen. *Metalloxid-Ableiter in Hochspannungsnetzen - Grundlagen*. 3rd. Siemens AG, 2012 (cit. on p. 22).

[Hin14] Volker Hinrichsen. “Overview of IEC Standards’ recommendations for lightning protection of electrical high-voltage power systems using surge arresters”. In: *Lightning Protection (ICLP), 2014 International Conference on*. Oct. 2014, pp. 1701–1707. DOI: 10.1109/ICLP.2014.6973402 (cit. on p. 22).

[Hin90] Volker Hinrichsen. “Simulation des elektrischen und thermischen Verhaltens von funkenstreckenlosen Metalloxid-Ableitern bei Betrieb an Wechselspannung”. PhD thesis. Technische Universität Berlin, 1990 (cit. on pp. 25, 30, 58, 60, 61, 64, 75, 137).

[HM89] Hermann A. Haus and James R. Melcher. *Electromagnetic Fields and Energy*. Prentice-Hall, 1989 (cit. on p. 75).

[HN12] Volker Hinrichsen and Mohammad H. Nazemi. *High Voltage Technology – Lecture Notes*. .1. Darmstadt: Fachgebiet Hochspannungstechnik, Technische Universität Darmstadt, 2012 (cit. on p. 13).

[HN98] A. Haddad and P. Naylor. “Finite-element computation of capacitance networks in multiple-electrode systems: application to ZnO surge arresters”. In: *IEE Proceedings - Science, Measurement and Technology* 145.4 (July 1998), pp. 129–135 (cit. on p. 30).

[HP89] Volker Hinrichsen and R. Peiser. “Simulation of the electrical and thermal behavior of metal oxide surge arresters under AC-stress”. In: *International Symposium on High Voltage Engineering*. New Orleans, LA, USA, Aug. 1989 (cit. on p. 30).

[IEC09] IEC 60099-4. *Surge arresters – Part 4: Metal-oxide surge arresters without gaps for a.c. systems*. 2.2. International Electrotechnical Commission (IEC), May 2009 (cit. on pp. 25–27, 30, 31, 43).

[IEC14] IEC 60099-4. *Surge arresters – Part 4: Metal-oxide surge arresters without gaps for a.c. systems*. 3rd ed. Geneva, Switzerland: International Electrotechnical Commission (IEC), June 2014 (cit. on pp. 14, 17, 18, 23–25, 28, 34, 39, 40, 42, 53, 55, 58, 79, 81, 93, 95, 103, 104, 110–113, 115).

[IEC17] IEC 60071-2. *Insulation co-ordination – Part 2: Application guidelines (Proposed horizontal standard)*. 3rd ed. International Electrotechnical Commission (IEC), 2017 (cit. on p. 15).

[KBM11] Frank Kreith, Mark Bohn, and Raj Manglik. *Principles of Heat Transfer*. 7th ed. Cengage Learning, Inc, 2011 (cit. on p. 62).

[Koc+18] Myriam Koch, Jens Hohloch, Isabell Wirth, Sebastian Sturm, Markus H. Zink, and Andreas Küchler. "Experimental and simulative analysis of the thermal behavior of high voltage cable joints". In: *VDE ETG – Fachtagung Hochspannungstechnik 2018*. (Berlin). Nov. 2018 (cit. on p. 14).

[Kos94] Arnulf Kost. *Numerische Methoden in der Berechnung elektromagnetischer Felder*. Springer-Lehrbuch. Springer Berlin, 1994 (cit. on p. 72).

[Küc17] Andreas Küchler. *Hochspannungstechnik*. 4th ed. Springer-Verlag GmbH, 2017 (cit. on p. 18).

[Lag+98] Jeffrey C. Lagarias, James A. Reeds, Margaret H. Wright, and Paul E. Wright. "Convergence Properties of the Nelder-Mead Simplex Method in Low Dimensions". In: *SIAM Journal of Optimization* 9 (1998), pp. 112–147 (cit. on pp. 95, 104).

[Lat83] M. V. Lat. "Thermal Properties of Metal Oxide Surge Arresters". In: *IEEE Transactions on Power Apparatus and Systems* PAS-102.7 (July 1983), pp. 2194–2202. DOI: 10.1109/TPAS.1983.318207 (cit. on pp. 22, 24, 28, 29, 58, 137).

[LNS04] R.W. Lewis, P. Nithiarasu, and K.N. Seetharamu. *Fundamentals of the finite element method for heat and fluid flow*. Wiley, 2004. DOI: 10.1002/0470014164 (cit. on p. 76).

[Lou19] Dimitrios Loukrezis. "Adaptive approximations for high-dimensional uncertainty quantification in stochastic parametric electromagnetic field simulations". PhD thesis. Technische Universität Darmstadt, 2019 (cit. on p. 135).

[LP75] Lionel M. Levinson and Herbert R. Philipp. "The physics of metal oxide varistors". In: *Journal of Applied Physics* 46.3 (Mar. 1975), pp. 1332–1341. DOI: 10.1063/1.321701 (cit. on pp. 20, 22).

[LP77] Lionel Levinson and Herbert Philipp. "ZnO Varistors for Transient Protection". In: *IEEE Transactions on Parts, Hybrids, and Packaging* 13.4 (Dec. 1977), pp. 338–343. DOI: 10.1109/tphp.1977.1135218 (cit. on pp. 20, 22).

[Mat71] Michio Matsuoka. “Nonohmic Properties of Zinc Oxide Ceramics”. In: *Japanese Journal of Applied Physics* 10.6 (June 1971), pp. 736–746. DOI: 10.1143/jjap.10.736 (cit. on pp. 16, 19).

[McA54] William H. McAdams. “Heat Transmission”. In: *Science* 120.3128 (1954), pp. 984–984. DOI: 10.1126/science.120.3128.984 (cit. on pp. 62, 63).

[Mor73] William G. Morris. “Electrical Properties of ZnO-Bi2O3 Ceramics”. In: *Journal of the American Ceramic Society* 56.7 (July 1973), pp. 360–364. DOI: 10.1111/j.1151-2916.1973.tb12686.x (cit. on p. 51).

[Net+04] E. T. W. Neto, E. G. da Costa, M. J. A. Maia, T. C. L. Galindo, and A. H. S. Costa. “Electro-thermal Simulation of ZnO Arresters for Diagnosis Using Thermal Analysis”. In: *2004 IEEE/PES Transmission and Distribution Conference and Exposition: Latin America (IEEE Cat. No. 04EX956)*. Nov. 2004, pp. 338–343 (cit. on p. 30).

[OO11] Dietrich Oeding and Bernd R. Oswald. *Elektrische Kraftwerke und Netze*. Springer Berlin Heidelberg, 2011. DOI: 10.1007/978-3-642-19246-3 (cit. on p. 13).

[Pop08] Czeslaw O. Popiel. “Free Convection Heat Transfer from Vertical Slender Cylinders: A Review”. In: *Heat Transfer Engineering* 29.6 (2008), pp. 521–536. DOI: 10.1080/01457630801891557 (cit. on p. 61).

[Rei09] Max Reinhard. “Experimentelle Untersuchungen zum Einzelimpulsenergieaufnahmevermögen von Metalloxidwiderständen eingesetzt in Hochspannungsnetzen unter Berücksichtigung eines komplexen Fehlerkriteriums”. Dissertation. TU Darmstadt, 2009 (cit. on p. 22).

[Ric11] Bernhard Richter, ed. *Overvoltage protection metal oxide surge arresters in medium voltage systems*. 5th ed. ABB Switzerland Ltd., May 2011 (cit. on pp. 14–17, 19, 21, 22).

[RN08] P. V. Reddy and G.S.V.L. Narasimham. “Natural convection in a vertical annulus driven by a central heat generating rod”. In: *International Journal of Heat and Mass Transfer* 51.19 – 20 (2008), pp. 5024–5032. DOI: http://dx.doi.org/10.1016/j.ijheatmasstransfer.2008.02.032 (cit. on p. 64).

[Rup19] Maren Greta Ruppert. “Electrothermal Analysis of Station Class Arresters Under Impulse Operating Duties”. Bachelor’s Thesis. Technische Universität Darmstadt, 2019 (cit. on pp. 36, 37, 53, 79, 80, 124–127, 159).

[SAC12] Tom Schierz, Martin Arnold, and Christoph Clauß. “Co-simulation with communication step size control in an FMI compatible master algorithm”. In: *Proceedings of the 9th International Modelica Conference*. Munich, Germany, Sept. 2012 (cit. on p. 77).

[Sch16] Robin Scheich. “Modeling and Simulation of a Thermal Equivalent for Surge Arresters”. Bachelor’s Thesis. Technische Universität Darmstadt, 2016 (cit. on pp. 26, 28, 29, 36, 37, 45, 79, 91, 117, 159).

[SF96] Peter P. Silvester and Ronald L. Ferrari. *Finite Elements for Electrical Engineers*. 2nd ed. Cambridge, UK: Cambridge University Press, 1996 (cit. on p. 72).

[SGD17] Yvonne Späck-Leigsnering, Erion Gjonaj, and Herbert De Gersem. *Optimization Of Electric Field Grading Systems for Surge Arresters*. In: *URSI Kleinheubacher Tagung (KHB 2017)*. Miltenberg: U.R.S.I. Landesausschuss in der Bundesrepublik Deutschland e.V., Sept. 2017 (cit. on p. 35).

[SGD18a] Yvonne Späck-Leigsnering, Erion Gjonaj, and Herbert De Gersem. "Electrothermal Optimization of Grading Ring Geometries for Station Class Surge Arresters". In: *VDE ETG – Fachtagung Hochspannungstechnik 2018*. Berlin, Nov. 2018 (cit. on p. 35).

[SGD18b] Yvonne Späck-Leigsnering, Erion Gjonaj, and Herbert De Gersem. "Field Grading System Optimization of Station Class Surge Arresters". In: *URSI Kleinheubacher Tagung (KHB 2018)*. Miltenberg: U.R.S.I. Landesausschuss in der Bundesrepublik Deutschland e.V., Sept. 2018 (cit. on p. 35).

[SGD18c] Yvonne Späck-Leigsnering, Erion Gjonaj, and Herbert De Gersem. "Optimization of Grading Ring Systems for Station Class Surge Arresters". In: *18th International IGTE Symposium*. Graz: Graz University of Technology, Sept. 2018 (cit. on p. 35).

[SGD19] Yvonne Späck-Leigsnering, Erion Gjonaj, and Herbert De Gersem. "Electrothermal Optimization of Field Grading Systems of Station Class Surge Arresters". In: *IEEE Journal on Multiscale and Multiphysics Computational Techniques* 4 (2019), pp. 29–36. DOI: 10.1109/JMMCT.2019.2896630 (cit. on pp. 35–37, 96–101, 103, 105–108).

[SGW11] Harald Songoro, Erion Gjonaj, and Thomas Weiland. "Numerical simulation of water droplets in presence of strong electric-fields". In: *International Conference on Electromagnetics in Advanced Applications (ICEAA)*. Sept. 2011, pp. 504–507. DOI: 10.1109/ICEAA.2011.6046392 (cit. on p. 71).

[SHH17] Maximilian Secklehner, Rashid Hussain, and Volker Hinrichsen. "Tailoring of new field grading materials for HVDC systems". In: *2017 INSUCON – 13th International Electrical Insulation Conference (INSUCON)*. IEEE, May 2017. DOI: 10.23919/insucon.2017.8097174 (cit. on p. 14).

[Sjö+10] Hans Sjöstedt, Lennart Stenström, David Pusch, and Jörg Ostrowski. "Voltage grading design of UHV surge arresters using 3D transient capacitive-resistive field simulations". In: *International Conference on High Voltage Engineering and Application (ICHVE)*. Oct. 2010, pp. 32–35. DOI: 10.1109/ICHVE.2010.5640871 (cit. on pp. 19, 30, 58, 93).

[Spä+15a] Yvonne Späck-Leigsnering, Erion Gjonaj, Herbert De Gersem, Thomas Weiland, Moritz Gießel, and Volker Hinrichsen. *Gekoppelte Simulation des elektrothermisch stabilen Dauerbetriebszustandes eines 550-kV-Freiluftableiters*. In: *URSI Kleinheubacher Tagung (KHB 2015)*. Miltenberg: U.R.S.I. Landesausschuss in der Bundesrepublik Deutschland e.V., Sept. 2015 (cit. on p. 35).

[Spä+15b] Yvonne Späck-Leigsnering, Erion Gjonaj, Herbert De Gersem, Thomas Weiland, Moritz Gießel, and Volker Hinrichsen. "Thermal analysis of a station class arrester model in continuous operation and under the operating duty test". In: *19th International Symposium on High Voltage Engineering*. Aug. 2015 (cit. on p. 35).

[Spä+16a] Yvonne Späck-Leigsnering, Erion Gjonaj, Herbert De Gersem, Thomas Weiland, Moritz Gießel, and Volker Hinrichsen. "Electroquasistatic-thermal modeling and simulation of station class surge arresters". In: *IEEE Transactions on Magnetics* 52.3 (Mar. 2016), pp. 1–4 (cit. on pp. 34, 36, 67).

[Spä+16b] Yvonne Späck-Leigsnering, Erion Gjonaj, Herbert De Gersem, Thomas Weiland, Moritz Gießel, and Volker Hinrichsen. "Investigation of thermal stability for a station class surge arrester". In: *IEEE Journal on Multiscale and Multiphysics Computational Techniques* 1 (2016), pp. 120–128 (cit. on pp. 34, 36, 37, 42, 43, 51, 76, 81, 84, 85, 112–114).

[Spä+17] Yvonne Späck-Leigsnering, Robin Scheich, Moritz Gießel, Erion Gjonaj, Herbert De Gersem, and Volker Hinrichsen. "Impulse Operating Duty Simulations for a Thermal Equivalent and a Station Class Arrester". In: *NUMELEC 2017*. Paris, France, Nov. 2017 (cit. on p. 35).

[Spä+19] Yvonne Späck-Leigsnering, Maren Greta Ruppert, Erion Gjonaj, Herbert De Gersem, and Volker Hinrichsen. "Thermal Instability Analysis of Station Class Arresters based on Electrothermal Finite Element Simulation". In: *20th Proceedings of the International Symposium on High Voltage Engineering (ISH)*. Budapest, Aug. 2019 (cit. on pp. 36, 37, 43, 44, 89, 123).

[Spä14] Yvonne Späck-Leigsnering. "Modeling and Simulation of a Station Class Surge Arrester". MA thesis. Darmstadt: TU Darmstadt, Nov. 2014 (cit. on pp. 36, 64, 65, 75, 76, 79, 80, 83).

[SPB15] Sebastian Sturm, Johannes Paulus, and Frank Berger. "Thermal-electrical interaction of losses in three-core submarine power cables". In: *19th International Symposium on High Voltage Engineering*. Aug. 2015 (cit. on p. 14).

[Ste+06] Thorsten Steinmetz, Moritz Helias, Georg Wimmer, Lars O. Fichte, and Markus Clemens. "Electro-Quasistatic Field Simulations Based on a Discrete Electromagnetism Formulation". In: *IEEE Trans. Magn.* 42.4 (Apr. 2006), pp. 755–758. DOI: 10.1109/TMAG.2006.872488 (cit. on pp. 30, 95).

[Ste+08] Thorsten Steinmetz, Nico Gödel, Georg Wimmer, Markus Clemens, Stefan Kurz, and Mario Bebendorf. “Efficient Symmetric FEM-BEM Coupled Simulations of Electro-Quasistatic Fields”. In: *IEEE Trans. Magn.* 44.6 (June 2008), pp. 1346–1349. DOI: 10.1109/TMAG.2008.915785 (cit. on pp. 30, 93).

[Ste98] Rolf Steinbuch. *Finite Elemente - Ein Einstieg*. Springer-Lehrbuch. Springer Berlin, 1998 (cit. on p. 72).

[Sto94] F. Richard Stockum. “Simulation of the nonlinear thermal behavior of metal oxide surge arresters using a hybrid finite difference and empirical model”. In: *IEEE Transactions on Power Delivery* 9.1 (Jan. 1994), pp. 306–313. DOI: 10.1109/61.277701 (cit. on p. 30).

[Str04] J. Strikwerda. *Finite Difference Schemes and Partial Differential Equations, Second Edition*. Society for Industrial and Applied Mathematics, 2004. DOI: 10.1137/1.9780898717938 (cit. on p. 71).

[TGD19] Kyle Taylor, Erion Gjonaj, and Herbert De Gersem. “Mesoscopic Modelling of ZnO Varistors”. In: *Proceedings of the IX ECCOMAS Thematic Conference on Smart Structures and Materials*. 2019 (cit. on pp. 20, 22).

[TH14] Maximilian Nikolaus Tuczek and Volker Hinrichsen. “Recent Experimental Findings on the Single and Multi-Impulse Energy Handling Capability of Metal-Oxide Varistors for Use in High-Voltage Surge Arresters”. In: *IEEE Transactions on Power Delivery* 29.5 (Oct. 2014), pp. 2197–2205. DOI: 10.1109/TPWRD.2013.2283911 (cit. on p. 88).

[Tor97] Virginia Torczon. “On the Convergence of Pattern Search Algorithms”. In: *SIAM Journal on Optimization* 7.1 (1997), pp. 1–25. DOI: 10.1137/S1052623493250780 (cit. on pp. 95, 104).

[Tuc15] Maximilian Nikolaus Tuczek. “Experimentelle Untersuchungen zur Mehrfachimpulsbelastbarkeit von Metalloxidvaristoren für Anwendungen in der elektrischen Energietechnik”. PhD thesis. Darmstadt: Technische Universität Darmstadt, Jan. 2015 (cit. on pp. 22, 54).

[VC97] Agnes Vojta and David R. Clarke. “Microstructural origin of current localization and “puncture” failure in varistor ceramics”. In: *Journal of Applied Physics* 81.2 (Jan. 1997), pp. 985–993. DOI: 10.1063/1.364226 (cit. on pp. 20, 22).

[VDI10] VDI-Gesellschaft Verfahrenstechnik und Chemieingenieurwesen, ed. *VDI Heat Atlas*. Springer, 2010 (cit. on pp. 36, 59–61, 64).

[WSC09] Daniel Weida, Thorsten Steinmetz, and Markus Clemens. “Electro-Quasistatic High Voltage Field Simulations of Large Scale Insulator Structures Including 2-D Models for Nonlinear Field-Grading Material Layers”. In: *IEEE Transactions on Magnetics* 45.3 (Mar. 2009), pp. 980–983. DOI: 10.1109/TMAG.2009.2012492 (cit. on p. 58).

[YCS13] Hanyu Ye, Markus Clemens, and Jens Seifert. “Electroquasistatic Field Simulation for the Layout Improvement of Outdoor Insulators Using Microvaristor Material”. In: *IEEE Transactions on Magnetics* 49.5 (May 2013), pp. 1709–1712. DOI: 10.1109/tmag.2013.2243423 (cit. on p. 14).

[ZB02] Zhong Zheng and Steven A. Boggs. “Efficient solution of transient nonlinear field problems”. In: *Conference on Electrical Insulation and Dielectric Phenomena, Annual Report*. 2002, pp. 130–133. DOI: 10.1109/CEIDP.2002.1048753 (cit. on p. 30).

[ZB03] Zhong Zheng and Steven A. Boggs. “Heat sink effects in thermal stability tests of ZnO arresters”. In: *Conference on Electrical Insulation and Dielectric Phenomena, Annual Report*. Oct. 2003, pp. 473–477. DOI: 10.1109/CEIDP.2003.1254895 (cit. on pp. 30, 111, 135).

[Zha+10] Chao Zhang, Jeffrey J. Kester, Charles W. Daley, and Stephen J. Rigby. “Electric field analysis of high voltage apparatus using finite element method”. In: *Electrical Insulation and Dielectric Phenomena (CEIDP), 2010 Annual Report Conference on*. Oct. 2010, pp. 1–4. DOI: 10.1109/CEIDP.2010.5723955 (cit. on pp. 30, 58).

[Zhe+10] Zhong Zheng, Steven A. Boggs, Toshiya Imai, and Ssusumu Nishiwaki. “Computation of Arrester Thermal Stability”. In: *IEEE Transactions on Power Delivery* 25.3 (July 2010), pp. 1526–1529. DOI: 10.1109/TPWRD.2010.2049163 (cit. on pp. 30, 31).

[ZR05] Peter Zeller and Michael Rabl. “Modell zur numerischen Simulation der thermischen Stabilität von Metalloxid Ableitern”. In: *Proceedings of the COMSOL Multiphysics User’s Conference*. Frankfurt, 2005 (cit. on p. 30).

List of Acronyms and Symbols

Acronyms

2D	2-dimensional
3D	3-dimensional
ac	alternating current
dc	direct current
DoFs	Degrees of Freedom
EM	electromagnetic
EQS	electro-quasistatic
EQST	coupled electro-quasistatic-thermal
FEM	finite element method
FE	finite element
MO	metal oxide
rms	root mean square
mr	multirate
p.u.	per unit
ZnO	zinc oxide
CFD	computational fluid dynamics

Symbols

A	surface
a	thermal diffusivity
B	finite element thermal boundary matrix
b	finite element thermal boundary vector
C	capacitance
C_d	differential capacitance
C_s	Stefan-Boltzmann constant
$c_\mathrm{p,v}$	specific heat and volumetric heat capacity

$\vec{D}$, $\boldsymbol{D}$	continuous and discrete electric displacement field
$\vec{E}$, $\boldsymbol{E}$	continuous and discrete electric field strength
e_{rel}	relative electric field deviation
f_{exc}	excitation frequency
g	acceleration due to gravity
Gr	GRASHOF number
$\vec{H}$	magnetic field strength
h	height along z
$\vec{J}$, $\boldsymbol{J}$	continuous and discrete current density
$\mathbf{K}_{\sigma}$,$\mathbf{K}_{\varepsilon}$	stiffness matrices
l	length of the virtual screen
l_{c}	convection length
l_{s}	length of the suspensions
$\mathbf{M}_{\mathrm{c_V}}$	mass matrix
dm	midpoint from the top electrode of the virtual electrode
$n_{\mathrm{period,el}}$	number of periods until an electric steady state is reached
Nu	NUSSELT number
Pr	PRANDTL number
Q	thermal energy
$\dot{Q}$	heat flow rate
$\dot{Q}_{\mathrm{eff}}$	effective heat flow rate
$\dot{Q}_{\mathrm{p}}$	electric loss of a zinc oxide resistor
$\dot{q}$	heat flux density
R	resistance
T	temperature
t	time
ΔT	temperature difference, $T_1 - T_2$
T_{amb}	ambient temperature
t_{gap}	interval between to impulse energy injections
T_{s}	steady state temperature
$\Delta t_{\mathrm{el,th}}$	electric and thermal time step, respectively
U_{basis}	voltage level basis for per unit computation
U_{c}	continuous operating voltage of a surge arrester
U_{ct}	corrected maximum continuous operating voltage of a surge arrester
u_j	DoFs for unknown potential
U_{L}	charging voltage of the impulse generator
U_{r}	rated voltage of a surge arrester
U_{res}	lightning impulse residual voltage
U_{s}	system voltage of a power grid
U_{sres}	switching impulse residual voltage of a surge arrester

V	volume
W_{imp}	injected electrical energy
W_{th}	rated thermal energy
W_{tot}	total injected energy
w_j	nodal shape function
X	virtual electrode parameters
Y	grading system parameters
Z	surge impedance of the power line
z	z-coordinate in cylindrical coordinates

Greek Symbols

α	nonlinearity exponent
α_{ht}	heat transfer coefficient
β	volumetric thermal expansion coefficient
Γ	line on the surface of a computational domain
δ	arrester gap width, $\varrho_1 - \varrho_2$
ε	electric permittivity
ε_{r}	relative permittivity
$\varepsilon_{\mathrm{rad}}$	emissivity
η	cooling rate
ϑ_j	DoFs for unknown temperature
λ	thermal conductivity
ν	kinematic viscosity
ξ	threshold of adaptive conductivity update
ρ	material density
ϱ	radius in cylindrical coordinates
σ	electric conductivity
$\widehat{\sigma}$	maximum sigma of an ac cycle
τ_{e}	charge relaxation time constant
τ_{el}	electro-quasistatic time constant
τ_{th}	thermal time constant
ϕ	electric potential
Ω	computational domain

Supervised Student Projects

In the context of this thesis, the following student projects were supervised:

- Florent Alji. “Modellierung des konvektiven Wärmeübergangs für Überspannungsableiter”. Bachelor’s Thesis. Technische Universität Darmstadt, 2016
- Yassine Allani. “Vergleich unterschiedlicher Methoden zur Bestimmung der Leitfähigkeit und Permittivität von Metalloxidvaristoren”. Bachelor’s Thesis. Technische Universität Darmstadt, 2016
- Christian Bergfried. “Electrothermal Analysis of a Pluggable Station Class Surge Arrester Grading System”. Bachelor’s Thesis. Technische Universität Darmstadt, 2019
- Laura A. M. D’Angelo. “Quasi-3D Finite-Element Method for Electroquasistatic-Thermal Simulation of High-Voltage Arresters”. Bachelor’s Thesis. Technische Universität Darmstadt, 2016
- Maren Greta Ruppert. “Electrothermal Analysis of Station Class Arresters Under Impulse Operating Duties”. Bachelor’s Thesis. Technische Universität Darmstadt, 2019
- Robin Scheich. “Modeling and Simulation of a Thermal Equivalent for Surge Arresters”. Bachelor’s Thesis. Technische Universität Darmstadt, 2016

Erklärung laut Promotionsordnung

§ 8 Abs. 1 lit. c PromO

Ich versichere hiermit, dass die elektronische Version meiner Dissertation mit der schriftlichen Version übereinstimmt.

§ 8 Abs. 1 lit. d PromO

Ich versichere hiermit, dass zu einem vorherigen Zeitpunkt noch keine Promotion versucht wurde. In diesem Fall sind nähere Angaben über Zeitpunkt, Hochschule, Dissertationsthema und Ergebnis dieses Versuchs mitzuteilen.

§ 9 Abs. 1 PromO

Ich versichere hiermit, dass die vorliegende Dissertation selbstständig und nur unter Verwendung der angegebenen Quellen verfasst wurde.

§ 9 Abs. 2 PromO

Die Arbeit hat bisher noch nicht zu Prüfungszwecken gedient.

Mühltal, den 02.07.2019,

Yvonne Thea Katharina Späck-Leigsnering